

IN-PLANE SHEAR BEHAVIOR OF GEOSYNTHETICS  
FROM BIAS BIAXIAL TESTS  
USING DIGITAL IMAGE CORRELATION

by

Emily Christine Schultz

A thesis submitted in partial fulfillment  
of the requirements for the degree

of

Master of Science

in

Civil Engineering

MONTANA STATE UNIVERSITY  
Bozeman, Montana

June 2019

©COPYRIGHT

by

Emily Christine Schultz

2019

All Rights Reserved

## DEDICATION

Wisdom, insight, and understanding are gifts from God, as is each day's work (Proverbs 2:6, Ecclesiastes 5:19). Apart from Him we can do nothing; with Him all things are possible (John 15:5, Matthew 19:26).

“We were burdened excessively, beyond our strength, so that we despaired ... indeed, we had the sentence of death within ourselves so that we would not trust in ourselves, but in God who raises the dead; ... He on whom we have set our hope. And He will yet deliver us.” (2 Corinthians 1:8b-10)

To God alone be the glory!

## ACKNOWLEDGEMENTS

To my fiancé, Andy, my parents, Kurt and Christine, and my soon-to-be in-laws, Kelly and Marie: thank you for all your encouragement and help during these last two years. I am also thankful for support from my brother, Steven, and from my friends.

I am very thankful for Dr. Steve Perkins' guidance and assistance throughout this project and for the invitation to do this research under him. Also, special thanks to Dr. Ladean McKittrick for the use of his personal Canon camera and associated Canon software, for the use of DIC software in the Subzero Lab at Montana State University (MSU), and for many hours of troubleshooting assistance. Thanks also to Eli Cuelho, who designed and built the biaxial device, and to Henry Haselton, who taught me how to use it and who developed the initial testing protocols and numerical analysis tools.

Thanks to Stephen Valero and Hanes Geo for providing geosynthetics and to the Western Transportation Institute (WTI) for the use of lab facilities and storage space. Audrey Wooding with MSU Facilities and the research staff at Spectrum Labs were a great help in keeping testing active during lab remodeling. Thanks also to Daniel Samborski and Linnea Zavala for assistance with load cell recalibration and other items.

Finally, I am deeply grateful to my funding sponsors. First-year funding was provided by the National Science Foundation (award number 1635029) and a scholarship from the MSU Civil Engineering Department. Second-year funding was provided by the American Society of Civil Engineering through the Trent R. Dames and William W. Moore Fellowship and by generous scholarships from the Graduate School and the Civil Engineering Department.

## TABLE OF CONTENTS

1. INTRODUCTION .....	1
Background .....	1
Previous Work on Biaxial Testing of Geosynthetics .....	2
Scope of Work .....	3
2. LITERATURE REVIEW.....	4
Introduction.....	4
In-Plane Shear Tests for Fabrics and Planar Polymeric Materials .....	5
Derivation of Shear Stress and Shear Strain Equations .....	8
Biaxial Testing Devices .....	12
Specimen Details .....	15
Loading Protocols .....	18
Shear Behavior .....	24
Digital Image Correlation .....	30
DIC on Geosynthetics .....	30
DIC on Biaxial Tests of Non-geosynthetics .....	36
Camera Systems.....	40
Synthesis of Literature Review .....	41
3. THEORY .....	44
Introduction.....	44
Constitutive Equations for Shear Modulus .....	44
Assumptions to be Checked.....	48
4. TESTING PROCEDURE DEVELOPMENT .....	49
Testing Procedure Objective.....	49
Biaxial Testing Overview .....	50
Biaxial Test Frame.....	52
Load Data Collection Rate.....	54
LVDT Validation of DIC Strain Measurement .....	54
Sample Preparation .....	54
DIC Strain Data Collection.....	60
DIC Stochastic Pattern Development .....	60
Camera Overview .....	63
Camera Jig and Focus .....	64
Camera Lighting .....	65
Strain Data Preprocessing .....	66
Timestamping .....	67

## TABLE OF CONTENTS CONTINUED

Data Reduction.....	67
Conversion to Image Stack.....	68
Data Reduction for Long-Term Tests.....	68
DIC Software .....	69
DIC Process Overview.....	69
Facet Parameters .....	71
Surface Creation and Stochastic Pattern Recognition .....	71
Segment Creation and Strain Export.....	73
Postprocessing.....	74
Strain Data Reduction.....	74
Line Load Conversion.....	77
Load-Strain Curve Generation.....	79
DIC Strain Error Detection.....	79
<b>5. VALIDATION OF STRAIN DATA ASSUMPTIONS .....</b>	<b>81</b>
Overview.....	81
LVDT-DIC Strain Comparison.....	82
Strain Uniformity Analysis.....	84
Geogrid Strain Uniformity.....	93
Geotextile Strain Uniformity .....	114
Strain Uniformity Summary and Discussion .....	126
Zero Shear Strain Assumption Check.....	129
Summary and Conclusions .....	145
<b>6. SHEAR MODULUS RESULTS .....</b>	<b>147</b>
Overview.....	147
Shear Modulus Determination .....	147
Load per Unit Width versus Strain .....	148
Shear Stress-Strain Plots.....	153
Shear Modulus Curve-Fit Ranges.....	161
Material Comparisons.....	172
Comparison of Measured versus Calculated Shear Stresses.....	176
Sources of Error .....	182
Limited Sample Material .....	182
Material Alignment in Grips.....	182
Manual Control of Machine Loaded Axis .....	183
Manual Axis Loading .....	183
Grip Slippage .....	183
Fisheye in Camera Lens.....	184
Camera Setup.....	184

## TABLE OF CONTENTS CONTINUED

Surface Errors in GOM Correlate .....	185
Pixel Resolution .....	185
DIC Sensitivity at Low Displacement .....	185
Summary and Conclusions .....	186
7. SUMMARY AND RECOMMENDATIONS.....	189
Summary of Testing and Analysis .....	189
Recommendations for Future Work.....	191
Specimen Preparation Improvements .....	191
Filming and Data Collection Improvements.....	192
Data Processing Automation.....	193
Biaxial Device Improvements.....	194
Further Testing.....	195
Finite Element Modeling .....	198
REFERENCES CITED .....	199
APPENDICES .....	205
APPENDIX A: Plots of COV versus Strain in the Loading Directions	206
APPENDIX B: Shear Stress-Strain Plots .....	229
APPENDIX C: Shear Modulus Trendline Fit Plots.....	242
APPENDIX D: Calculated versus Measured Shear Stress Plots .....	268

## LIST OF TABLES

Table	Page
1. Summary of load protocols discussed in the literature .....	18
2. Differences between the shear loading histories from Gao et al. (2018). .....	22
3. Shear behavior reported in the literature. ....	24
4. Average shear modulus (kN/m) in second and third cycles from Gao et al. (2018) .....	28
5. Summary of materials and test types. ....	52
6. DIC stochastic pattern marking methods. ....	61
7. Canon camera settings .....	64
8. DIC software parameters .....	70
9. Approximate COV asymptotes. ....	128
10. Bias geotextile maximum average shear strain $\gamma_{xy}$ . ....	131
11. Bias geogrid estimated shear strain $\gamma_{xy}$ .....	134
12. Shear modulus values for three strain ranges.....	167
13. Shear modulus values for shear stress comparison. ....	178
14. Recommended shear modulus values. ....	187
15. Shear modulus values for shear stress comparison. ....	269

## LIST OF FIGURES

Figure	Page
1. Architectural membrane (polymer-coated fiberglass) showing double curvature (Birdair Inc. 2004). .....	5
2. Picture frame test (left); bias-biaxial test (right) (Colman et al. 2014) .....	7
3. Preloaded tension/compression bias biaxial test (Galliot and Luchsinger 2010). .....	8
4. Mohr's circle stress transformations for bias-biaxial tests (Gunderson and Rowlands 1983).....	9
5. Three-extensometer method for obtaining shear strain (Galliot and Luchsinger 2010). .....	10
6. Biaxial testing device and cruciform sample from Galliot and Luchsinger (2010). .....	13
7. Shear ramp on a traditional (non-bias) cruciform sample (Galliot and Luchsinger 2010). .....	13
8. Biaxial testing device at the Chinese Space Structures Research Center (Gao et al. 2018, Chen et al. 2018, Shi et al. 2018).....	15
9. Biaxial sample from Chen et al. (2018) showing arm slits and corner radii. ....	17
10. Non-bias (0/90) shear ramp specimen (top); 45-degree bias specimen with 0/90 non-bias welded arms (bottom) from Galliot and Luchsinger (2010). .....	17
11. Example load history after Mollaert et al. (2016).....	19
12. Cyclic test profile (shear angle versus time) from Colman et al. (2014). .....	20
13. Cyclic test profile from Shi et al. (2018). .....	21
14. Three types of cyclic shear loading performed by Gao et al. (2018). .....	22

## LIST OF FIGURES CONTINUED

Figure	Page
15. Stress-stress-strain surface for biaxial shear test (Galliot and Luchsinger 2010). .....	23
16. Concaved load-strain response from Sharma et al. (2003) showing lock-up at 65-70 degrees of shear.....	25
17. Bias-biaxial shear stress-strain curves from Galliot and Luchsinger (2010).....	26
18. Shear stress-strain plots from Shi et al. (2018). .....	27
19. Shear stress-strain curves from Gao et al. (2018).....	29
20. Typical image frame for Aydilek et al. (2004) .....	32
21. Poisson-induced horizontal strain fields for woven geotextiles in uniaxial loading (Mishra et al. 2017).....	34
22. DIC results for a polymer geotextile in uniaxial loading (Mishra et al. 2017) .....	35
23. Shear strain uniformity of architectural membrane (Galliot and Luchsinger 2010). .....	38
24. Shear strain uniformity for 45/45 bias test on architectural membrane (Gao et al. 2018).....	38
25. Biaxial test specimen oriented at a 45-degree bias to the loading directions.....	45
26. Assumed state of stress and strain in a bias biaxial test specimen.....	46
27. Transformation of strain. ....	46
28. Transformation of stress. ....	47
29. Biaxial testing device at MSU. ....	53
30. Initial adhesive reinforcement masking pattern.....	55
31. Strain in loading direction, initial adhesive reinforcement pattern.....	56

## LIST OF FIGURES CONTINUED

Figure	Page
32. Geotextile sample showing dimensions, fully glued arms, and 6-12-6-18-6-12-6 slit pattern.....	58
33. Strain in loading direction, full adhesive reinforcement with 2 inch slit spacing and 6-12-6-18-6-12-6 inch slit lengths .....	59
34. Stochastic pattern development .....	62
35. High contrast green background with white spray paint speckle.....	63
36. Left: Through-hole focus mechanism. Right: Rigid camera jig. ....	65
37. Left: Lamps. Right: Light diffuser sheet.....	66
38. GOM Correlate surface quality report generated during surface creation.....	72
39. Typical concentric regions for strain averages .....	75
40. Segments and strain field in the X loading direction for a woven sample (GtA).....	76
41. Segments and strain field in the Y loading direction for a woven sample. ....	77
42. Bias biaxial geogrid (GgE) showing width calculation for MD and XMD arms.....	78
43. Bias biaxial geogrid (GgF) showing width calculation for MD and XMD arms.....	79
44. DIC self-detected erroneous node locations (red) and misidentified node (yellow circles).....	80
45. LVDT-DIC strain data comparison.....	83
46. Typical concentric regions for strain averages for non-bias tests.....	87
47. Typical concentric regions for strain averages for bias tests. ....	88
48. Regional trends of strain uniformity: bias square geogrid.....	89

## LIST OF FIGURES CONTINUED

Figure	Page
49. Regional trends of strain uniformity: bias rectangular geogrid .....	90
50. Regional trends of strain uniformity: non-bias square geogrid .....	91
51. Regional trends of strain uniformity: non-bias rectangular geogrid .....	92
52. Strain heatmaps from GgE bias trial 6 (Mode 3) .....	95
53. Strain heatmaps from GgE bias trial 6 (Mode 3), continued .....	96
54. Strain heatmaps from GgE bias trial 6 (Mode 3), continued .....	97
55. Typical COV trend for bias square geogrids .....	98
56. Worst COV trend for bias square geogrids .....	99
57. Typical COV trend for bias square geogrids .....	100
58. Strain heatmaps from GgB bias trial 2 .....	103
59. Strain heatmaps from GgA bias trial 1 .....	104
60. Typical COV trend for bias rectangular geogrids .....	105
61. Least typical COV trend for bias rectangular geogrids .....	106
62. Strain heatmaps from non-bias GgC (Mode 1) .....	109
63. Strain heatmaps from non-bias GgC (Mode 1), continued .....	110
64. Strain heatmaps from non-bias GgB (Mode 1) .....	111
65. Statistical strain uniformity (GgC non-bias Mode 1, monotonic test) .....	112
66. Statistical strain uniformity (GgB non-bias Mode 1, monotonic test) .....	113
67. Strain heatmaps from bias GtB. Strain in X .....	117
68. Strain heatmaps from bias GtB (continued). Strain in Y .....	118

## LIST OF FIGURES CONTINUED

Figure	Page
69. Strain heatmaps from bias GtB. Strain in X .....	119
70. Strain heatmaps from bias GtB (continued). Strain in Y .....	120
71. Type 1 COV trend for geotextiles (GtA bias trial 3) .....	121
72. Type 2 COV trend for geotextiles (GtB bias trial 4).....	122
73. Strain heatmaps from non-bias GtB, monotonic test. Strain in X .....	124
74. Strain heatmaps from non-bias GtB, monotonic test (continued). Strain in Y .....	125
75. Statistical strain uniformity (GtB non-bias Mode 1, monotonic test).....	126
76. Left: Non-zero shear strain $\gamma_{xy}$ . Right: Zero shear strain $\gamma_{xy}$ . .....	129
77. Illustrated definition of $\epsilon_{xy}$ and $\gamma_{xy}$ .....	130
78. Folded paper template for 45-degree bias alignment at grips .....	134
79. GgF bias trial 1, stage 22, showing good biaxial behavior with minimal rotation.....	136
80. GgF bias trial 1, stage 122, showing clear rotational behavior later in the test.....	137
81. GgF bias trial 1, stage 122, showing X and Y components of displacement .....	138
82. GgD bias trial 1, stage 28, showing good biaxial behavior with minimal rotation.....	139
83. GgD bias trial 1, stage 76, showing clear rotational behavior later in the test .....	140
84. GgD bias trial 1, stage 76, showing X and Y components of displacement .....	141
85. Non-bias GgC, stage 40, showing excellent Mode 1 biaxial behavior.....	142

## LIST OF FIGURES CONTINUED

Figure	Page
86. Non-bias GgB, stage 31, showing excellent Mode 1 biaxial behavior.....	143
87. Vector analysis for non-bias Mode 1 geotextile test, stage 28, showing slight rotation.....	144
88. Line load vs. strain in the loading directions ( $\epsilon_x$ and $\epsilon_y$ ) (GgF bias trial 1). .....	150
89. Line load vs. strain in the loading directions ( $\epsilon_x$ and $\epsilon_y$ ) (GgE bias trial 6, Mode 3). .....	151
90. Line load vs. strain in the loading directions ( $\epsilon_x$ and $\epsilon_y$ ) (GtB bias trial 4). .....	152
91. Example square geogrid shear stress-strain plots .....	155
92. Shear stress-strain plot for GgE bias trial 4 showing initial low modulus slope. ....	156
93. Example rectangular geogrid shear stress-strain plots.....	158
94. Example geotextile shear stress-strain plots .....	160
95. Shear modulus trendline fit for GgC: shear strain range 1.0-2.5%.....	163
96. Shear modulus versus trendline $R^2$ value for square geogrids.....	164
97. Shear modulus versus trendline $R^2$ value for rectangular geogrids.....	165
98. Shear modulus versus trendline $R^2$ value for geotextiles.....	166
99. Box and whisker plots for square geogrids.....	169
100. Box and whisker plots for rectangular geogrids .....	170
101. Box and whisker plots for geotextiles.....	171
102. Square geogrid shear modulus summary by load step.....	173
103. Rectangular geogrid shear modulus summary by load step.....	174

## LIST OF FIGURES CONTINUED

Figure	Page
104. Geotextile shear modulus summary by load step.....	175
105. Average shear modulus values for each material by shear strain range (%). .....	176
106. GgB calculated vs. measured shear stress, average trendline G. ....	179
107. GgB calculated vs. measured shear stress, best fit G.....	179
108. GgF calculated vs. measured shear stress, average trendline G. ....	180
109. GgF calculated vs. measured shear stress, possible best fit G. ....	180
110. GgE calculated vs. measured shear stress, average trendline G. ....	181
111. GgE calculated vs. measured shear stress, possible best fit G.....	181
112. Biaxial cyclic shear loading schedule from Bögner (2004). .....	196
113. Additional sprocket location for release axis.....	197
114. GgA bias trial 1. ....	208
115. GgA bias trial 2. ....	209
116. GgB bias trial 1. ....	210
117. GgB bias trial 2. ....	211
118. GgF bias trial 1.....	212
119. GgF bias trial 2.....	213
120. GgC bias trial 1. ....	214
121. GgC bias trial 2. ....	215
122. GgD bias trial 1. ....	216
123. GgD bias trial 2. ....	217
124. GgE bias trial 3 (Mode 3). ....	218

## LIST OF FIGURES CONTINUED

Figure	Page
125. GgE bias trial 4. ....	219
126. GgE bias trial 5. ....	220
127. GgE bias trial 6 (Mode 3). ....	221
128. GtA bias trial 1 (no arm slits). ....	222
129. GtA bias trial 2. ....	223
130. GtA bias trial 3. ....	224
131. GtB bias trial 1 (only one load step). ....	225
132. GtB bias trial 2. ....	226
133. GtB bias trial 3. ....	227
134. GtB bias trial 4. ....	228
135. Top: GgA bias trial 1. Bottom: GgA bias trial 2. ....	231
136. Top: GgB bias trial 1. Bottom: GgB bias trial 2. ....	232
137. Top: GgF bias trial 1. Bottom: GgF bias trial 2. ....	233
138. Top: GgC bias trial 1. Bottom: GgC bias trial 2. ....	234
139. Top: GgD bias trial 1. Bottom: GgD bias trial 2. ....	235
140. Top: GgE bias trial 3. Bottom: GgE bias trial 4. ....	236
141. Top: GgE bias trial 5. Bottom: GgE bias trial 6. ....	237
142. GtA bias trial 1. ....	238
143. Top: GtA bias trial 2. Bottom: GtA bias trial 3. ....	239
144. Top: GtB bias trial 1. Bottom: GtB bias trial 2. ....	240
145. Top: GtB bias trial 3. Bottom: GtB bias trial 4. ....	241

## LIST OF FIGURES CONTINUED

Figure	Page
146. GgA bias trials 1-2, 1-5% shear strain range. ....	244
147. GgA bias trials 1-2, 1-2.5% shear strain range. ....	245
148. GgA bias trials 1-2, 1-2% shear strain range. ....	246
149. GgB bias trials 1-2, 1-5% shear strain range. ....	247
150. GgB bias trials 1-2, 1-2.5% shear strain range. ....	248
151. GgB bias trials 1-2, 1-2% shear strain range. ....	249
152. GgF bias trials 1-2, 1-5% shear strain range. ....	250
153. GgF bias trials 1-2, 1-2.5% shear strain range. ....	251
154. GgF bias trials 1-2, 1-2% shear strain range. ....	252
155. GgC bias trials 1-2, 1-5% shear strain range. ....	253
156. GgC bias trials 1-2, 1-2.5% shear strain range. ....	254
157. GgC bias trials 1-2, 1-2% shear strain range. ....	255
158. GgD bias trials 1-2, 1-5% shear strain range. ....	256
159. GgD bias trials 1-2, 1-2.5% shear strain range. ....	257
160. GgD bias trials 1-2, 1-2% shear strain range. ....	258
161. GgE bias trials 3-6, 1-5% shear strain range. ....	259
162. GgE bias trials 3-6, 1-2.5% shear strain range. ....	260
163. GgE bias trials 3-6, 1-2% shear strain range. ....	261
164. GtA bias trials 1-3, 1-5% shear strain range. ....	262
165. GtA bias trials 1-3, 1-2.5% shear strain range. ....	263
166. GtA bias trials 1-3, 1-2% shear strain range. ....	264

## LIST OF FIGURES CONTINUED

Figure	Page
167. GtB bias trials 1-4, 1-5% shear strain range. ....	265
168. GtB bias trials 1-4, 1-2.5% shear strain range. ....	266
169. GtB bias trials 1-4, 1-2% shear strain range. ....	267
170. GgA calculated vs. measured shear stress, average trendline G. ....	270
171. GgB calculated vs. measured shear stress, average trendline G. ....	270
172. GgB calculated vs. measured shear stress, best fit G. ....	271
173. GgF calculated vs. measured shear stress, average trendline G. ....	271
174. GgF calculated vs. measured shear stress, possible best fit G. ....	272
175. GgC calculated vs. measured shear stress, average trendline G. ....	272
176. GgD calculated vs. measured shear stress, average trendline G. ....	273
177. GgE calculated vs. measured shear stress, average trendline G. ....	273
178. GgE calculated vs. measured shear stress, possible best fit G. ....	274
179. GtA calculated vs. measured shear stress, average trendline G. ....	274
180. GtB calculated vs. measured shear stress, average trendline G. ....	275

## GLOSSARY

AOI	Area of Interest; the central square of the cruciform test specimen.
Aperture	In a geogrid, the void spaces framed by the ribs and nodes.
Bias	Warp and weft directions rotated from the directions of loading (rotation of 45 degrees for this thesis).
Biaxial Test	Two axes of loading or constraint operated simultaneously.
CCD	Charge Coupled Device.
CMOS	Complimentary Metal Oxide Semiconductor.
COV	Coefficient of Variance; $COV = \text{standard deviation} / \text{average (mean)}$ .
Cruciform	Shape of the planar sample used for biaxial testing; has four equal-length arms projecting from a square central area of interest.
DIC	Digital Image Correlation.
DSLR	Digital Single Lens Reflex.
FEM	Finite Element Modeling
fps	Frames per second.
G	In-plane shear modulus.
Geogrid	Geosynthetic formed by a regular network of integrally connected elements with apertures greater than 6.35 mm (1/4 in.) to allow interlocking with surrounding soil, rock, earth, and other surrounding materials to primarily function as reinforcement.
Geosynthetic	Product manufactured from polymeric material used with soil, rock, earth, or other geotechnical engineering related material as an integral part of a man-made project, structure, or system.
Geotextile	Any permeable textile material used with foundation, soil, rock, earth, or any other geotechnical engineering related material, as an integral part of a man-made project, structure, or system
Hz	Hertz; frequency; 1/second.
Line Load	Load per Unit Width: the typical measure of stress for planar materials with negligible thickness such as geosynthetics.
LVDT	Linear Variable Differential Transformer.
MD	Machine Direction; also warp, Y, or 2-Direction: the direction of geosynthetic along the length of the roll.
Mode 1	Tensile loading created by equal displacement in both X and Y machine axes.
Mode 2	Tensile or shear loading created by displacing the X machine axis while the Y machine axis is held fixed.

## GLOSSARY CONTINUED

Mode 3	Tensile or shear loading created by displacing the Y machine axis while the X machine axis is held fixed.
Node	Point where geogrid ribs are interconnected to provide structure and dimensional stability.
Non-Bias	Warp and weft directions aligned to the directions of loading.
Rib	For geogrids, continuous elements of a geogrid, which are typically in the machine or cross-machine direction as manufactured.
Uniaxial Test	Loading or constraint applied in one axis only.
UTS	Ultimate Tensile Strength.
XMD	Cross-Machine Direction; also weft, X, or 1-Direction: the direction of geosynthetic across the width of the roll, perpendicular to the Machine Direction.
$\gamma_{xy}$	In-plane shear strain in the loading coordinate system.
$\gamma_{12}$	In-plane shear strain in the material coordinate system.
$\epsilon_x$	Strain in the X loading axis.
$\epsilon_y$	Strain in the Y loading axis.
$\sigma_x$	Stress in the X loading axis.
$\sigma_y$	Stress in the Y loading axis.
$\tau_{xy}$	In-plane shear stress in the loading coordinate system.
$\tau_{12}$	In-plane shear stress in the material coordinate system.

## ABSTRACT

Geosynthetics are polymeric membranes used for structural reinforcement of soils in a variety of roadway and foundation applications, many of which create biaxial loading on the geosynthetic. Orthotropic linear elastic models have been used to represent geosynthetic behavior at working load levels for engineering design purposes. Typically, the models rely on index parameters obtained from test methods that do not represent the biaxial field loading conditions. Proper calibration of these models requires load-strain data obtained from tests that have controlled stress and strain boundaries such as biaxial tension tests. Previously at Montana State University, Haselton (2018) successfully used a custom biaxial device to perform biaxial tension tests on cruciform shaped geosynthetic specimens, producing a partial set of resilient elastic constants for two woven geotextiles and six biaxial geogrids. To complete the set of elastic constants by determination of the in-plane shear modulus, another mode of loading was necessary. Literature from biaxial shear tests of architectural membranes suggested cutting the cruciform shaped samples with the principal material directions on a 45-degree bias, which causes the sample to shear when the cruciform axes are unequally loaded. This test mode was successfully implemented with the existing biaxial device to determine the resilient in-plane shear modulus using an orthotropic linear elastic model. Full-field strain measurements were captured using digital imaging correlation (DIC) software available at Montana State University. DIC was shown to produce equivalent strain measurements to the mechanical instrumentation (LVDTs) used by Haselton, enabling a combined dataset. The full-field DIC strain measurements were then used to validate Haselton's assumption regarding the region of uniform strain and to identify the region of uniform strain for data collection in this thesis. DIC also showed reasonably pure biaxial tension in the cruciform samples, validating the elastic constant derivations for both Haselton and this thesis.

## CHAPTER ONE

## INTRODUCTION

Background

Geosynthetics are polymeric membranes used for structural reinforcement of soils in applications such as retaining walls, constructed slopes, roadways, and granular load transfer platforms. These applications create biaxial loading on the geosynthetic such that the material experiences load in both principal directions simultaneously. Biaxial loading can include in-plane shear stresses and strains (for applications such as roadways) as well as plane strain induced by the Poisson effect (for applications such as retaining walls).

Numerical modeling is commonly used to evaluate new applications for geosynthetics and to develop robust design methods. However, the material constants currently in use have been developed from wide-width uniaxial testing. The wide width of specimens and the unrestrained material edges create an unknown stress and strain state, which makes the material constants derived unrepresentative of the material response to biaxial loading found in field conditions. For orthotropic linear elastic models to appropriately represent geosynthetic behavior under working load conditions, these models should be calibrated from load-strain data obtained from tests with controlled stress and strain boundaries. Biaxial tension tests accomplish this requirement as well as provide the ability to load simultaneously in both principal directions.

To fully characterize biaxial stress-strain properties, biaxial tension tests must be performed in two different orientations: with the materials' warp and weft directions oriented the same as the biaxial tension directions (0 and 90 degrees), and then with the warp and weft directions placed on a bias (-45 and 45 degrees). For this thesis, "non-bias" refers to the 0/90 orientation, and "bias" refers to the -45/45 orientation. A biaxial testing device has been built specifically for geosynthetics testing at the Western Transportation Institute (WTI) at Montana State University and was used in this study.

#### Previous Work on Biaxial Testing of Geosynthetics

This research continues the overall project started by Haselton (2018) for biaxial testing of geosynthetics using the WTI biaxial testing device. Haselton used non-bias biaxial testing to successfully determine the modulus of elasticity for both principal material directions and the in-plane Poisson's ratio for a selection of eight materials (biaxial geogrids and woven geotextiles, the same as used in this research). For Haselton's work, strain was captured using LVDT instrumentation. However, for the one trial triaxial geogrid in Haselton's study, the LVDTs produced inconsistent and erratic strains, and a similar problem was anticipated for bias biaxial tests (the primary scope of this research). Also, even when the LVDTs worked well, they only provided a single strain measurement in each direction of loading, which was assumed to be representative of the entire central gage area. Because of this, an improved strain measurement system was necessary for this study. Digital image correlation (DIC) was selected because of its ability to provide a complete strain field using a non-contacting measurement system.

DIC is commonly used in polymer and fabric tensile testing because it avoids potential damage to specimens caused by affixing strain gages and because it provides a more reliable, accurate measurement.

### Scope of Work

The goal of this research is to conduct 45-degree bias biaxial tests in geosynthetics to determine the in-plane shear modulus, using DIC to collect strain data. DIC techniques for geogrids were developed, and techniques were validated by one-to-one comparison of strains in biaxial non-bias tests also instrumented with LVDTs. DIC was then used to evaluate the region of uniform strain in non-bias and 45-degree bias biaxial tests and to confirm assumptions regarding a state of pure biaxial tension in the cruciform samples. The product of this research is a finished set of elastic constants for eight common geosynthetics and an experimental procedure for DIC analysis of 45-degree bias biaxial testing of biaxial geogrids and woven geotextiles.

## CHAPTER TWO

## LITERATURE REVIEW

Introduction

In-plane shear tests are well-documented for structural fabrics and polymeric architectural membranes, which exhibit similar material characteristics to geosynthetics, including viscous behavior, and phenomena such as “lock-up” of fabrics in shear may also be pertinent to woven geotextiles. Typical in-plane biaxial shear test devices, loading protocols, specimen details, and shear modulus values were examined for these similar materials, together with a brief review of biaxial shear stress and shear strain equation derivations found in the literature. Readers are directed to Haselton (2018) for an extensive review of biaxial testing performed on geosynthetics, which will not be discussed here since only non-bias biaxial tests (no biaxial shear tests) have been reported at this time. In several biaxial shear studies in the architectural membrane community, full-field strain measurement using digital image correlation (DIC) has been used successfully to measure strains and to assess regions of strain uniformity. Although no biaxial studies using DIC on geosynthetics were found, other literature reporting DIC on wide-width tensile tests of geosynthetics was also examined concerning software, techniques, and results. Finally, camera systems for DIC were reviewed to assess the suitability of equipment available for this project.

### In-Plane Shear Tests for Fabrics and Planar Polymeric Materials

In-plane shear tests have been long established to determine material properties of fabrics, and in recent years, also for architectural membranes (polymer foils and polymer-coated fabrics). The presence or absence of a polymeric coating significantly affects fabric shear behavior. Uncoated fabrics, including those used in composites forming, typically have low shear resistance in comparison to their tensile strength (Skelton 1976, Colman et al. 2014). In contrast, architectural membranes must have sufficient shear strength to perform well in tensioned applications which are typically double-curved structures (Figure 1) (Colman et al. 2014). According to Colman et al. (2014), “the shear stiffness of architectural fabrics is predominantly governed by the protective polymeric coating and is routinely assumed to be linear.”



Figure 1: Architectural membrane (polymer-coated fiberglass) showing double curvature (Birdair Inc. 2004).

Architectural membranes are relevant cousins to geosynthetics based on their material characteristics: both categories include planar, polymeric or composite materials that exhibit nonlinear (elastic and plastic) biaxial stress-strain behavior that is time-dependent (hysteretic), temperature-dependent, and direction-dependent (anisotropic) (Colman et al. 2014, Galliot and Luchsinger 2010, Perkins 2000, McGown et al. 2004). Woven geosynthetics are anticipated to behave similarly to uncoated fabrics due to their unbonded weave, whereas the integral or welded junctions of geogrids are anticipated to create comparatively high shear resistance, similar to polymer-coated fabrics used as architectural membranes.

For architectural membranes as well as geosynthetics, uniaxial tests provide only an approximate description of material behavior in the field (Beccaralli 2015, Haselton 2018). A lack of test standards has resulted in a proliferation of biaxial test protocols for architectural membranes, but of these, plane biaxial testing is considered to be the only reliable method (Beccaralli 2015). Biaxial materials experience shear when loads are applied off-axis from the material directions. To accurately determine the elastic moduli, shear is undesirable in the sample; for example, care must be taken when biaxially testing woven materials that do not have a 90-degree angle between warp and weft directions so as not to introduce shearing (Lomov et al. 2007, Bridgens et al. 2011, Colman et al. 2014). Consequently, when shear *is* desired in the sample, it is only necessary to rotate the warp/weft directions with respect to the loading directions to produce off-axis loading and therefore shear.

For shear modulus determination, both the 45-degree bias biaxial test and the picture frame test are preferred (Galliot and Luchsinger 2010, Beccaralli 2015, Colman et al. 2014). The picture frame test (Figure 2 left) creates a change of angle between warp and weft fibers during shearing, whereas the 45-degree bias biaxial test (Figure 2 right) induces shear without changing this angle (Colman et al. 2014). Shear with angle change is required for architectural fabrics to achieve curved surfaces, making the picture frame test more representative of field loading for these materials (Colman et al. 2014). However, geosynthetics are generally used in planar applications, so bias-biaxial tests are more representative for geosynthetics. Other biaxial shear tests without angle change include the “shear ramp” developed by Galliot and Luchsinger (2010), which used multiple actuators to apply a load gradient to each arm of a 0/90 (non-bias) cruciform specimen. The shear ramp offers the advantage of performing all tests for elastic and shear moduli on a single, easily-fabricated specimen, but it requires advanced biaxial test equipment and load control capability (Galliot and Luchsinger 2010).

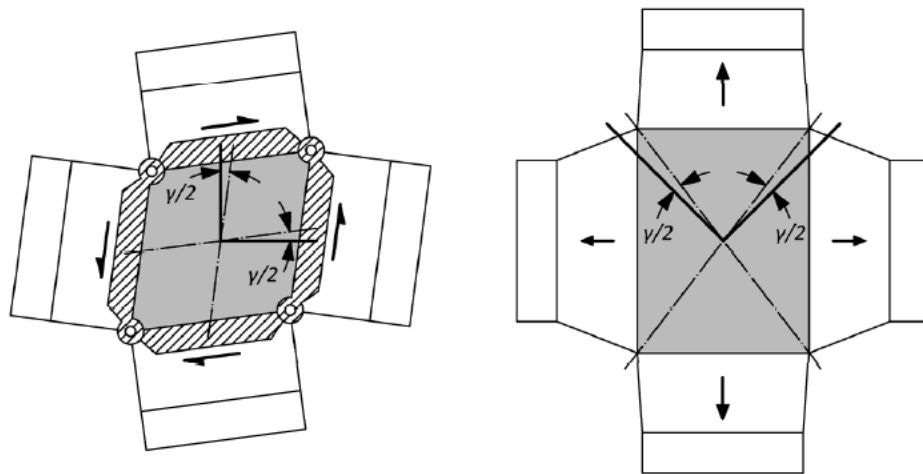


Figure 2: Picture frame test (left); bias-biaxial test (right) (Colman et al. 2014). Dashed lines show warp and weft directions.

For rigid materials, bias biaxial tests may be performed with one axis in tension and one in compression (e.g. Gunderson and Rowlands 1983). However, since membranes cannot be loaded in compression, Galliot and Luchsinger (2010) describe a bias biaxial test protocol where all four cruciform arms are pretensioned. Shear is induced by then applying additional load to one axis while load is released along the other axis, allowing the sample to deform as shown in Figure 3. This method was also used by Gao et al. (2018), Chen et al. (2018), and Shi et al. (2018) on polymer-coated fabrics.

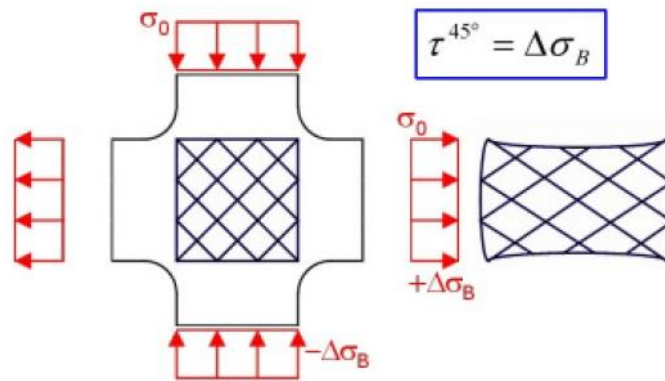


Figure 3: Preloaded tension/compression bias biaxial test (Galliot and Luchsinger 2010).

#### Derivation of Shear Stress and Shear Strain Equations

Gunderson and Rowlands (1983) offer the probable first exploration of shear stress data for a 45-degree bias cruciform test. They demonstrated the stress transformations using a graphic approach based on Mohr's circle as shown in Figure 4, but they did not provide mathematical derivations, nor did they discuss the shear strains: All strength envelopes were determined graphically from shear-normal stress-stress plots, with no investigation of stiffness.

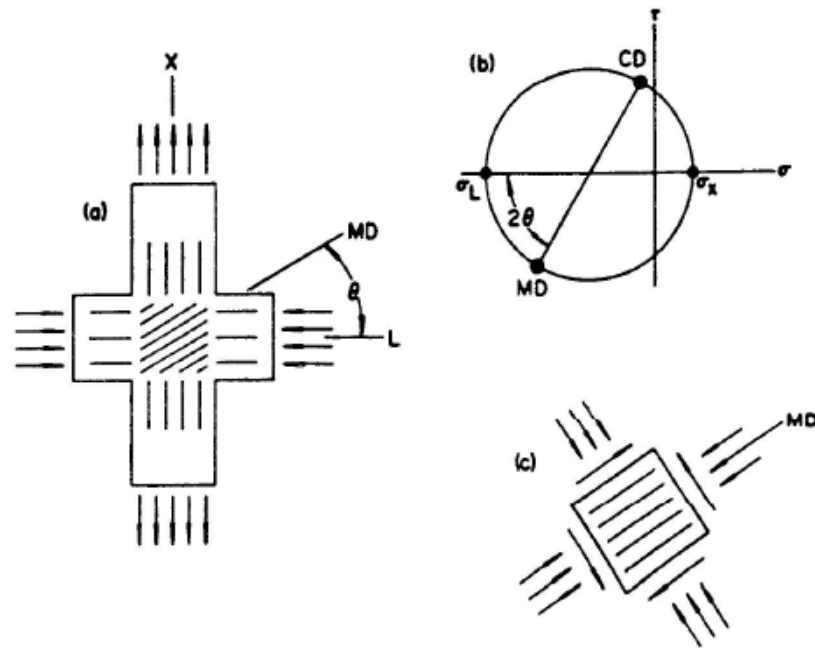


Figure 4: Mohr's circle stress transformations for bias-biaxial tests (Gunderson and Rowlands 1983).

Sharma et al. (2003) based their analysis on shear angle rather than shear strain, measuring the shear angle directly from the aspect ratio change of the interior region using photo-optics and trigonometry. For shear stress, they resolved the applied forces into their components in the material directions (longitudinal and shear). Colman et al. (2014) and Becarralli (2015) also describe equations that rely on the shear angle; these equations are primarily geared toward picture frame type tests.

Galliot and Luchsinger (2010) describe a simple method for obtaining shear strain from a 45-degree bias test using three extensometers positioned in a triangle as shown in Figure 5. Shear strain is determined from the change in angle, which is found using trigonometric relationships of the strains in the triangle legs.

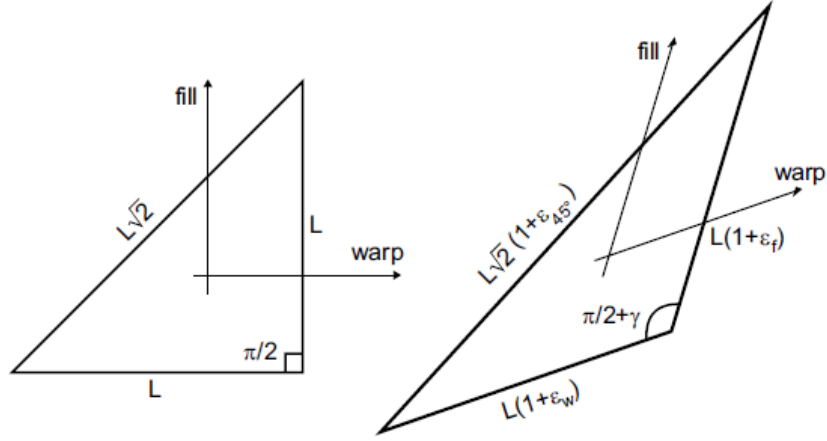


Figure 5: Three-extensometer method for obtaining shear strain (Galliot and Luchsinger 2010).

Chen et al. (2007) calculated the shear modulus (Equation 5) for off-axis uniaxial extension tests in multiple orientations using the elastic moduli and Poisson's ratios and the off-axial constitutive relationships shown in Equations 1-3. Subscripts 1, 2 indicate material directions, subscripts x, y indicate load directions, and  $\theta$  is the off-axial angle relative to the material direction 1. Equations 2-3 simplify to Equation 4, in which  $E_{45}$  and  $\nu_{45}$  are the data from the 45-degree bias test. The Poisson's ratios were calculated from photo-optic strain measurements in both the loading and transverse directions.

$$\frac{1}{E_x} = \frac{\cos^4\theta}{E_1} + \left( \frac{1}{G_{12}} - \frac{2\nu_{12}}{E_1} \right) \cos^2\theta \cdot \sin^2\theta + \frac{\sin^4\theta}{E_2} \quad (1)$$

$$\frac{\nu_{xy}}{E_x} = \frac{\nu_{12}}{E_1} - \left( \frac{1}{E_1} + \frac{1}{E_2} - \frac{1}{G_{12}} + \frac{2\nu_{12}}{E_1} \right) \cos^2\theta \cdot \sin^2\theta \quad (2)$$

$$\frac{1}{G_{xy}} = \frac{1}{G_{12}} + \left( \frac{1}{E_1} + \frac{1}{E_2} - \frac{1}{G_{12}} + \frac{2\nu_{12}}{E_1} \right) 4 \cdot \cos^2\theta \cdot \sin^2 \quad (3)$$

$$\frac{1}{G_{12}} = \frac{E_{45}}{2(1 + \nu_{45})} \quad (4)$$

$$\frac{1}{G_{xy}} = \frac{1}{G_{12}} + 4 \left( \frac{\nu_{12}}{E_1} + \frac{\nu_{xy}}{E_x} \right) \quad (5)$$

Rigorous mathematical derivations for bias-biaxial shear stress and shear strain have been provided more recently by Gao et al. (2018), Chen et al. (2018), and Shi et al. (2018), colleagues working on biaxial tests of architectural membranes in China's Space Structures Research Center. Their shear strain derivations are based on trigonometric relationships for the angle ( $\alpha$ ) between warp and weft directions and the linear strain ( $\epsilon_x$  and  $\epsilon_y$ ) in the two loading directions. The advantage of this method is that it requires only two extensometers. Since shear strain ( $\theta$ ) can be related to the warp-weft angle  $\alpha$ , this is used to obtain an expression for shear strain in terms of the linear strains  $\epsilon_x$  and  $\epsilon_y$ :

$$\theta = \alpha - \frac{\pi}{2} = 2 * \arctan\left(\frac{1 + \epsilon_x}{1 + \epsilon_y}\right) - \frac{\pi}{2} \quad (6)$$

To derive equations for shear stress, force equilibrium is applied, and stresses in the loading directions are transformed to normal and shear stresses in the material directions:

$$\sigma_{\text{warp}}^n = \sigma_{\text{weft}}^n = \frac{1}{2}(\sigma_x + \sigma_y) + \frac{1}{2}(\sigma_x - \sigma_y) \cos \alpha \quad (7)$$

$$\tau = \frac{1}{2}(\sigma_x - \sigma_y) \sin \alpha \quad (8)$$

Assuming a very small shear angle such that the warp-weft angle  $\alpha$  remains close to 90 degrees, the stress equations further simplify:

$$\sigma_{\text{warp}}^n = \sigma_{\text{weft}}^n = \frac{1}{2}(\sigma_x + \sigma_y) \quad (9)$$

$$\tau = \frac{1}{2}(\sigma_x - \sigma_y) \quad (10)$$

### Biaxial Testing Devices

Details regarding biaxial test frames were provided by Galliot and Luchsinger (2010), Bridgens et al. (2011), and researchers at the Chinese Space Structures Research Center (Gao et al. 2018, Chen et al. 2018, Shi et al. 2018). These devices were custom-built and employ computer-controlled load actuation, enabling the execution of precise, complex loading programs including cyclic loading. Other biaxial frames reviewed by Becarralli (2015) in a round-robin study have similar control capability.

Galliot and Luchsinger's (2010) frame has five electromechanical drives mounted on transverse bearings for each tensile arm (Figure 6). Each drive connects to a 10 kN load cell for independent control, enabling their unique "shear ramp" loading method which applies a stepped stress to each arm as shown in Figure 7. Grips were designed for use on architectural membranes. Both LVDTs and DIC were used for strain measurement.

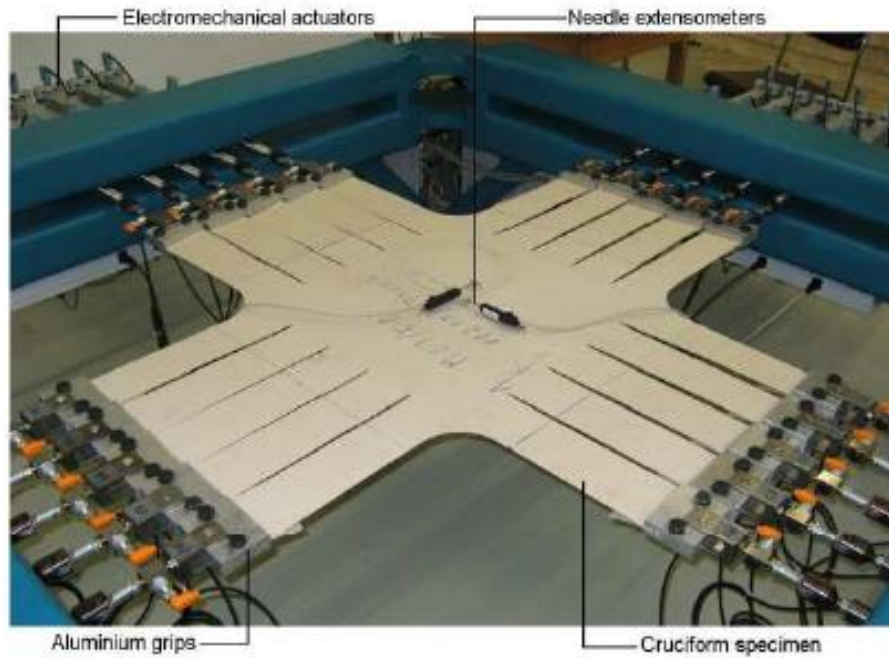


Figure 6: Biaxial testing device and cruciform sample from Galliot and Luchsinger (2010).

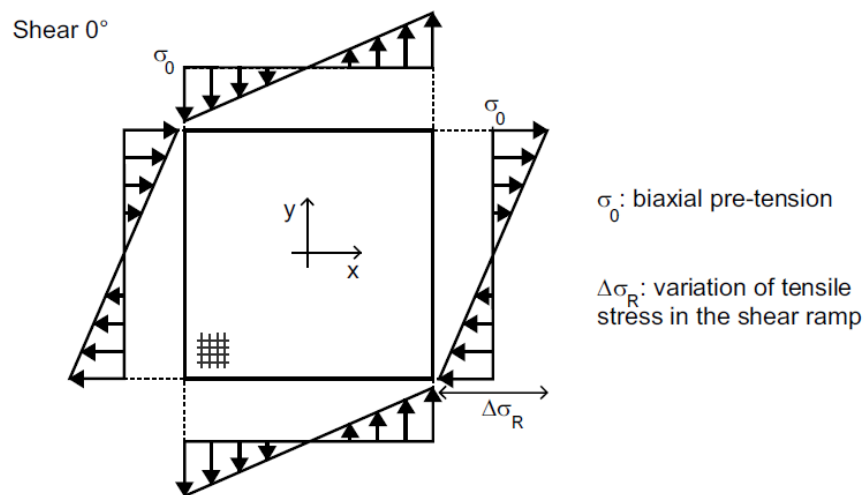


Figure 7: Shear ramp on a traditional (non-bias) cruciform sample (Galliot and Luchsinger 2010).

Bridgens et al. (2011) describes details for two different biaxial frames used in a comparative study of biaxial tension tests (shear behavior was not investigated). One, at the Taiwanese Textile Research Institute, is comparable to that of Galliot and Luchsinger (2010), except with seven independent servomotors for each sample arm. The second, at Newcastle University, uses a floating frame for tests of fabrics with non-orthogonal warp-weft directions; this device applies load using a single servo-hydraulic actuator and load cell for each direction. Both frames used LVDTs to measure strains.

For the biaxial frame at the Chinese Space Structures Research Center (Figure 8), fully automatic loading up to 20 kN is applied by four independent servo-hydraulic cylinders operated by a computer control and data acquisition system. Load control is provided by a 3-ton, 0.03% precision force sensor fixed between each cylinder and a hydraulic clamp-type grip. Proprietary software provides capability for load control or displacement control testing, with 10 Hz real time data feedback control. Testing rates are 1-10 mm/min for constant rate of strain, or 0.5-10 kN/m/min for constant rate of load. Both LVDTs and DIC were used for strain measurement.

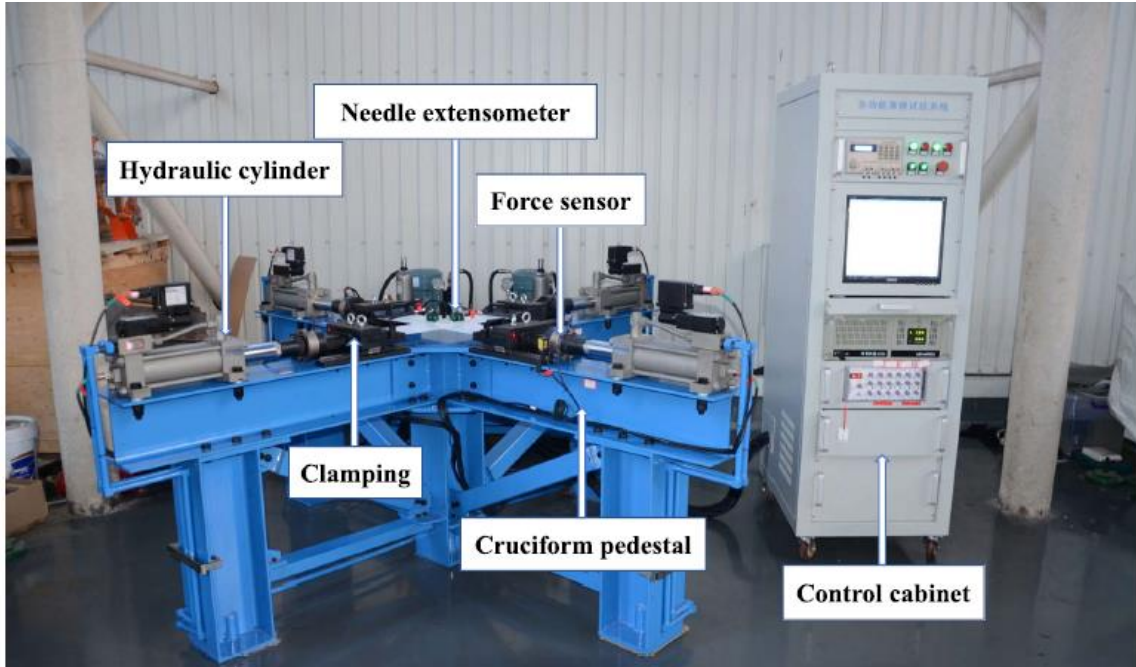


Figure 8: Biaxial testing device at the Chinese Space Structures Research Center (Gao et al. 2018, Chen et al. 2018, Shi et al. 2018).

### Specimen Details

Bias cruciform specimens reported in the literature range from a 75x75 mm to a 500x500 mm interior square, with arm lengths of 60% to 100% of the interior length. Tests generally used arms with slits on polymer-coated fabrics, but not necessarily for uncoated fabrics. Also, multiple researchers noted the use of corners cut on a radius for the junctions between arms. Radii ranged from 10 mm (e.g. Gao et al. 2018) to 55 mm (Galliot and Luchsinger 2010).

For shear tests on polymer-coated fabrics, the Chinese Space Structures Research Center used a cruciform sample with a 160x160 mm interior region and 160 mm arm length outside the grip cut by three slits (Gao et al. 2018, Shi et al. 2018, Chen et al. 2018). Gao et al. (2018) and Shi et al. (2018) both used full-length slits, but Chen et al.

(2018) used slits of varying length as shown in Figure 9. Galliot and Luchsinger used a larger cruciform specimen for their shear ramp and 45-degree bias biaxial tests, with 500 mm interior dimensions and 300 mm arm lengths cut by four full-length slits (Figure 6). Additionally, they specified a welding process for attaching non-bias arms to a 45-degree bias center as shown in Figure 10; their shear ramp specimen negated any need for welding. Galliot and Luchsinger (2010) observed that the welding process made bias sample fabrication difficult, and they suggested outsourcing the work to specialists. Colman et al. (2014) also noted difficult fabrication for 45-degree bias cruciform specimens. Instead of a bias cruciform specimen, Colman et al. (2014) used a 300 mm square specimen in a picture frame test; no slits were used since arm lengths were negligible (the frame was adjacent to the interior region).

For shear tests on uncoated woven fabrics, Sharma et al. (2003) used a 45-degree bias cruciform sample with 75 mm interior dimensions and 200 mm overall length outside the grips in each of the loading directions. No slits were mentioned. Their bias cruciform sample geometry was based on ASTM D1774-93 for uniaxial bias extension tests (essentially the dimensions of two uniaxial bias extension samples crossed perpendicularly in the middle); however, this standard has been withdrawn without replacement.

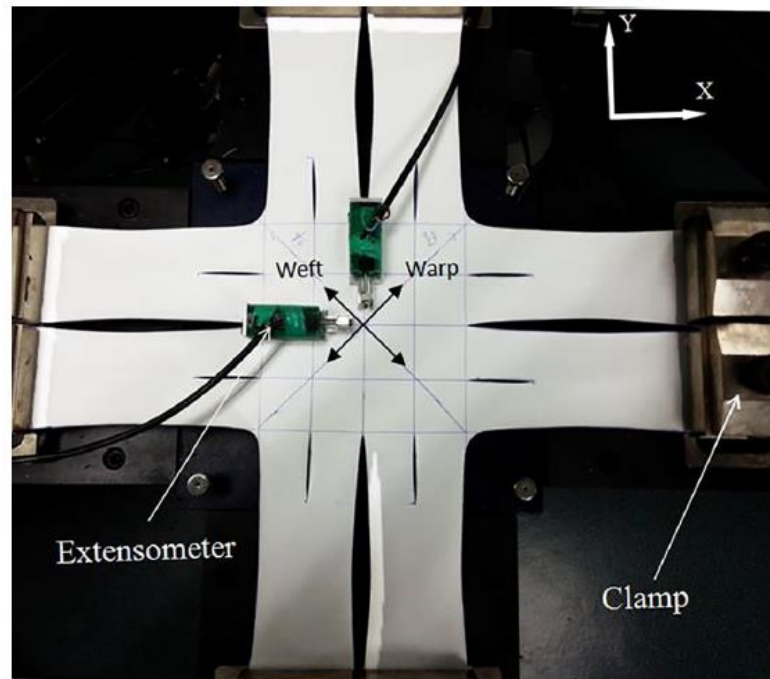


Figure 9: Biaxial sample from Chen et al. (2018) showing arm slits and corner radii.

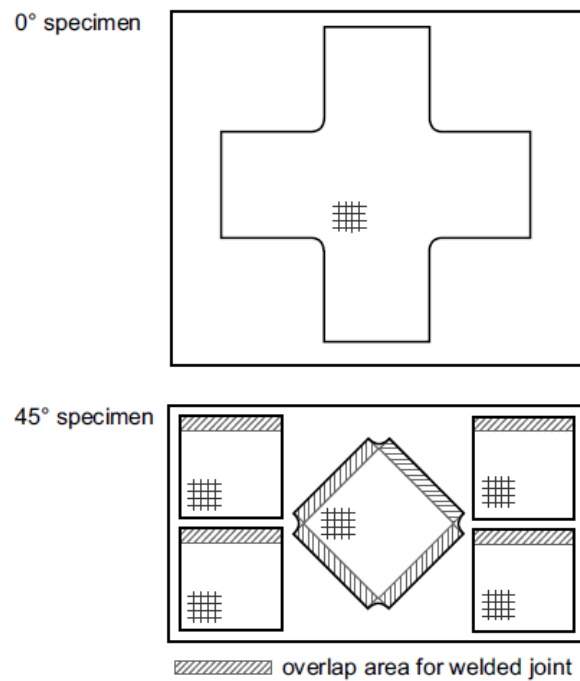


Figure 10: Non-bias (0/90) shear ramp specimen (top); 45-degree bias specimen with 0/90 non-bias welded arms (bottom) from Galliot and Luchsinger (2010).

### Loading Protocols

Most researchers in the literature used a similar loading approach, with a cyclic shear load applied at varying load ratios as shown in Table 1. Load ratio as used in the table describes the maximum proportion of increased load in one axis ( $+\Delta\sigma_B$ ) to released load in the other axis ( $-\Delta\sigma_B$ ) as was previously shown in Figure 3. Example load histories are shown in Figure 11 – Figure 14. A precursor report to the European Design Guide for Tensile Membrane Structures (Mollaert et al. 2016) also supports cyclic loading, but no specific test data was given other than the illustration shown in Figure 11. In this figure, warp and weft stresses are shown in blue and red, and the resultant shear stress is shown in green.

Table 1: Summary of load protocols discussed in the literature. UTS = ultimate tensile strength.

First Author	Load Ratios	No. of Cycles	Prestress (% UTS)	Max Stress (% UTS)
Sharma (2003)	Monotonic only	N/A	None	Failure
Bridgens (2011)	1:1, 2:1, 1:2, 10:1, 1:10, 1:1 (non-bias)	1	1.3 to 2.5	25
Galliot (2010)	1:0, 11:1, 5:1, 3:1, 2:1, 7:5, 1:1, 5:7, 1:2, 1:3, 1:5, 1:11, 0:1	5	4	20
Colman (2014)	1, 3, and 6 degrees of shear	3	3, 6, 9	Not given
Jackson (2007)	2, 7, 2, 15, and 2 degrees of shear	5	1.3	27.5
Chen (2018)	Approx. 4:1, 1:4 (preload approx. 2:2)	4	Not given	Not given
Shi (2018)	Approx. 4:1, 1:4 (preload approx. 2:2)	3	Not given	Not given
	Approx. 6:1, 1:6 (preload approx. 3:3)			
Gao (2018)	See Figure 14 top	3	2	8
	See Figure 14 middle	3	5	8
	See Figure 14 bottom	3	2 to 5	8

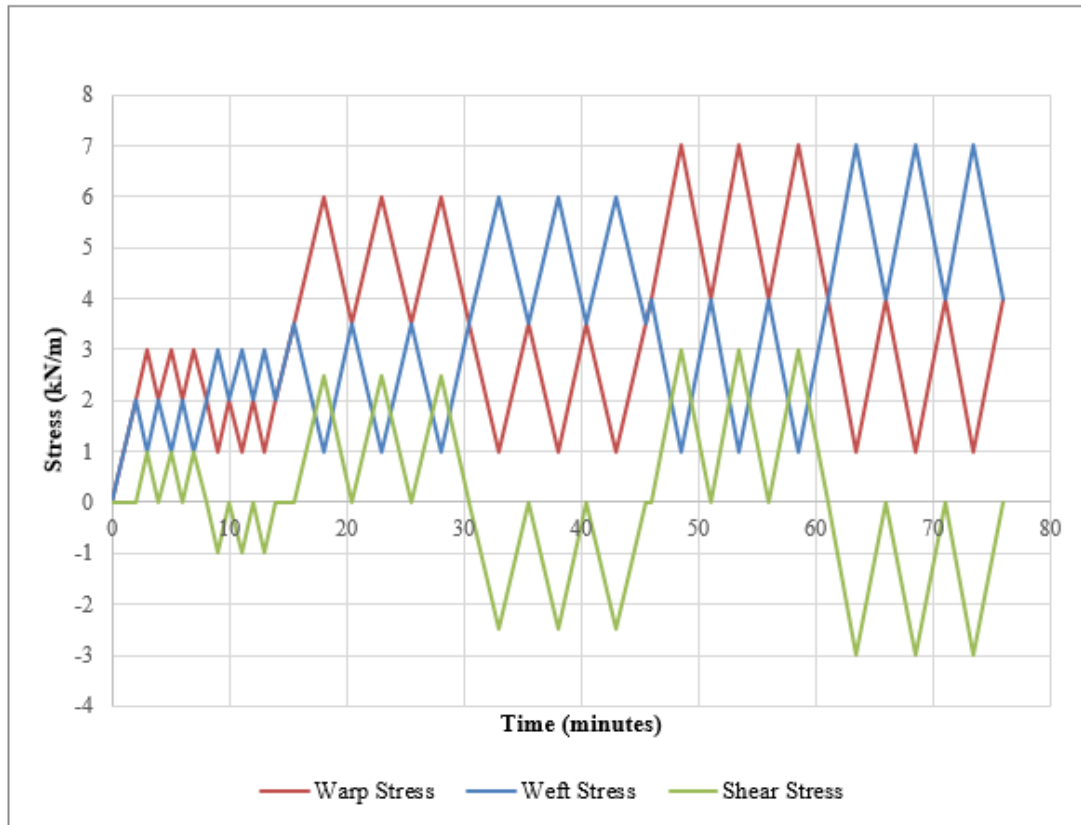


Figure 11: Example load history after Mollaert et al. (2016).

Bridgens et al. (2011) discuss the significance of prestress on non-bias biaxial tests of architectural membranes, noting that the load-strain behavior from subsequent load cycles is fundamentally different from that of the first cycle. To obtain “repeatable, conditioned behavior,” they performed extensive testing to develop load protocols. In brief, their protocol consists of 12 hours of prestress at 1.3% to 2.5% of ultimate tensile strength, followed by cyclic mechanical conditioning at 1:0, 0:1, and 1:1 warp-fill load ratios between the prestress and 25% of ultimate strength. After conditioning, cyclic loading for data of record is applied at various load ratios (Table 1), with maximum loads of 25% of ultimate strength. Cycle time for conditioning was 2.5 minutes for each

loading/unloading path, with rest intervals of 2 minutes at prestress between cycles; for data of record, the cycle time increased to 5 minutes for each loading/unloading path, keeping the same rest interval. The rest time at prestress assisted with removing residual strains that developed as a result of the materials' viscoelastic properties.

Galliot and Luchsinger (2010) performed cyclic testing at 13 load ratios with five cycles per load ratio (Table 1). To ensure no residual strains, only the last cycle for each load ratio was kept as the data of record. With their method, the level of biaxial prestress did not appear to affect the shear stress-strain response.

Colman et al. (2014) performed cyclic picture frame testing at three shear deformation ratios (1, 3, and 6 degrees). Thirteen sets of three cycles formed the load profile shown in Figure 12. They noted an increased shear stiffness with increased biaxial prestress.

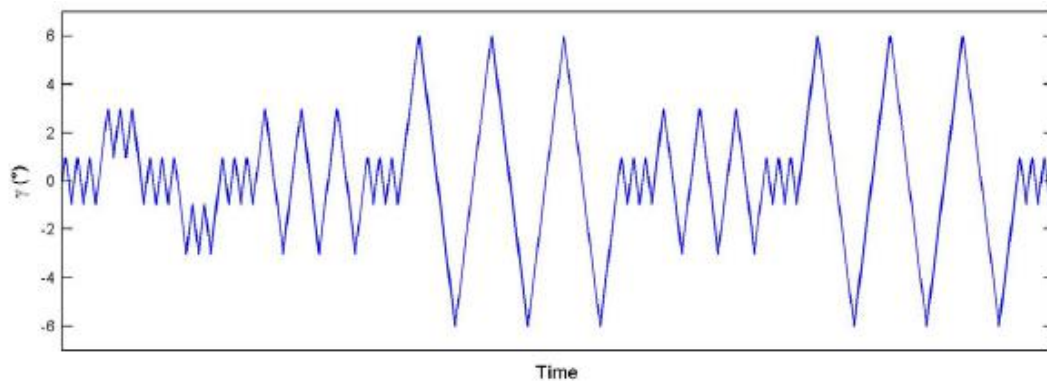


Figure 12: Cyclic test profile (shear angle versus time) from Colman et al. (2014).

Chen et al. (2018) and Shi et al. (2018) used similar cyclic shear loading protocols, with a preload immediately followed by three to four cycles in positive shear,

then three to four cycles in negative shear (Figure 13). Rather than allow recovery time between cycles, additional stress was applied to remove residual strains.

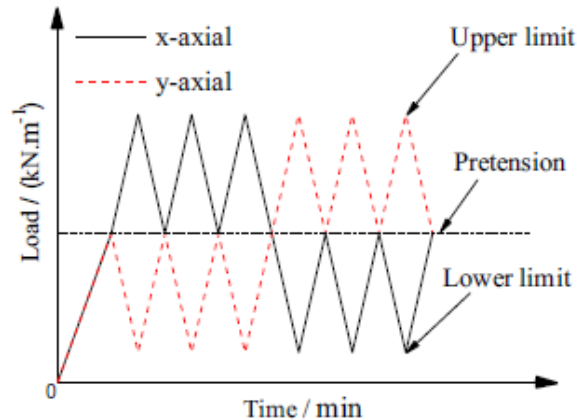


Figure 13: Cyclic test profile from Shi et al. (2018).

Gao et al. (2018) performed expanded cyclic shear testing with three different loading patterns as shown in Figure 14. The differences between the loading histories is summarized in Table 2. Constant ideal normal stress means that the stress in the material directions is always the same across load steps as calculated by Equation (9); it is shown in the load histories where all the shear loads are symmetrical about a single preload axis. Zero shear stress was achieved by cycling both axes at equal tension levels rather than the opposite-magnitude tension levels for shearing. Shear cycles were 20 minutes each, with equal tension cycles of 10 minutes. Like Bridgens et al. (2011), Gao et al. (2018) also noted in SLH-3 that zero-shear-stress cycles helped to remove residual shear strains. Shear stiffness appeared to be somewhat load-history dependent as discussed further in the

Shear Behavior section, below.

Table 2: Differences between the shear loading histories from Gao et al. (2018).

Feature	SLH-1	SLH-2	SLH-3
Constant ideal normal stress	No	Yes	Yes
Zero-shear-stress condition	No	No	Yes

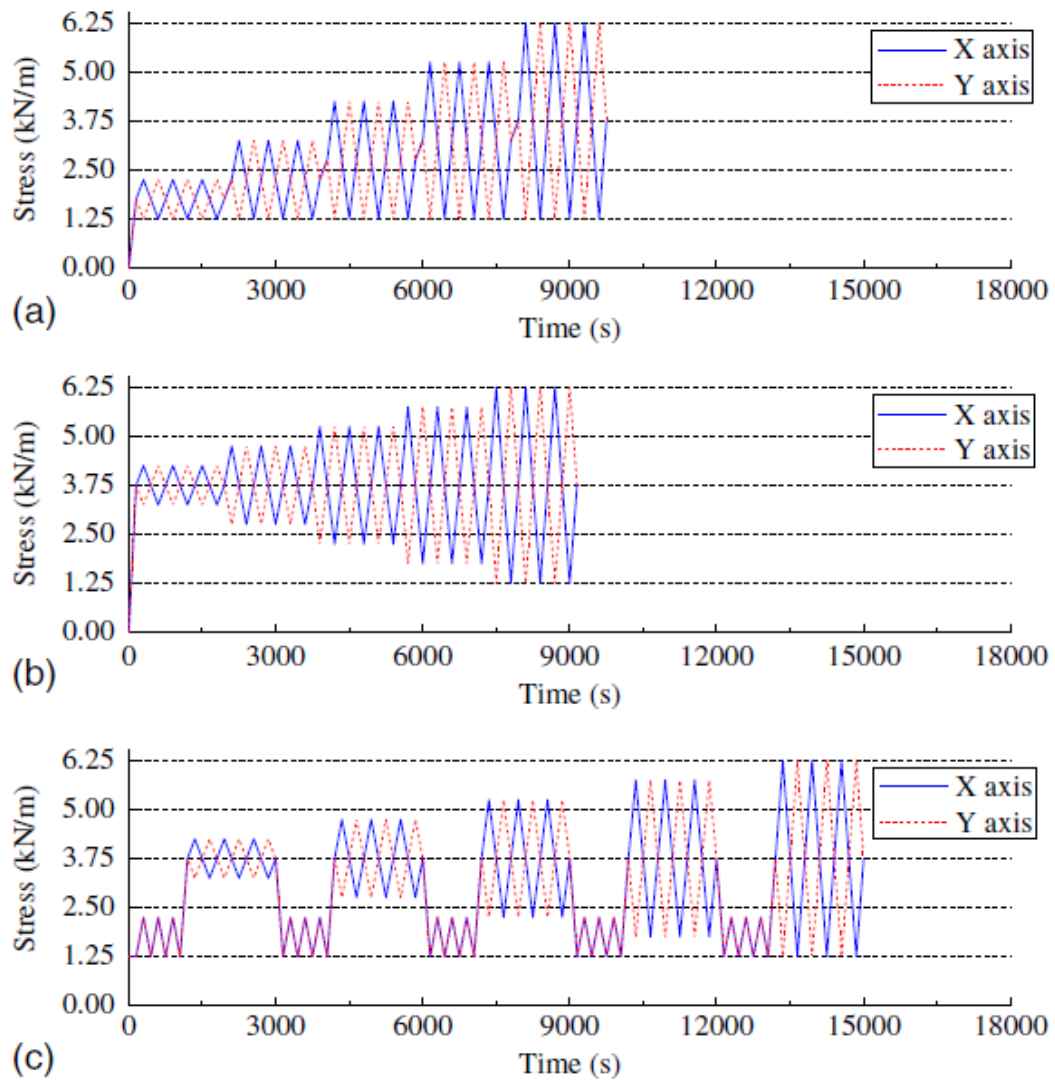


Figure 14: Three types of cyclic shear loading performed by Gao et al. (2018).

To compare non-bias biaxial test data from multiple test programs using different biaxial devices, Bridgens et al. (2011) recommended using an interpolated stress-stress-strain response surface generated in 3-D, which enables comparison of surfaces rather than discrete data points (which may not be directly comparable due to variances in testing programs). A similar approach was also used by Galliot and Luchsinger (2010) to compare bias-biaxial test data with model predictions (Figure 15). Alternately, Bridgens et al. (2011) suggested comparison of the elastic constants derived from each dataset rather than comparison of the load-strain curves themselves.

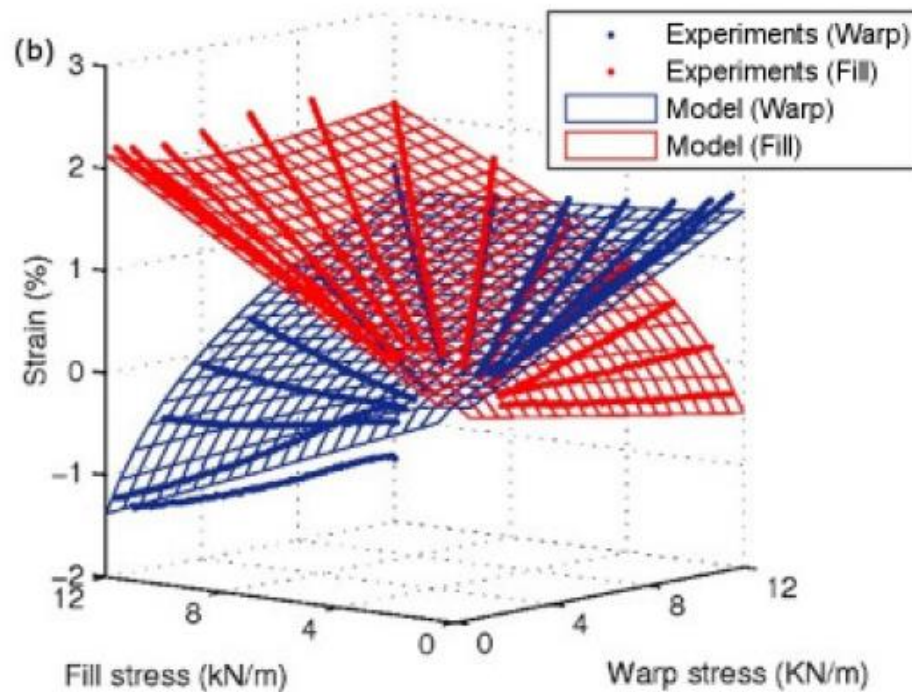


Figure 15: Stress-stress-strain surface for biaxial shear test (Galliot and Luchsinger 2010).

### Shear Behavior

Shear behavior observed in the literature include viscous effects and locking of fibers at a maximum shear angle. A summary of shear modulus values from the literature is provided in Table 3.

Table 3: Shear behavior reported in the literature.

First Author	Material	Shear Modulus (kN/m)	Max shear angle	Shear locking?	Viscous behavior?
Sharma (2003)	Dry woven carbon fiber	N/A	65°	Yes	No
Galliot (2010)	PVC-coated woven polyester	12.2	24°	No	Yes
	PVC-coated woven polyester	11.0	24°	No	Yes
	PVC-coated woven polyester	11.2	24°	No	Yes
	PVC-coated woven polyester	12.0	24°	No	Yes
	PVC-coated woven polyester	8.2	24°	No	Yes
	PVC-coated woven polyester	10.9	24°	No	Yes
	PVC-coated woven polyester	12.0	24°	No	Yes
	PTFE-coated woven fiberglass	32.2	9°	No	Yes
PTFE-coated woven fiberglass	40.0	9°	No	Yes	
Colman (2014)	PVC-coated woven PET	21.8-28.0	6°	No	Yes
	PVC-coated woven fiberglass	22.6-29.3	6°	No	Yes
	PTFE-coated woven fiberglass	99.2-120.5	6°	No	Yes
Jackson (2009)	PVC-coated woven polyester	26.0	14.5°	No	Yes
	PVC-coated woven polyester	12.6	14.5	No	Yes
Chen (2018)	PVDF-coated woven polyester	~13.9	14°	No	Yes
		11.8	-14°	No	Yes
Shi (2018)	PVDF-coated woven polyester	10.5	15°	No	Yes
	PVDF-coated woven polyester	13.9	13°	No	Yes
	PTFE-coated woven fiberglass	38.3	12°	No	Yes
	PTFE-coated woven fiberglass	45.5	10°	No	Yes
Gao (2018)	PVDF-coated woven polyester	3.9-6.3	21°	No	Yes
		4.3-7.7	21°	No	Yes
		4.2-7.9	21°	No	Yes

Sharma et al. (2003) observed concaved load-strain curves for biaxial bias tests of dry woven composites (Figure 16), with a sharp increase occurring in all samples at a shear angle of about 65-70 degrees. This was attributed to “lock-up” of the fibers, which

prevented continuing deformation in the interior region. Lock-up was explicitly noted not to be present in other studies due to testing at lower maximum shear angles than the locking angle (Jackson et al. 2009, Galliot and Luchsinger 2010, Gao et al. 2018).

However, in biaxial bias tests on architectural membranes, Gao et al. (2018) suggested that a similar lack of interfiber movement might be the cause of a hysteresis phenomenon observed at the beginning of unloading cycles.

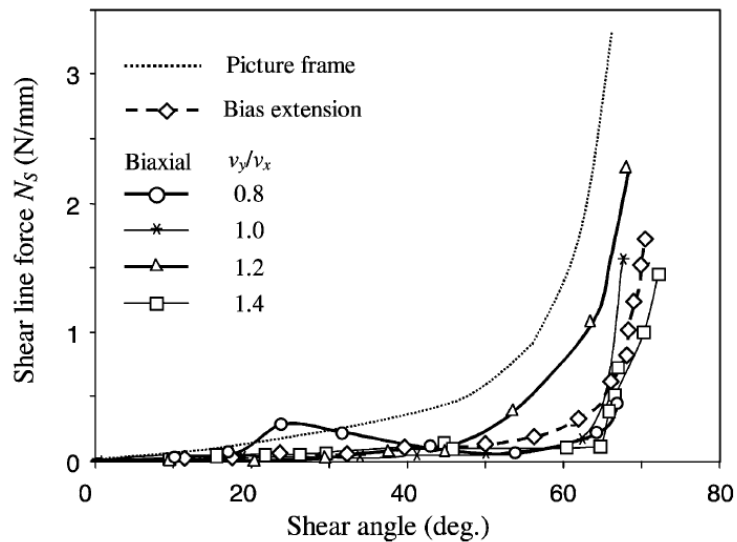


Figure 16: Concaved load-strain response from Sharma et al. (2003) showing lock-up at 65-70 degrees of shear.

For all the architectural membranes in their study, Galliot and Luchsinger (2010) noted an initial nonlinear shear stress-strain response that became linear after a certain level of shear stress (Figure 17). The linearity was assumed to be governed by the polymeric coating of the materials since the shear angle remained less than the locking angle for all tests. Visco-elastic-plastic behavior was also reported by Shi et al. (2018) and Chen et al. (2018) for architectural membranes. At low shear stresses, Shi et al.

(2018) observed nonlinear, clearly viscous behavior; however, the second half of the initial loading curve became relatively linear, so the slope of this portion was taken as the original shear stiffness. Subsequent cycles showed similar effects during loading but definite nonlinearity during unloading. Consequently, shear modulus for these cycles was taken from the slope of the best fit line of the loading portion. Transfer shear stiffness (between positive to negative shearing cycles, after removal of residual strains) was found to be linear and close to the value of the original (first-cycle) shear stiffness. Chen et al. (2018) observed slightly greater stiffness for positive shearing versus negative; the difference averaged about 15% (2.1 kN/m). Both Shi et al. (2018) and Chen et al. (2018) noted the presence of residual shear strains due to plasticity. PVDF-coated polyester fabrics exhibited residual strains of about 20% of the maximum shear strain, but for PTFE-coated fiberglass fabrics, the residual rose to 65%. Most of this plastic deformation appeared to occur in the initial cycle: Both Shi et al. (2018) and Chen et al. (2018) observed that the first shear cycle produced quite different shear stress-strain behavior compared to subsequent cycles.

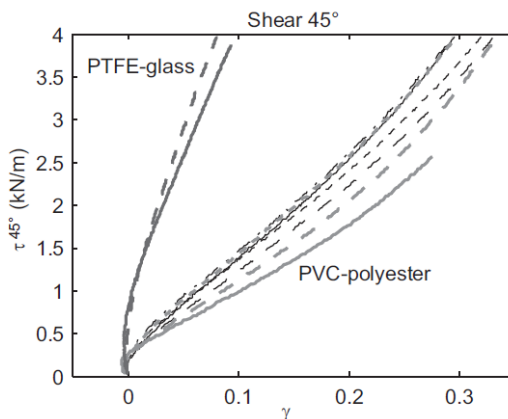


Figure 17: Bias-biaxial shear stress-strain curves from Galliot and Luchsinger (2010).

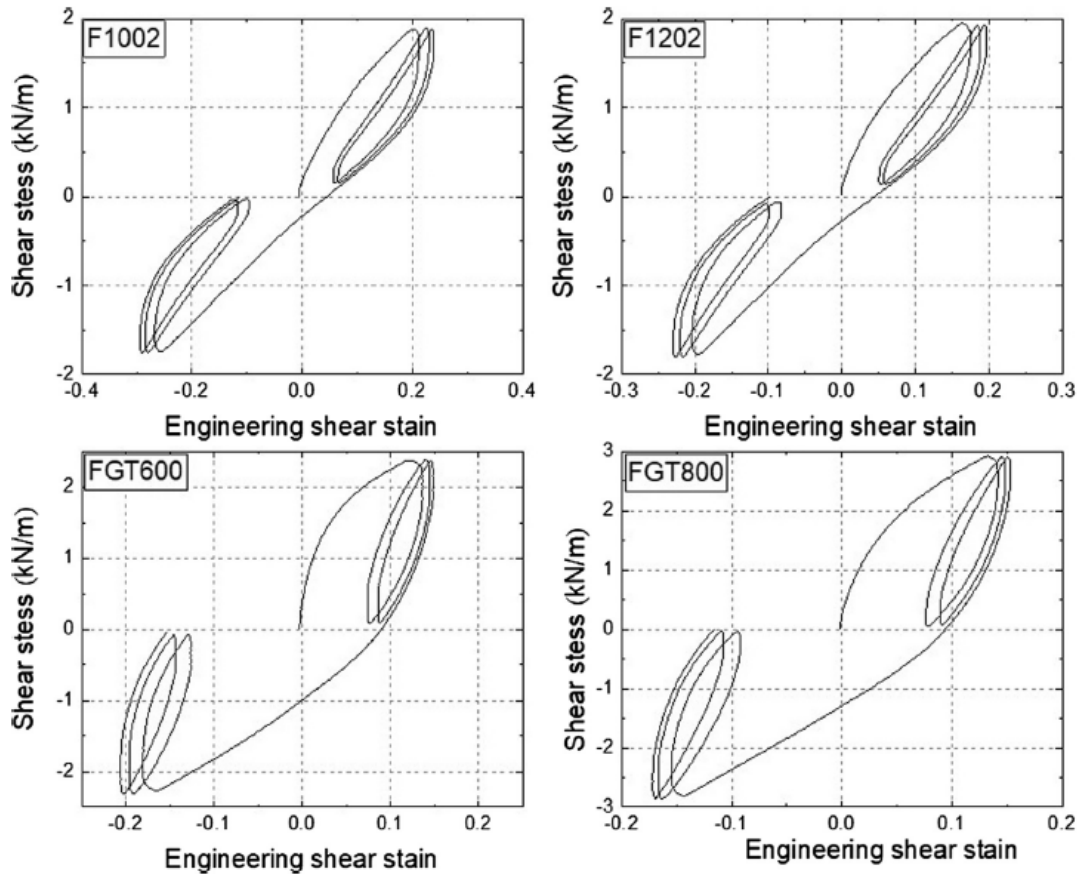


Figure 18: Shear stress-strain plots from Shi et al. (2018). Top: PVDF-coated woven polyester. Bottom: PTFE-coated woven fiberglass.

Gao et al. (2018) observed a hysteresis effect in which shear deformation lagged the load application. Shear stress-strain curves (Figure 19) showed an inverse S-shape except at the lowest load level (0.5 kN/m), which was too low for precise control with their device. Shear behavior was determined from the last two cycles of each three-cycle phase since these produced the most consistent data (similar to Chen et al. 2007, Jackson et al. 2009, Shi et al. 2018, and Chen et al. 2018). The method of removing the first cycle is also supported by Becarralli et al. (2015), who then additionally recommended averaging the second and third cycles. Shear modulus was determined from the linear

portion of the shear stress-strain curves, specifically from half the negative maximum shear strain to half the positive maximum shear strain. Modulus was taken as the average slope of lines fitted to the second and third cycles of each phase, and results are shown in Table 4. Tip-to-tip stiffness was also evaluated as a quick estimate method. Shear stiffness decreased nonlinearly with increasing maximum shear stress; however, it increased as biaxial tension increased (this trend was also observed in picture frame tests, e.g. Colman et al. 2014). Shear stiffness appeared to be load-history dependent, as the material exhibited different maximum shear strains for the same maximum shear stress in each loading history. Also, the maximum shear strain was shown to be a linear function of the maximum shear stress. Jackson et al. (2009) and Colman et al. (2014) observed many of these same shear behaviors from architectural membranes in picture frame tests. According to Jackson et al. (2009), the modulus should be determined only from the slope of the linear portion of the curve, since the tip-to-tip stiffness is not representative of the overall behavior (due to hysteresis).

Table 4: Average shear modulus (kN/m) in second and third cycles from Gao et al. (2018). SLH = shear loading history.

Shear stress (kN/m)	SLH-1	SLH-2	SLH-3
1	6.33	7.70	7.92
1.5	4.85	5.94	6.06
2	4.14	5.08	4.81
2.5	3.92	4.27	4.15

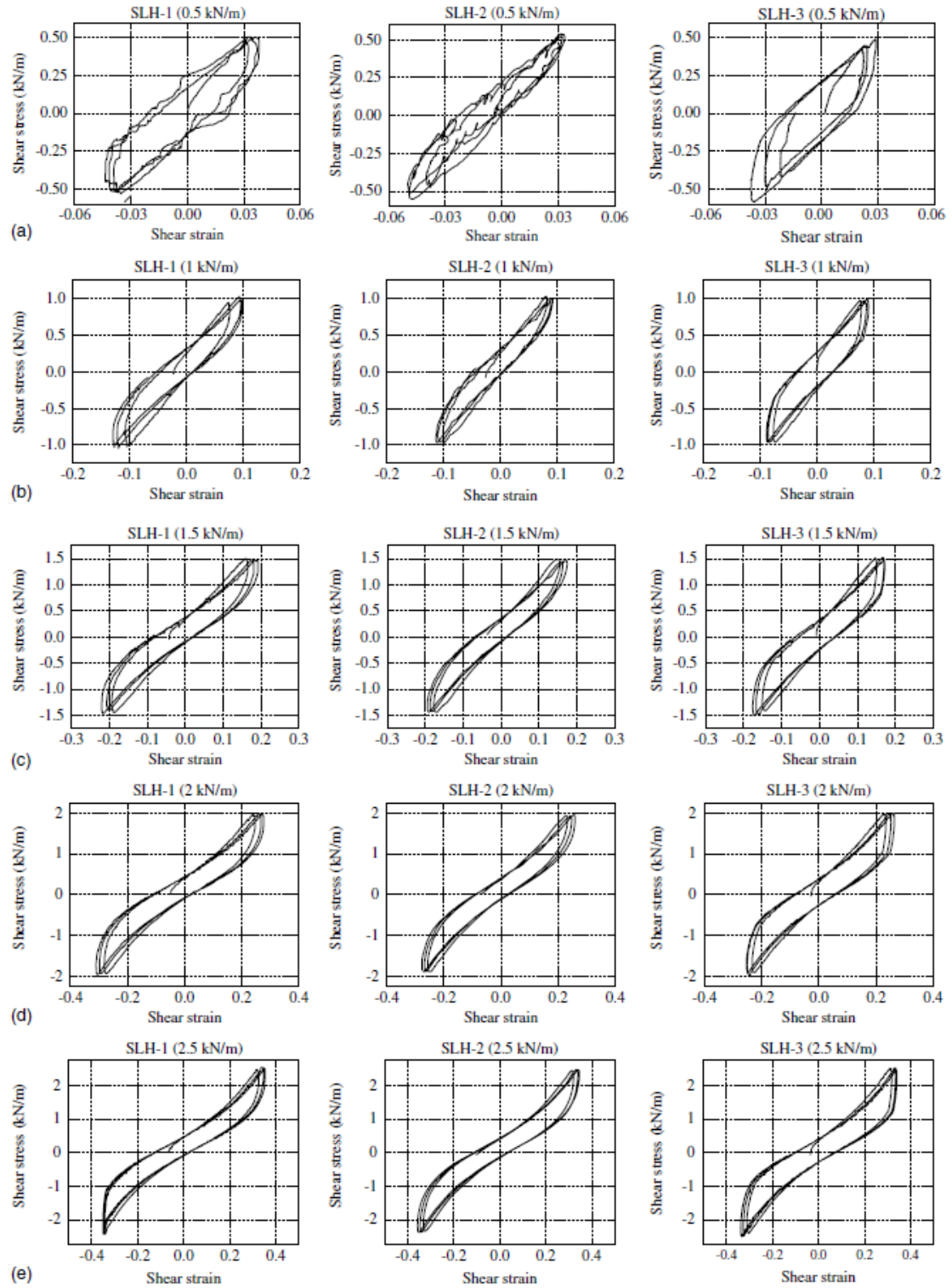


Figure 19: Shear stress-strain curves from Gao et al. (2018) at five stress levels for the three different loading histories shown in Figure 14.

### Digital Image Correlation

Digital image correlation (DIC) is an established method for non-contact, full-field strain evaluation. DIC works by optically tracking a stochastic pattern as it moves in comparison to a reference frame, and the technology is capable of very high accuracy measurements in 2-D and in 3-D (using stereo imagery) (www.GOM.com 2019). DIC is often used for measuring strains in fabrics and in thin materials that would be damaged or disturbed by traditional contact extensometers (e.g. Galliot and Luchsinger 2010, Colman et al. 2014, Iadicola et al 2013). DIC is also used for high-strain tests and tests on very flexible materials, where strain gages would be stiffer than the test sample or displacements larger than the allowable gage range (Nilsson 2017, Aydilek et al. 2004, Cen et al. 2018). Additionally, DIC offers the ability to fully examine local behaviors, as opposed to the average strain obtained by extensometers (Aydilek et al. 2004, Galliot and Luchsinger 2010).

#### DIC on Geosynthetics

DIC has frequently been used in geotechnical engineering for soil particle deformation analysis (e.g. Giang et al. 2010, Stanier et al. 2015), including with transparent soils to analyze geosynthetic pullout tests (e.g. Ezzein and Bathurst 2014, Bathurst and Ezzein 2015, Ferreira and Zornberg 2015). Forerunners to full-field DIC on in-air tensile tests of geosynthetics included laser extensometry (Skochdopole et al. 2000) and video extensometry (Jones 2000, Shinoda and Bathurst 2003, Shinoda and Bathurst 2004). Since then, full-field DIC has been applied in wide width tensile testing as

reported by Aydilek et al. (2004), Kutay et al. (2016), Mishra et al. (2017), Cen et al. (2018), Aboelwafa (2018) and Aboelwafa et al. (2019). Several of these papers provided significant details regarding DIC setup, processes, and results, which are discussed below.

Shinoda and Bathurst (2004) used commercially available software from Messphysik GmbH of Austria to perform 2-D video extensometry for vertical and lateral strains on wide-width tensile tests. Their materials included punched and drawn geogrids and knitted geotextiles. The software tracked 2 mm “white-out” paint dots placed on the nodes of the materials (also on the tensile webs for uniaxial geogrids). Up to 100 dots could be tracked simultaneously at a frequency of 25 Hz, and the software provided real-time load-strain data. The filming system comprised one monochrome CCD camera positioned with the lens parallel to the specimen surface. Arc lamps, positioned at an angle to the specimen for best contrast, provided lighting. Image resolution was smaller than 2  $\mu\text{m}$  at the 1 m optimum distance for their camera/lens system, and strain accuracy was estimated from manufacturer’s technical data sheets to be  $\pm 0.005\%$  for 10% strain,  $\pm 0.01\%$  for 20% strain, and  $\pm 0.02\%$  for 30% strain. Shinoda and Bathurst (2004) demonstrated repeatable results; differences between LVDT and video extensometer strains were attributed to slip of the LVDTs that caused them to underestimate the material stiffness at high strain levels.

Aydilek et al. (2004) used an in-house LABVIEW algorithm to analyze images of geosynthetics in wide-width tensile tests, including woven, nonwoven, geogrid, and geocell materials. The stochastic pattern consisted of high-contrast paint marker gridlines

at 10-mm spacings, and a typical image frame capturing an area of approximately 64 mm by 48 mm is shown below in Figure 20. The camera system was an analog CCD camera with a close focus zoom lens, mounted using a through-hole focusing jig. Zoom was scaled at 640 by 480 pixels, or roughly 10 pixels per millimeter. “The image acquisition rate was determined based on the displacement in terms of pixel counts between successive frames,” and a 10-second image capture interval was used with a machine strain rate of 1 mm/min (Aydilek et al. 2004). Fiber optics were used for specimen lighting. To validate DIC results, strain gages and an extensometer were mounted to the back side of the specimens. DIC strains were found to be comparable to results from both the strain gages and the extensometers, with a maximum difference of under 11% (one geogrid produced an outlier of 18% difference). Only strain measurement equivalency was investigated; no attempts were made to evaluate load-strain curves.

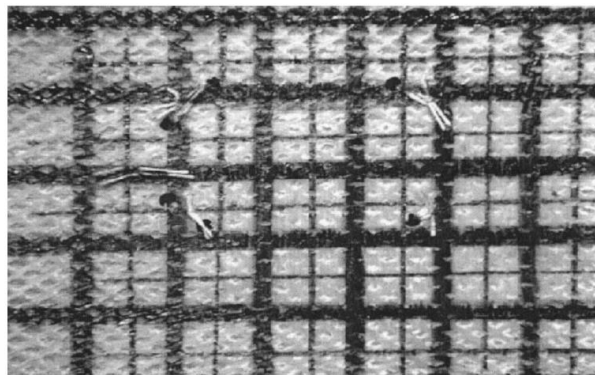


Figure 20: Typical image frame for Aydilek et al. (2004). Shown on geocell specimen with extensometer holes.

Mishra et al. (2017) conducted wide-width uniaxial tension tests on polymer and natural fiber geotextiles using 2-D DIC. For DIC processing, they used GeoPIV-RG, an improved version of the open-source MATLAB GeoPIV code developed for analysis of

granular movements and usually used on soil particle deformation analysis. GeoPIV-RG is desirable for its improved accuracy in large-strain conditions. With the original GeoPIV code, two options are available for analysis of large deformations: 1) reference every subsequent image to the initial image (reference frame) and ignore data loss at displacing edges (in essence, accept a much-reduced final analysis area), or 2) reference every image to the preceding image and let the analysis area expand with the deformation. Option (2) risks accumulation of small random errors and reduces the overall accuracy. GeoPIV-RG offers a compromise to maintain reasonable accuracy, where the reference frame is updated periodically but not at every frame. Reference frame update is controlled by user-defined parameters, which are selected based on trial and error. When any facet fails the user-defined correlation tolerance, the reference image automatically updates to the last successful iteration. Additional verification using known locations of markers is recommended for dimensional analyses (e.g. displacements), but this is not necessary for non-dimensional analyses (e.g. strains). Mishra et al (2017) captured images using a Nikon D5300 DSLR digital camera and a Samsung Galaxy J5 smartphone. Cameras were controlled remotely through a PC. Comparable accuracy was obtained for DSLR still image series (0.33 Hz), DSLR HD video (reduced to 0.33 Hz), and Samsung Galaxy J5 smartphone still image series (1 Hz). Resolution of images obtained from video was significantly smaller than resolution of still images (~2 vs ~24 megapixels), and facet size was adjusted to the resolution available from each image acquisition method. With the highest pixel resolution, the DSLR still image series provided the most accuracy but required longer DIC processing

time. A facet overlap of 50% was selected by trial and error for highest-accuracy results, and DIC strains were well inside the 2% error bound for strains calculated from the crosshead movement. Results were plotted as displacement vector fields and as strain heatmaps, and strains in the direction of loading were observed to be non-uniform as shown in Figure 22. At the unconstrained edges of the sample, Poisson-induced strains perpendicular to loading (Figure 21) were about  $\pm 4\%$  at the edges of the woven polymer geotextile (0% down the centerline).

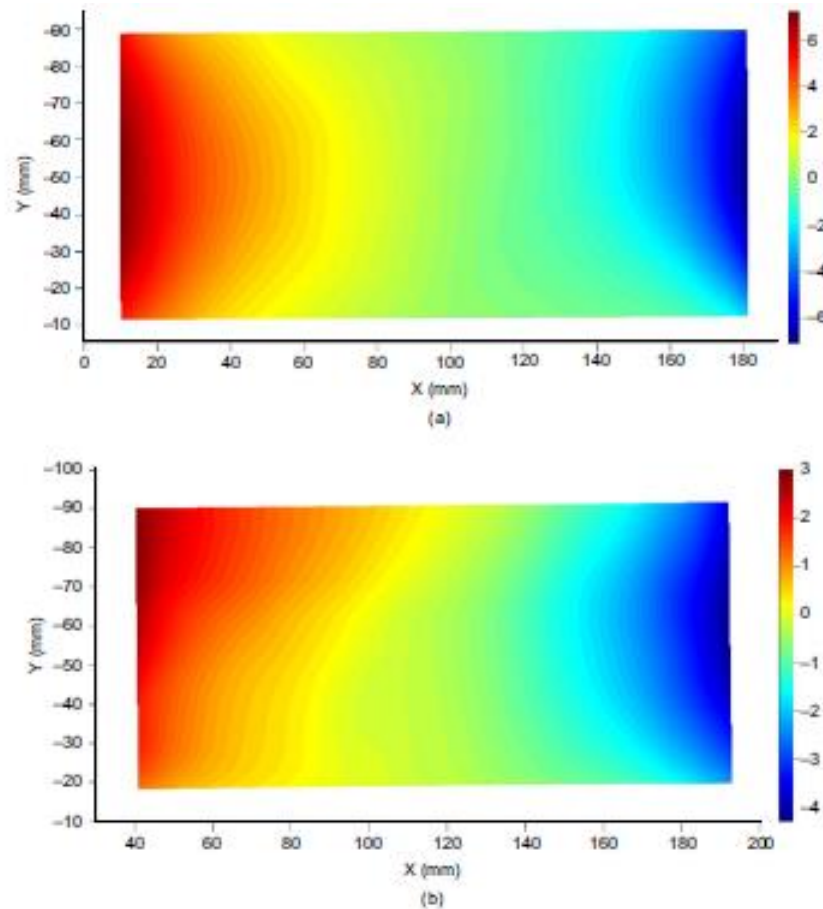


Figure 21: Poisson-induced horizontal strain fields for jute (top) and polymer (bottom, with grip slippage) woven geotextiles in uniaxial loading (Mishra et al. 2017). Strain color scale is in percent.

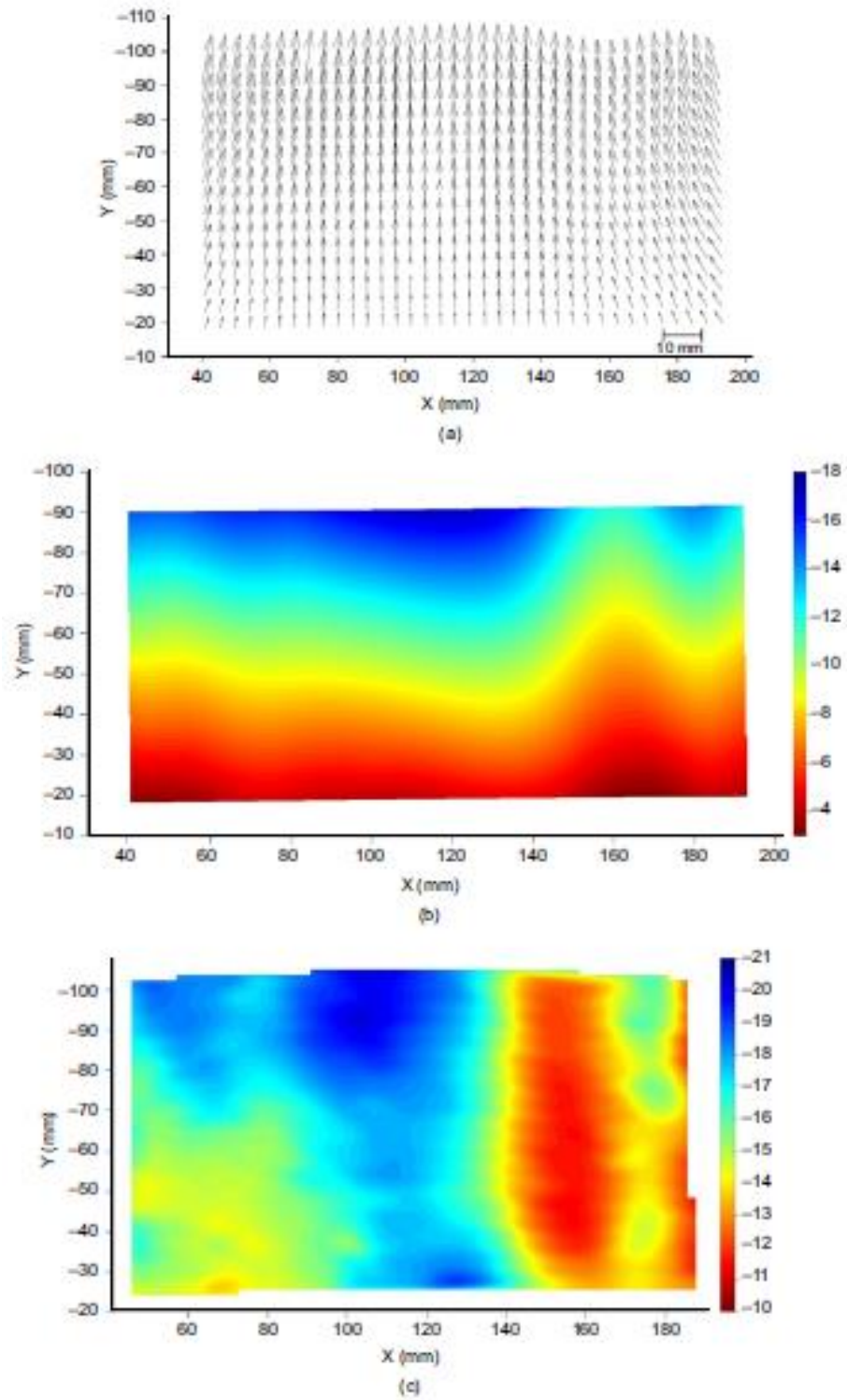


Figure 22: DIC results for a polymer geotextile in uniaxial loading (Mishra et al. 2017). Grip slippage is apparent on the right side of the sample. Top: Displacement vectors. Middle: Vertical deformation field. Bottom: Vertical strain field (strain in percent).

Ezzein and Bathurst (2014) used 2-D DIC with Canon Rebel XSi DSLR cameras to evaluate pullout tests of geosynthetics in transparent soil. Scattered opaque particles made up the stochastic pattern used for displacement tracking. The cameras were outfitted with EFS 18-55IS lenses, and maximum camera resolution was 4272 x 2848 pixels. All cameras were controlled from the PC, and simultaneous data capture with load and displacement measurements was obtained using gang shutter triggering. Images were captured at 15-second intervals; 3.5-second intervals were used for a few tests of shorter-length specimens. Potential for higher frequency image capture was noted to be dependent on camera buffer capacity and data acquisition equipment. DIC facet size was set to 32 x 32 pixels, with a 16-pixel (50%) facet overlap, and results were found to be accurate to 0.1 pixel (0.03 mm over the 2 m specimen length). Preprocessing and DIC image analysis were conducted using the commercial software PIVview2C V3.3 (PivTec 2011) as well as GeoPIV opensource MATLAB code, and results were checked using extensometers. Postprocessing was done in Excel spreadsheets with VBA macros.

#### DIC on Biaxial Tests of Non-geosynthetics

Significantly more literature was available for DIC-instrumented biaxial testing of other planar materials, including architectural membranes, polymer films, and sheet metal. Several of these papers are included here for their contributions to DIC methodology and error analysis; also, the tests on architectural membranes may be relevant literature for tests on geotextiles.

Colman et al. (2014) used DIC to measure strains for bias biaxial testing of architectural membranes using the picture frame technique. To ensure a good stochastic

pattern and highest quality strain data, they resorted to speckling by hand with a permanent marker pen instead of spray painting. The DIC software was Correlated Solutions' Vic-Snap and Vic-3D, which are USA-produced and used by NASA, United States national laboratories, MIT, Boeing, and others ([www.correlatedsolutions.com](http://www.correlatedsolutions.com) 2019). Images were taken at 30-second intervals for a shear angle change of 0.5 to 0.6 degrees per minute. Colman et al. (2014) note specifically that strain uniformity assumptions must be validated. Based on work by Galliot and Luchsinger (2010), strain was considered to be uniform where “standard deviations of the shear strain across the entire sample do not exceed 5% of the average shear strain” (Colman et al. 2014).

Galliot and Luchsinger (2010) performed 3-D DIC analysis for a comparison of two biaxial shear methods including a 45/45 bias shear test and their shear ramp test for architectural membranes. For their materials, strain was not uniform throughout the full area of interest for either test method except at the very center of the specimens as shown in Figure 23. Their results suggest that the most uniform strain data may be obtained from a small central region of analysis rather than from the full area; in their case, this small region was 150x150 mm out of an overall area of 500x500 mm. The standard deviation of shear strain in the small region was determined to be insignificant at less than 4% of the average shear strain. Additionally, a correction factor was necessary for accurate comparison of applied shear stress (calculated from load applied to the membrane arms) to FEA-calculated shear stress in the central region.

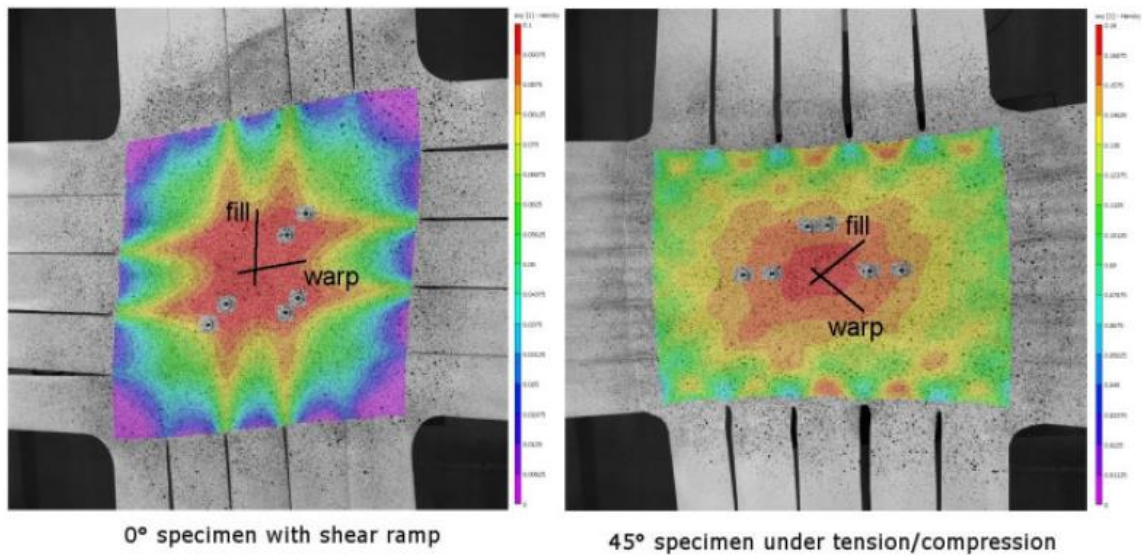


Figure 23: Shear strain uniformity of architectural membrane (Galliot and Luchsinger 2010). Gray dots show locations of needle extensometers in smaller central region.

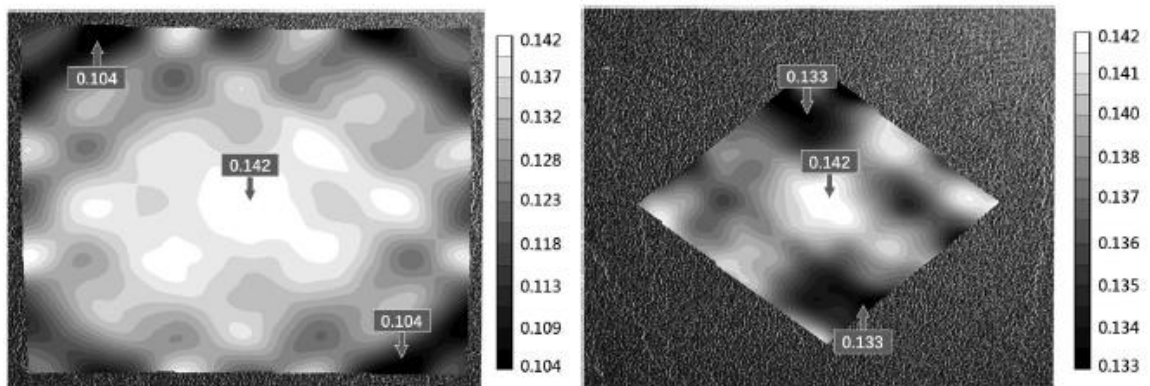


Figure 24: Shear strain uniformity for 45/45 bias test on architectural membrane (Gao et al. 2018).

Gao et al. (2018) used 2-D DIC for strain uniformity analysis of bias-biaxial tests of architectural membranes. Equipment was a Nikon D3000 CCD camera with Vic-2D 2009 software, and the speckle pattern was created using water transfer paper pasted on the specimen. Images were captured at zero and maximum deformation for comparison

(LVDTs supplied continuous data). Full-field shear strain (Figure 24 left) did not meet uniformity constraints; however, a small central region was acceptably uniform (Figure 24 right), with standard deviation not more than 1% of the average shear strain.

Iadicola et al. (2013) provide a detailed description of their process for biaxial testing of sheet metals using DIC at the National Institute of Standards and Technology (NIST). 2-D DIC was used for real-time feedback for strain-controlled tests, and 3-D DIC data was postprocessed for data of record. X-ray diffraction was used to measure the stress state of samples during testing. Two 3-D DIC camera systems were used to evaluate both the full 200x200 mm cruciform sample (including arms) and also a zoomed-in 50x50 mm central region. Camera equipment was two pair of Point Grey GRAS-50S5M-C five-megapixel CCD cameras outfitted with 1) Sigma 105mm f/2.8 EX DG telephoto macro lenses and 2) Kreuzach XenoPlan 1.9/35-0901 compact lenses. Maximum frame rate was 5 Hz. Iadicola et al. (2013) estimated noise and systematic errors by an analysis of the undeformed reference image. Synchronization of data from independent capture systems was observed to be challenging.

Nilsson (2017) performed biaxial testing on polymer film using 2-D DIC. He noted that pseudo strains can result from 2-D DIC if the camera lens is not kept parallel to the area of interest, and that pseudo strains will affect calculation of accurate Poisson's ratios.

Karadogan and Tamer (2017) performed biaxial testing on sheet metal using 2-D DIC, and their test frame limited the angle of the camera view such that the lens was

significantly nonparallel to the sample surface. This introduction of error was noted, but results were still considered reasonable enough for publication.

### Camera Systems

To evaluate the DIC suitability of the cameras available for this research, a brief review into camera systems was conducted. According to Teledyne DALSA (2019) (a specialist in high performance digital imaging component design and manufacturing), the two primary types of image sensors used in digital camera systems are CCD (charge coupled device) and CMOS (complementary metal oxide semiconductor). Each sensor type offers distinct advantages depending on the intended application. The primary difference between CCD and CMOS is that CCD sensors process all pixel data in sequence through typically a single output converter, whereas CMOS sensors process pixel data in parallel, with an output converter built into every pixel (www.teledynedalsa.com 2019). This difference results in fast processing speed and low power draw for CMOS, but higher output uniformity and therefore potential for better image quality for CCD. Historically, CCDs dramatically outperformed CMOS, but enormous investments in CMOS technology from the cell phone camera industry has reversed that situation for all but a few select applications. In nearly all commercial applications such as cell phones, scanners, and machine vision, CMOS provides better performance. Exceptions where CCDs still dominate include near-infrared, ultraviolet, and high-speed, low-light sensing. According to Diffraction Limited (another high-performance scientific imaging specialist), CCD is still the technology of choice for very high performance imaging such as for astronomy due to advantages in sensitivity, long

exposure shots, and large array sensors (George 2018). However, CMOS imaging has begun to appear in scientific applications, and the performance gap is closing (George 2018). Of the DIC literature reviewed, most researchers used CCD cameras, often with 3-D DIC. However, a few researchers used CMOS technology, with cameras including a Canon Rebel XSi DSLR, a Nikon D5300 DSLR, and a Samsung Galaxy J5 smartphone (Ezzein and Bathurst 2014, Mishra et al. 2017).

### Synthesis of Literature Review

Bias biaxial testing of fabrics initially suggested the feasibility of bias biaxial testing for geosynthetics. Since fabrics and geosynthetics cannot be loaded in compression for a tension-compression biaxial stress state, shear deformation may be accomplished by unequal tension on the biaxial arm pairs. Given the limitations of the biaxial device available for this research, this unequal tension may be created by pretensioning both loading directions, then continuing to load in only one direction. The available biaxial device lacks the sophistication necessary to perform the cyclic loading protocols found in the literature, including shearing at various load ratios. However, resilient testing at a single load ratio following the method of Haselton (2018) is still achievable. Arm slits may or may not be necessary for woven geotextile samples; biaxial shear tests from fiber composites did not use slits, but tests on coated fabrics did. For slits to be successful in a fully bias-cut sample, a similar structural coating may need to be applied to the arms of the geotextile.

The stiffening effect of polymeric coatings on the shear behavior of woven fabrics suggests that geogrids with integrally-formed or welded junctions will exhibit a higher shear modulus than woven geotextiles. Woven geotextiles may exhibit lock-up after a certain degree of shear, similar to other uncoated woven fabrics. However, lock-up as a structural phenomenon should not apply to geogrids. Shear stress-strain curves for polymer geosynthetics will likely show visco-elastic-plastic effects similar to those of architectural membranes, and initial loading curves may be quite unrepresentative of resilient behavior. Additionally, shear stress-strain behavior may be load-history dependent. Modulus values are anticipated to be on the order of 10 kN/m, possibly as high as 20 kN/m or as low as 5 kN/m.

DIC has been used successfully on wide-width tensile tests of geosynthetics as well as in many other biaxial testing applications, including on architectural membranes and polymer films. Multiple analysis tools exist, including commercially available software and open-source MATLAB codes. Keys to obtaining high quality DIC include a good stochastic pattern scaled to the zoom level of the image, good lighting, and careful camera setup. For accurate 2-D DIC strains, the camera lens must be kept parallel to the surface of interest. Aydilek et al. (2004) indicate that the number of images should be scaled to the strain rate to ensure sufficient movement between frames for strain calculation and to avoid bogging down DIC computations. Strain uniformity must be evaluated across the surface of interest before selecting any gage area as a representative measurement. Based on the literature, strains can be considered uniform if the standard deviation is less than about 5% of the average strain.

The two DSLR cameras available for DIC data collection in this project are a Sony CyberShot DSC H-300 and a Canon Rebel T2i. The Sony camera was released in early 2014 and uses CCD technology, while the Canon camera was released in early 2010 and uses CMOS technology. Since both cameras are relatively new, both should deliver usable quality for DIC, especially under controlled normal-spectrum lighting and at non-extreme distances (e.g., not astronomic or microscopic). Also, the Canon camera is reasonably comparable to the DSLR cameras reported in the literature for use with DIC. Both cameras are capable of shooting video, but Canon camera offers higher video resolution (1920 x 1080 pixels versus 1280 x 720 pixels for the Sony). For shooting series of still photos, the Canon camera is capable of up to 4 fps, whereas the maximum for the Sony camera is 0.8 fps. Iadicola et al. (2013) suggest that an uncertainty analysis should be performed on the reference image to obtain an estimate of inherent error.

## CHAPTER THREE

## THEORY

Introduction

An orthotropic linear elastic model was used to describe the material response of geosynthetics subjected to 45°/45° bias biaxial tensile loading. Throughout this thesis, stress will be expressed as force per length, which is the typical expression for geosynthetics (as opposed to dividing by the material thickness to obtain true stress units). The focus of this thesis is the calculation of the shear modulus obtained from bias biaxial test data.

Constitutive Equations for Shear Modulus

For planar membrane materials, Hooke's law for orthotropic materials simplifies to the plane stress case shown in Equation (11):

$$\begin{Bmatrix} \sigma_1 \\ \sigma_2 \\ \tau_{12} \end{Bmatrix} = \begin{bmatrix} C_{11} & C_{12} & 0 \\ C_{21} & C_{22} & 0 \\ 0 & 0 & C_{66} \end{bmatrix} \begin{Bmatrix} \varepsilon_1 \\ \varepsilon_2 \\ \gamma_{12} \end{Bmatrix} \quad (11)$$

where:

$$C_{66} = G \quad (12)$$

$$\tau_{12} = G \gamma_{12} \quad (13)$$

Figure 25 and Figure 26 show a biaxial test specimen oriented on a bias with the principal material directions (1 and 2) at 45 degrees to the directions of loading (x and y). The

stresses and strains in the directions of loading ( $\epsilon_x, \epsilon_y, \sigma_x, \sigma_y$ ) are measured in the test, and the shear strain in the loading coordinate system ( $\gamma_{xy}$ ) is assumed to be zero. As demonstrated later in this section, the applied shear stress may also be assumed to be zero with no change to the resulting shear modulus equation.

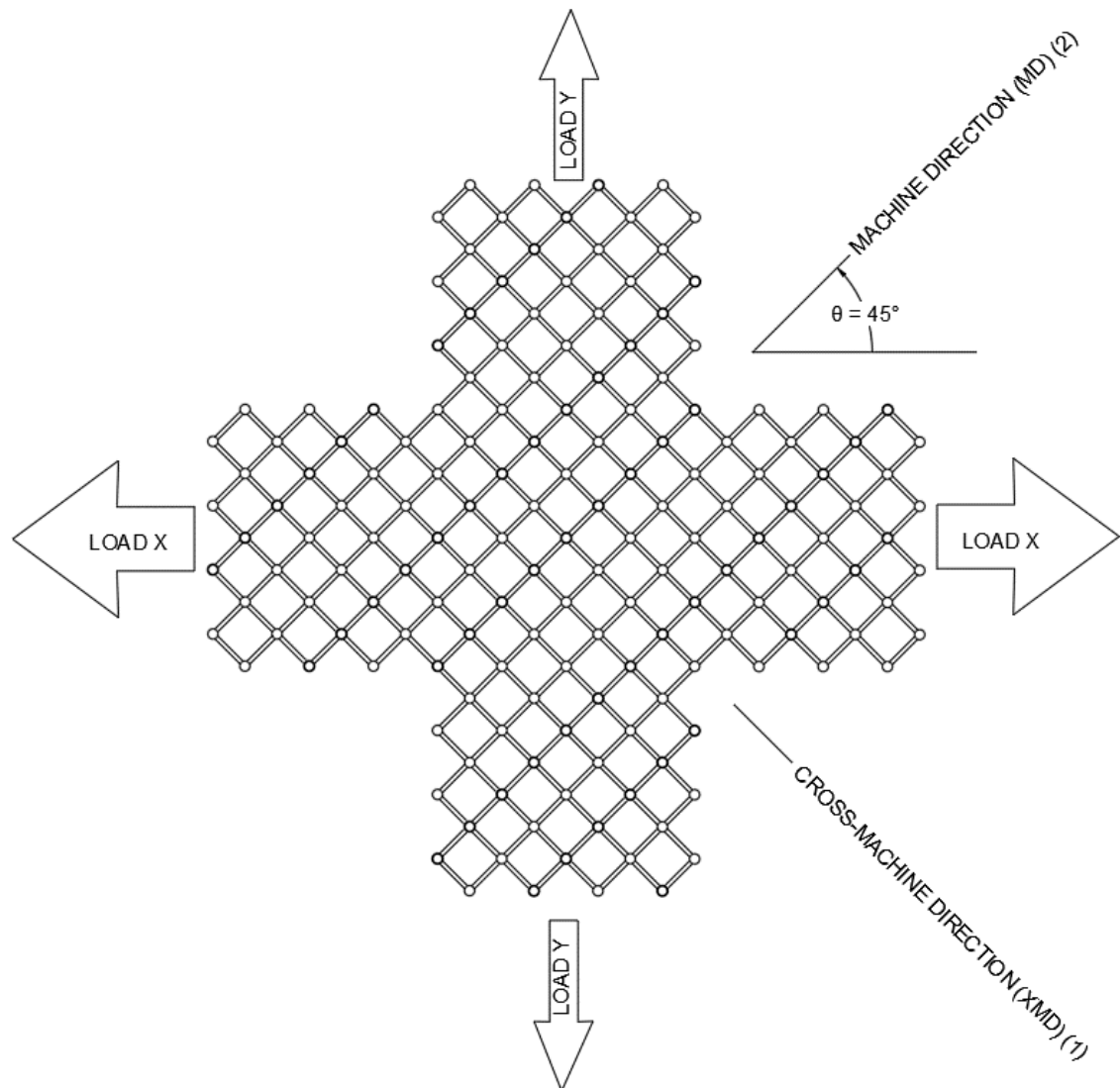


Figure 25: Biaxial test specimen oriented at a 45-degree bias to the loading directions.

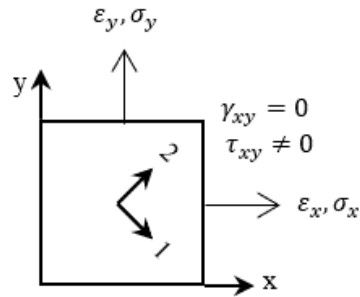


Figure 26: Assumed state of stress and strain in a bias biaxial test specimen.

Mohr's circle can be used to show the transformations of stress and strain from the loading coordinate system to the material coordinate system, similar to the work of Gunderson and Rowlands (1983). Figure 27, the Mohr's circle of strain, produces the strain transformation summarized by Equation (14). Note that to generate a non-zero shear strain in the material coordinate system ( $\gamma_{12}$ ), the applied strains in the loading directions ( $\epsilon_x, \epsilon_y$ ) cannot be equal.

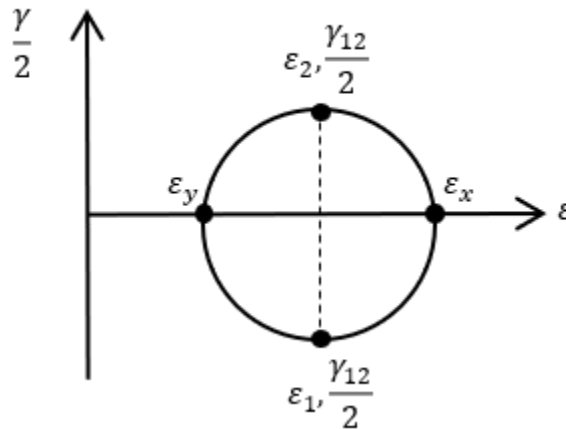


Figure 27: Transformation of strain.

$$\gamma_{12} = (\epsilon_x - \epsilon_y) \quad (14)$$

Transformation of stress is shown in Figure 28, the Mohr's circle of stress, where it is assumed that  $\varepsilon_x > \varepsilon_y$ . The triangle on the right side of Mohr's circle has a leg  $b = \sigma_x - \sigma_y/2$ . From the triangle on the left side of Mohr's circle, the leg  $b = \tau_{12}$ .

Therefore:

$$\tau_{12} = \frac{\sigma_x - \sigma_y}{2} \quad (15)$$

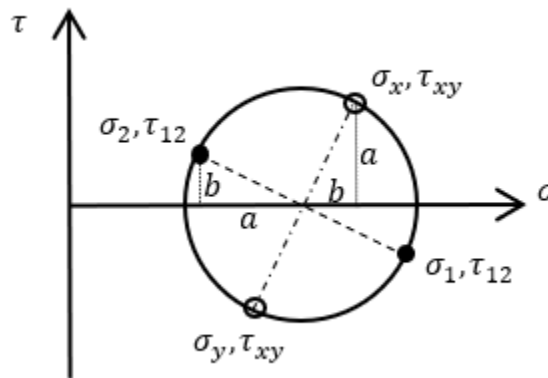


Figure 28: Transformation of stress.

Finally, the shear modulus ( $G$ ) may be derived from Equations (13), (14), and (15):

$$G = \frac{\sigma_x - \sigma_y}{2(\varepsilon_x - \varepsilon_y)} \quad (16)$$

As mentioned at the beginning of this section, Equation (16) is also obtained if the shear stress  $\tau_{xy}$  in Figure 28 is assumed to be zero.

Equation (15) was also obtained by Gao et al. (2018), Chen et al. (2018), and Shi et al. (2018) using mathematical force transformations, again based on the assumption of a negligible shear angle as discussed in Chapter 2. Their shear strain equation was derived from trigonometric relationships between the shear angle and the strain in the loading directions ( $\varepsilon_x, \varepsilon_y$ ). If the same assumption of a negligible shear angle is applied to their equation for shear strain, an equation for the shear modulus can be developed that is identical to Equation (16).

#### Assumptions to be Checked

The above derivation relies on the validity of the assumed state of stress and strain portrayed in Figure 26, specifically that the shear strain in the loading directions ( $\gamma_{xy}$ ) is zero. Full-field DIC strain imaging will enable these assumptions to be checked and modified as needed.

## CHAPTER FOUR

## TESTING PROCEDURE DEVELOPMENT

Testing Procedure Objective

The goal of this research project was to quantitatively describe the mechanical behavior of geosynthetics subjected to loading in multiple directions that simulated field loading conditions in applications such as reinforced pavements. Haselton's (2018) work on biaxial loading of geosynthetics produced three of the four elastic constants for an orthotropic linear elastic constitutive model: namely, the elastic moduli in each of the two principal directions and the in-plane Poisson's ratio. This previous testing was performed with the material's principal directions (warp and weft directions) aligned with the directions of loading. To obtain the fourth constant and complete the stiffness matrix for each material, the in-plane shear modulus must be determined using a different loading form. In-plane shear testing performed on dry woven fabrics for fiber composites suggested the feasibility of using biaxial loading with the material's principal directions placed on a bias. Consequently, to complete the final test series, the existing biaxial device was used with the geosynthetic materials placed on a 45-degree bias.

Previously, strain was measured mechanically via LVDTs, but these failed to produce repeatable data for the trial triaxial geogrid in Haselton's (2018) testing. The inconsistent LVDT strain was suspected to be related to the triaxial grid geometry (as compared to that of the biaxial grids). Triaxial grid nodes selected for LVDT instrumentation likely experienced strains that were misaligned to the LVDTs' axis of

measurement. Since the bias tests would likely also produce misaligned strains, a new method for obtaining strain was required. DIC software available through the Subzero Lab at Montana State University was selected as a non-contact strain measurement system capable of capturing movement in any direction. The DIC strain components in the principal loading directions were then matched to datalogger load records via time.

### Biaxial Testing Overview

The biaxial testing procedure was adapted from Haselton's (2018) method, which was based on ASTM D7556 and results from additional uniaxial testing. The warp direction, or Machine Direction (MD) is referred to as the Y or 2-Direction in this thesis, following Haselton's notation. The weft direction, or Cross-Machine Direction (XMD), is referred to as the X or 1-Direction.

Biaxial loading could be applied in three different ways. Mode 1 applied tensile load to cause equal displacement in both principal directions (XMD and MD). Mode 2 displaced the XMD while maintaining constant displacement in the MD. Mode 3, the reverse of Mode 2, displaced the MD while maintaining constant displacement in the XMD. The definition of modes 1-3 is consistent with Haselton's (2018) methods and nomenclature. Based on the literature (e.g. Galliot and Luchsinger 2010), bias tests for this research were performed using Mode 2 or Mode 3 loading only, and samples were cut so that the material principal directions (XMD and MD) were now rotated 45 degrees from the principal directions of loading. For 45-degree bias tests, Mode 2 and Mode 3

loadings should produce the same results, and this assumption was verified on one material (Geogrid E). The materials included in this research are summarized in Table 5.

Due to the lack of real-time strain data feedback, resilient tests were load controlled rather than strain controlled as in previous work by Haselton (2018). The test format was to preload both axes, allow the sample to sit for 20 minutes for stress relaxation and creeping, then load only one axis up to the next preload level while holding the displacement of the second axis constant to induce shearing. After this, the fixed axis was manually tensioned to the same preload as the machine-controlled axis so that both axes experienced the same preload before each new load step. Preload levels were 5, 10, 15, 20, and 25% of ultimate tensile strength, with a 20-minute hold time after each load step. After the final hold time, samples were loaded until imminent failure (audible cracking) or until the test frame reached its capacity of 2000 lbs. The first three load steps of 5%, 10%, and 15% were selected based on expectations for significantly lower shear resistance than the tensile strength in the primary directions. These were then expanded to include 20% and 25% after tests showed the capability for additional data capture. For materials with different ultimate strengths in MD and XMD, load steps were determined from the average ultimate tensile strength so that both axes were preloaded equally.

A summary of all materials and the number of samples tested in each mode is presented in Table 5. Additional tests were performed during the development of the DIC process and for strain uniformity analyses, but these are excluded from Table 5.

Table 5: Summary of materials and test types.

Geosynthetic Type	Manufacturer and Product	Generic Name	Bias Trials by Mode (2,3)
Biaxial Geogrid	Tensar BX1100	Geogrid A (GgA)	2,0
Biaxial Geogrid	Tensar BX1200	Geogrid B (GgB)	2,0
Biaxial Geogrid	BOSTD E1616	Geogrid C (GgC)	2,0
Biaxial Geogrid	BOSTD E2020	Geogrid D (GgD)	2,0
Biaxial Geogrid	BOSTD E3030	Geogrid E (GgE)	2,2
Biaxial Geogrid	BOSTD RX1200	Geogrid F (GgF)	2,0
Woven Geotextile	TenCate RS380i	Geotextile A (GtA)	3,0
Woven Geotextile	TenCate RS580i	Geotextile B (GtB)	4,0

### Biaxial Test Frame

Testing was performed using the same biaxial test frame as Haselton (2018) (Figure 29), which was developed and built by the Western Transportation Institute (WTI) at Montana State University (MSU) specifically for geosynthetic testing. The maximum interior dimensions for cruciform specimens in this device are 450 mm by 450 mm, and the maximum length of the cruciform arms is 600 mm.

Load is applied evenly to the cruciform arms by chains and sprockets linked to a central bottom load plate, which is displaced vertically by an electric motor, gear reducer, and worm screw. By pretensioning the chains equally, a constant rate of displacement in all four directions (Mode 1 loading) is possible such that the sample remains centered in the frame. Displacing in one direction while maintaining constant displacement in the second (Mode 2 and Mode 3 loading) is accomplished by detaching the chains in the constant-displacement direction from the bottom load plate and attaching them to a fixed plate. Grips consist of textured steel plates connected to the loading chain at the end of each cruciform arm. The grips are clamped manually by torquing nuts, which drive the

two grip plates together. Manual tensioning, required for bias tests to bring samples back to a state of equal biaxial tension between successive load (shearing) steps, is performed by using a wrench to tighten the nut that adjusts the position of the grip sprocket from the end of each biaxial arm (Figure 29).

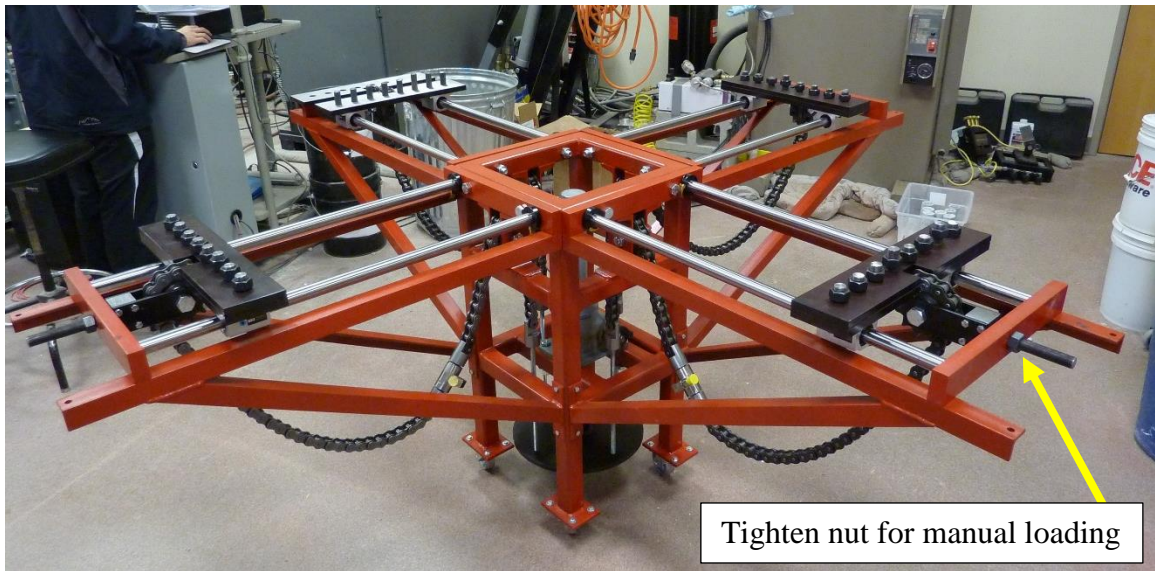


Figure 29: Biaxial testing device at MSU.

Loading speed and direction is set manually on a motor control panel by a knob and digital readout. To measure tension, the device has one load cell linked into the chain for each principal loading direction. The biaxial device is connected to a laptop computer, and load data monitoring and collection is accomplished using RTDAQ software from Campbell Scientific (Logan, UT) [CR1000 data logger]. RTDAQ is also used for monitoring and collection of LVDT-measured strains as described below. For a more detailed description of the biaxial loading frame and data acquisition system, refer to Haselton (2018).

### Load Data Collection Rate

Load data was collected at a frequency of 2.5 Hz. This was the fastest time increment that the datalogger PC could process that would also match one-to-one with strain video data reduced from 25 fps. (Processing speed limitations for the datalogger PC capped the absolute fastest time increment at 3.066 Hz.)

### LVDT Validation of DIC Strain Measurement

For one-to-one comparisons of DIC strain to LVDT strains previously used for geosynthetic testing, LVDTs were set up following methods established by Haselton (2018). Strain was measured across the gage distance using both LVDTs and DIC, and the results compared. Results and discussion are found in the LVDT-DIC Strain Comparison section beginning on page 82.

### Sample Preparation

Samples were cut and prepared following Haselton's (2018) procedure, except that no ribs were snipped in the cruciform arms due to the 45-degree bias material geometry. As in Haselton's work, geotextile ribs were snipped as necessary in the grip region to facilitate the passage of the threaded rods that make up the grip clamping system, and holes were melted in the geotextile arm tips (shown later in Figure 32) for this same purpose. To reduce necking of woven geotextiles cut on a 45-degree bias and to enhance load transfer into the center region, latex-based flexible construction adhesive was applied with a putty knife to both sides of the cruciform arms. The grip zone was not reinforced with adhesive. Initially, the construction adhesive was masked out of the full

shear zone as shown in Figure 30 to enable perpendicular straining. This test showed stress concentrations at the corners with reduced stress along the sides of the interior square region (Figure 31), which was probably a result of constraint perpendicular to the loading directions preventing even biaxial expansion. A contributing factor may have been the fibers' range of ability to strain in the loading direction: Fibers toward the corners were increasingly adhesive-reinforced, permitting less strain compared to fibers toward the center of each side.

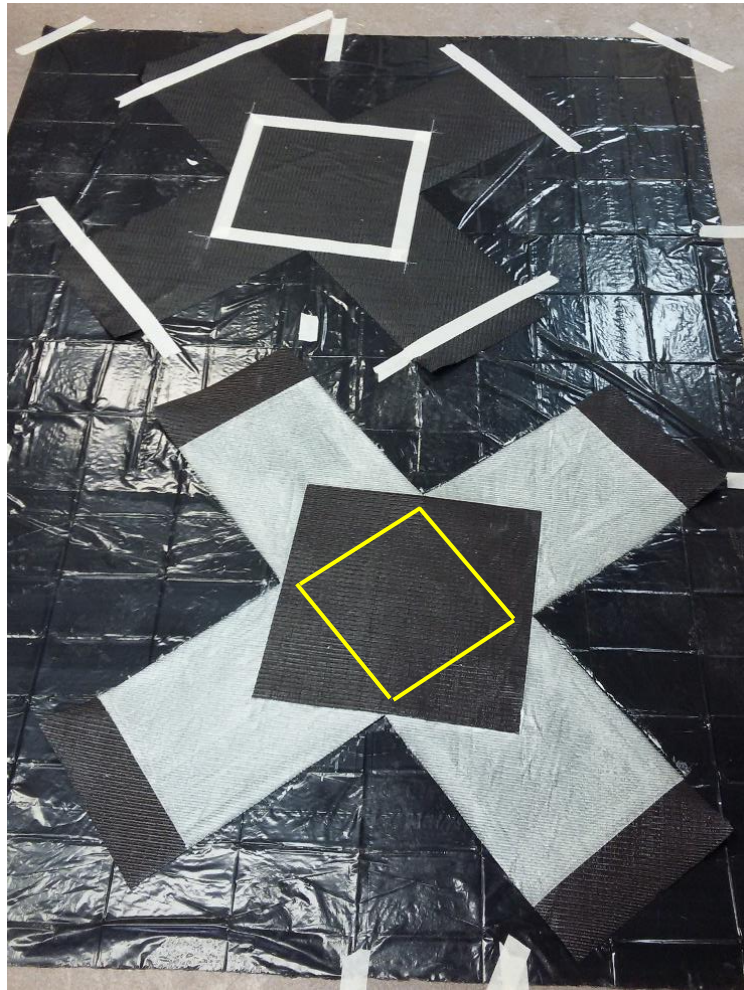


Figure 30: Initial adhesive reinforcement masking pattern. Yellow box marks approximate analysis region for Figure 31.

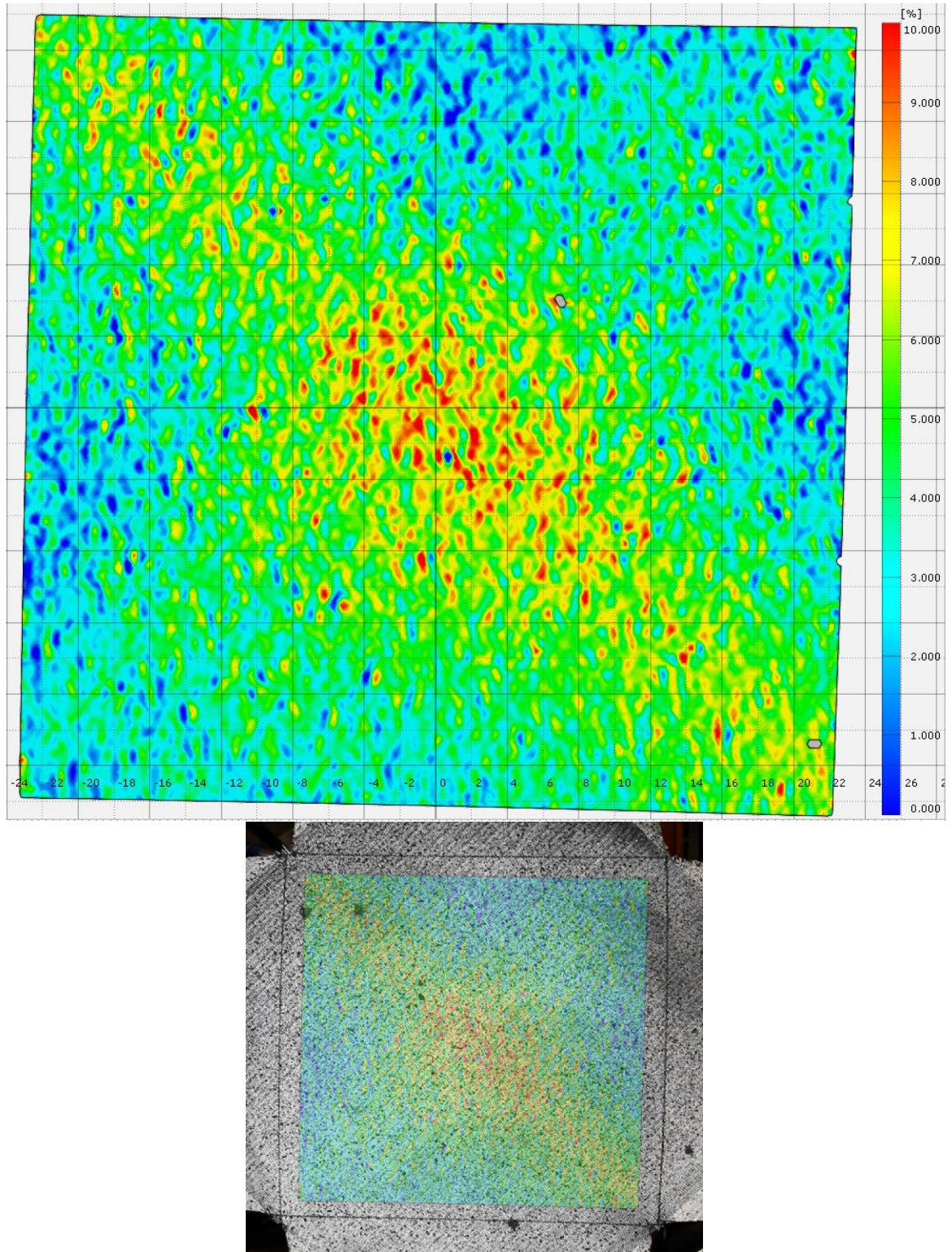


Figure 31: Strain in loading direction, initial adhesive reinforcement pattern (GtA). Strain scale is from zero to ten percent. No DIC pattern errors have been corrected.

To determine the feasibility of applying adhesive to the full length of each arm and cutting slits to enable perpendicular strain, uniaxial tests of 2-inch adhesive-reinforced straps were conducted. Two results were investigated: 1) whether the required load per unit width could be transmitted without breaking a narrower strap, and 2) whether increased necking from narrower straps would exhaust the displacement range of the biaxial device before required loads could be reached. Stiffness (full-scale necking behavior) was approximated by a 20-inch gage length, and ultimate strength was determined from a 10-inch gage due to the maximum uniaxial test displacement of 4 inches. Grips were not available to test 20-inch gages of wider specimens. The tests showed excessive necking for a slit spacing of 2 inches. Rather than pursue an in-depth uniaxial testing program, a compromise slit pattern was tested where slit spacing was kept at 2 inches, but slit length was varied as follows: 6-12-6-18-6-12-6 inches (Figure 32), respectively, based on the sample pattern from Gao et al. (2018). This method worked well for Geotextile A as shown in Figure 33, which has better strain uniformity through more of the AOI in comparison to the x-pattern developed in the unslit specimen (Figure 31). However, Geotextile B exhibited much more necking in the unslit arm portions than Geotextile A under comparable biaxial loading, such that the biaxial device extension range was exhausted at the 10% load step. With an additional glue coat added to both sides of the arms and the load increment lowered to 2% of the average tensile strength, Geotextile B reached 16% of its average ultimate strength before running the biaxial device out of range. (Material failure still did not occur.) The excessive necking

for Geotextile B may be due to a greater imbalance in principal strength directions than for Geotextile A.

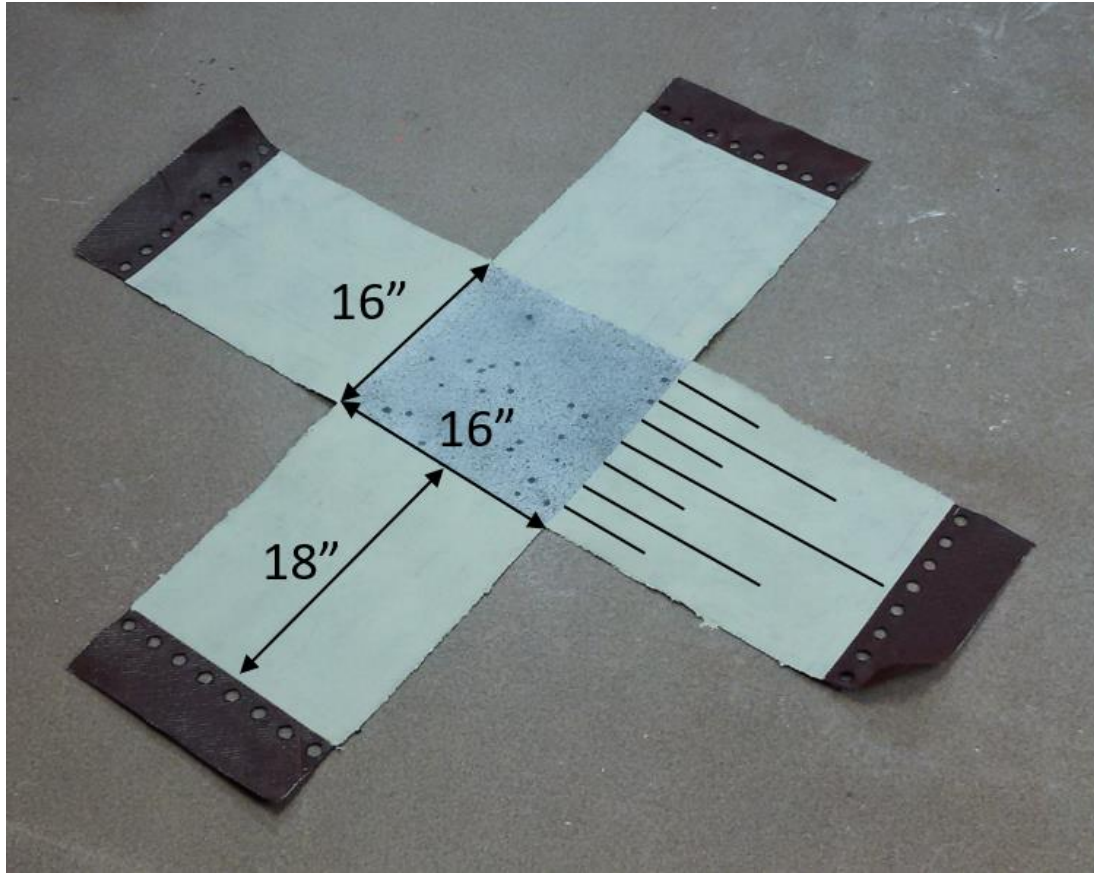


Figure 32: Geotextile sample showing dimensions, fully glued arms, and 6-12-6-18-6-12-6 slit pattern.

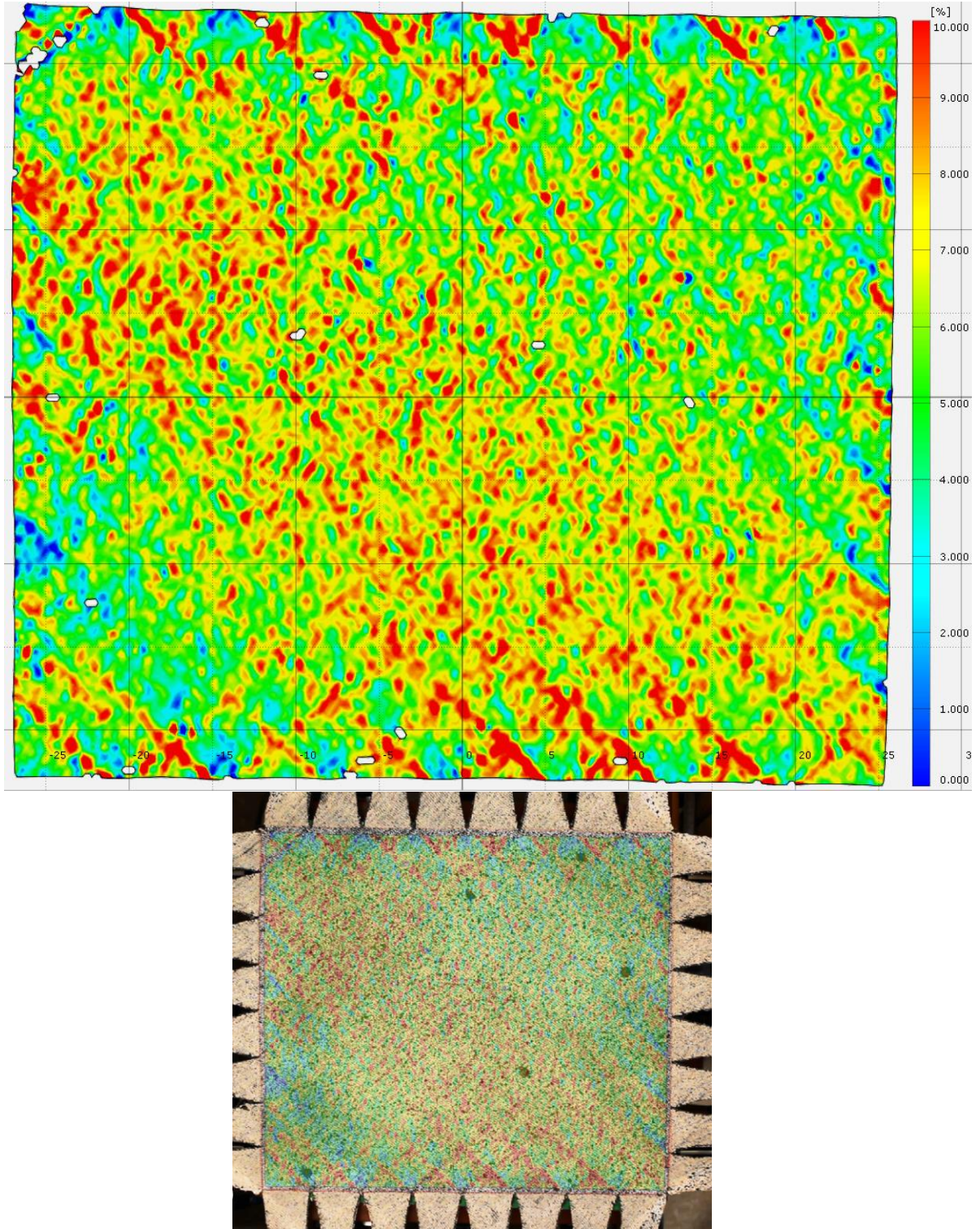


Figure 33: Strain in loading direction, full adhesive reinforcement with 2 inch slit spacing and 6-12-6-18-6-12-6 inch slit lengths (GtA). Strain scale is from zero to ten percent. No DIC pattern errors have been corrected.

## DIC Strain Data Collection

### DIC Stochastic Pattern Development

The DIC stochastic pattern went through several iterations before arriving at a final technique. Initially, only high contrast dots were placed on two gage nodes for X and two for Y (equivalent to the LVDT placement), with hopes that the DIC software would be able to ignore the remainder of the surface and only track the movement of the nodes. This method resulted in highly inconsistent tracking in the DIC software (ARAMIS). Placing high-contrast dots on every node improved the DIC pattern recognition slightly, and it became evident that the DIC software was attempting to process the entire surface rather than track only the few points of interest at the nodes. For large scale stochastic patterns, DIC literature suggested using a dot stencil for spray paint or drawing a grid in marker, and for small scale patterns, a spray paint speckle technique was recommended (ARAMIS User Manual – Software 2007). Based on the large-scale pattern suggestion, placing high contrast dots over the entire geosynthetic material produced highly consistent stochastic pattern recognition and good pattern quality (as assessed from the zero-strain reference image). Due to the success of the overall pattern, the spray pattern was also tried, with good results. The primary benefit of the spray paint speckle was its speed and adaptability to batch processing, although it required careful attention while spraying to ensure pattern consistency.

Three different backgrounds were tried in the process of obtaining better DIC data. Initial videos were filmed without changing the background previously used with LVDT-instrumented tests. This busy, multicolor background was quickly modified to a

solid color, and additionally then to a flat surface by placing the blocking under the central background instead of on top of it. Both a matte black color and a high-contrast fluorescent green color were evaluated. The black color was selected with hopes that the geogrids would disappear against it such that only the high-contrast node markings would be tracked in the DIC software; however, the software continued to attempt to track the entire geogrid surface. Consequently, the background was changed to a high-contrast green for better edge definition of the geogrid apertures. The flat surface was desirable to reduce shadowing (and secondarily to eliminate blocking edge lines, which the DIC software frequently identified as part of the geogrid surface).

Table 6 shows a summary of DIC stochastic pattern marking methods explored. Photos of the different backgrounds and stochastic markings are shown in Figure 34 and Figure 35.

Table 6: DIC stochastic pattern marking methods.

Marking Method	Marking Technique	Results
Silver permanent marker	Gage nodes for X Gage nodes for Y	Poor recognition and tracking of gage nodes.
Silver permanent marker	All nodes	Improved recognition and tracking of nodes, but not consistent throughout image stack.
Matte white grease marker	All nodes	Improved recognition and tracking of nodes, but not consistent throughout image stack. Potentially less glare due to matte surface.
Matte white grease marker	All nodes and webs (“multi-dot”)	Good stochastic pattern quality. Consistent recognition and tracking of nodes throughout image stack for biaxial grids. Potentially less glare due to matte surface.
Matte white spray paint speckle	All nodes and webs	Good stochastic pattern quality. Consistent recognition and tracking of nodes throughout image stack for biaxial grids. Potentially less glare due to matte surface. Improved sample marking speed; ability to batch-spray.

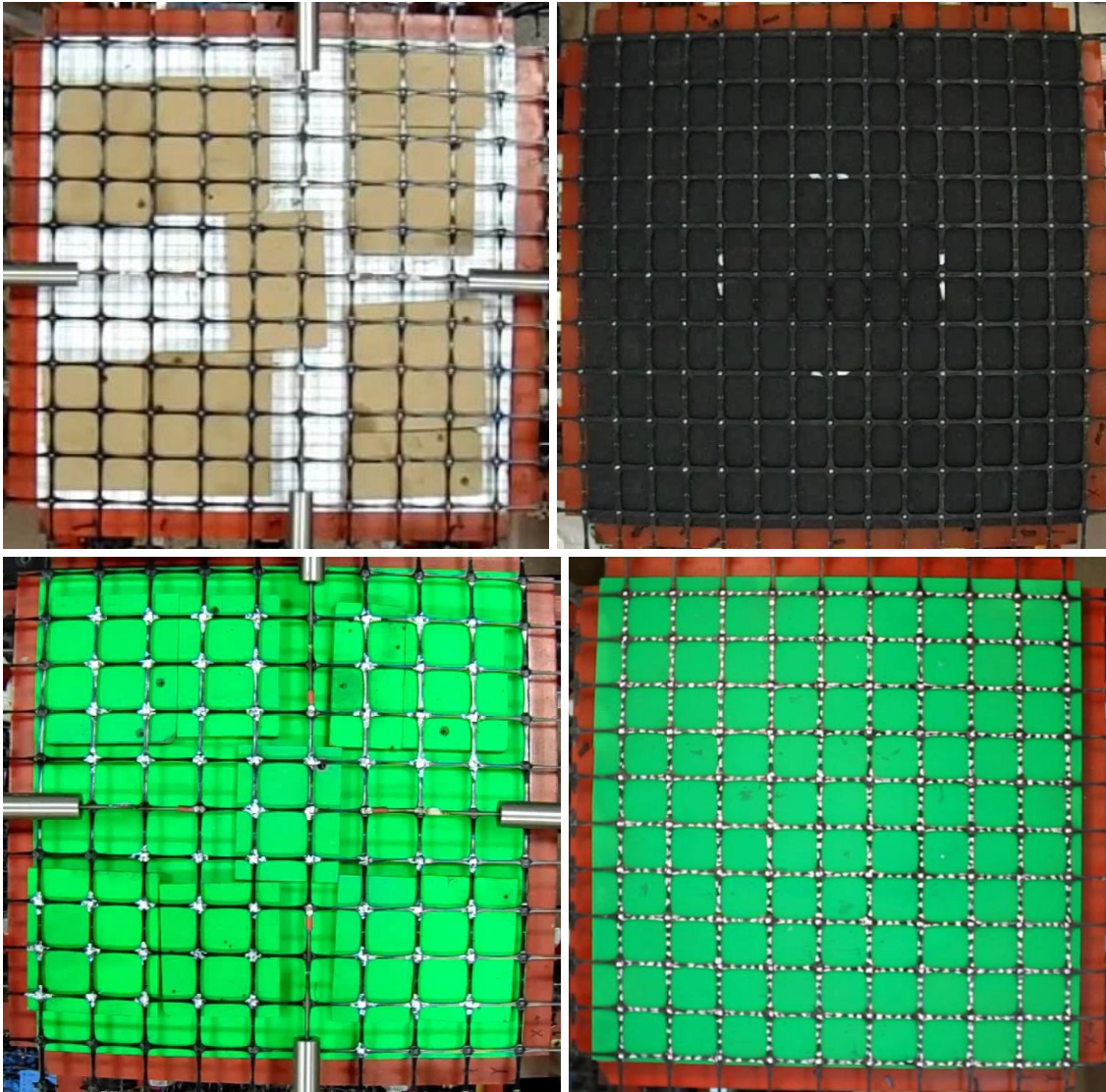


Figure 34: Stochastic pattern development. Clockwise from top left: Original background with surface blocking; black background with silver sharpie on all nodes; high-contrast green background with silver sharpie multidot pattern; high-contrast green background with surface blocking and silver sharpie on all nodes. Silver LVDTs also appear in the left two images.

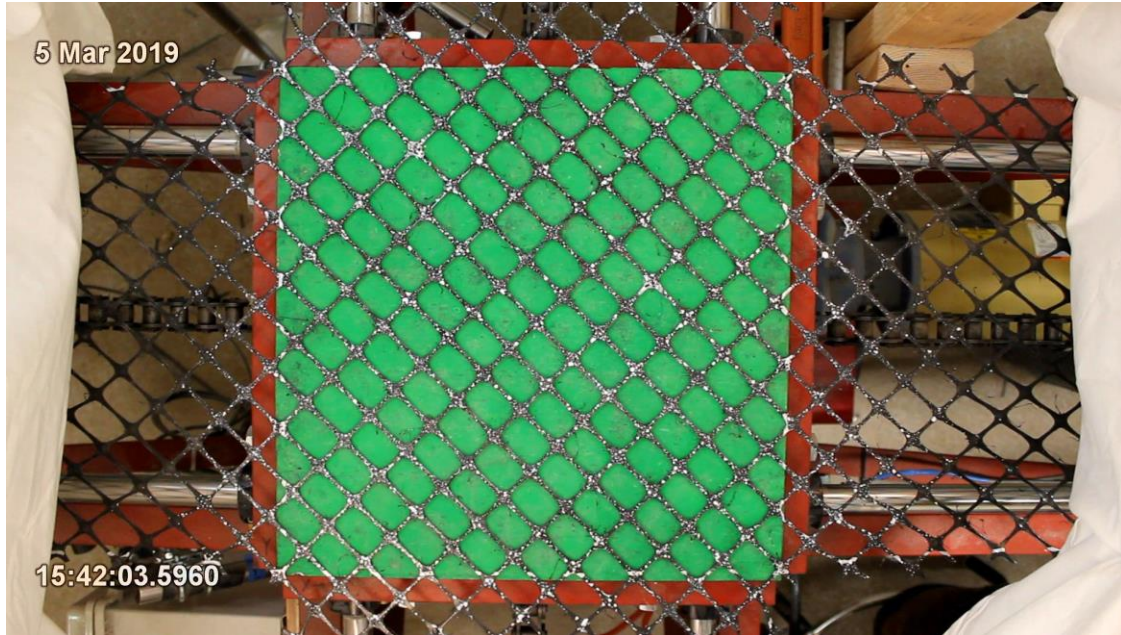


Figure 35: High contrast green background with white spray paint speckle.

### Camera Overview

The initial camera used for DIC process development was a Sony Cyber-Shot DSC H-300 DSLR; however, this camera was quickly abandoned due to no precise way to match load-strain curves via time. The camera used for the remainder of development and testing was a Canon EOS Rebel T2i DSLR, which had the capability for remote control from a laptop computer (PC) using a USB cable. Canon EOS Utility (2010) software was used to set the camera time from the PC and provide remote control of the camera and viewscreen from the PC. Camera settings were selected to facilitate easy one-to-one matchup with 2.5 Hz datalogger records and for high image resolution for DIC processing. Sequential still photos (interval timer automatic shooting) were investigated as a higher resolution alternative to video, but the minimum time increment of 5 seconds between photos for the Canon camera was unsuitable for the short loading

period of these tests. This time increment may have been limited by PC processing capability, according to the Canon software manual (EOS Utility 2010). Canon camera settings used for testing are listed in Table 7.

Table 7: Canon camera settings

Setting	Option	Explanation
Camera setting	A-DEP	Enable Live View Movie recording (camera control from PC).
Video setting	PAL	Avoid fractional frame rate (fps).
Frame rate (fps)	25	Lowest FPS setting available. Avoid excessive frames (bogs down DIC software). Match 1-to-1 with 2.5 Hz datalogger records after thinning.
Resolution	1920x1080 (Full HD)	Highest resolution available for video with this camera. Increase precision of DIC analysis.
Exposure	Auto	Worked fine.
Daylight setting	Auto	Worked fine.

### Camera Jig and Focus

The camera was positioned using an overhead through-hole focusing jig as shown in Figure 36 (left) so that the lens was parallel to the test surface. Initial tests were performed using a cantilevered jig so that the camera was fully separate from the test frame. This setup was subsequently modified such that the camera jig was rigidly attached to the test frame as shown in Figure 36 (right). If any vibrations traveled from the frame into the jig during testing, no problems were observed. Camera focus, centering, and the apparent digital quality of the stochastic pattern were checked prior to each test using the large-screen PC display. Zoom was set so that the minimum field of view was the extents of the square interior region of the test frame, as shown above in Figure 35.



Figure 36 Left: Through-hole focus mechanism. Right: Rigid camera jig.

### Camera Lighting

Lighting was provided by warm-toned overhead fluorescent lights and several large north-facing windows. Direct lighting on the sample was controlled by draping a white sheet over the camera jig and test frame to create diffuse lighting. Three lamps with a combination of warm white, bright white, and cool white lightbulbs were used to brighten the diffuse lighting. Figure 37 shows the lamps and light diffuser sheet. These lighting protocols were developed to help with DIC stochastic pattern recognition

consistency, which appeared to be affected by dim lighting and especially by glare from non-diffuse lighting.



Figure 37 Left: Lamps. Right: Light diffuser sheet.

### Strain Data Preprocessing

Preprocessing for the video data involved adding a timestamp to each frame, trimming the timestamped file, exporting the trimmed file to a 5 Hz frame rate, and slicing the 5 Hz video into an image stack.

### Timestamping

Timestamping was done using vMTS64 software with the video output size set to native, with the output video bitrate set manually based on the input bitrate found in the video properties (Visual MP4/MOV Time Stamp 1.4.0, 2017). A timestamp format of HH:MM:SS.SSS was used, and the date was also stamped to aid with file management. The vMTS64 timestamp software automatically exported the input MOV video file into an mp4 format; this was a hardcoded software feature and not adjustable. Spot check comparisons of file size indicated no or minimal data loss.

### Data Reduction

Trimming and frame rate reduction were performed on the timestamped .mp4 files using VSDC Free Video Editor software (2017). Trimming the videos minimized excess data to process through the DIC software and ensured a valid zero-strain reference image. Trimming points were taken just prior to the audible “click” from turning on the load cell and just prior to unloading or material failure. Files were exported to .AVI video format (required for MATLAB image stack slicer code) using highest quality video settings and a 5 fps frame rate. Multiple export frame rates were tested to try to improve DIC stochastic pattern recognition, but no improvement was observed using faster frame rates (25, 12, and 8 fps).

### Conversion to Image Stack

For image stack slicing, a basic MATLAB script was borrowed and adapted. The script's functionality was limited to slicing the exact frame rate (i.e., every frame) from .AVI video files. The sliced image stack was then ready for DIC processing.

### Data Reduction for Long-Term Tests

For long-term (one-hour-plus) stress relaxation / strain creep tests, video data was condensed by splicing. The test length was too long for either of the cameras to film as a single video, so filming was limited to the loading portions of the test since they were of primary interest. After the videos were trimmed and sliced, a further reduced frame rate of 2.5 Hz was obtained by deleting every other image in each of the 5 Hz image stacks; this helped to reduce DIC processing time. Next, the image stacks were spliced into a single dataset for DIC so that all successive reloading frames would be measured from the true zero-strain reference frame at the very beginning of the test. Lastly, the images in the spliced stack were renumbered sequentially (required for DIC processing).

Image stack splicing was successful using the following conditions: GOM Correlate DIC software, spray paint speckle stochastic pattern, and fully remote camera operation. For these conditions, splicing the load steps directly together worked fine, with no need for additional intermediate filming. Unsuccessful preliminary development involved a temperamental older version of ARAMIS DIC software, earlier iterations of the stochastic pattern, and manual camera control that introduced jiggle into the video.

### DIC Software

The initial DIC software investigated was GOM Correlate, a free software for two-dimensional analysis of displacements and strains (2018). However, while the free version could perform all the analysis required, numerical data export was restricted to the licensed version, GOM Correlate Professional. Since an older DIC software, ARAMIS, was already available through the MSU Subzero Lab, ARAMIS was used for developing most of the filming and preprocessing protocols (2008). Both ARAMIS and GOM Correlate are licensed from the same developer (Trilion), and GOM Correlate includes an updated version of ARAMIS together with additional software functionality. Later, the MSU Subzero Lab software was updated to the full GOM Correlate Professional, so it was used for all data processing except the one-to-one LVDT-DIC strain comparisons, which were already complete using ARAMIS. The older ARAMIS version was highly temperamental, and updating the software improved all DIC performance aspects.

### DIC Process Overview

The basic processing method was the same for both ARAMIS and GOM Correlate Professional. For the imported image stack, a surface was created on the reference image (initial frame) for the displacing geosynthetic, and overall surface strains were calculated. Next, points were created on every geogrid node center, point-to-point distances were created between every two nodes in the principal loading directions, and strains over the point-to-point distances (“segments”) were recalculated for the entire

image stack. The point and segment method was developed for geogrids because their punched-and-drawn polymeric architecture primarily strains at the nodes rather than along the webs (i.e., an overall surface strain field would not provide useful information for global strain behavior of geogrids.) For geotextiles, segments were created within the region of uniform strain determined for each sample. Finally, all segment strains for all images were exported numerically to an ASCII file to be matched with load data in Excel. Strain output was also available in video heatmap format, which was useful for evaluating surface tracking consistency throughout the test.

Table 8 summarizes the primary software parameters used for ARAMIS and GOM Correlate Professional.

Table 8: DIC software parameters

Parameter	ARAMIS	GOM Correlate Professional
Stochastic patterns tested:	All except spray paint speckle	Grease marker multi-dot Spray paint speckle
Facet size:	10 - 24 pixels	10 pixels
Facet spacing (overlap):	7 - 12 pixels	5 pixels
Surface masking:	Interior cruciform region	Interior cruciform region or none
Surface quality:	High Accuracy	High Accuracy
Node point type:	Stage Point	Facet Point
Segment line type:	Point-Point Distance	2-Point Distance
Strain calculation tool:	Line strain (technical)	Length change (X) and (Y)
Strain export:	File/Export Statistics	View data in table > Export Table Contents
Export file type:	Delimited ASCII	Delimited CSV
Macro recording:	Yes; not tested	Yes; easy
Processing time:	Long (1-4 days)	Short to Medium (1 to 6 hours)

### Facet Parameters

Facet size was selected to be very small while still maintaining good identification of the stochastic pattern. The smaller facet size enabled better local resolution of strains, but the facets had to be large enough to capture a unique greyscale pattern; consequently, the fine spray paint stochastic pattern enabled the use of much smaller facets.

Facet spacing was selected for 50% facet overlap, the maximum recommended in the literature (ARAMIS User Manual - Software, 2007). High overlap provided better global resolution of strains due to increased density of measuring points. Also, in ARAMIS, point creation was restricted to the selection of existing facets, so high overlap provided maximum positioning flexibility for node center points. (In GOM Correlate Professional, points could be created without restriction.)

Multiple facet sizes ranging from 10 to 24 pixels and multiple facet spacings ranging from 7 to 12 pixels were explored in ARAMIS to reduce flicker in the data, but facet size and spacing did not appear to have a strong control over stochastic pattern recognition, especially as compared to lighting and marking techniques. Additionally, changing the facet shape from rectangular to quadrangular (as recommended in the literature for high strains) did not appear to reduce the flicker in ARAMIS results.

### Surface Creation and Stochastic Pattern Recognition

Surface creation parameters were set for high accuracy. During surface creation, before processing the entire surface, a surface quality report (Figure 38) was produced based on the stochastic pattern of the reference image. This was particularly useful in that a single photo of the ready-to-run biaxial test could be imported to evaluate surface

quality before running the test; in ARAMIS, inconsistent surface recognition was directly indicative of data loss from the nodes. Masking was used to restrict analysis to the interior of the cruciform specimens. Ultimately, it was discovered that in GOM Correlate, the nodes reported much more consistently than the flickery DIC pattern recognition had indicated, so the value of surface creation for GOM Correlate processing appears to be negligible for geogrids.

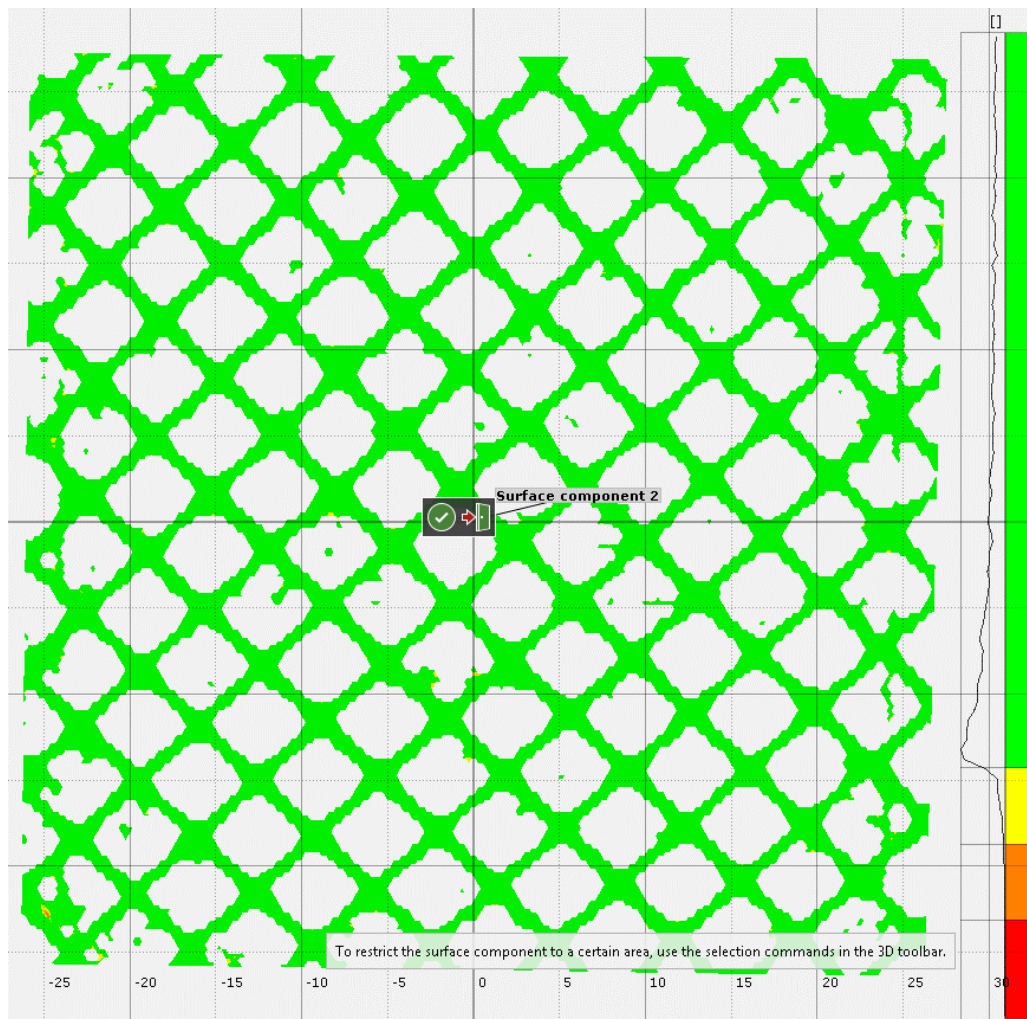


Figure 38: GOM Correlate surface quality report generated during surface creation. The stochastic pattern was the spray paint speckle shown in Figure 35.

### Segment Creation and Strain Export

For geogrids, node center points were created using facet points, which were created manually to ensure accurate placement. Node center points were numbered in the same order for every dataset, which enabled a macro to batch process the creation of segments and the strain export. To handle the variations among the grid geometries and orientations, several versions of the macro were built using GOM Correlate's macro recording tool. Segments were created using the 2-point distance tool, and strains in the primary loading directions were obtained using the length change inspection tool. Numbering of segments was necessary to correctly spatially map the exported strains. Numerical strain data was exported via the PIP/Table/Diagram explorer popup: with all segments selected, the table display was set to "Values," displaying the epsLY and epsLX properties. These were then exported to a csv file by clicking the "Export Table Contents" icon. Geogrid processing in GOM Correlate Professional was relatively fast, approximately 1-6 hours depending on the use of macros; however, processing in ARAMIS typically required multiple days. The processing time could have been shortened by increasing the facet spacing and not selecting a high-accuracy surface, but this would tend to reduce the quality of the output strain data. The magnitude of potential quality loss, however, was not explored and quantified.

For geotextiles, full-surface strain behavior was used to select arbitrary gage lengths along both loading axes for strain export. Direct export of shear strain was explored, but the GOM Correlate shear strain field appeared to be much more sensitive to small DIC pattern errors than the principal loading direction strains. Consequently, shear

strain was calculated from principal loading direction strains following the method used for the geogrids.

## Postprocessing

### Strain Data Reduction

For geogrids, depending on the number of segments, DIC analysis typically produced around 150 strain-vs-time datasets in each principal loading direction. Since the datalogger only captured one load-vs-time dataset in each principal loading direction, the strains had to be condensed to a single, best-representative strain-vs-time dataset to pair with the load dataset. Both spatial averages and single gage lengths were considered, but spatial averages were determined to be more reliable since they were less sensitive to non-uniform strains or data loss due to flicker. For each sample, four concentric regions were selected for comparison as shown in Figure 39. Average strains from each region were mapped to the load dataset and the results compared through each stage of analysis. This was done to evaluate the consistency and quality of the regional averages and to help identify outlier values (from non-uniform strains) that might otherwise be difficult to determine.

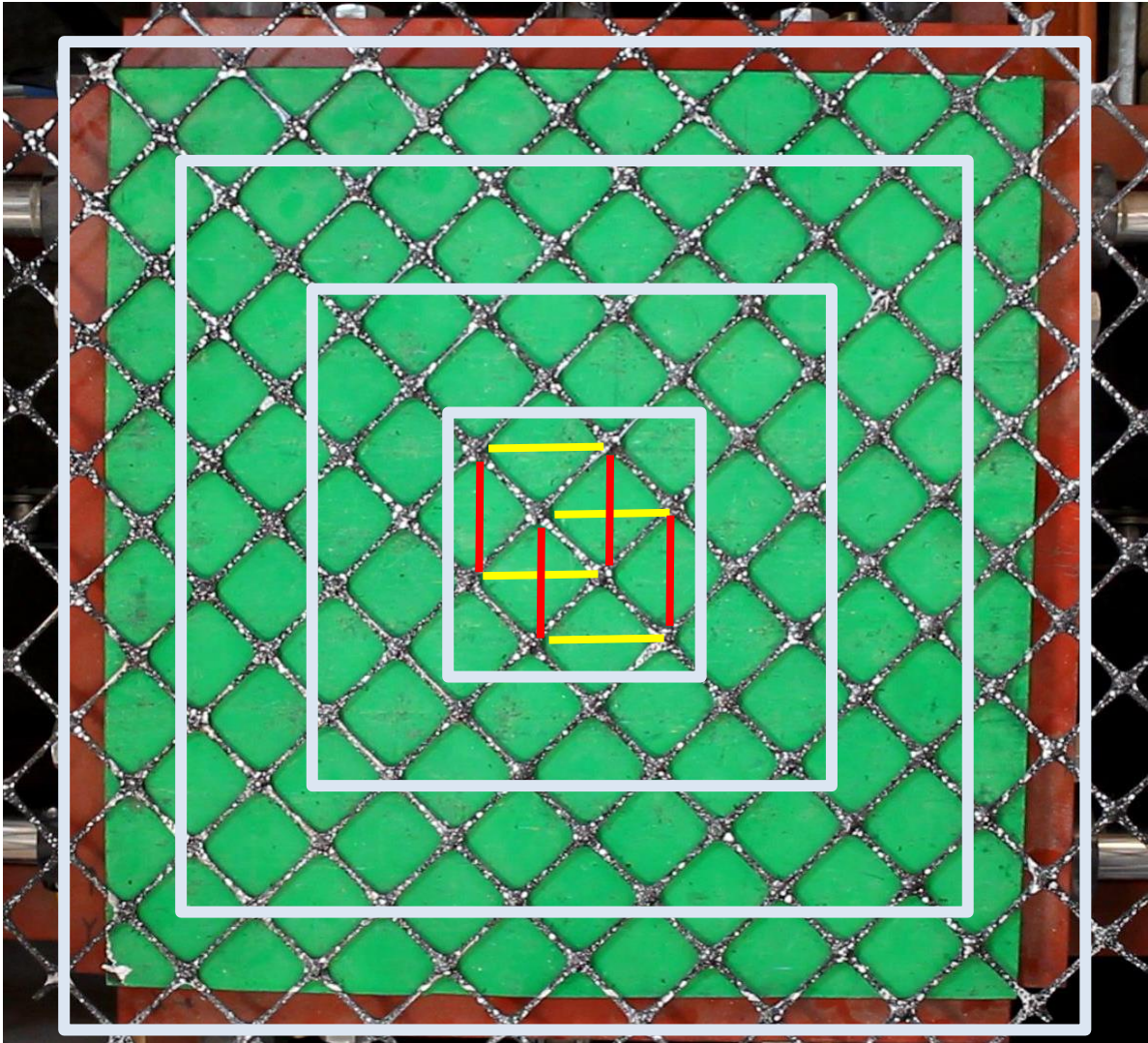


Figure 39: Typical concentric regions for strain averages. For the innermost region, yellow bars show typical X strain segments, and red bars show typical Y strain segments.

For woven geotextiles, strains were exported from segments created in the region of uniform strain for each sample. For better confidence in the data, five segments in each loading direction were selected for comparison as shown in Figure 40 and Figure 41. Of these, the three axis-centric segments in each direction were then plotted versus load.

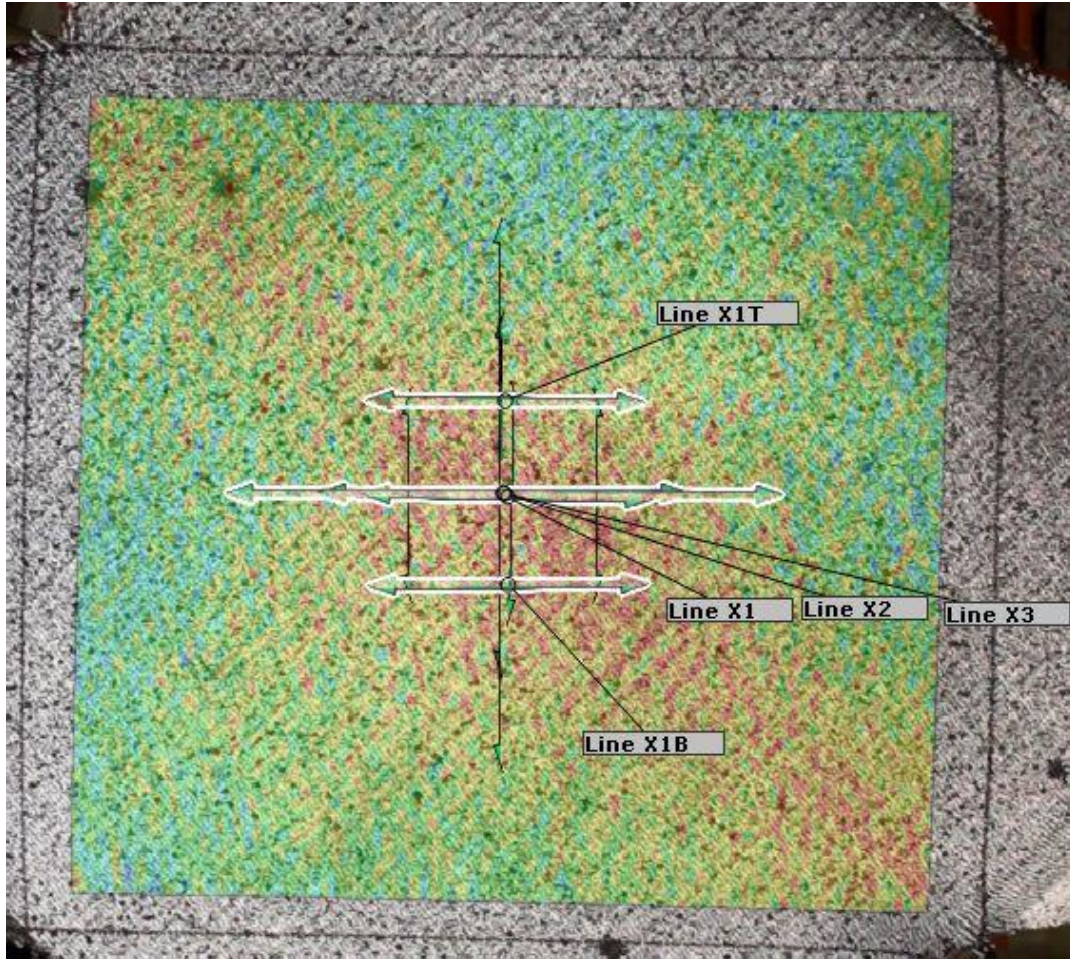


Figure 40: Segments and strain field in the X loading direction for a woven sample (GtA).

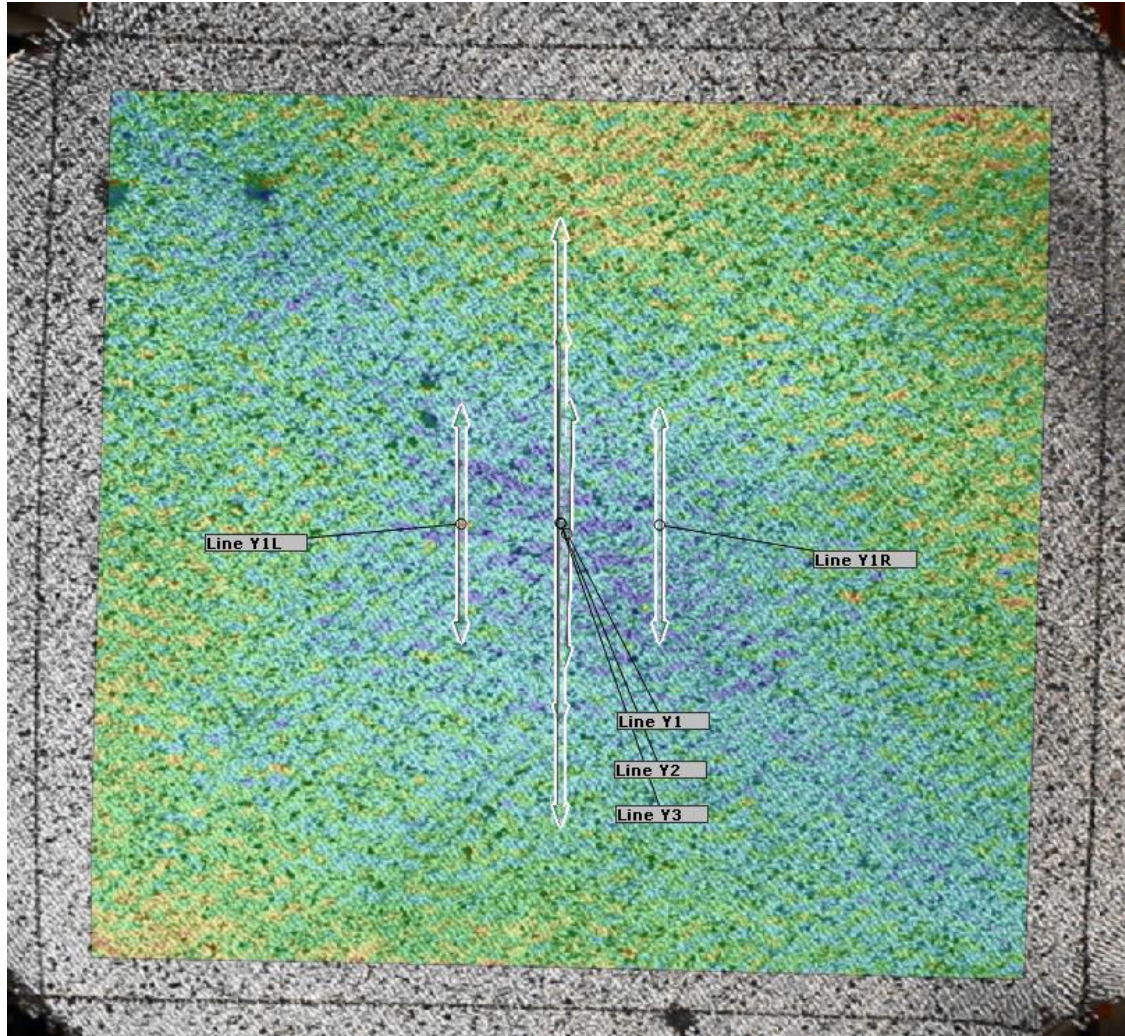


Figure 41: Segments and strain field in the Y loading direction for a woven sample (GtA, same sample and data point as Figure 40).

### Line Load Conversion

Load was converted to line load (load per unit width of material) following standard convention for geosynthetic materials in accordance with ASTM D6637 (2015). This was done by dividing the load by the width of the cruciform arm carrying the load. For woven geotextiles, the width for line load conversion was taken as the width across the sample arm. For the geogrids, the width for line load conversion was determined for

each sample as the distance across the arm at its widest point of contribution to the central stress distribution, measured from mid-node to mid-node perpendicular to the direction of loading. Figure 42 and Figure 43 illustrate this measurement for two biaxial grids. The traditional method for determining width for line load (as described in ASTM D6637 and used for previous work by Haselton (2018)) was considered; however, this did not seem ideal for the bias tests since widths determined by extension of the traditional method were not exactly perpendicular to the direction of loading due to non-square apertures of the geogrids. For example, Geogrid C, Geogrid D, and Geogrid E appear to have square apertures as shown in Figure 42, but the average tensile web length in each of the principal directions is slightly unequal. The other three geogrids in this study had clearly rectangular apertures as shown in Figure 43.

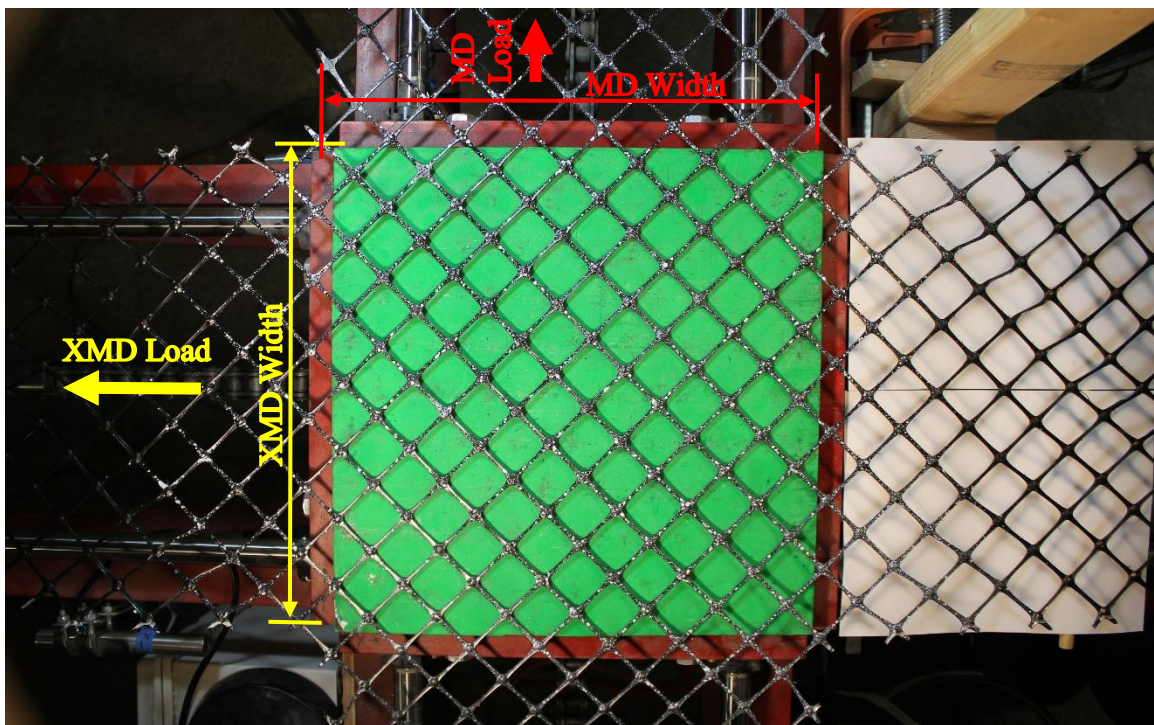


Figure 42: Bias biaxial geogrid (GgE) showing width calculation for MD and XMD arms.

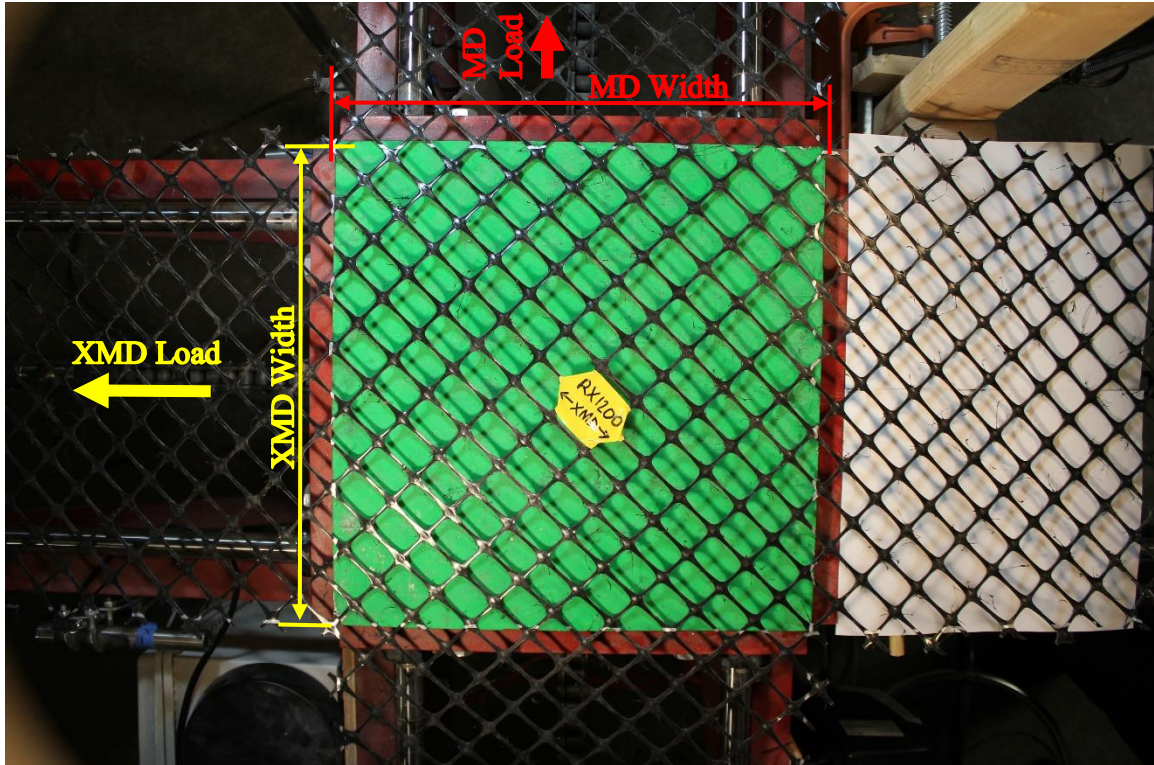


Figure 43: Bias biaxial geogrid (GgF) showing width calculation for MD and XMD arms.

#### Load-Strain Curve Generation

Strain and line load records were correlated by their starting timestamp and common time increment to produce load-strain curves. The time increment for the strains was determined from the timestamp on the initial frame and the frame rate from video data reduction. For long-term tests with multiple load steps in a single spliced image stack, the starting time and time increment was reset for each successive load step.

#### DIC Strain Error Detection

Errors in the DIC strain data were partially auto-eliminated by the DIC software, which, if it detected problems in its stochastic pattern mapping, would discard the

numerical strain values built from problematic nodes and report a value of “???”

However, on rare occasions, the DIC software would identify the wrong location as the node (e.g., the surface pattern was not perfectly stochastic) as shown in Figure 44. This type of error tended to show up as extreme spikes in the data. To scan for extreme spike errors, standard deviation of all segments in each image frame was used. Standard deviation in excess of 1% strain generally proved to be a good indicator of erroneous high strain values, which were then manually evaluated and discarded.

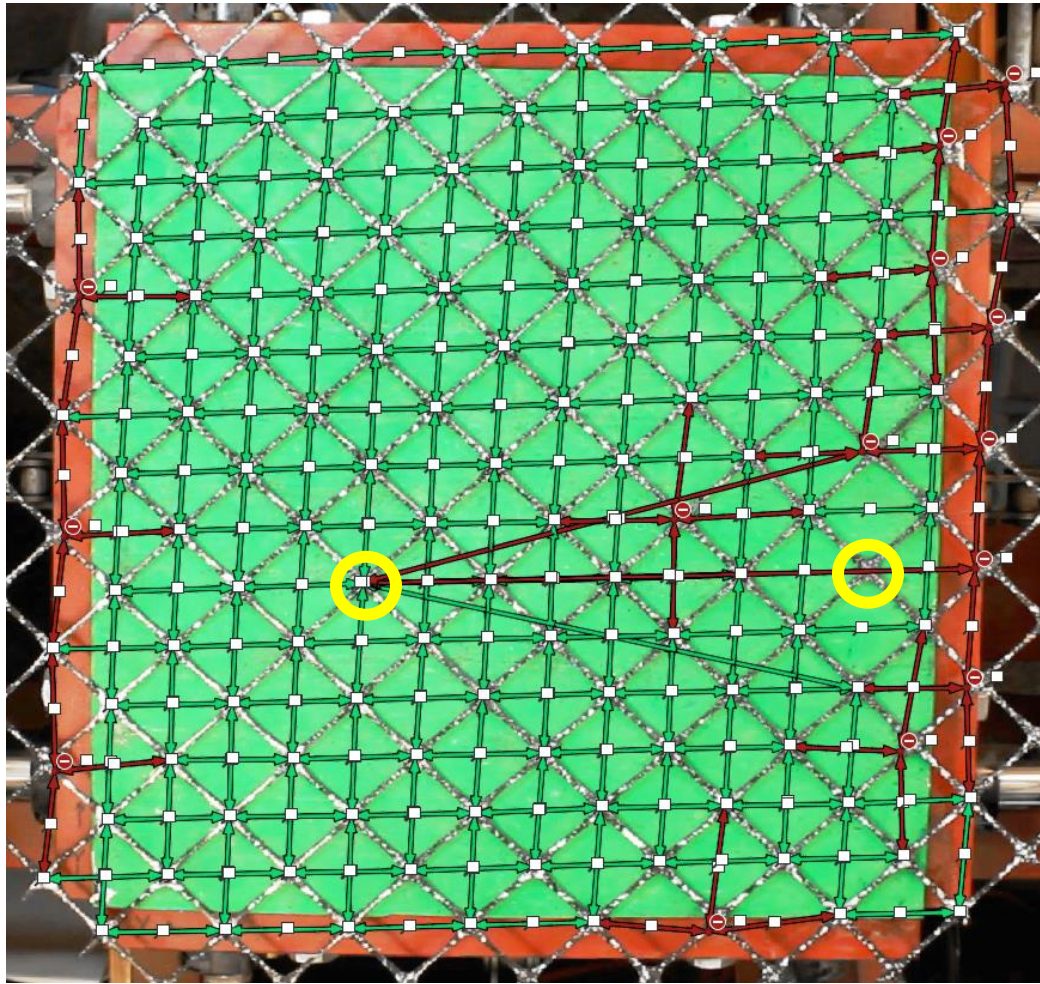


Figure 44: DIC self-detected erroneous node locations (red) and misidentified node (yellow circles). Double-headed arrows are segments constructed in the DIC software.

## CHAPTER FIVE

## VALIDATION OF STRAIN DATA ASSUMPTIONS

Overview

The biaxial test procedure used for this thesis and for previous work by Haselton (2018) relied on several assumptions regarding the strain behavior of the samples, and the full strain field captured by DIC in this work enabled these assumptions to be checked. The assumptions were that 1) DIC and LVDT strain measurement systems produced equivalent data such that tests using both methods could be combined into a single dataset; 2) there exists a region within the interior of the cruciform sample where strain can be said to be uniform; and 3) the biaxial test procedure creates a state of biaxial tension only, with no shear in the loading directions (i.e., negligible  $\gamma_{xy}$  as mentioned in Chapter Three). To validate the equivalence of DIC-collected strains in comparison to previous tests instrumented using LVDTs, a dual-instrumented test was performed. Strain uniformity within the central rectangular or square portion of the test specimen was evaluated using DIC for representative materials from each architecture type, and both spatial variability (heatmaps) and statistical variability were considered. These analyses were performed to validate the LVDT gage length and location from prior testing (Haselton 2018) and to determine the sampling region for strains in this research. To evaluate the assumption of pure biaxial tension, the magnitude of the shear strain ( $\gamma_{xy}$ ) in bias and non-bias tests was evaluated using DIC and compared to the magnitude

of the strains in the loading directions ( $\epsilon_x$  and  $\epsilon_y$ ) for representative materials from each architecture type.

### LVDT-DIC Strain Comparison

To demonstrate that the DIC system produced equivalent strain readings to those of the LVDTs previously used (Haselton 2018), a non-bias Mode 1 test was run on a biaxial geogrid using both instruments simultaneously, and the LVDT strains were compared to DIC strains from the identical gage points. Equivalent strain measurements were necessary to enable the combination of datasets from both LVDT and DIC methods to produce the complete set of elastic constants for each material tested. This test was performed before precise timestamp matching was developed for the camera system, so strains were only approximately related via time. Approximate matching was done by clipping the video manually as close as possible to the audible “click” from load actuation and by selecting a corresponding “zero” strain in the datalogger by picking the first record with increased strain (from loading). Exact matching of data values was not expected, but the slopes of the load-strain curves from each method were of particular interest and were evaluated to examine equivalency. Figure 45 shows the results of this Mode 1 non-bias test, with X axis (XMD) data in red/orange and Y axis (MD) data in blue/grey. As seen in this figure, the DIC strains (hollow circle data points) exhibited a slightly less-smooth curve, partly due to scatter present in the DIC method and partly due to collecting twice as many DIC readings as LVDT records (filled circle data points), but the overall slope of each curve was essentially identical. These results demonstrated

satisfactory data equivalence between the two strain measurement systems. This test was performed using an older software, ARAMIS, which was subsequently updated to a newer software (GOM Correlate) from the same developer. A recheck validation was not considered necessary after the update since the new software performed significantly better overall. Moreover, scrolling through image stacks in GOM Correlate clearly showed the movement of user-created node points tracking with the geogrid node movements as if they were pinned to the material in the video, which corroborated its ability to track the geogrid movements accurately, similar to a physically pinned LVDT.

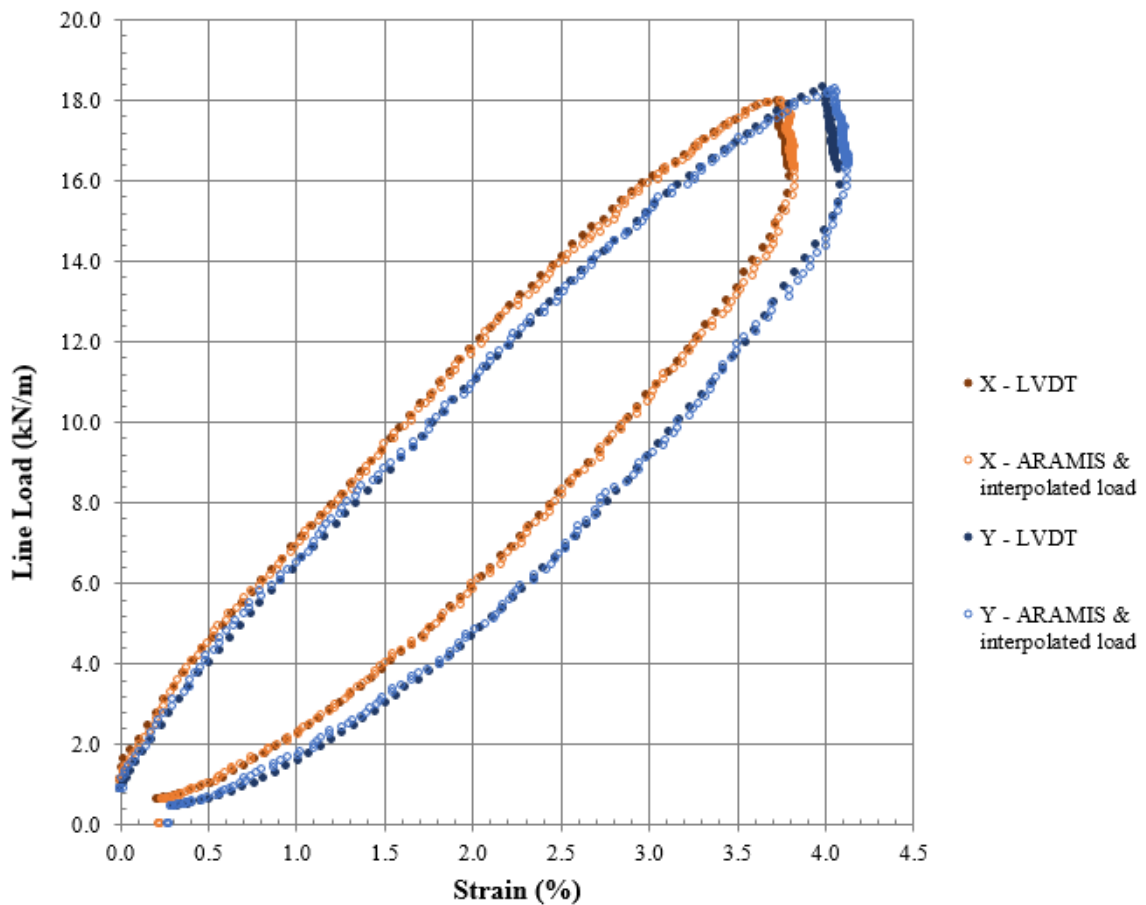


Figure 45: LVDT-DIC strain data comparison (Mode 1 test results from Geogrid C).

### Strain Uniformity Analysis

An underlying assumption to the LVDT-instrumented tests was that the single LVDT gage strain measurements accurately reflected the macro behavior of the sample (i.e., the interior of the cruciform specimen). To verify this assumption, DIC strain heatmap plots were created and compared for strains at several stages throughout a selection of both bias and non-bias tests. Additionally, if the strain was not uniform across the surface, this analysis was expected to highlight regions of better consistency or of best representative strain to use for this research instead of a single gage length.

For the bias tests, strain uniformity data was drawn directly from samples in the shear modulus dataset. For the non-bias tests, the 20-minute hold times were assumed to have no impact on strain uniformity patterns, so the non-bias samples were run as monotonic tests. To further reduce the testing burden, non-bias Mode 1 tests were assumed to be sufficiently representative of non-bias Mode 2 and Mode 3 strain uniformity.

Heatmaps for each bias test were compared at 1% shear strain (1% re-zeroed shear strain for subsequent load steps.). Heatmaps for the non-bias tests were compared at 1% strain in the loading directions and also at advanced stages of the test. For the geogrids, heatmaps were generated using SigmaPlot for the DIC segment strains across the entire surface in each loading direction, i.e., for  $\epsilon_x$  and  $\epsilon_y$  (“SigmaPlot 14.0” 2017). Each heatmap was auto-scaled to emphasize spatial variations at a given time, rather than scaling to show the progression of strain from minimum to maximum throughout the test. For the geotextiles, the heatmap analysis was performed in the DIC software for the

entire surface of the area of interest (AOI). The heatmaps for the geotextiles were easily produced for the complete image stack, not just selected stages.

Additionally, statistical measures of strain uniformity were explored. The literature indicated that strains could be considered uniform if at any given point during the test, the standard deviation of strains was 5% or less of the average of the strains. This measure is hereafter referred to as the coefficient of variation, or COV. The 5% COV benchmark is somewhat arbitrary, since it was derived from tests on architectural membranes, which are much smoother and more continuous materials as compared to geogrids and geotextiles. Discontinuous materials such as geogrids may inherently have worse uniformity, and rough surface texture such as for the geotextiles may also cause worse uniformity due to higher noise in DIC analyses. Surface continuity was expected to be a more important uniformity factor than surface roughness (i.e., the geotextiles were anticipated to come closer to meeting a 5% COV benchmark than were the geogrids).

The COV was calculated and plotted throughout each test for both the geogrid segments and for the surfaces of the geotextiles. Up to four concentric regions (Figure 46 and Figure 47) were assessed for each test to determine whether the entire area satisfied strain uniformity criteria or whether a reduced central area would produce better data. For the innermost regions in Figure 46 and Figure 47, yellow bars show typical X strain segments, and red bars show typical Y strain segments (geogrids only). Also in Figure 46, circles mark typical LVDT locations from Haselton (2018) and the LVDT-DIC strain comparison in this thesis. Figure 48 through Figure 51 show typical data spreads. In these figures, the frame number on the X axis is a proxy for time (2.5 Hz data increment)

with all load steps spliced end-to-end into a single plot. Load steps are apparent from discontinuities in the data trends. As seen in Figure 48 through Figure 51, the non-bias strain data was not significantly affected by strain region, with the innermost region only slightly more uniform. However, for the bias tests, data from the innermost region was significantly more uniform than that of the broader regions; consequently, only this inner region is used to determine the statistical strain uniformity and the shear modulus (discussed in Chapter Six). This innermost region approximately corresponds to the gage spacing used for the LVDTs in prior research by Haselton (2018) and for the LVDT-DIC accuracy check in this research. Consequently, this validates Haselton's (2018) data as derived from the region of best uniform strain. As a final note, DIC strain data trends tend to be less smooth from the innermost region, indicating that the inner data may be more accurate but less precise than that from the broader regions.

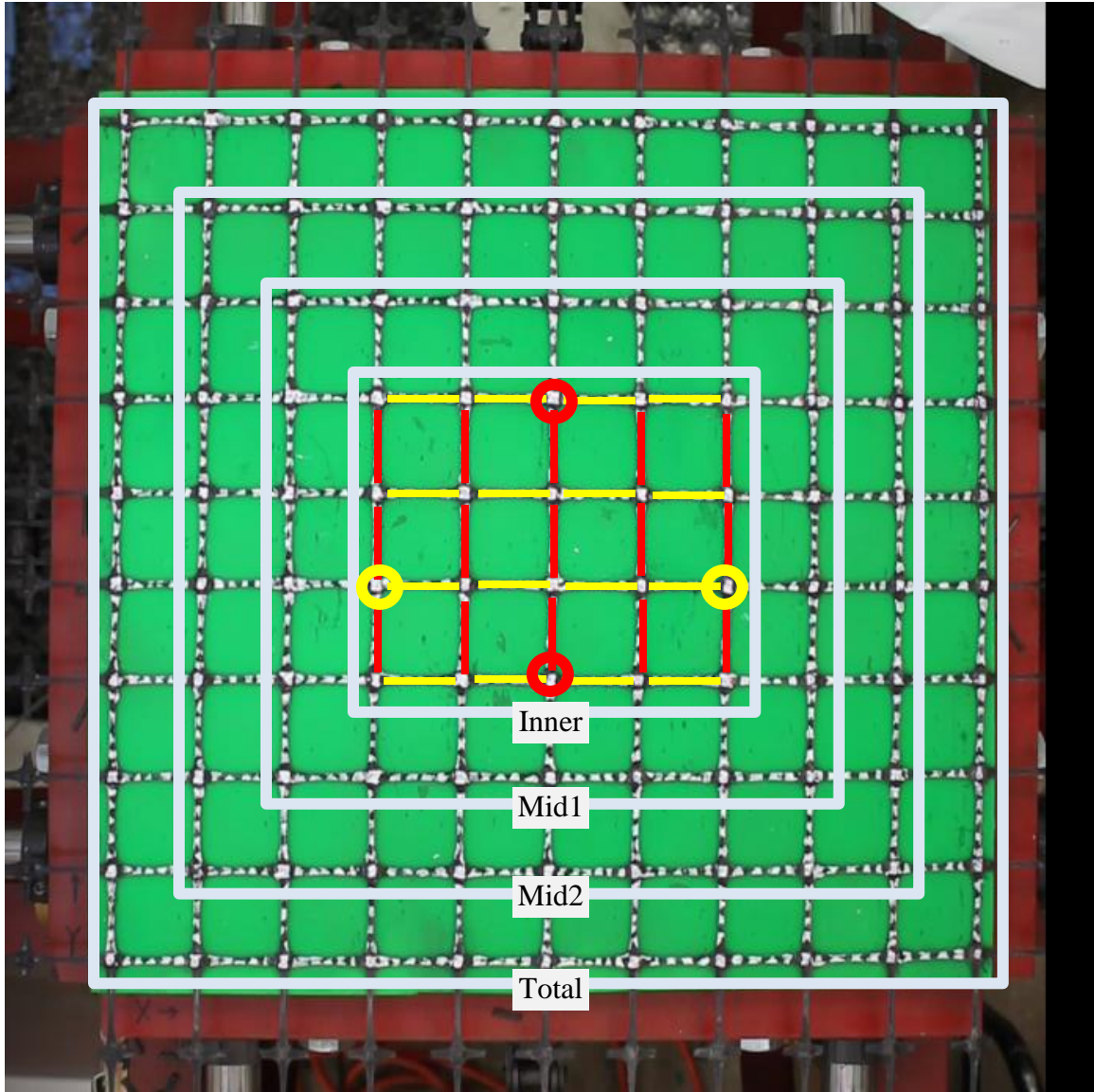


Figure 46: Typical concentric regions for strain averages for non-bias tests.

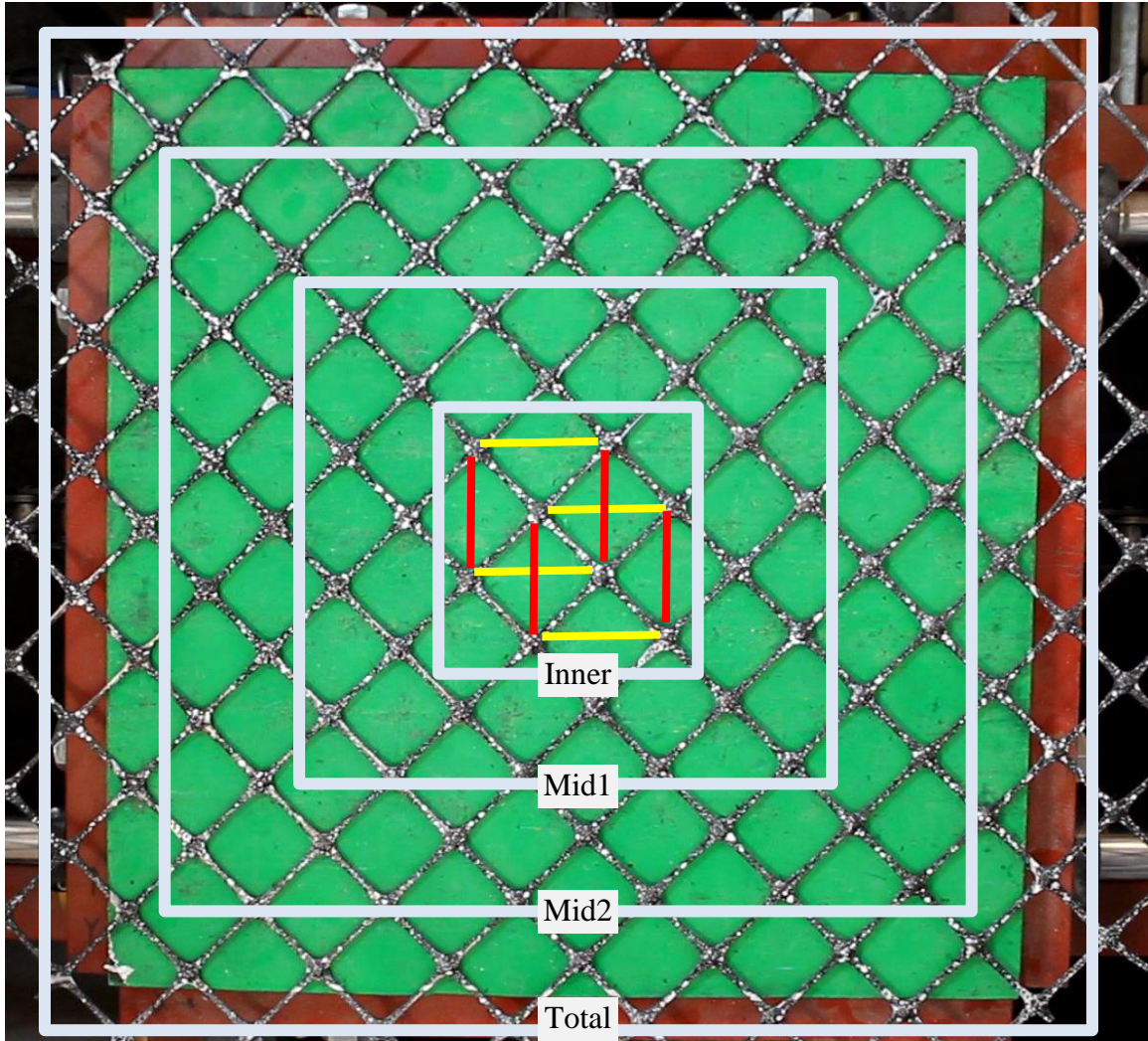


Figure 47: Typical concentric regions for strain averages for bias tests.



Figure 48: Regional trends of strain uniformity: bias square geogrid (GgD).

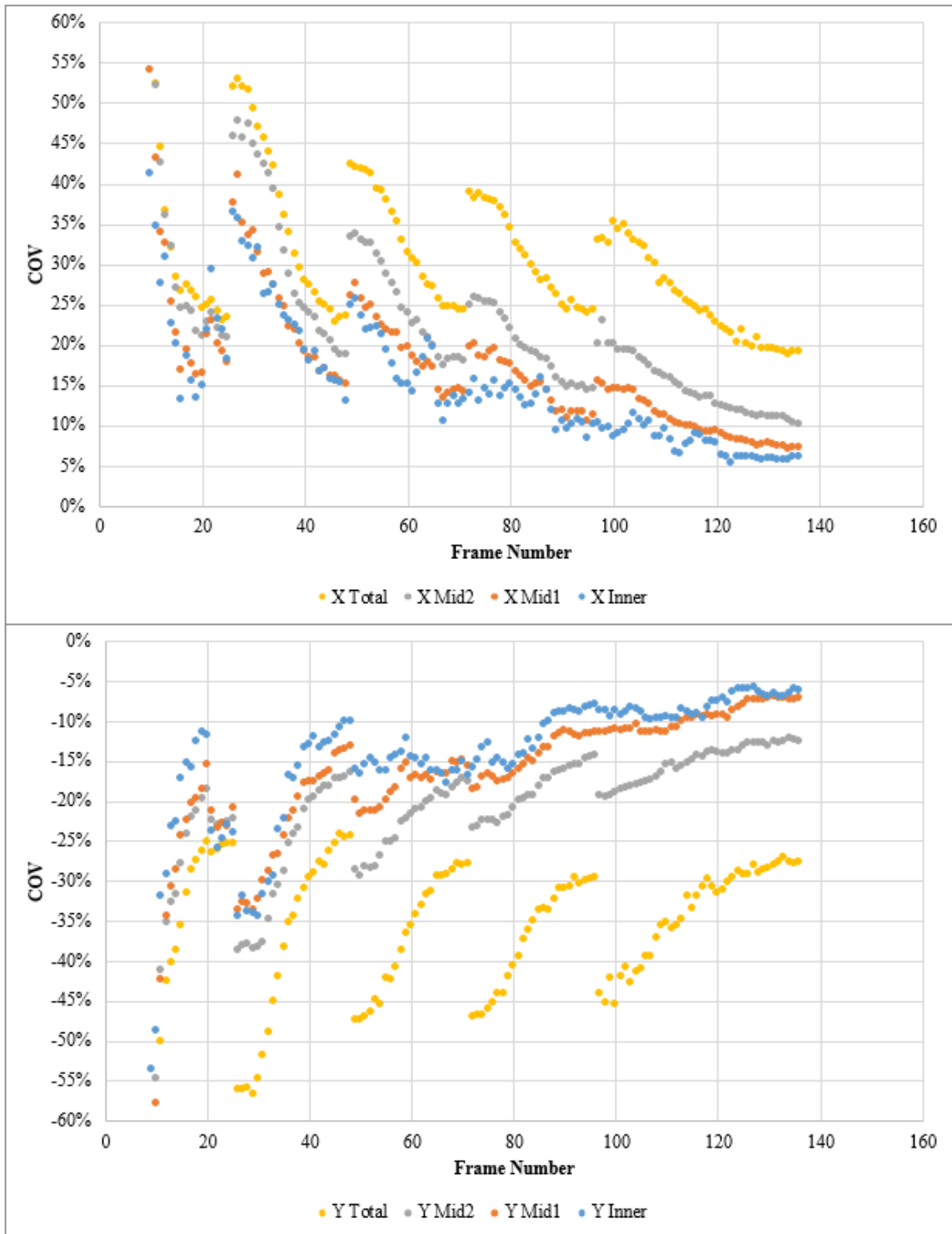


Figure 49: Regional trends of strain uniformity: bias rectangular geogrid (GgB).

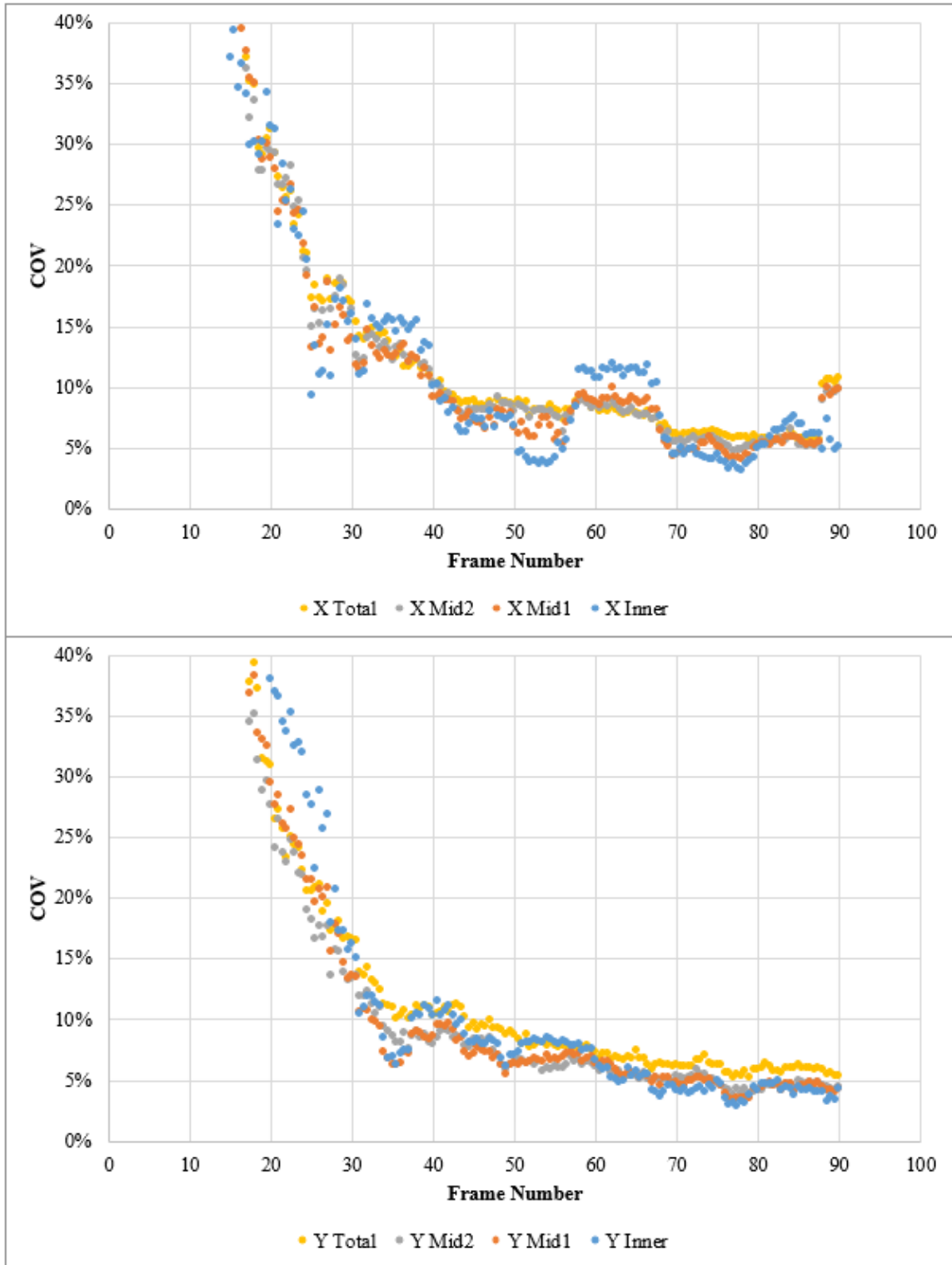


Figure 50: Regional trends of strain uniformity: non-bias square geogrid (GgC, Mode 1 monotonic).

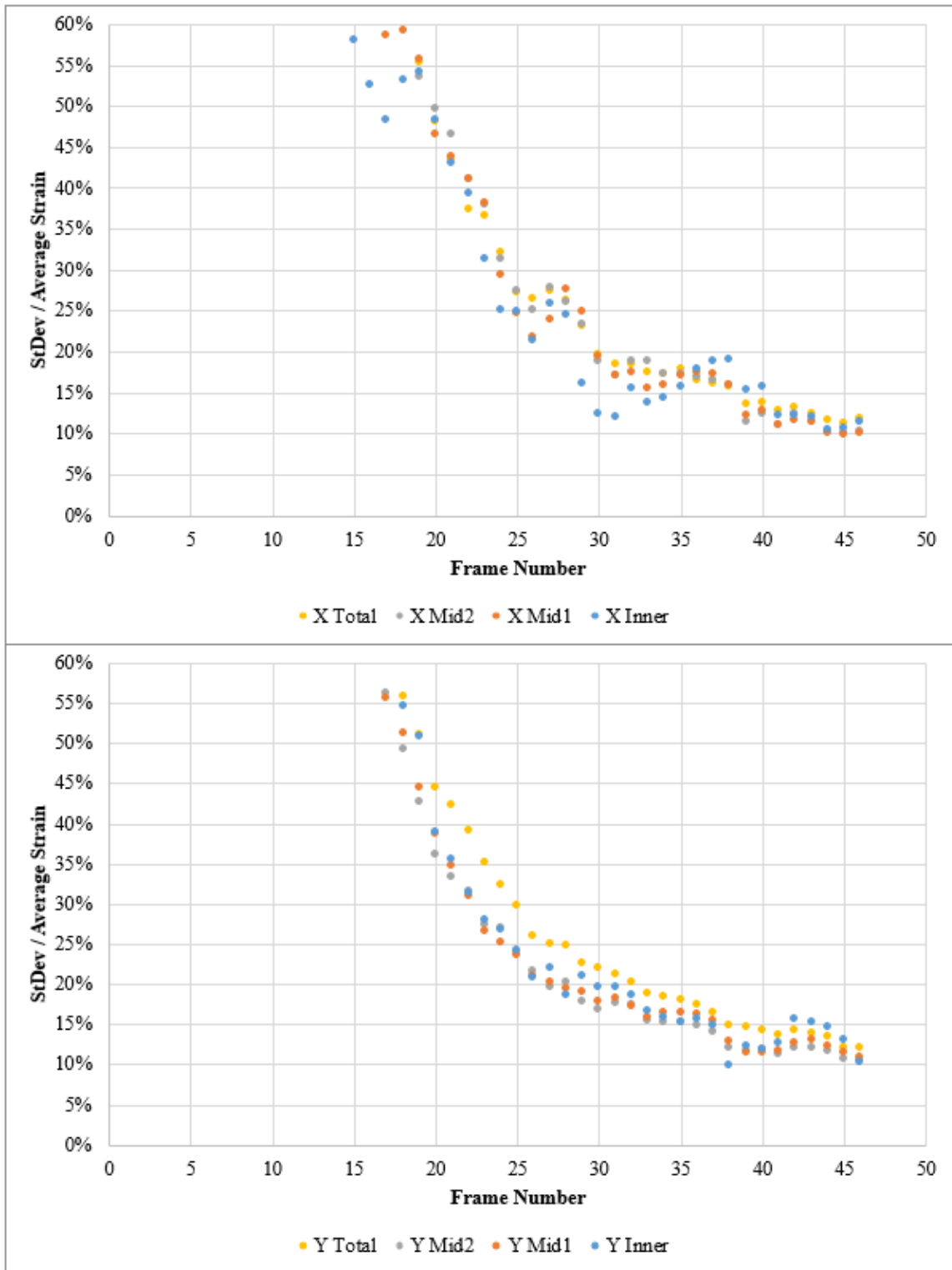


Figure 51: Regional trends of strain uniformity: non-bias rectangular geogrid (GgB, Mode 1 monotonic).

### Geogrid Strain Uniformity

Two geogrid architectures were tested, one series with nearly square apertures (referred to hereafter as “square geogrids”) and one series with rectangular apertures (referred to hereafter as “rectangular geogrids”). The square geogrids comprised Geogrid C, Geogrid D, and Geogrid E, and the rectangular geogrids comprised Geogrid A, Geogrid B, and Geogrid F. Significant differences were observed in the strain uniformity trends for these two architectures in the bias tests, with the square geogrids exhibiting less scatter and better uniformity than the rectangular geogrids. However, the non-bias tests showed comparable strain uniformity regardless of aperture type.

Bias Square Geogrids. Typical heatmaps for the bias square geogrids are shown in Figure 52 through Figure 54, which present spatial uniformity of strain at three different points in the same test. Figure 52 shows 1% shear strain for the first load step, and Figure 53 and Figure 54 show 1% and 1.5% re-zeroed shear strain for the second load step, respectively. These heatmaps show fairly good consistency as the test progressed as seen in Figure 53 and Figure 54, but not for the initial load step (Figure 52), which has a mixture of high and low strains scattered throughout the area of interest (AOI). Later load steps appear to have slightly unbalanced strains as seen in Figure 54 (top and bottom) by comparing strain levels along the Y axis maximum and minimum values, or as seen in Figure 54 bottom by comparing strain levels along the X axis maximum and minimum values. Also in Figure 54 bottom, the region of peak strains is off-center, shifted up (Y-positive) and slightly left (X-negative). Some of this off-centering/unbalancing is probably due to the manual tensioning of the non-machine-

loaded axis (see Chapter Four, Biaxial Testing Overview), which could not be precisely controlled due to rapid stress relaxing and creeping.

Statistical strain uniformity for the bias square geogrids is shown in Figure 55 through Figure 57. See Appendix A for additional plots. Note that the strains are not re-zeroed for each load step; they are all measured relative to the initial un-displaced position. For clarity, data spread greater than  $\pm 50\%$  is not shown in these plots. Figure 55 shows a typical test, and Figure 56 shows the test with the least smooth trends. Only minor improvements were present in the best-looking test, specifically, a more consistently smooth COV trend after 1% strain. The data does not meet the suggested 5% COV criterion very well, particularly not at the start of the test; but for most tests, data from the innermost region does eventually hover around and below that mark. All tests showed the large COV spike in the first load step, and COV always improved asymptotically as displacement (average strain) increased from the original reference location. For Geogrid E, both Mode 2 (Figure 55) and Mode 3 (Figure 57) tests were performed to validate that these modes produce equivalent results for 45-degree bias tests. Mode 3 bias tests are indicated by the negative (Poisson-induced) X strain and positive Y strain, which is the reverse of Mode 2 bias.

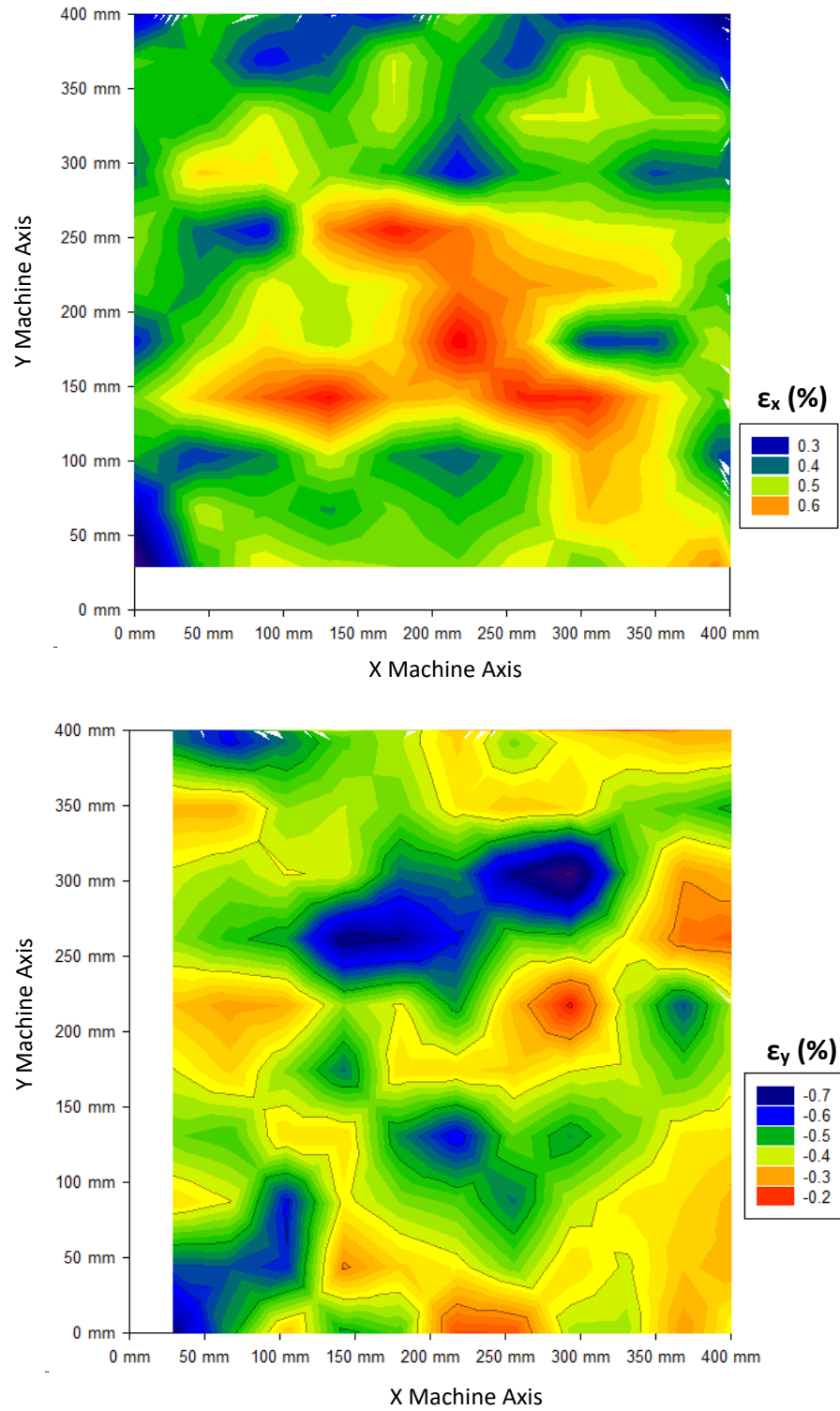


Figure 52: Strain heatmaps from GgE bias trial 6 (Mode 3). Frame 14 (load step 1, 1% shear strain).

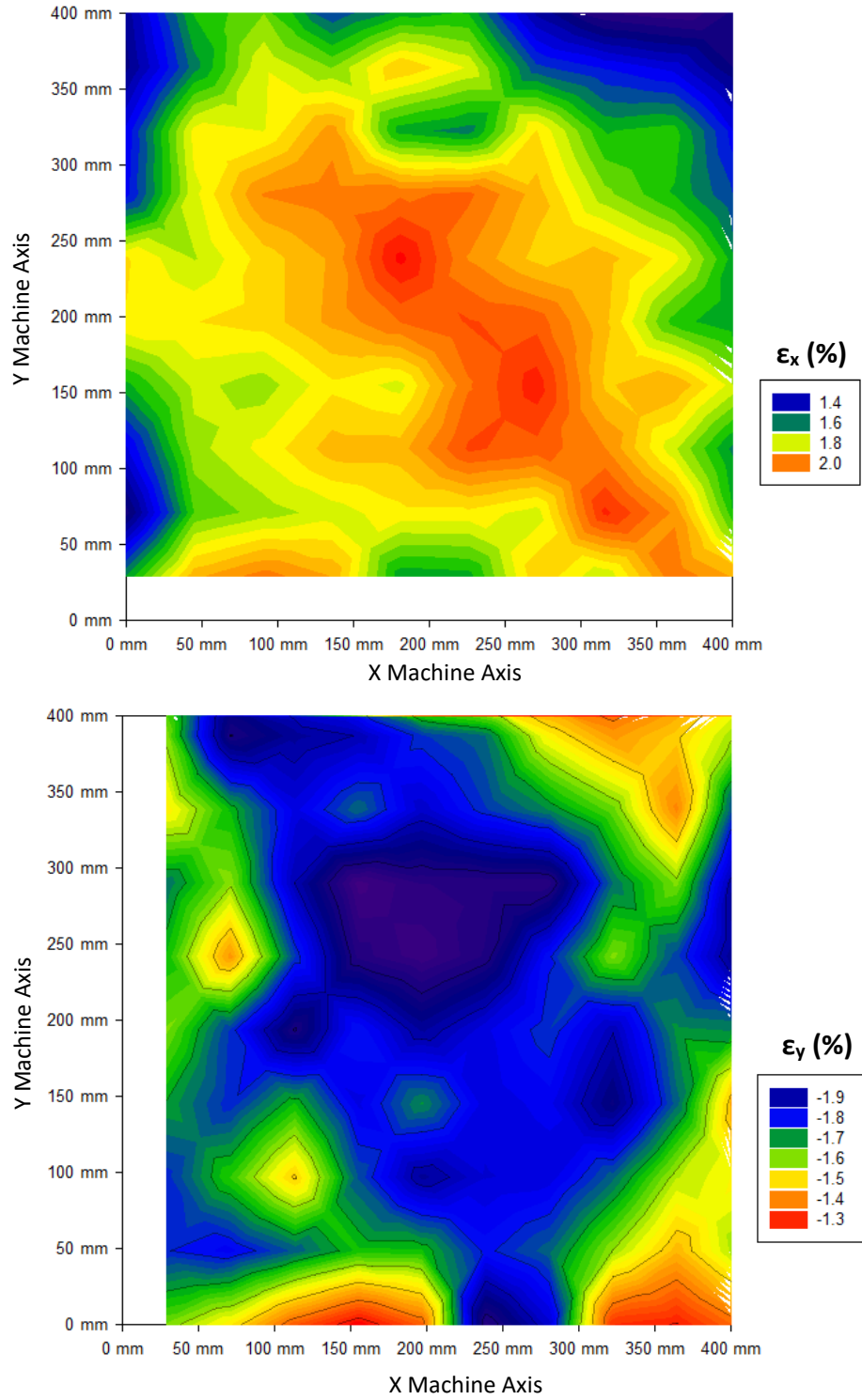


Figure 53: Strain heatmaps from GgE bias trial 6 (Mode 3), continued. Frame 65 (load step 2, 1% re-zeroed shear strain).

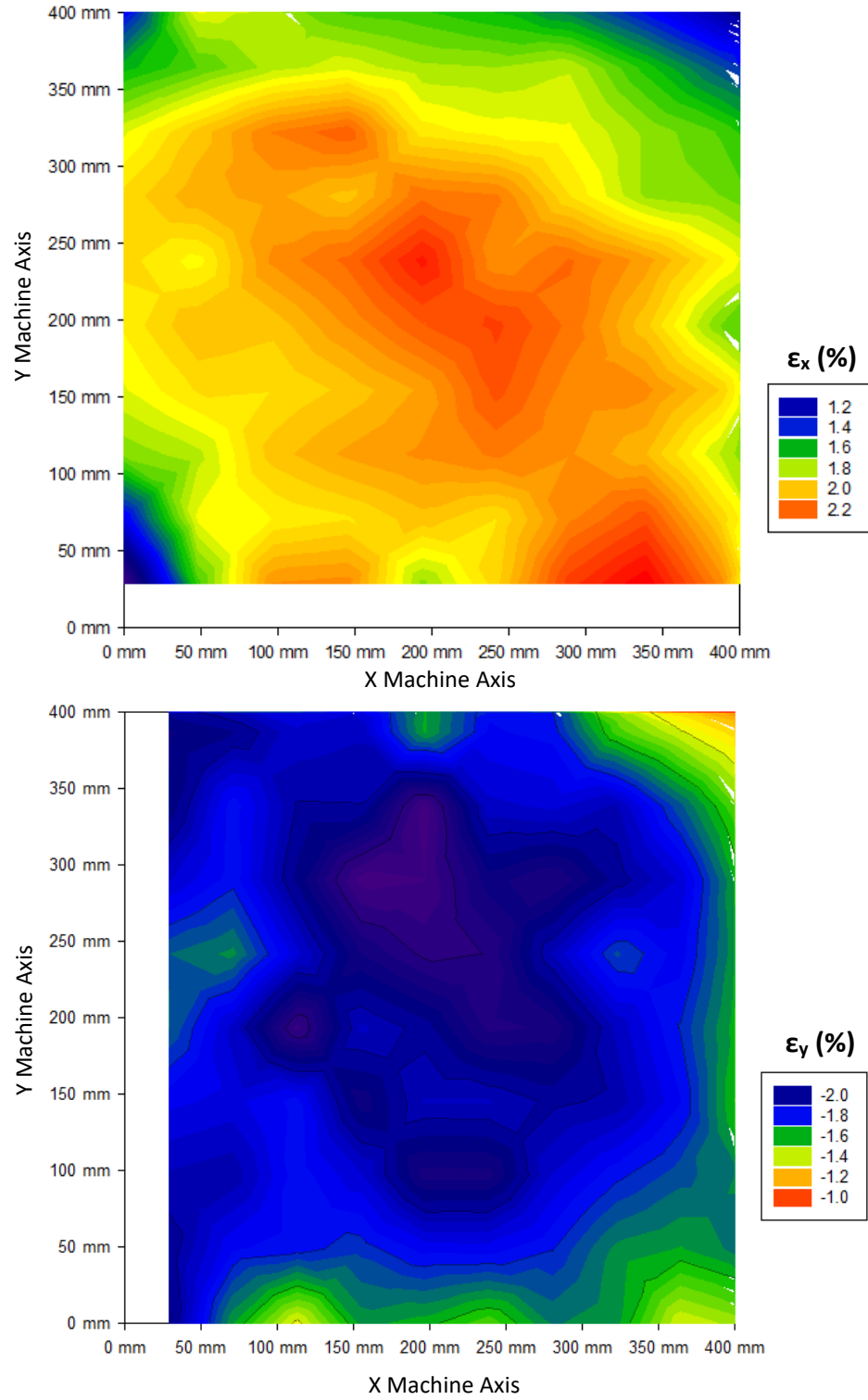


Figure 54: Strain heatmaps from GgE bias trial 6 (Mode 3), continued. Frame 67 (load step 2, 1.5% re-zeroed shear strain).

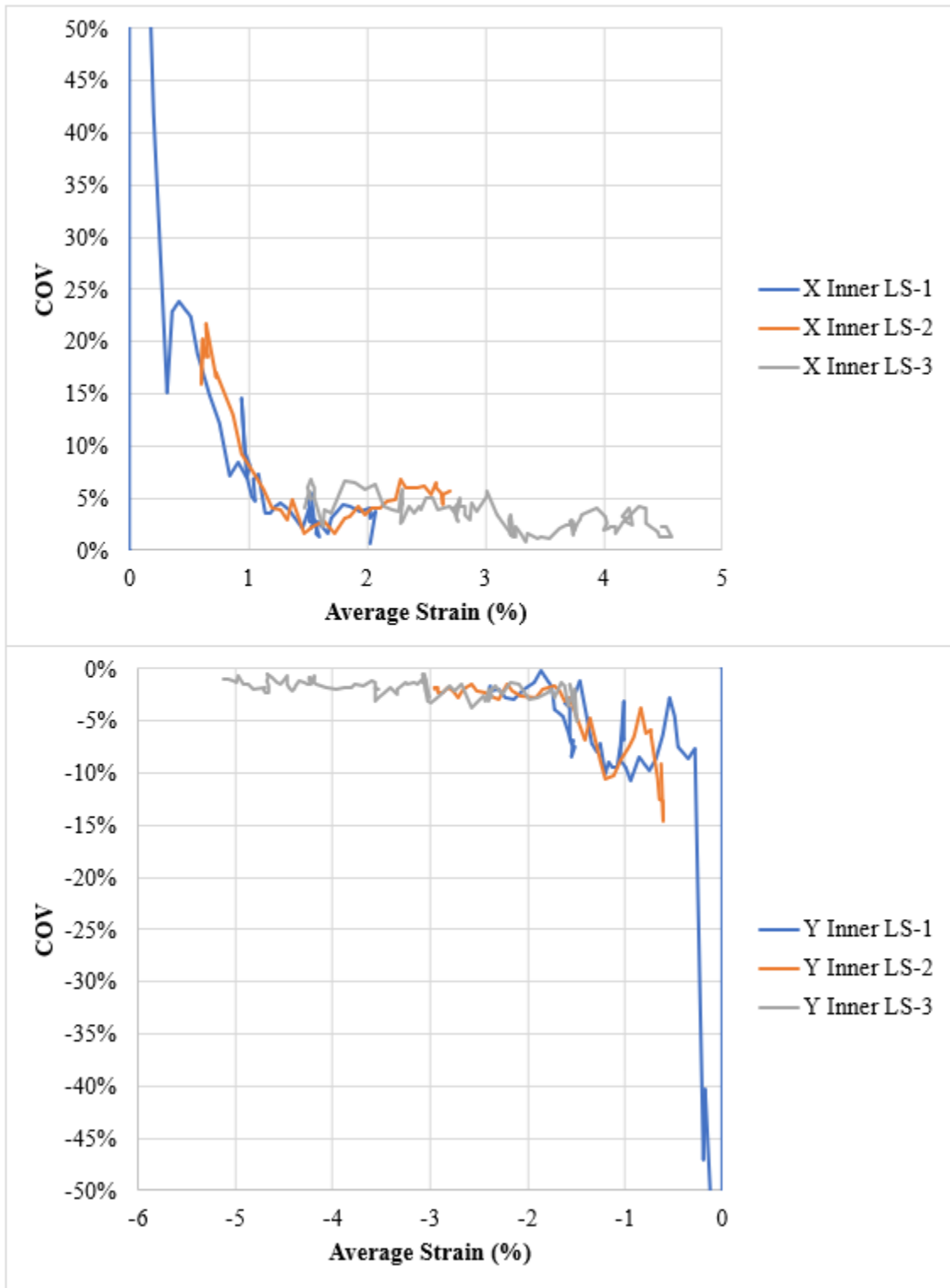


Figure 55: Typical COV trend for bias square geogrids (GgE bias trial 5). LS = Load Step.

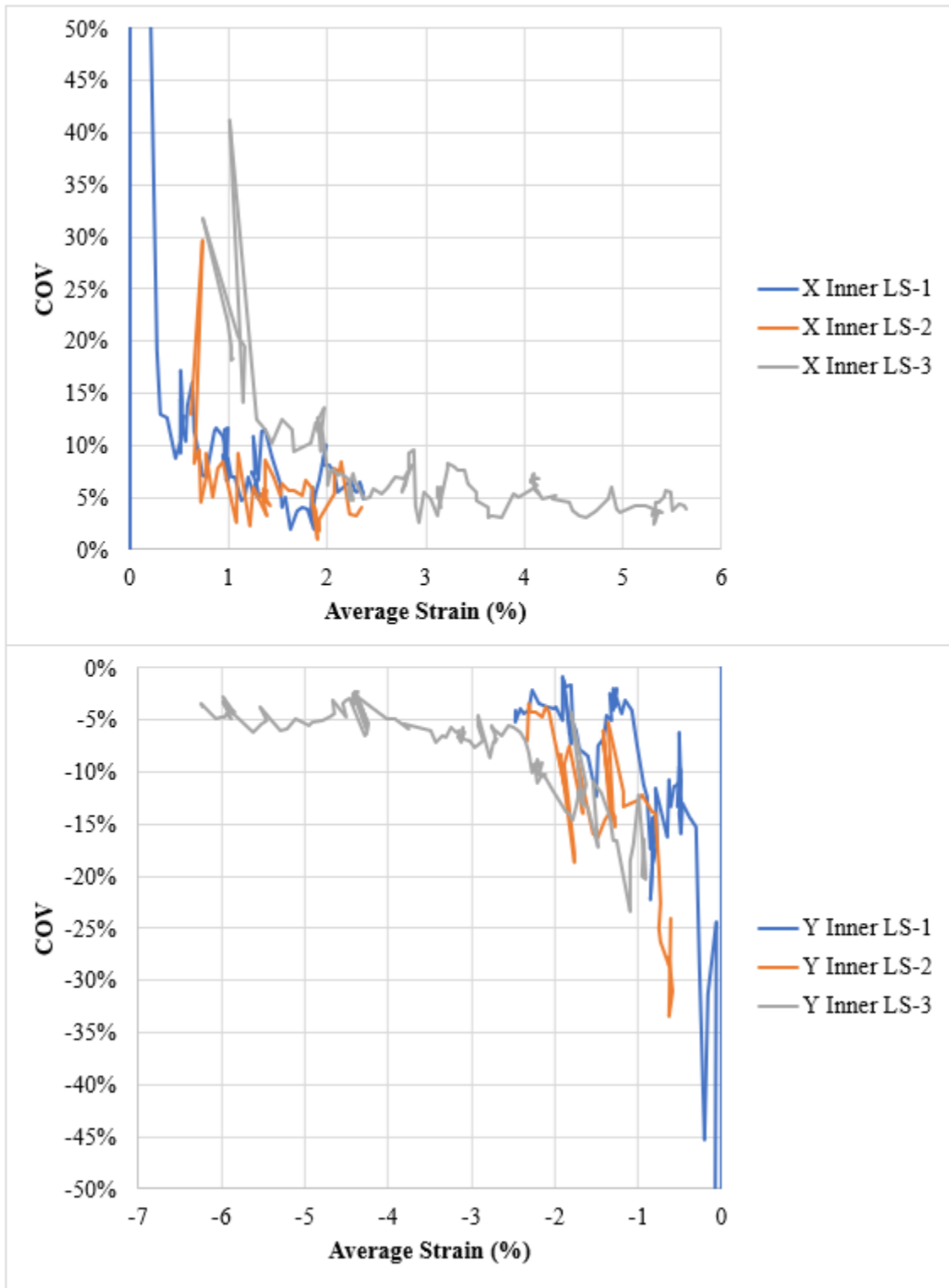


Figure 56: Worst COV trend for bias square geogrids (GgC bias trial 2). LS = Load Step.

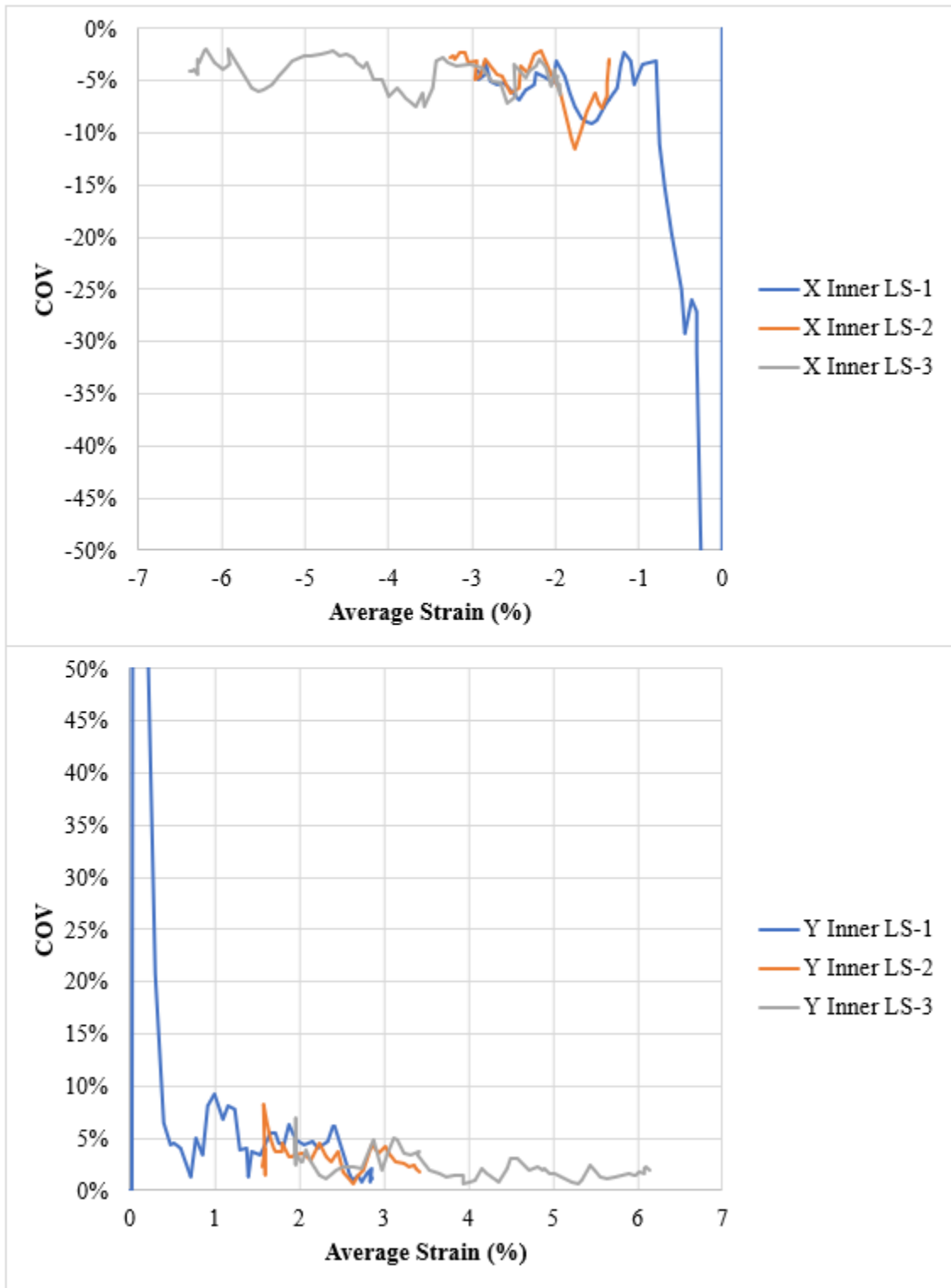


Figure 57: Typical COV trend for bias square geogrids, Mode 3 test (GgE bias trial 6).  
LS = Load Step.

Bias Rectangular Geogrids. Typical strain heatmaps for the bias rectangular geogrids are shown in Figure 58 and Figure 59, which present two different tests at 1% re-zeroed shear strain for the third load step. These tests showed the same trend as for the square geogrids, with much more variability in the first load step than in subsequent load steps. Even among the rectangular geogrids, different strain heatmap patterns appeared for Geogrid A versus Geogrid B and Geogrid F. As seen for example in Figure 58 bottom, the latter two geogrids showed distinct strain variations (particularly in the Y strain) running diagonally through the area of interest. These strain variations suggest a rotational tendency in the AOI due to off-axis forces, such that one off-axis tensile web path may be carrying most of the load and attempting to align with the direction of loading. The magnitude of rotation was investigated for a few tests, and these results are presented in the Zero Shear Strain Assumption Check section starting on page 129.

Statistical strain uniformity for the bias rectangular geogrids is shown in Figure 60 and Figure 61. Additional plots are contained in Appendix A. Strains are not re-zeroed for each load step; they are all measured relative to the initial un-displaced position. For clarity, data spread greater than +/-50% is not shown in these plots. Figure 60 shows a typical test, and Figure 61 shows the single non-typical test, which had a much longer strain range and ultimately reached a lower consistent COV. Most of the rectangular geogrid tests (including Figure 60) did not appear to have fully reached an asymptote value, and the majority of the load steps stopped around +/-10% COV. The small strain range may have affected the minimum COV: other than the outlier test shown in Figure 61, most of the rectangular geogrid tests do not appear to have fully

reached an asymptote. Whereas the square geogrid COVs dropped to their asymptote value by about 1% strain, the rectangular geogrid COVs generally decrease more gradually as seen by comparing Figure 55 and Figure 60.

Even though it is an outlier test, Figure 61 presents an interesting case study due to very clear distinctions between load steps. As seen in this figure, the second load step started at a higher level of strain relative to the reference position at the start of the first load step, avoiding the approximately 0-1% strain range that contained the spike in the other two load steps. This demonstrates a clear link between small movement from the reference position and high COV. Small strain increments are captured without issue as seen in the second load step, which has no spike even for the portion of loading with motor spool-up. However, the third load step starts close to the original un-displaced location (strain starts near zero)—and the initial COV spike is back. Conversely, the COV improves dramatically as the average strain increases, eventually tapering to an apparent asymptote of 5% COV as strain continues to increase. These observations indicate that the COV spikes have much more to do with DIC noise near the reference position than with the actual material uniformity, and that the material uniformity may be best represented by the asymptote COV value. In light of this, extrapolation of the COV trends for the typical tests such as Figure 60 suggests that they also would have achieved a 5% COV asymptote if test displacement had been large enough to dissipate the DIC noise.

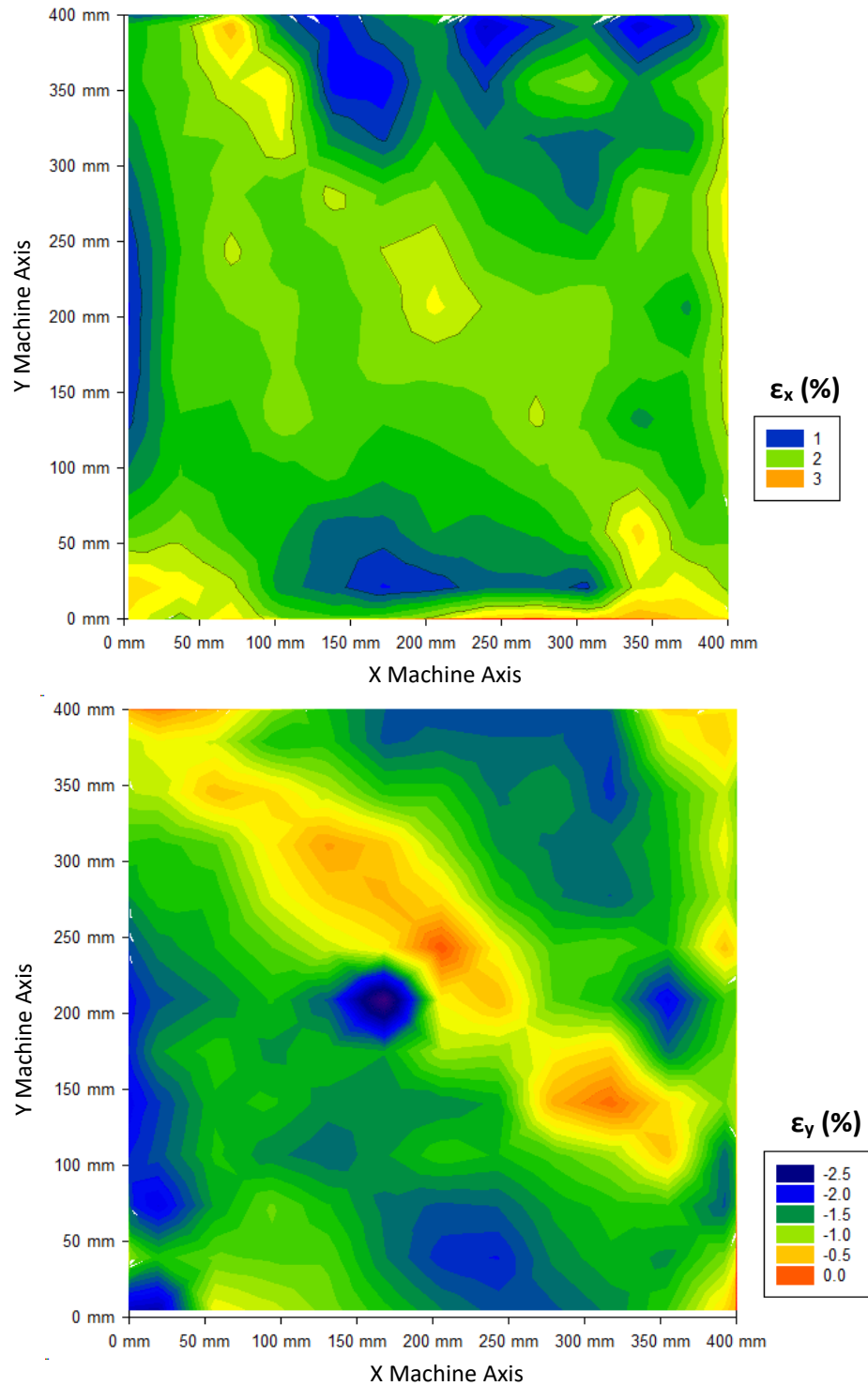


Figure 58: Strain heatmaps from GgB bias trial 2. Frame 59 (load step 3, 1% re-zeroed shear strain).

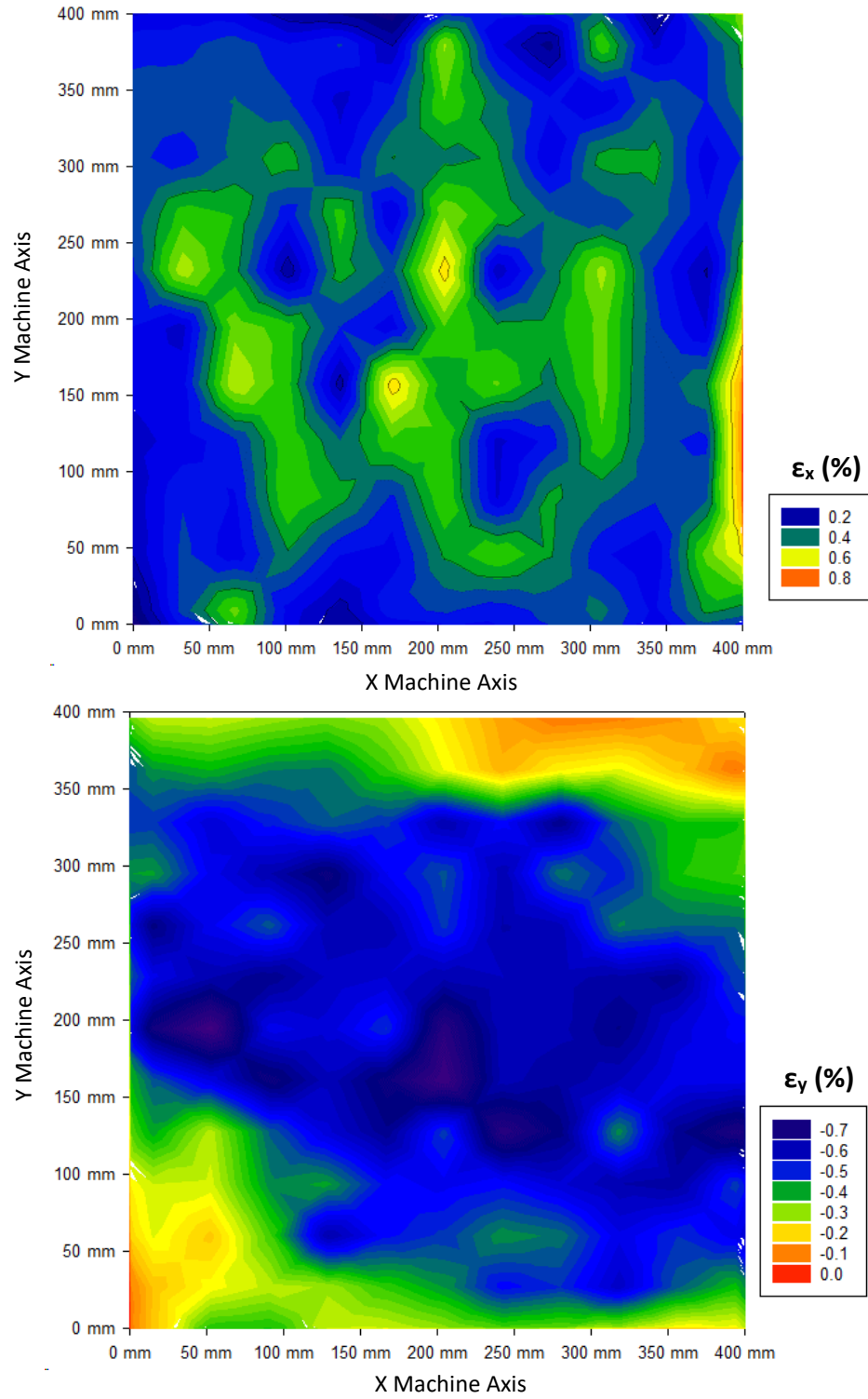


Figure 59: Strain heatmaps from GgA bias trial 1. Frame 283 (load step 3, 1% re-zeroed shear strain).

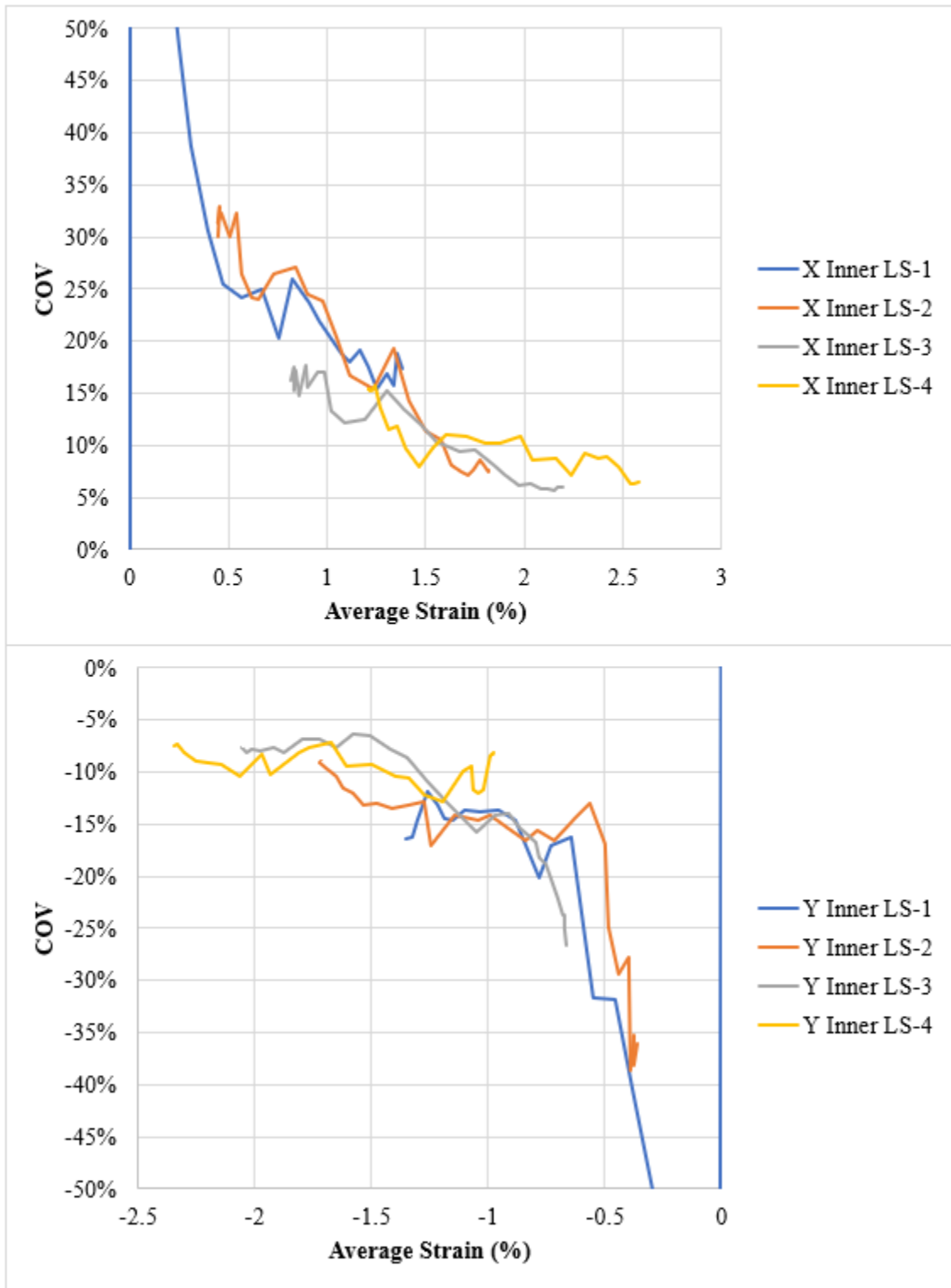


Figure 60: Typical COV trend for bias rectangular geogrids (GgF bias trial 2). LS = Load Step.

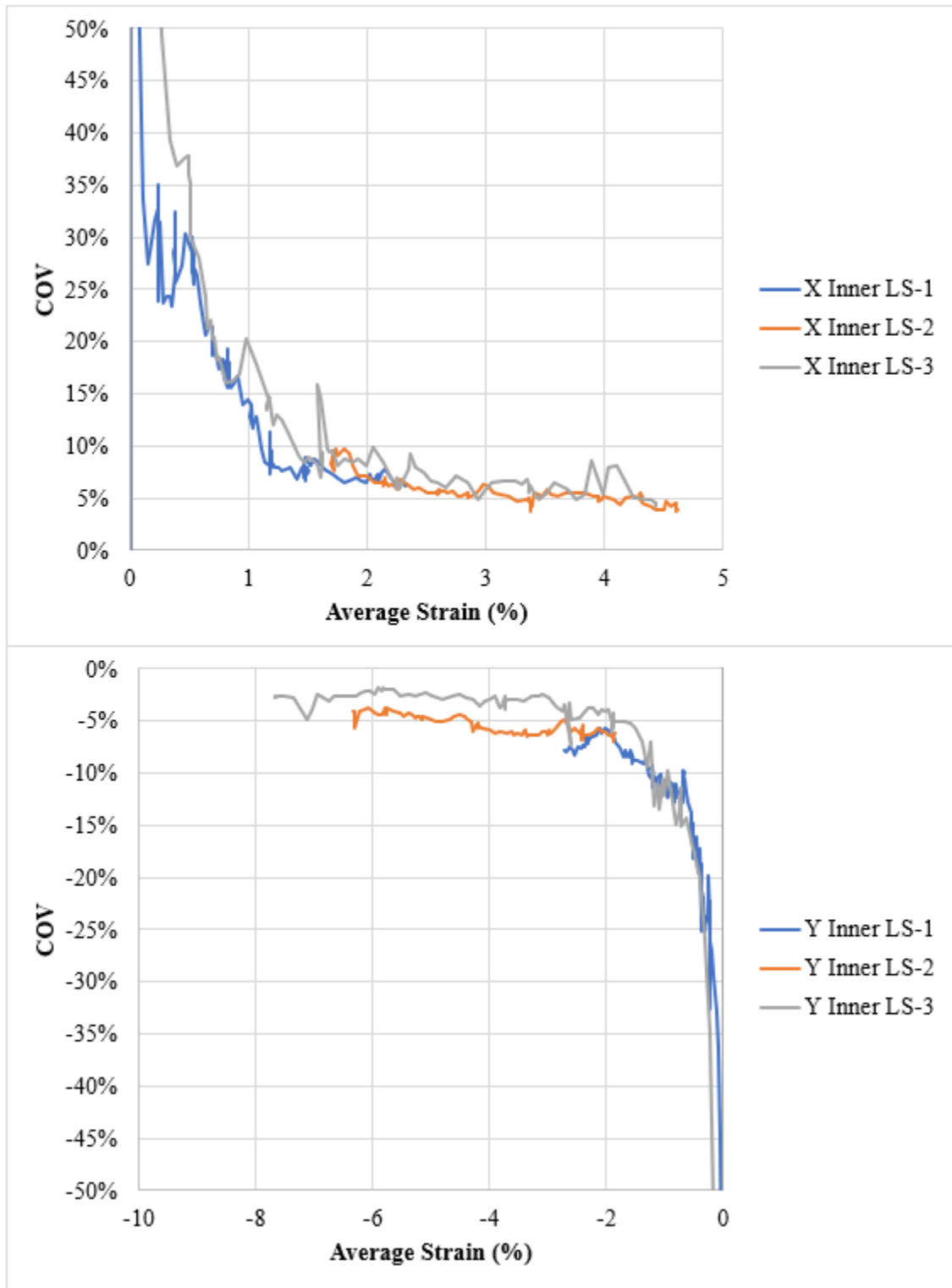


Figure 61: Least typical COV trend for bias rectangular geogrids (GgA bias trial 1). LS = Load Step.

Non-Bias Square and Rectangular Geogrids. The non-bias geogrids were anticipated to give similar trends for strain uniformity regardless of aperture shape since all tensile webs were aligned to the directions of loading for both square and rectangular geogrids. Typical heatmaps are shown in Figure 62 through Figure 64. Figure 62 shows a square geogrid test at roughly 1% average inner strain in X and Y, and Figure 63 shows the same test at roughly 4.5% average inner strain in X and Y. Figure 64 shows a rectangular geogrid test at roughly 1% average inner strain in X and Y. Surprisingly, these heatmaps are not as visually uniform as anticipated, with high and low strain values intermixed and scattered across the AOI. This scatter remained throughout the entire test (compare Figure 62 and Figure 63), in contrast to the bias tests which showed similar scatter in early stages but a more consistent and smooth gradient as the test advanced. Both square and rectangular non-bias geogrids showed similar heatmap patterns in this regard. The square geogrid was evaluated using earlier software (ARAMIS), and the rectangular geogrids were evaluated using the new software (GOM Correlate). The old software does not appear to be the cause of the scatter since similar results are present in both geogrid analyses regardless of which version of the program was used.

Statistical strain uniformity is shown in Figure 65 and Figure 66. For clarity, data spread greater than 40% COV is not shown. The data again does not meet the suggested 5% criterion very well at the start of the test; but as expected, these follow the same strain uniformity trend even though one is from a square geogrid (Figure 65) and one is from a rectangular geogrid (Figure 66). Asymptotic behavior is less obvious in Figure 66 because the data range for this test is significantly shorter than in Figure 65. For both

tests, COV values drop steeply from the beginning of the test to 10-15% COV around 1.5% average strain (shown on the X axis), then gradually decrease to 5-10% for the rest of the test. COV values for all regions of the non-bias tests were generally very comparable as shown earlier in Figure 50 and Figure 51, sometimes with slightly better uniformity from wider regions as shown for example in Figure 65 top.

The statistical uniformity analysis appears to give a better result than the heatmaps, but this may be explained by the following factors: The bias tests generally exhibit a smooth, concentric pattern which is not there in the non-bias tests. Consequently, the non-bias tests look worse, even though the strain ranges are comparable (1% for the bias tests and 0.6 to 1% for the non-bias tests). Their worse appearance is exacerbated in the non-bias tests due to localized strain spikes, low and high. Since the strain spikes are spatially infrequent, they do not affect the regional COV trends in the same methodical way as the bias tests are affected. If these spikes were removed, the heatmap and COV uniformity would both probably appear better for the non-bias tests than for the bias tests, whereas currently the COV uniformity is about equivalent.

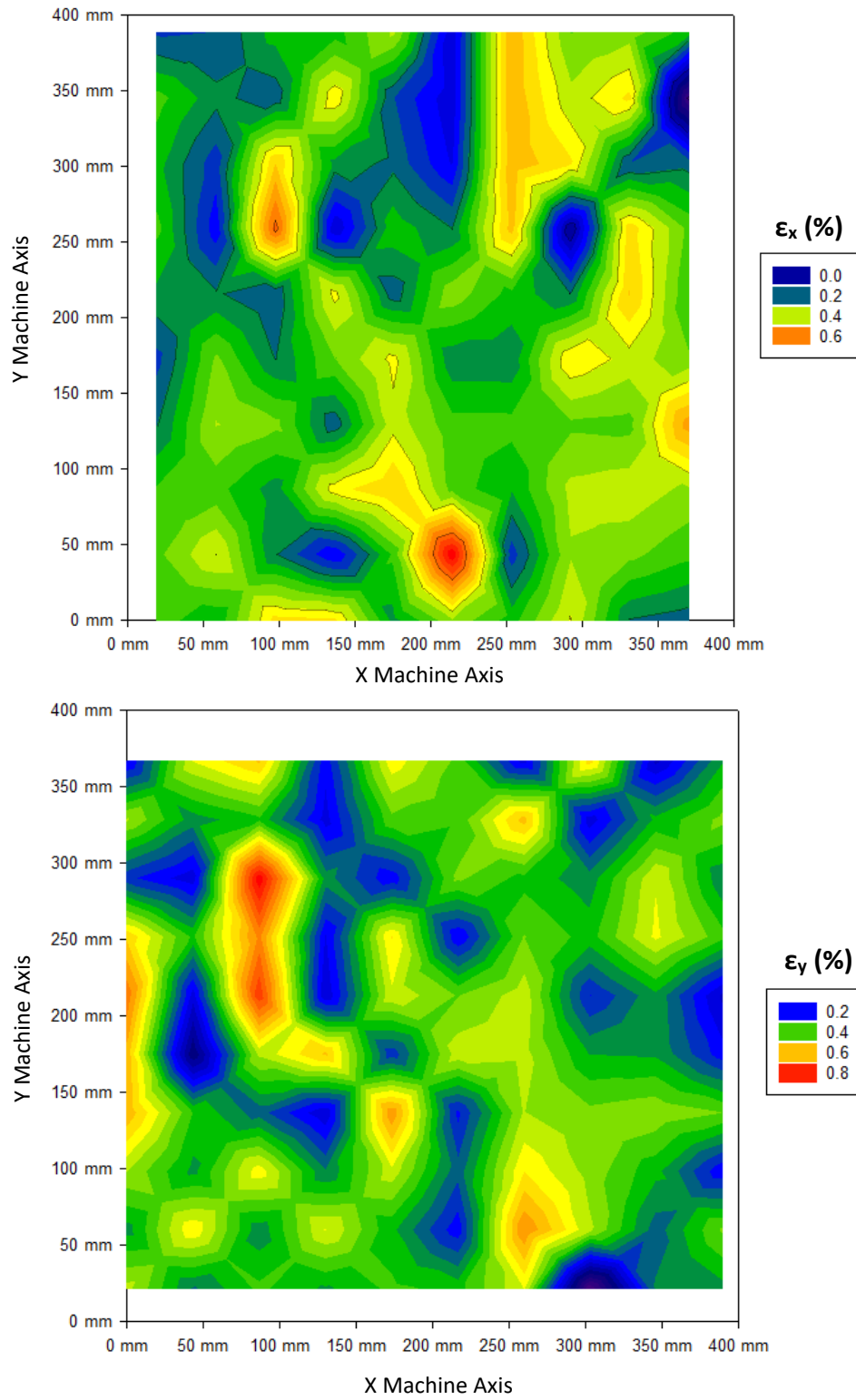


Figure 62: Strain heatmaps from non-bias GgC (Mode 1). Monotonic test, frame 15.

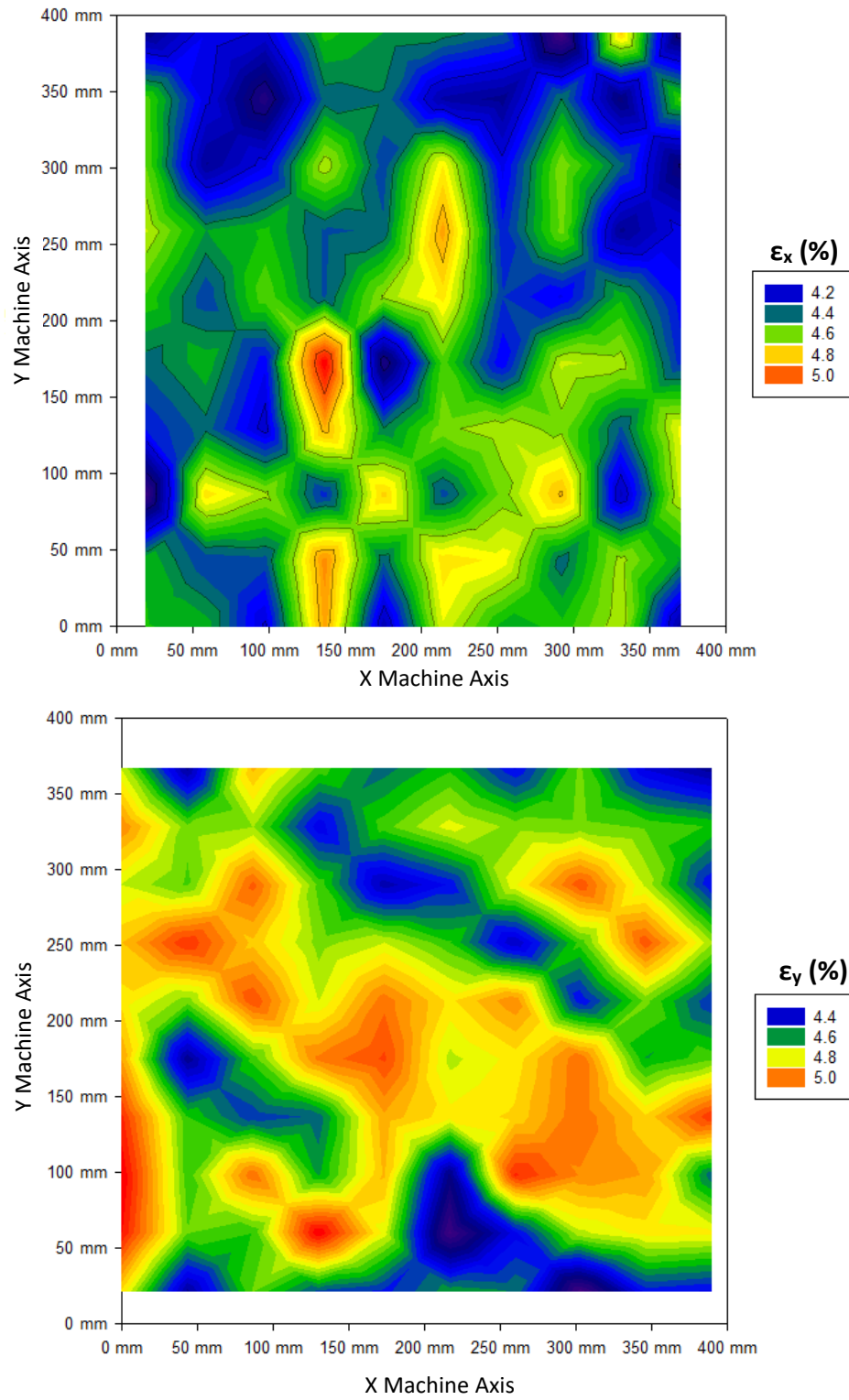


Figure 63: Strain heatmaps from non-bias GgC (Mode 1), continued. Monotonic test, frame 86 (just before failure).

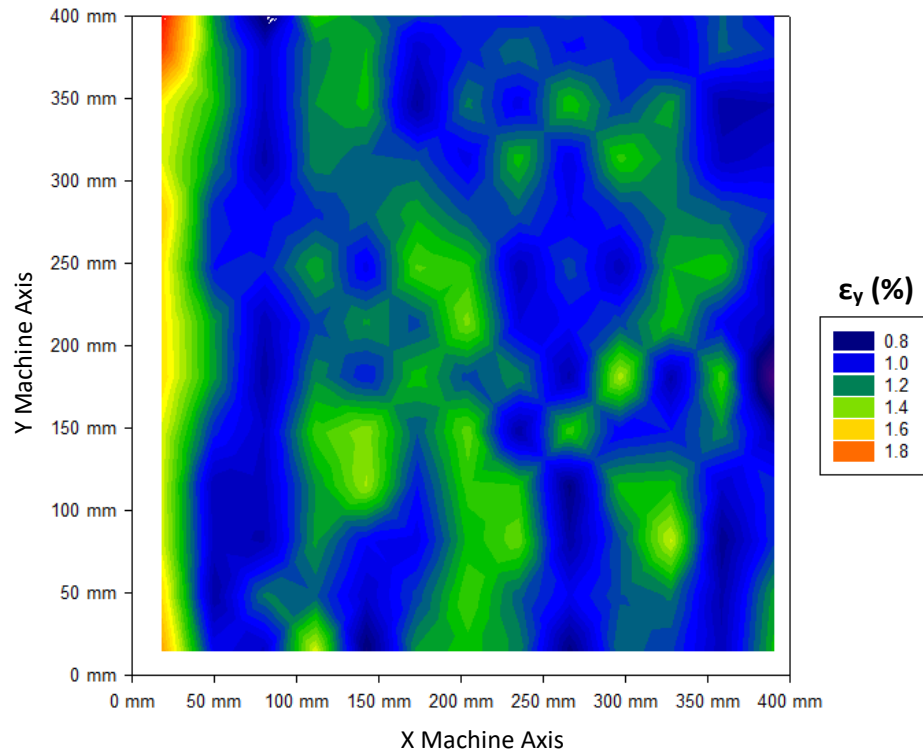
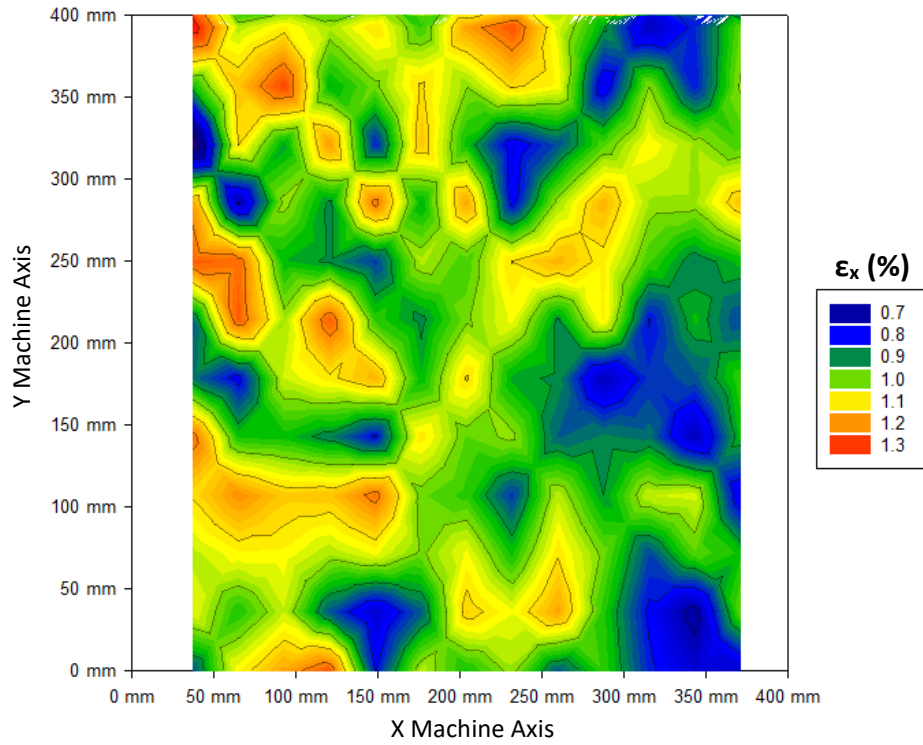


Figure 64: Strain heatmaps from non-bias GgB (Mode 1). Monotonic test, frame 30.

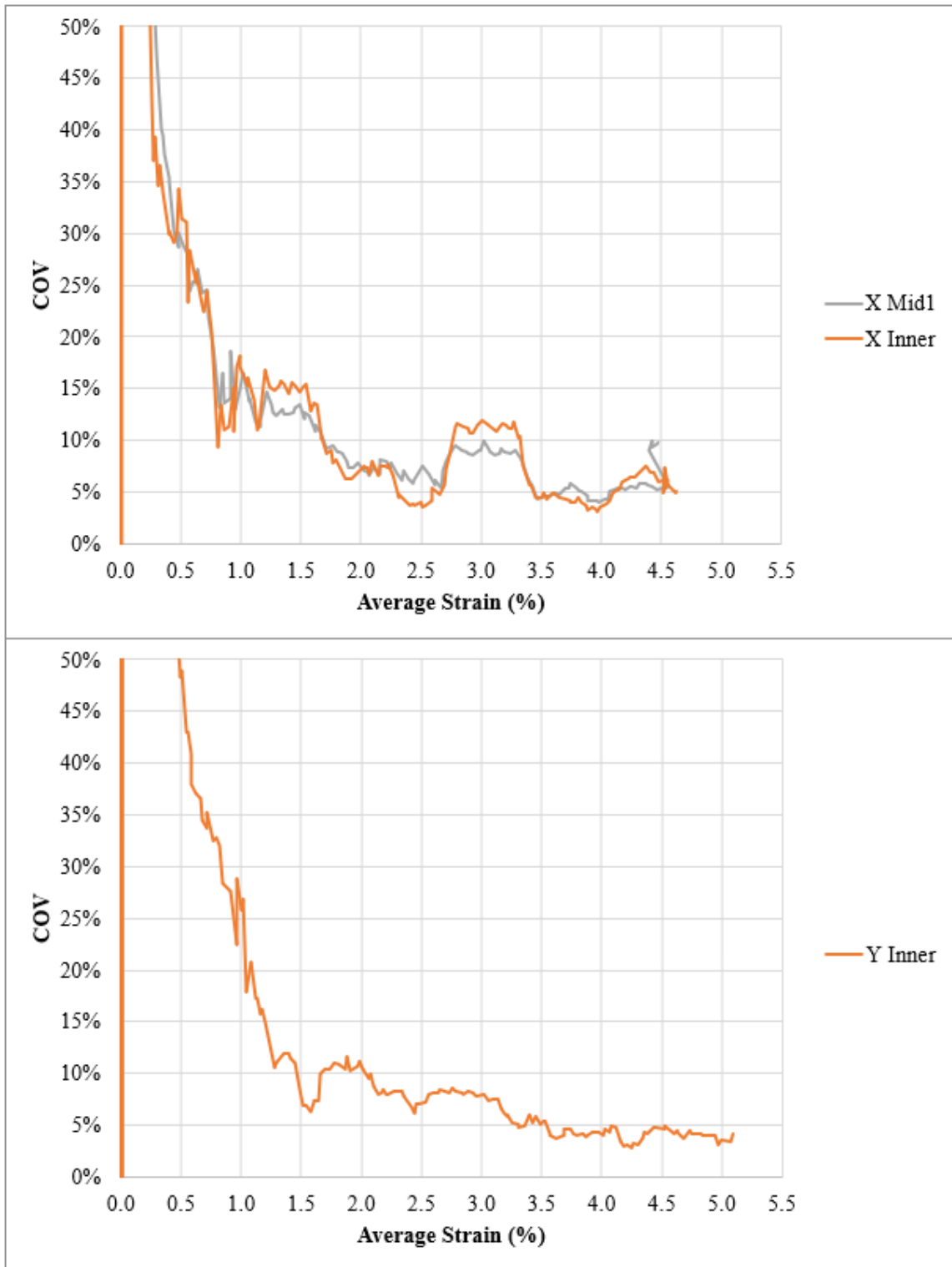


Figure 65: Statistical strain uniformity (GgC non-bias Mode 1, monotonic test).

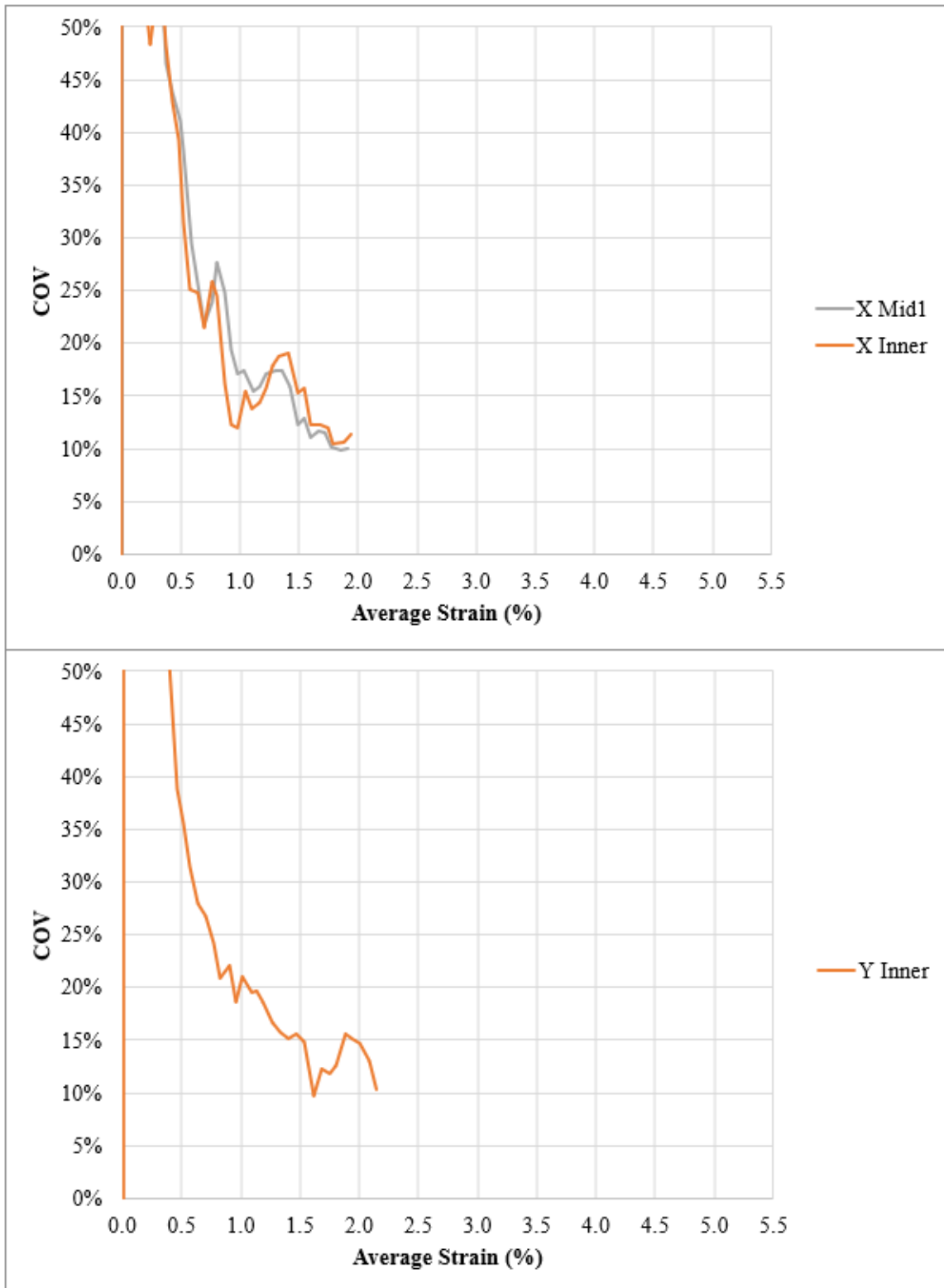


Figure 66: Statistical strain uniformity (GgB non-bias Mode 1, monotonic test).

### Geotextile Strain Uniformity

For both the bias and non-bias geotextile tests, significant numbers of small DIC surface errors such as twinning (false high/low strains immediately next to one another) and moiré effect or aliasing (false strain values occurring in repeated stripes or patterns) could be observed depending on the strain scale and facet size, but the overall visual assessment appeared to be reasonable. Some of these errors are known to occur from surface texture (Correlated Solutions 2017), and a full exploration to minimize these errors was not conducted. To smooth out these error spikes and help obtain a better representative standard deviation of strain, the DIC facet size for the geotextiles was increased to 40x40 pixels from the original 10x10 pixel size that was used with good success in the geogrid processing. Facet overlap was kept at 50% (20 pixels).

Bias Geotextiles. Typical strain heatmaps for the bias geotextiles are shown in Figure 67 through Figure 70 (heatmaps from Geotextile B bias trial 3). Figure 67 and Figure 67 show the first load step at 1% shear strain, and Figure 68 and Figure 69 show the third load step at 1% re-zeroed shear strain. Like the geogrids, the geotextiles generally showed better overall uniformity in later load steps than at the beginning of the tests, although a small central area showed relatively consistent strain from an early stage. Later in the test (Figure 69 and Figure 70), non-uniform patterns occur near the edges due to stress concentrations from the arm slits, but the spatial variation of strains appears very uniform in the inner region.

Statistical strain uniformity for the geotextiles is shown in Figure 71 and Figure 72. As for the preceding materials, note that these strains are not re-zeroed for each load

step; they are all measured relative to the initial un-displaced position. For clarity, data spread greater than +/-50% is not shown in these plots. The geotextile COV trends were not as consistent as for the other architectures, and two primary trend forms appeared. Figure 71 shows the first trend type: an initial COV spike for the first load step, followed by very good uniformity for the remainder of the load steps—however, note that these load steps begin with large displacement from the initial position. Figure 72 shows the second trend type: all load steps begin very close to the reference location as indicated by low strain on the X axis, and all show the large initial COV spike. Most of the geotextile tests fell somewhere between these two extremes (see Appendix A for the full plot set). The typical COV asymptote was about 5%, and a few tests reached a 3% asymptote (e.g. Figure 71). Interestingly, the noise (COV spike) tapers off more slowly for the geotextiles than for the geogrids; this may be a result of the surface texture of the geotextiles. High noise appears to be associated with strains less than 2% for the geotextiles, as compared to about 1% for the geogrids.

A comparison of Figure 71 and Figure 72 reveals an interesting phenomenon. In Figure 71, the DIC system is perfectly capable of capturing the small strain increments at the start of load steps 2-4, and the COV for these load steps is consistently low (good), following the asymptote line. However, Chapter Six analyses clearly show the “high quality” load steps 2-4 for Figure 71 to be in shear lock-up. On the other hand, in Figure 72, each load step shows the large COV spike before tapering to the asymptote, but Chapter Six shows that the test in Figure 72 is of significantly higher quality. These figures demonstrate 1) that the DIC system is able to capture small strain increments

accurately, even for rough-surfaced geotextiles, and 2) that the COV spikes occur only at low strain relative to the initial reference image, not at low strain increments in general such as occur due to motor spool-up at the start of every load step. Consequently, the COV asymptote values seen in Figure 71 for the locked-up load steps 2-4 are indicative of the material uniformity, and the COV spikes seen in Figure 72 reflect DIC sensitivity issues (high noise). The load steps in Figure 72 had been manually tensioned enough to bring their starting position close to the original reference position as evidenced by the strain scale. From these figures and others in Appendix A, it appears that the DIC methods used in this research perform best for strains of about 1% or greater for the geogrids and about 2% or greater for the geotextiles, with excessive noise occurring at lower strains. In this context, strain is relative to the initial un-displaced reference image at the start of the first load step (not re-zeroed for each load step).

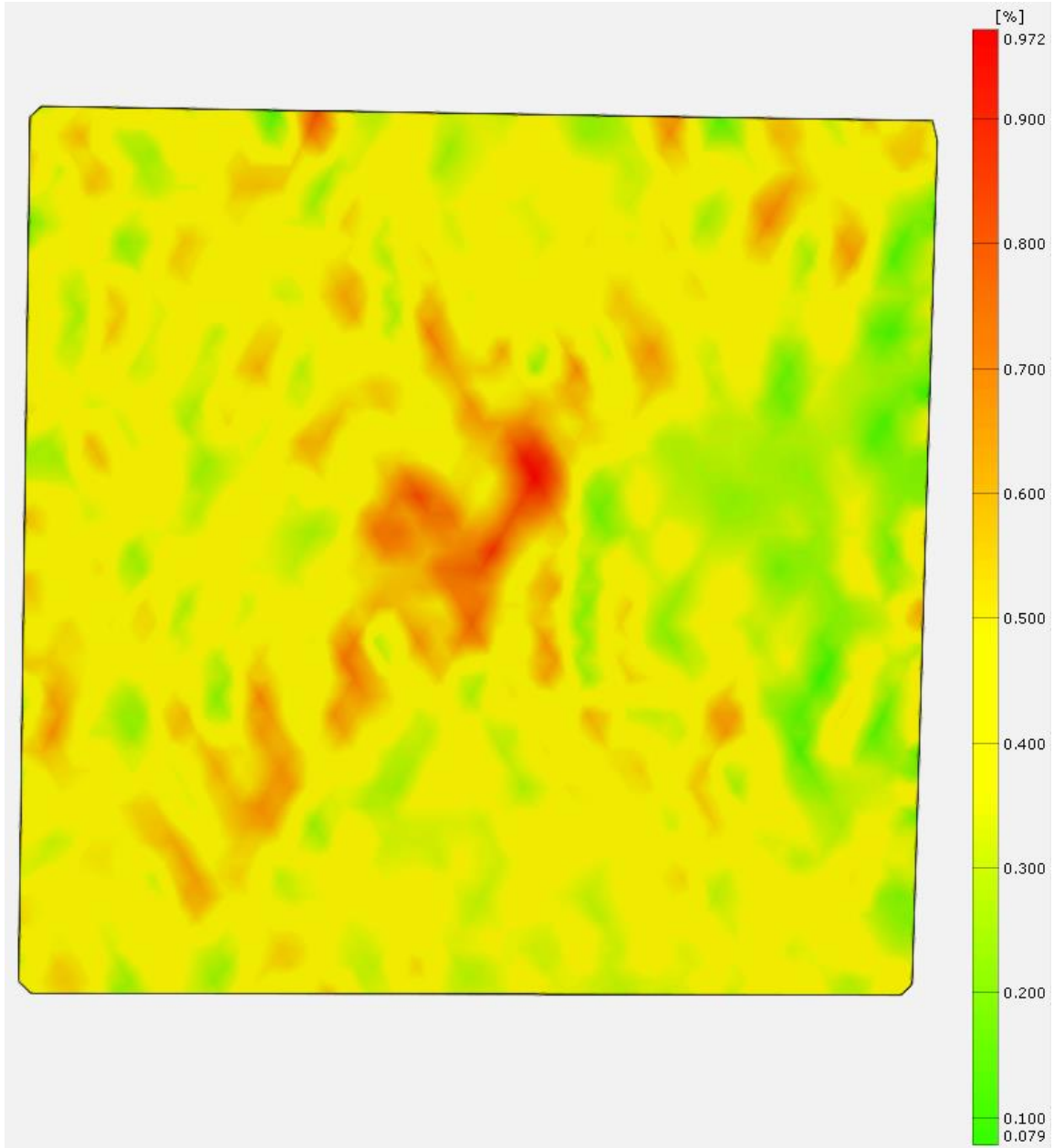


Figure 67: Strain heatmaps from bias GtB. Strain in X (machine loaded axis). Strain is in percent. Frame 15 (load step 1, 1% shear strain).

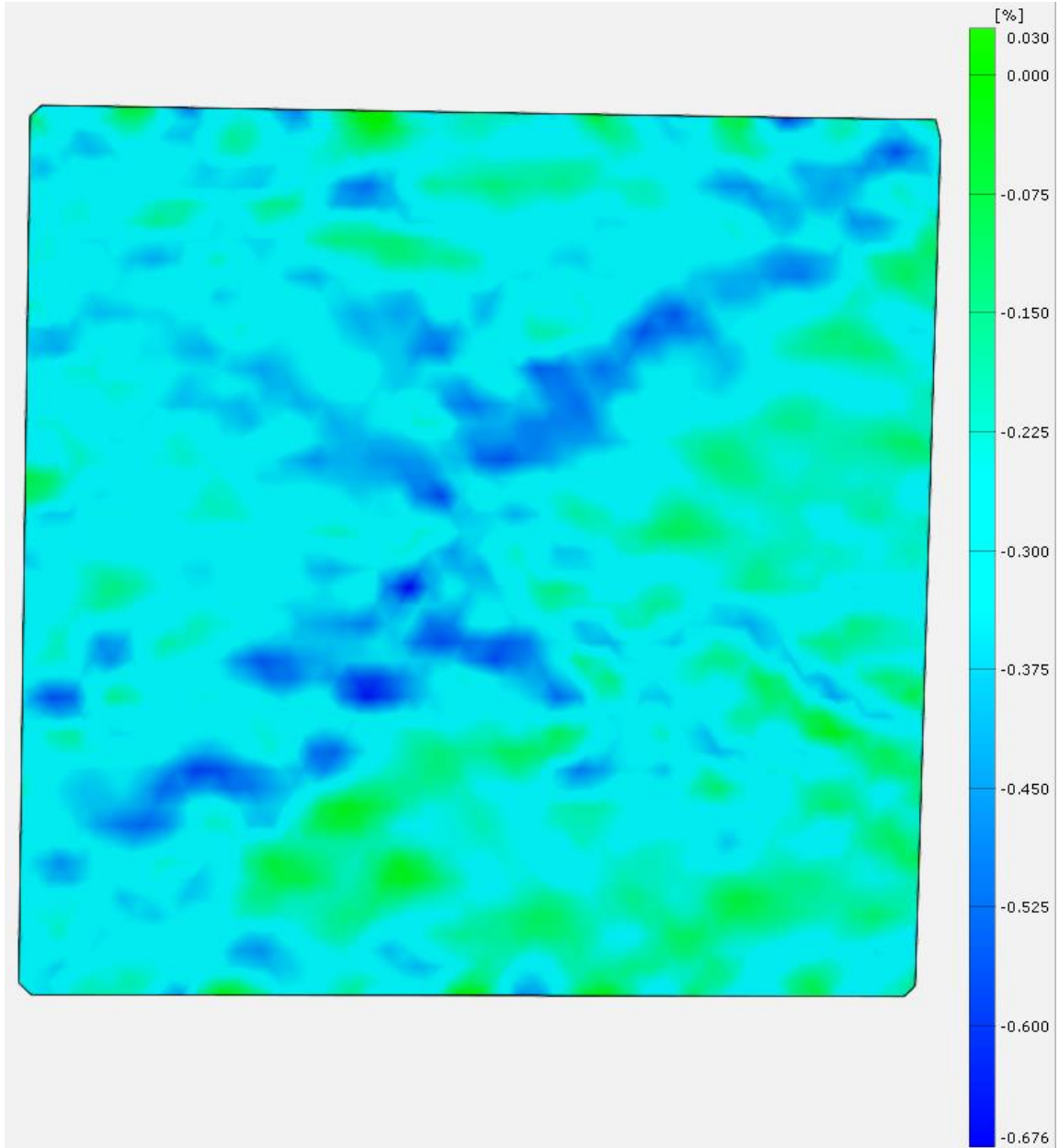


Figure 68: Strain heatmaps from bias GtB (continued). Strain in Y (Poisson-induced). Strain is in percent. Frame 15 (load step 1, 1% shear strain).

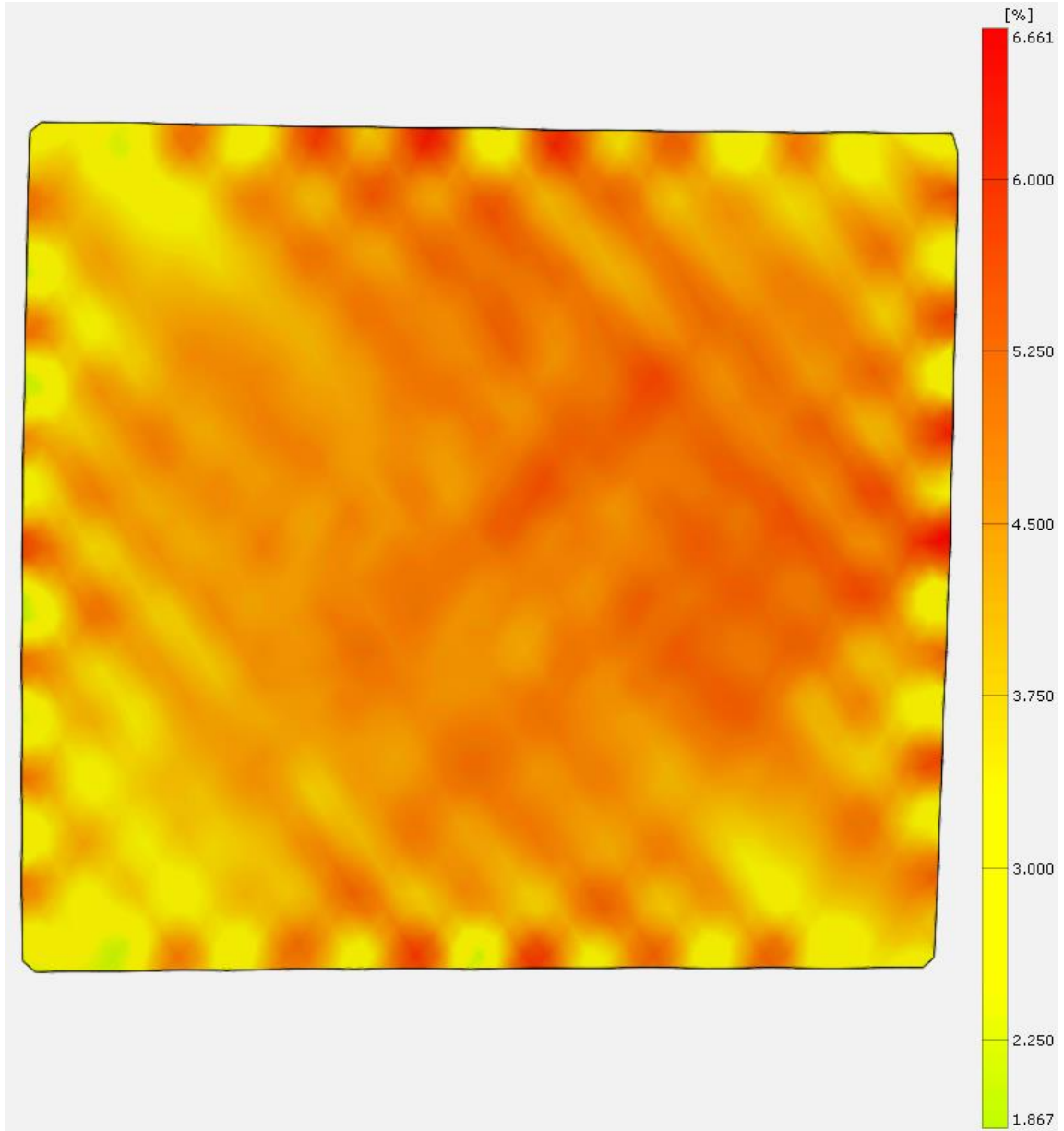


Figure 69: Strain heatmaps from bias GtB. Strain in X (machine loaded axis). Strain is in percent. Frame 190 (load step 3, 1% re-zeroed shear strain).

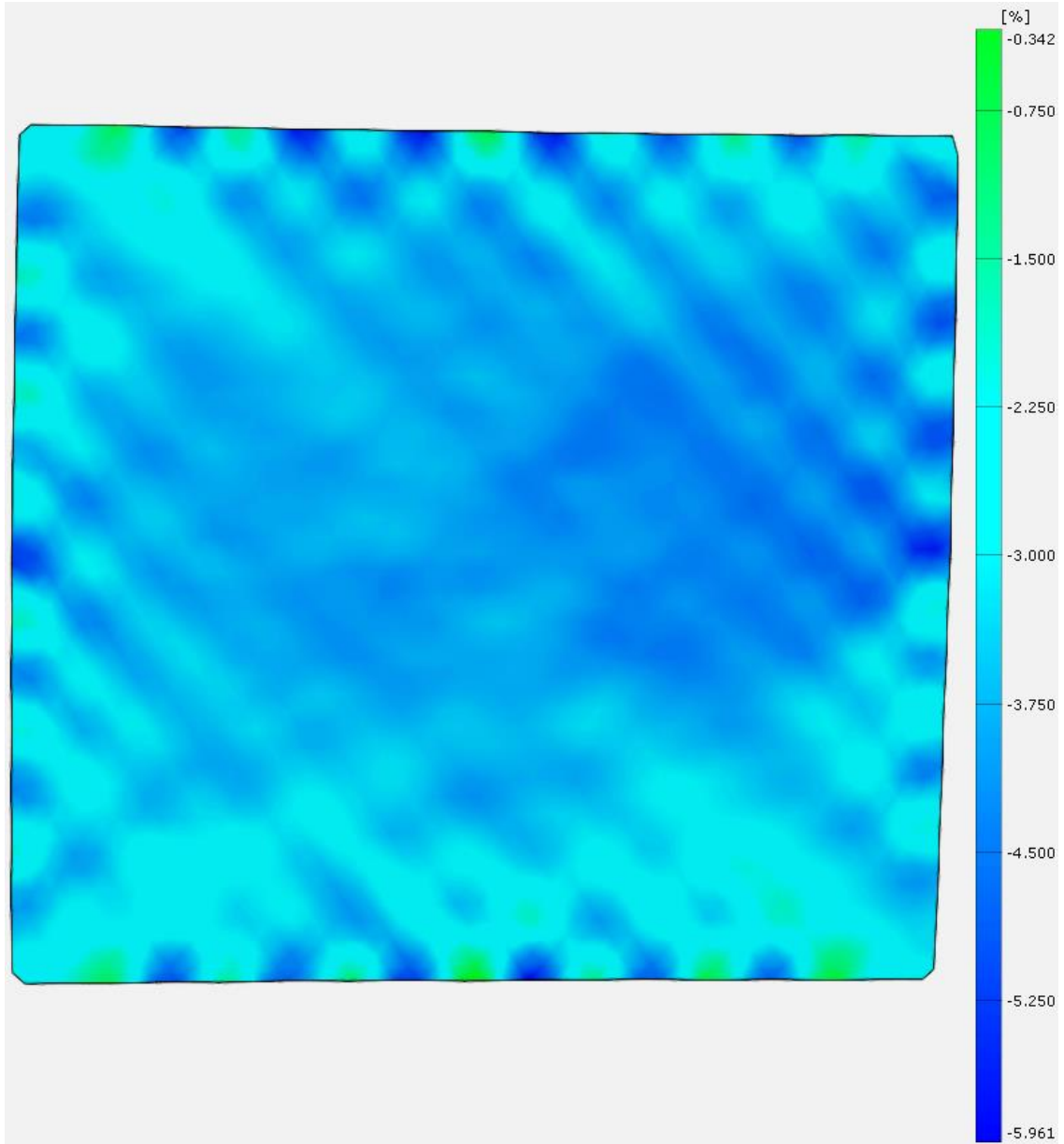


Figure 70: Strain heatmaps from bias GtB (continued). Strain in Y (Poisson-induced). Strain is in percent. Frame 190 (load step 3, 1% re-zeroed shear strain).

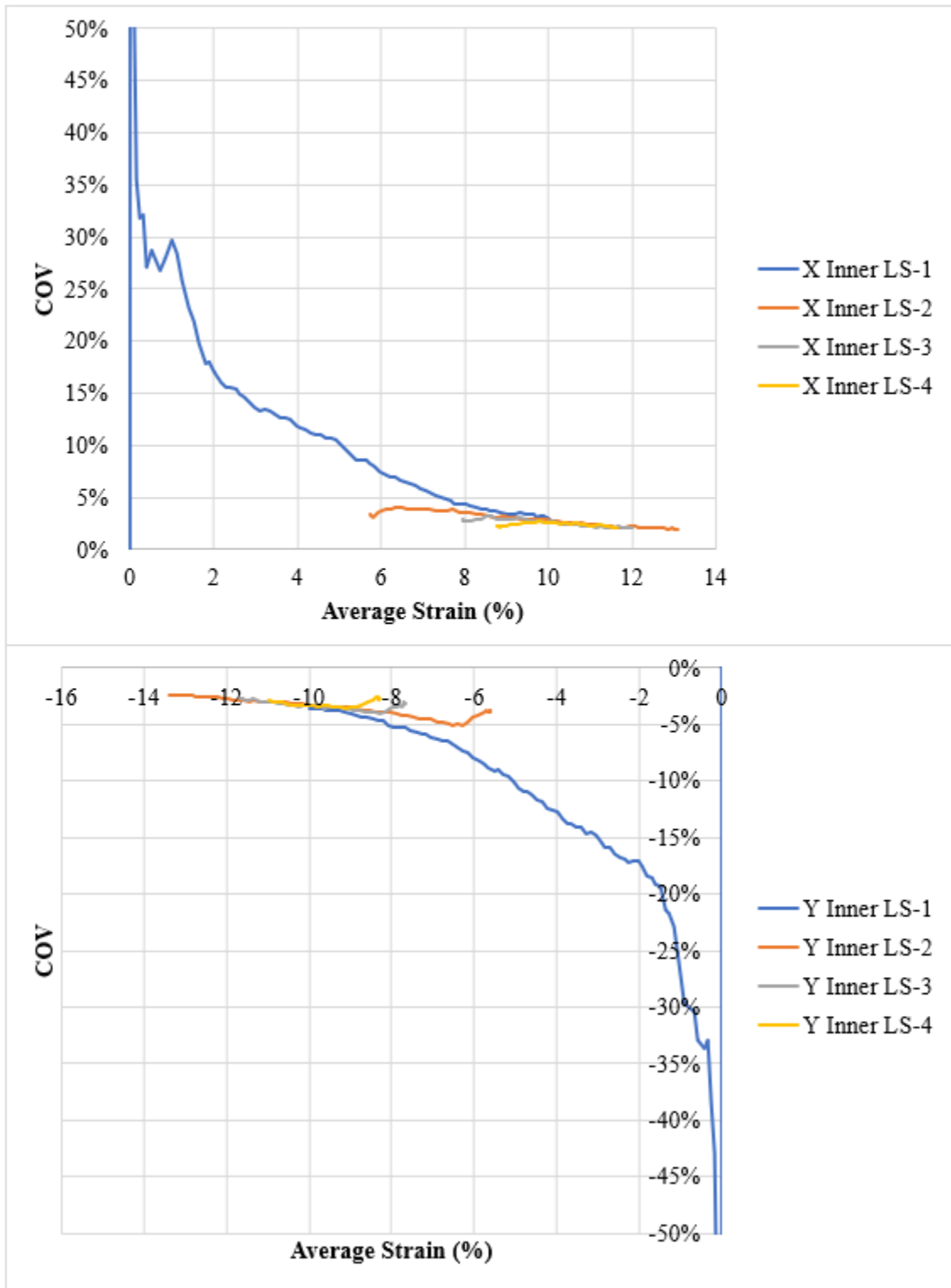


Figure 71: Type 1 COV trend for geotextiles (GtA bias trial 3). LS = Load Step.

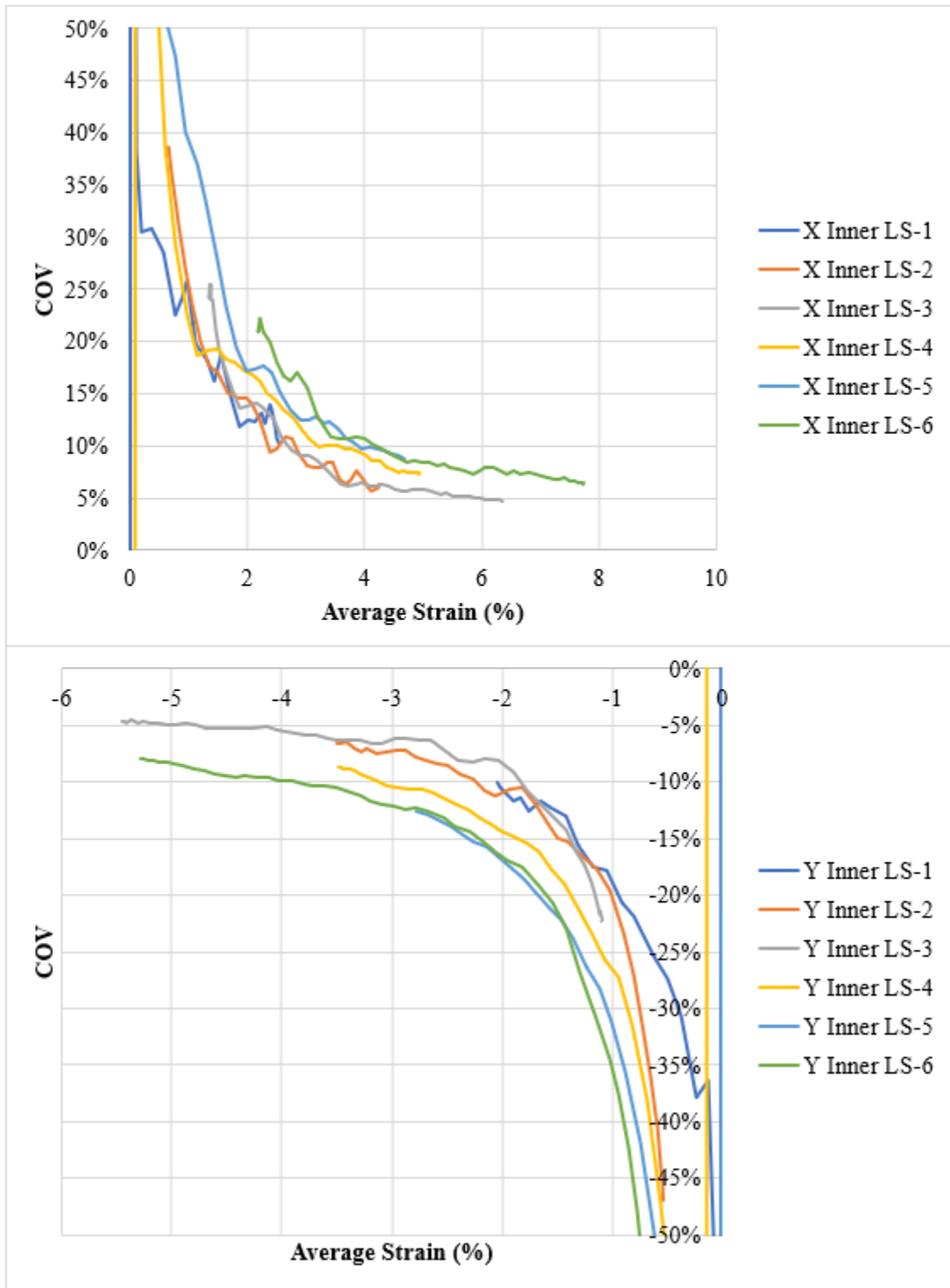


Figure 72: Type 2 COV trend for geotextiles (GtB bias trial 4). LS = Load Step.

Non-Bias Geotextiles. Only one non-bias geotextile test was evaluated (with 2-inch-wide full-length slits), which appeared to have very good uniformity as shown in Figure 73 and Figure 74. The heatmaps are shown for the final image from the test (the lowest COV), which reached just over 1% X strain and 1.1% Y strain. Moiré effect appeared more strongly in the non-bias test than in the bias tests, possibly because the strain levels were overall much smaller in the non-bias test (1% or less, versus up to 13% in the bias geotextile tests). Moiré patterns can be observed particularly in Figure 74, which appears to have stripes of higher strain values. Normally these stripes would indicate stress concentrations, but in this test, the stripe locations move rapidly across the surface and the number of stripes fluctuates, suggesting that these are artifacts. Moreover, the stripe locations are not always consistent with the locations of the arm slits that might legitimately create stripes of stress concentrations.

Statistical strain uniformity is shown in Figure 75, where for clarity, data spread greater than 70% or lower than 0% is not shown. The COV for this test followed the same trend of improvement with higher strain, ultimately reaching 10% COV. The trend has not completely tapered to an asymptote by the end of the test, which suggests that the COV would likely continue to drop if testing had continued. (The test was stopped when the load cells reached their limit rather than because of material failure.) Considering the higher noise present in the heatmaps, it is reasonable to see a worse COV for this test in comparison to the bias tests.

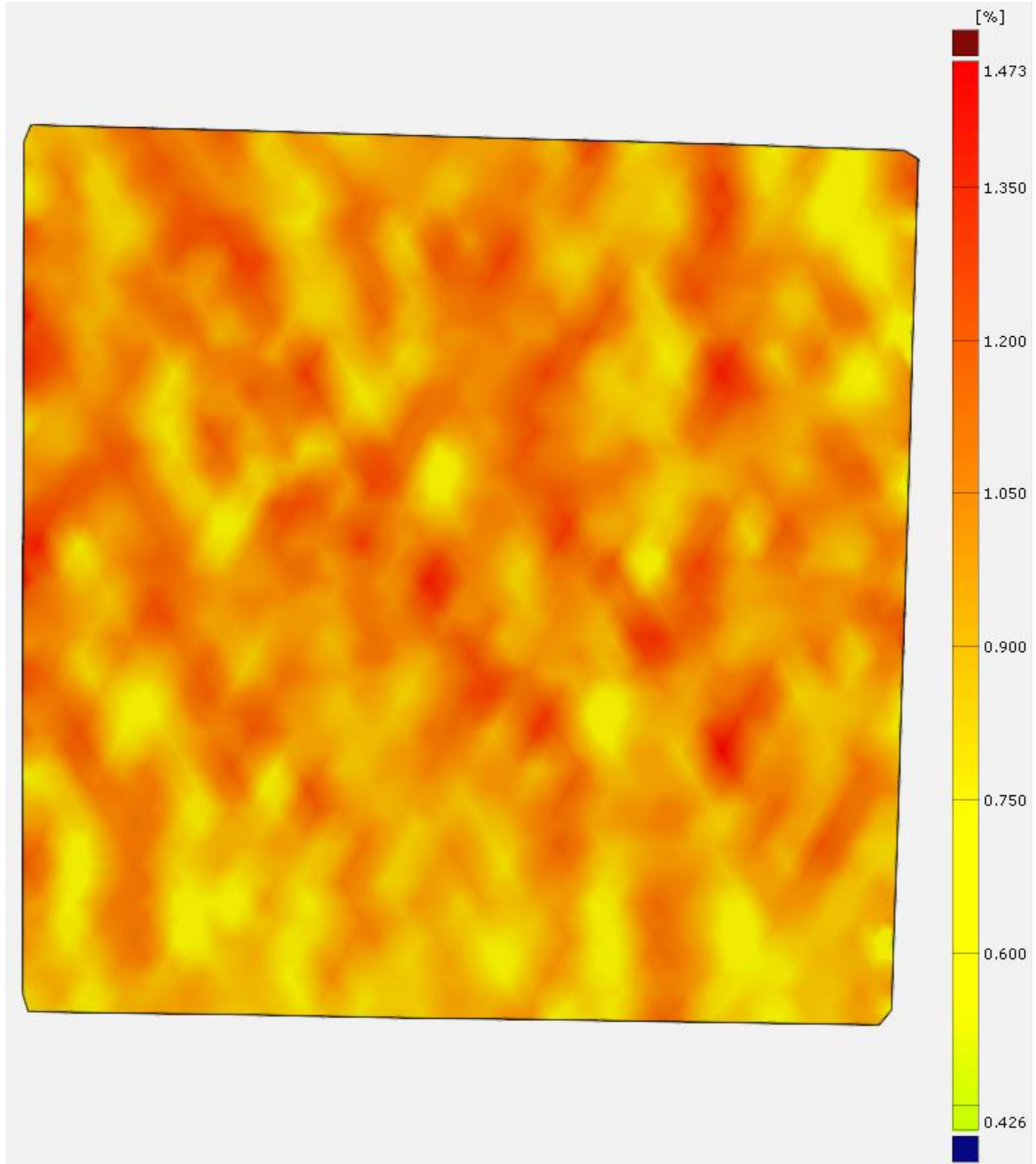


Figure 73: Strain heatmaps from non-bias GtB, monotonic test. Strain in X. Strain is in percent.

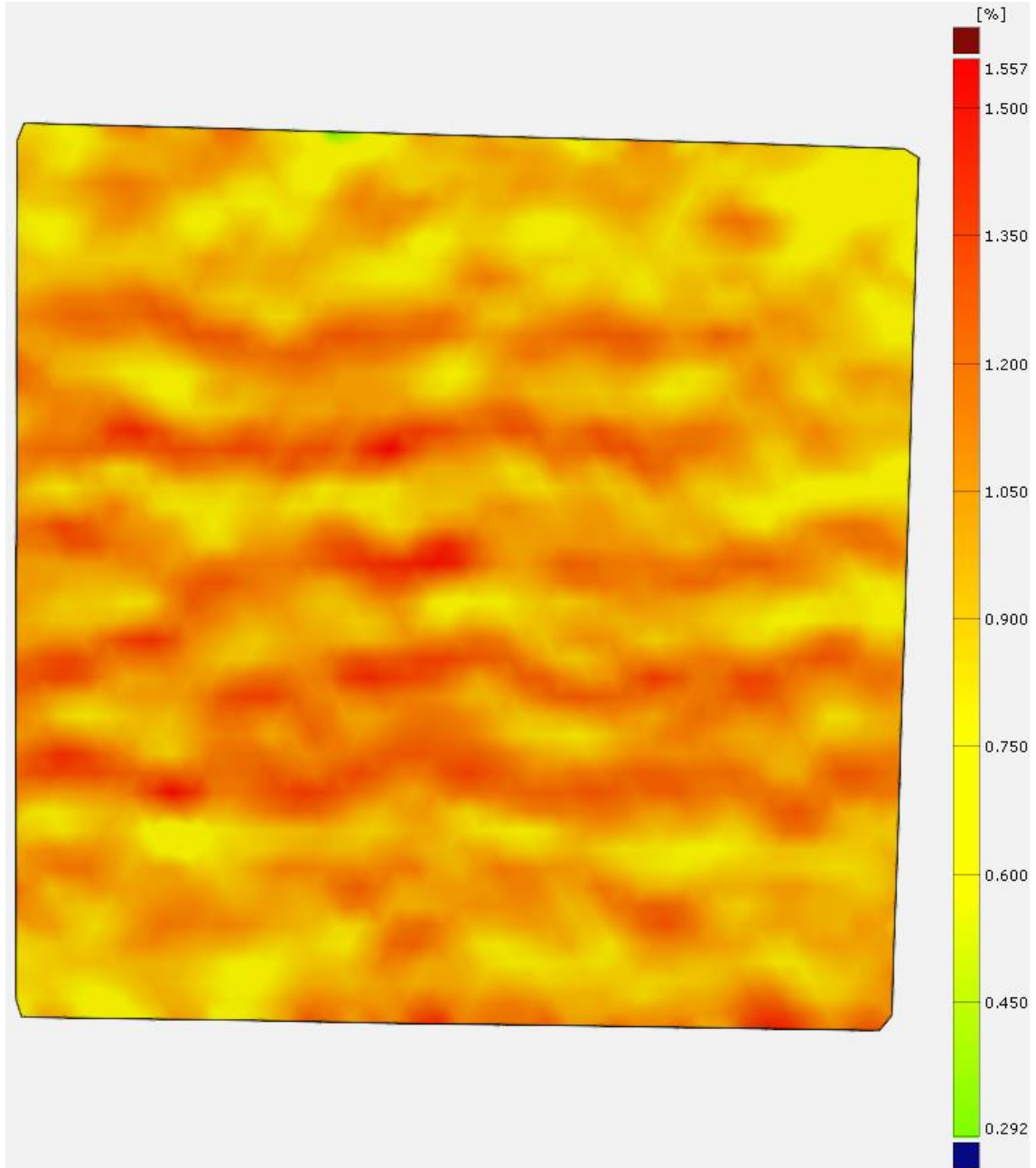


Figure 74: Strain heatmaps from non-bias GtB, monotonic test (continued). Strain in Y. Strain is in percent.

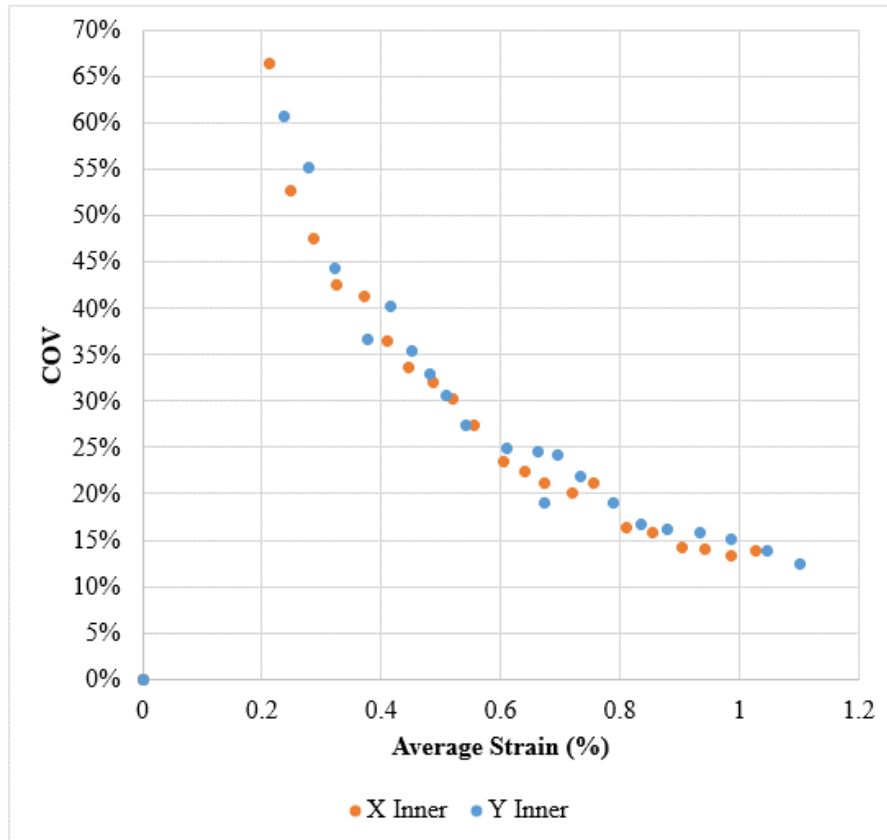


Figure 75: Statistical strain uniformity (GtB non-bias Mode 1, monotonic test).

### Strain Uniformity Summary and Discussion

The strain heatmaps for both geogrids and geotextiles generally showed better uniformity toward the interior of the sample as opposed to the edges of the region of interest, which was confirmed statistically by comparison of the four concentric regions. For both bias and non-bias tests on geogrids, the heatmaps also revealed that even within this inner region, the locations of high and low strain values fluctuated as the tests progressed, implying that the geogrids do not have perfect representative or ideal gage nodes. These results suggest that even if boundary conditions are perfectly controlled, the geogrid materials may not be as uniform as was hoped. In particular, the punched-

and-drawn production method may leave residual strains that interfere with ideal uniform strain behavior. Consequently, the regional averaging method discussed in the Postprocessing section (page 74) was adopted for use on all geogrid tests in this thesis. If a single gage must be used, the centerline of the inner region (such as was used in prior work by Haselton 2018) appears to be the best location to minimize inconsistencies. The bias tests appeared to be more sensitive to regional influences on strain uniformity than the non-bias tests, which supports the decision to use DIC for this research.

The coefficient of variation (COV) of 5% was derived from literature on architectural membranes, which are very smooth and continuous materials. Discontinuous materials such as the geogrids in this study were expected to have a higher (worse) COV than continuous materials such as the geotextiles. Additionally, the rough surface texture on the geotextiles should increase the COV in comparison to the very smooth surface of an architectural membrane. The fact that the square geogrids consistently reach the COV standard set by architectural membranes reflects very well on the uniformity for these materials, and for the rectangular geogrids to consistently reach a COV of 10 to 15% does not indicate unacceptable uniformity. Furthermore, the rectangular geogrids often did not reach the COV asymptote suggested by their COV trend due to their short strain range. With additional strain range, the rectangular COV would also likely have reached 5% COV. The geotextiles generally reached or exceeded the 5% COV, but their rough surface texture may have created more noise for the DIC analysis as evidenced by the longer delay in reaching their asymptote value.

DIC system sensitivity was reflected in load steps for all tests by an initial COV spike in the first load step. As the geosynthetic moved farther from the zero-strain position (always measured from the initial un-displaced position at the start of load step 1), the COV improved down to a consistent asymptote. Load steps that started with higher displacement from the reference position did not exhibit the COV spike, which showed that the spike is due to DIC noise at low displacement rather than material behavior during the early portion of loading. Consequently, the asymptote COV value appears to be best representative of material uniformity throughout the test. Average strain values did not appear to be substantially affected by the DIC noise, based on consistent trends observed in Chapter Six. However, even if the average strains were not impacted, the standard deviation of strain would reflect DIC noise and easily skew the COV, since it is defined here as the standard deviation divided by the average. Approximate COV asymptotes are summarized in Table 9, which shows overall excellent uniformity for all materials tested. High noise at low displacement from the reference image would agree well with the poorer COV observed for the non-bias geotextile, which exhibited very low strain (1% or less) throughout the entire test. Consequently, its COV of 10% (Table 9) is most likely an outlier that would have dropped further if the test had not reached the maximum capacity of the load cells.

Table 9: Approximate COV asymptotes.

<b>Material</b>	<b>Bias</b>	<b>Non-Bias</b>	<b>Material</b>	<b>Bias</b>	<b>Non-Bias</b>
Geogrid A	+/-5%	n/a	Geogrid E	+/-3%	n/a
Geogrid B	+/-5%	+5%	Geogrid F	+/-5%	n/a
Geogrid C	+/-5%	+5%	Geotextile A	+/-3 to 5%	n/a
Geogrid D	+/-3%	n/a	Geotextile B	+/-5%	+10%

### Zero Shear Strain Assumption Check

A fundamental assumption in both the shear modulus derivation for this research and the derivations in Haselton's (2018) work is that the shear strain in the loading directions ( $\gamma_{xy}$ ) is assumed to be zero. Figure 76 left shows a possible schematic diagram of the effect of non-zero shear strain  $\gamma_{xy}$  created by off-axis load transfer paths (red arrows). As seen here, the sample becomes distorted and rotation appears in the AOI. Figure 76 right shows an ideal test with balanced biaxial expansion/contraction, zero shear strain  $\gamma_{xy}$ , and no rotation. Dashed lines show the sample with no displacement. Note that Figure 76 right is typical for a Mode 2 or Mode 3 test (all bias tests), whereas a Mode 1 test would have expansion in both axes instead of in one axis only. As discussed in Chapter Two, shear is created intentionally in the bias tests purely by the orientation of the material directions (XMD, 1, and MD, 2) in the sample; this intentional shear strain is  $\gamma_{12}$  as distinct from  $\gamma_{xy}$ .

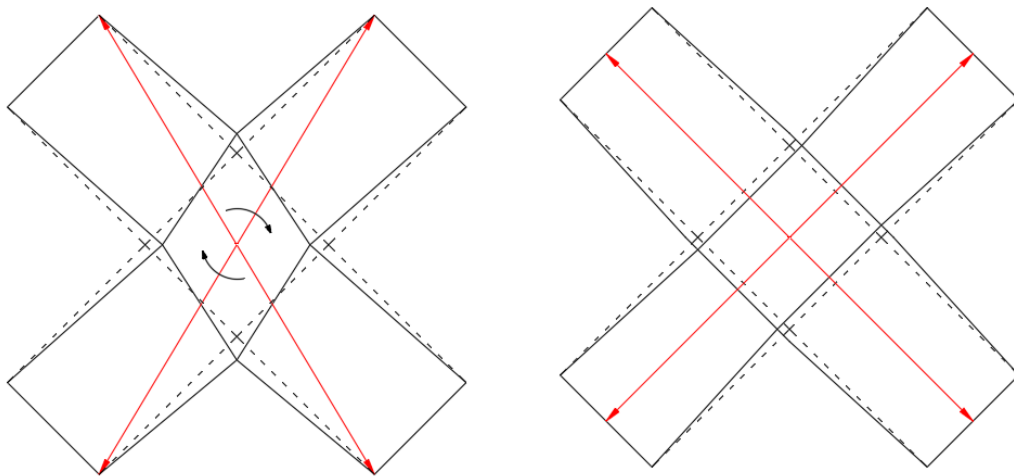


Figure 76 Left: Non-zero shear strain  $\gamma_{xy}$ . Right: Zero shear strain  $\gamma_{xy}$ .

The engineering shear strain  $\gamma_{xy}$  is a measure of the total shear in the X-Y plane. It can be calculated from the shear strain tensor  $\varepsilon_{xy}$ , which is the average of the shear strain on the X face in the Y direction ( $dv/dx$ ), and on the Y face in the X direction ( $du/dy$ ), as shown in Equations (17) and (18) and illustrated in Figure 77:

$$\varepsilon_{xy} = \varepsilon_{yx} = \frac{dv}{dx} + \frac{du}{dy} \quad (17)$$

$$\gamma_{xy} = \frac{dv}{dx} + \frac{du}{dy} = 2\varepsilon_{xy} \quad (18)$$

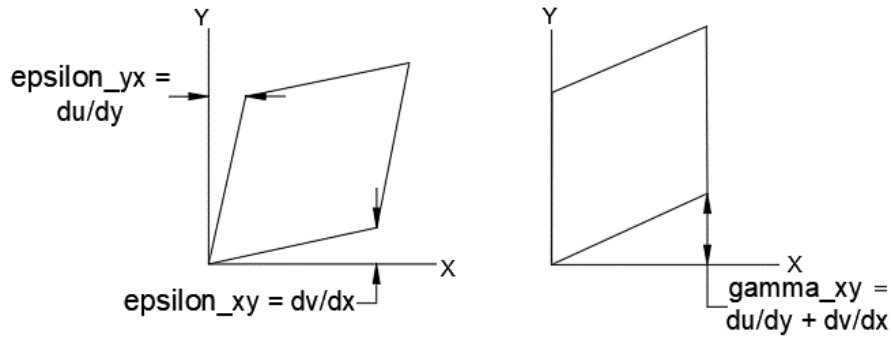


Figure 77: Illustrated definition of  $\varepsilon_{xy}$  and  $\gamma_{xy}$ .

To validate the zero  $\gamma_{xy}$  assumption for the geotextile tests,  $\gamma_{xy} = 2\varepsilon_{xy}$  was calculated. The DIC analysis tools did not have a measure for obtaining  $\gamma_{xy}$  directly, but DIC calculation of  $\varepsilon_{xy}$  was a similar analysis to what was performed for the heatmap evaluations of  $\varepsilon_x$  and  $\varepsilon_y$ . To calculate  $\gamma_{xy}$ , the maximum average  $\varepsilon_{xy}$  for the innermost region (corresponding to the geotextile COV statistical analyses) was used as shown

below in Table 10. The maximum average was used instead of the maximum  $\varepsilon_{xy}$  to minimize the impact of high magnitude, lower frequency DIC surface errors (such as twinning) discussed in the previous section. For all geotextile tests,  $\gamma_{xy}$  was generally 1.6% or less, and it was as low as 0.2% for several tests. In comparison, the maximum average  $\varepsilon_x$  and  $\varepsilon_y$  values for the bias tests ranged from 5.5% to over 13% as shown in Table 10. The non-bias test exhibited nearly the lowest  $\gamma_{xy}$  (0.4%) out of all the geotextile tests, but the  $\varepsilon_x$  and  $\varepsilon_y$  values are also much lower—just over 1%. As discussed earlier, the low strains in this test may be on the borderline of the DIC sensitivity for the methods used in this thesis, so additional tests at higher strain levels would be good to make sure that the 0.4%  $\gamma_{xy}$  is not significant here. (Strain levels for this test were limited by the load cell capacity of the biaxial test frame.)

Table 10: Bias geotextile maximum average shear strain  $\gamma_{xy}$ .

Material	Trial	$\varepsilon_{xy}$ for Inner Region		$\gamma_{xy} = 2\varepsilon_{xy}$ (%)	Absolute Value Maximum Average for Inner Region	
		Absolute Value Maximum Average ( $\varepsilon_{xy}$ ) (%)	Maximum Standard Deviation (%)		$\varepsilon_x$ (%)	$\varepsilon_y$ (%)
GtA	Bias 1	0.1	0.1	0.2	8.1	7.6
	Bias 2	0.5	0.1	1.0	6.9	6.3
	Bias 3	0.5	0.1	1.0	13.1	13.4
GtB	Bias 1	0.6	0.1	1.2	9.2	9.3
	Bias 2	0.7	0.1	1.4	8.3	6.4
	Bias 3	0.1	0.2	0.2	8.0	6.8
	Bias 4	0.8	0.1	1.6	7.8	5.5
	Non-bias	0.2	0.2	0.4	1.03	1.10

For the geogrid bias tests,  $\gamma_{xy}$  was estimated based on vector deformation of selected points across the area of interest as shown in Figure 79 through Figure 83. The

arrows in these figures indicate the direction of displacement for a point on the geogrid, and the magnitude of displacement is indicated by both the color and the length of the arrows. (Since this study was primarily geared toward investigation of strains, no DIC calibration was performed for distance measurements; consequently, distance measurements are approximately calibrated from the 400 x 400 mm area of interest (the dimensions of the square green backdrop). Input of a distance scale was required for the DIC software to perform this type of motion study.) For each architecture type, one bias geogrid test was evaluated using this method.

The first figure for each test (Figure 79 and Figure 82) shows one axis displacing outward from the center of the AOI due to machine loading and the second axis displacing toward the center of the AOI due to the Poisson effect. This is an example of good biaxial behavior which is also illustrated in Figure 76 right. The second figure for each test (Figure 80 and Figure 83) occur later in the test and show rotation in the AOI. Rotation is undesirable, since Figure 76 left shows rotation to be an evidence of non-zero  $\gamma_{xy}$ . For the two tests evaluated, rotation was not always concentric to the middle of the AOI, and both tests flickered back and forth between good biaxial behavior and rotation. The first few load steps showed much better consistency in good biaxial behavior, with rotation appearing mid-test and becoming dominant in the later load steps. The third figure for each test (Figure 81 and Figure 84) is the same as the second figure for each test, except here the vectors are broken into their  $\Delta x$  and  $\Delta y$  components. To calculate  $\gamma_{xy} = \frac{dv}{dx} + \frac{du}{dy}$  as given by Equation (18),  $dy$  and  $dx$  were set equal to a side length  $L$  of 100 mm for the inner region or 400 mm for the full AOI, and vector deformations  $\Delta x$  and

$\Delta y$  were used to approximate  $du$  and  $dv$  along the perimeter of each region defined by  $L$ . Results are shown in Table 11, along with maximum average  $\varepsilon_x$  and  $\varepsilon_y$  values for comparison. Surprisingly, the square geogrid test showed higher  $\gamma_{xy}$  than the rectangular geogrid test. In particular, for the square geogrid test, the quality worsened away from the central region, reaching 3.75%  $\gamma_{xy}$  at the edges of the AOI. The large quality difference between the inner and total regions for the square geogrid underlines the importance of using data from the inner region only. In the inner region,  $\gamma_{xy}$  values for both tests were relatively small in comparison to the maximum strains in the loading directions: less than 0.8%  $\gamma_{xy}$  for the square geogrid (GgD) and less than 0.5%  $\gamma_{xy}$  for the rectangular geogrid (GgF). A second square geogrid test (GgE bias trial 6 stage 131) was spot-checked as shown in Table 11, and this test had even more rotation: 4%  $\gamma_{xy}$  for both inner and total regions.

The higher  $\gamma_{xy}$  seen in the square geogrid tests may be the result of tweaking the test alignment method partway through the materials (the square geogrids were the first to be tested). For the bias tests, the material axes were to be oriented at 45 degrees to the load axes. Alignment was easy to ensure at the central AOI, but less so out at the grip. Initially, the central AOI was aligned and the arms smoothed out to the grips from there. Partway through testing, a 45-45-90 triangle template was discovered as an easy way to ensure grip alignment as shown in Figure 78 in addition to alignment of the central AOI. Two edges of the template were aligned to the material principal axes, and the third edge was then aligned to the grip. However, this highlighted the occasional warping present in the samples, since they did not always lay perfectly flat when aligned this way. It is not

known whether the data would receive a greater impact from warping or from any slight misalignment from the initial method, and it is possible that they create similar levels of noise. However, the  $\gamma_{xy}$  for the square geogrids (especially in comparison to the results from the rectangular geogrid) suggests that this alignment tweak was a significant test improvement.

Table 11: Bias geogrid estimated shear strain  $\gamma_{xy}$ . Dimensions are approximate.

Material	Trial	Region	$\Delta x$ (mm)	$\Delta y$ (mm)	Side length, L (mm)	$\gamma_{xy} \approx$ $(\Delta x + \Delta y)/L$ (%)	Absolute Value Maximum Avg	
							$\varepsilon_x$ (%)	$\varepsilon_y$ (%)
GgD	Bias 1	Total	7.5	7.5	400	3.75	5.95	7.53
		Inner	0.4	0.4	100	0.8	6.57	6.59
GgE	Bias 6	Total	8	8	400	4.0	5.79	5.49
		Inner	2	2	100	4.0	6.39	6.14
GgF	Bias 1	Total	1	0.6	400	0.4	3.79	3.21
		Inner	0.2	0.2	100	0.4	4.07	3.79

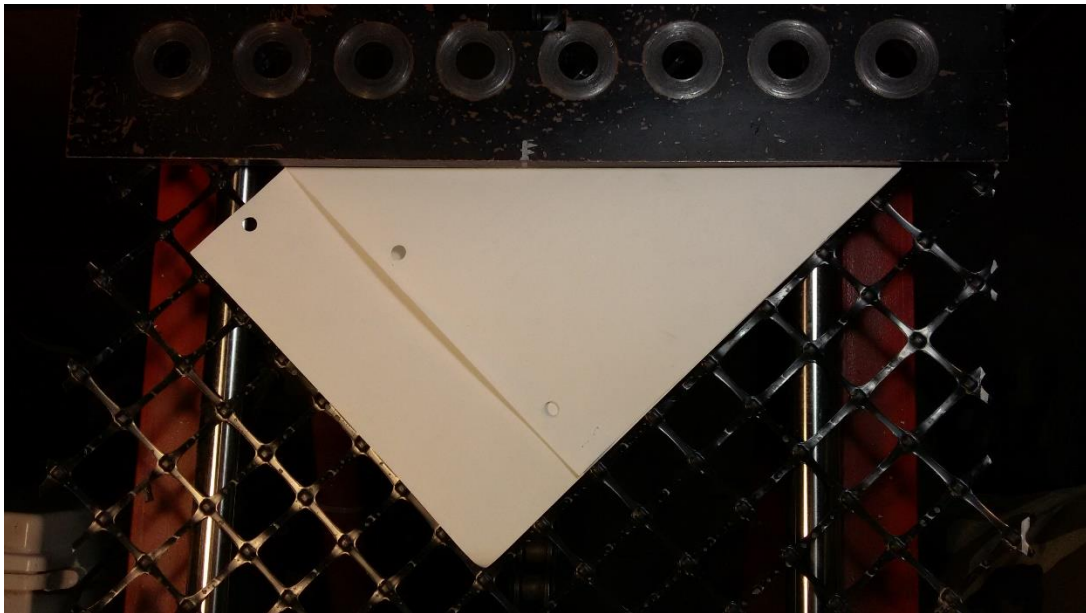


Figure 78: Folded paper template for 45-degree bias alignment at grips.

For the non-bias geogrid tests,  $\gamma_{xy}$  evaluation was performed using the same method as the bias geogrid tests. Only Mode 1 tests were examined, similar to the non-bias geotextiles. Figure 85 (square geogrid) and Figure 86 (rectangular geogrid) show the displacement vector patterns typical to these tests. Throughout these tests, no rotation was observed, indicating that  $\gamma_{xy}$  for the non-bias geogrid tests is basically zero. The higher  $\gamma_{xy}$  observed in the non-bias geotextile test may be due to noise at low strain or other factors such as slight misalignment of the melted grip holes. To verify that the difference was not due to lower precision in the geogrid analysis method, the non-bias geotextile test was also run using the vector method (Figure 87), which also indicated a slight rotation.

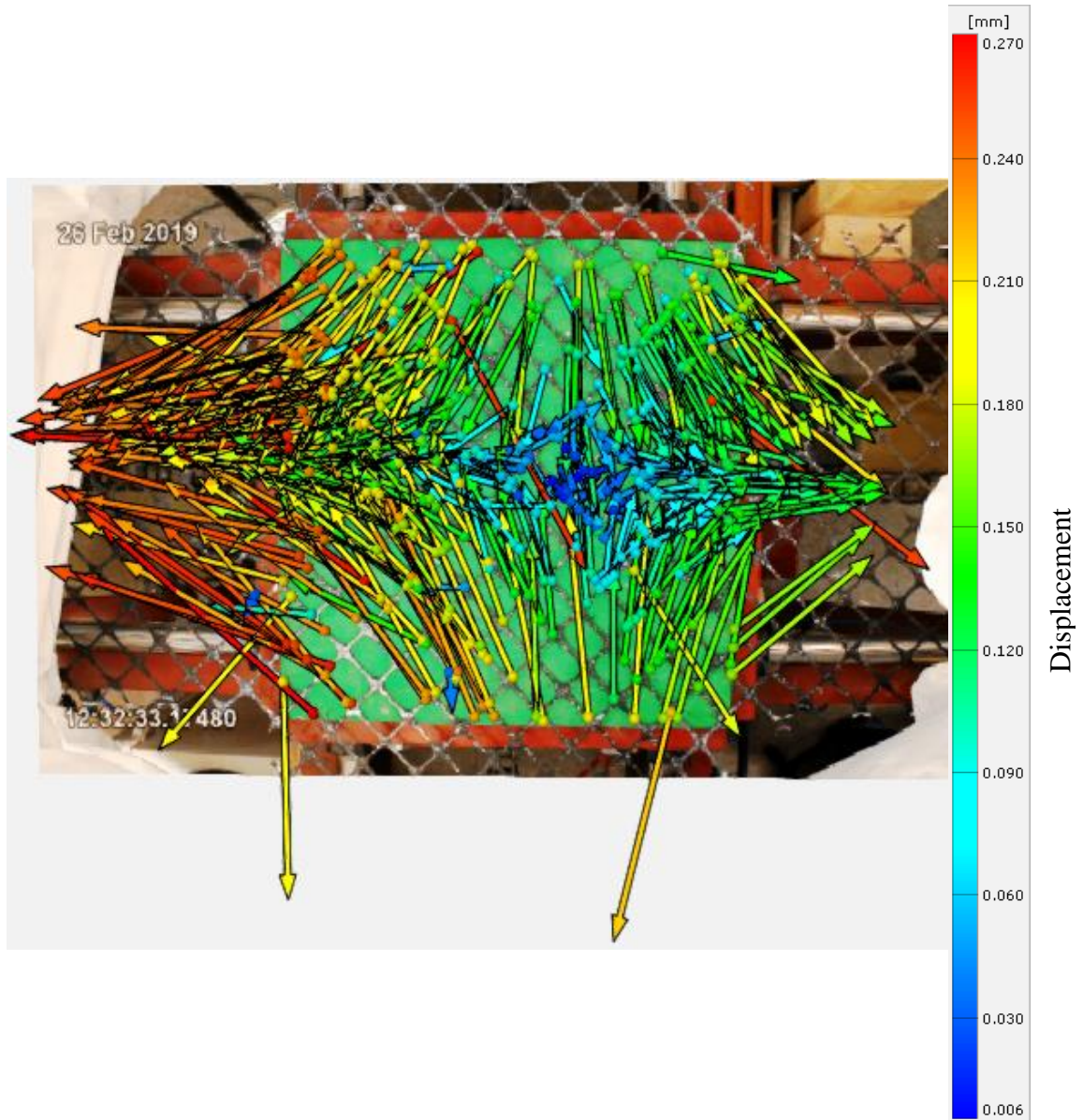


Figure 79: GgF bias trial 1, stage 22, showing good biaxial behavior with minimal rotation. Scale is approximate (units of mm).

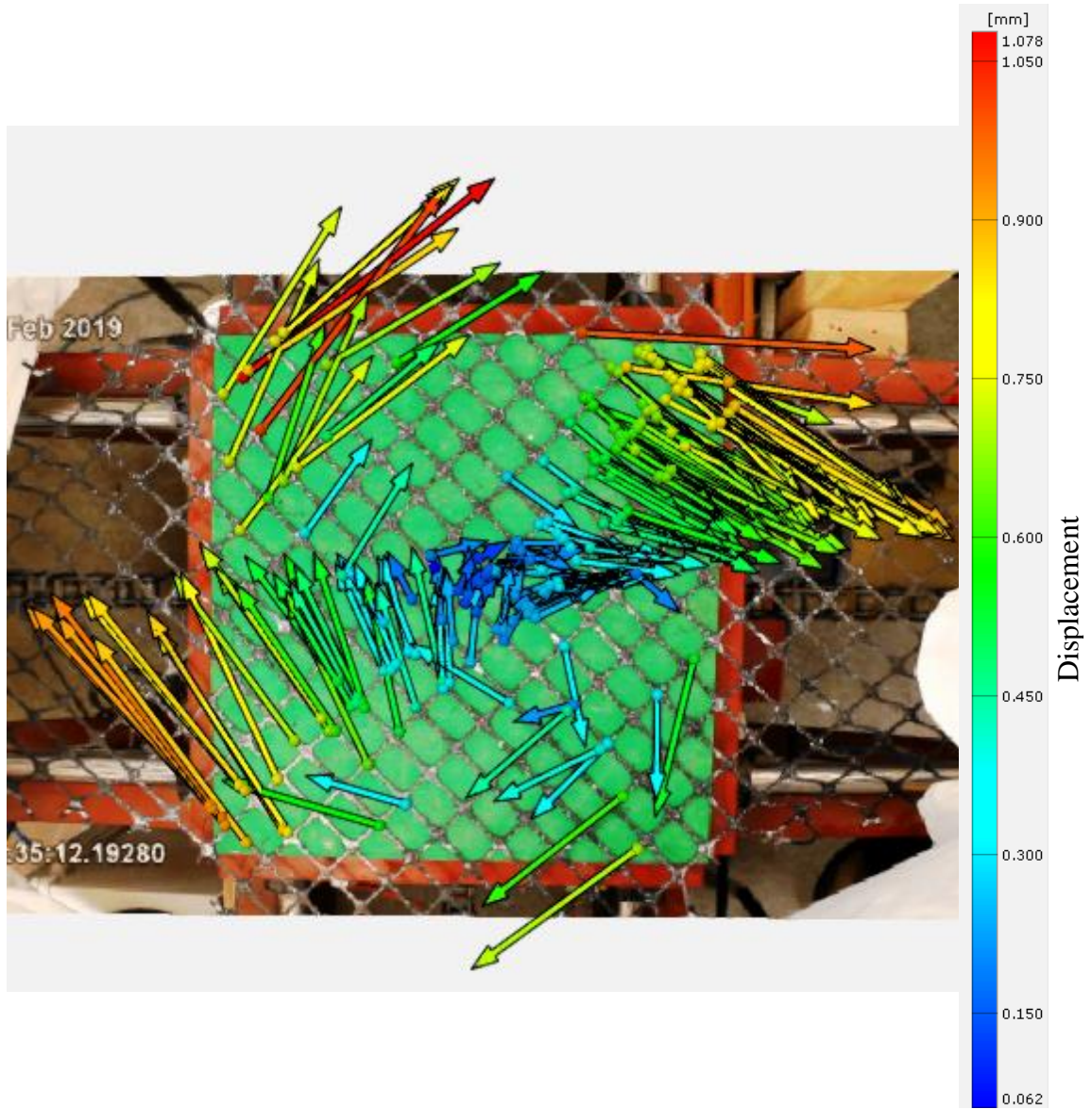


Figure 80: GgF bias trial 1, stage 122, showing clear rotational behavior later in the test. Scale is approximate (units of mm).

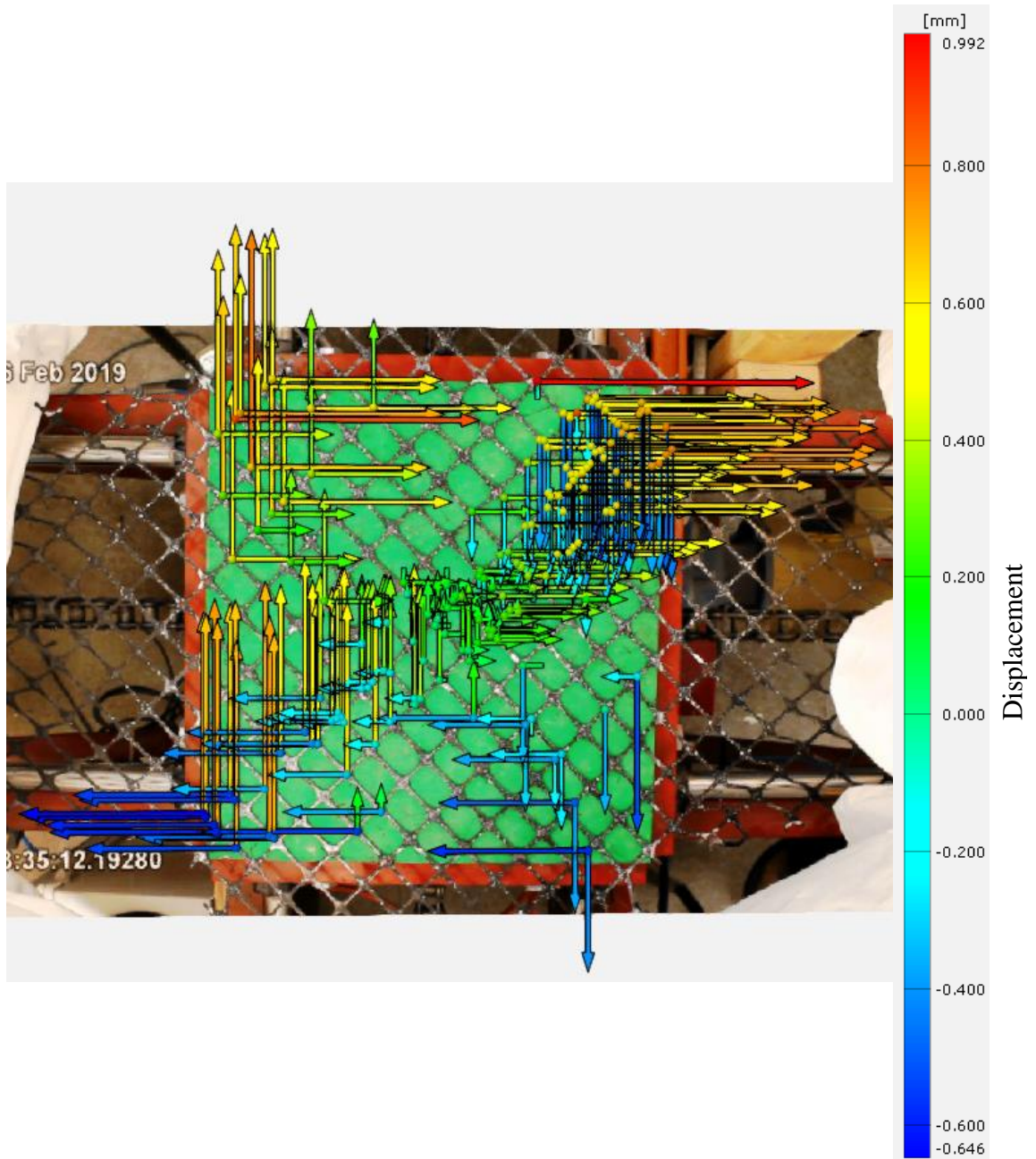


Figure 81: GgF bias trial 1, stage 122, showing X and Y components of displacement. Scale is approximate (units of mm).

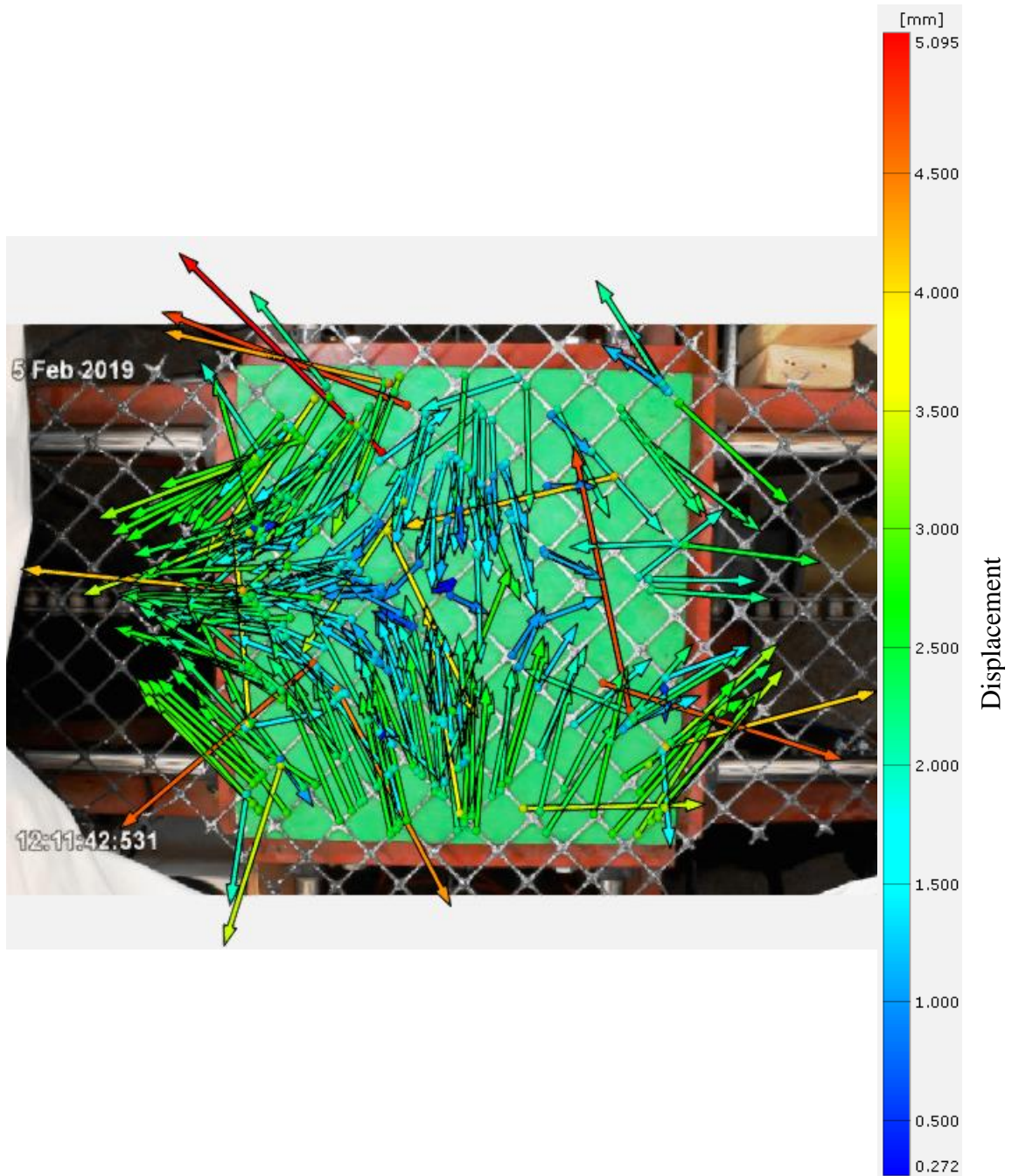


Figure 82: GgD bias trial 1, stage 28, showing good biaxial behavior with minimal rotation. Scale is approximate (units of mm).

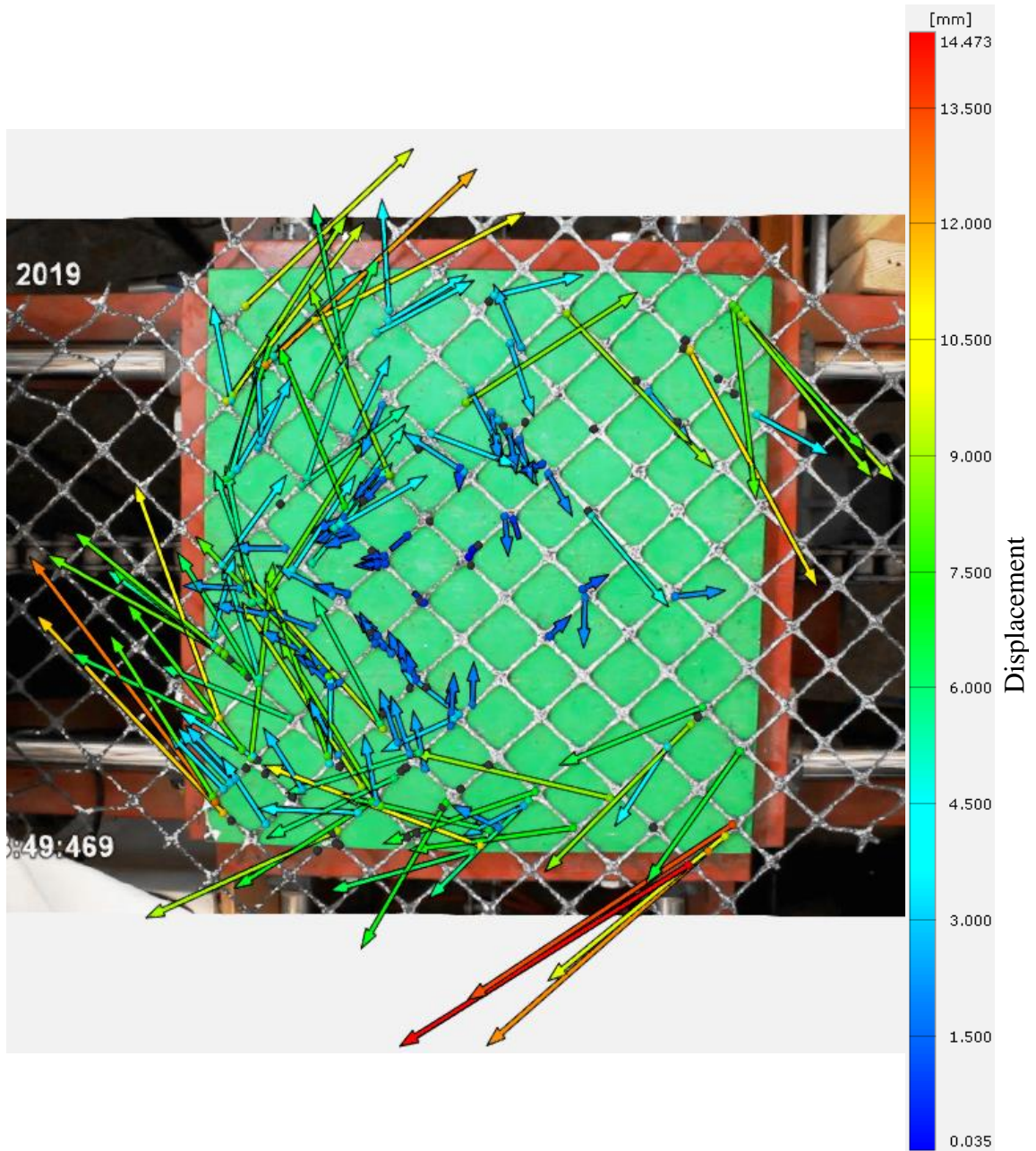


Figure 83: GgD bias trial 1, stage 76, showing clear rotational behavior later in the test. Scale is approximate (units of mm).

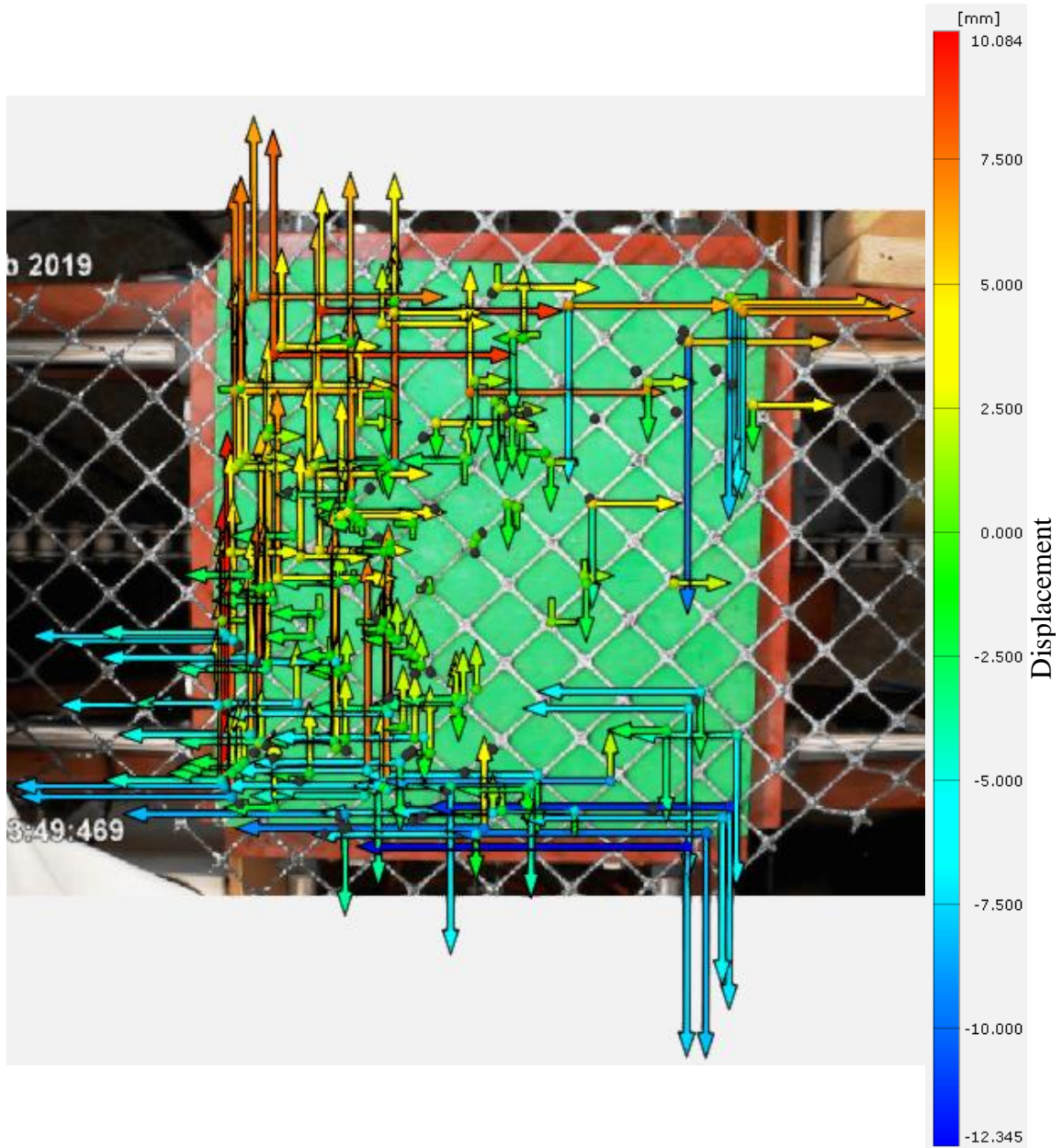


Figure 84: GgD bias trial 1, stage 76, showing X and Y components of displacement. Scale is approximate (units of mm).

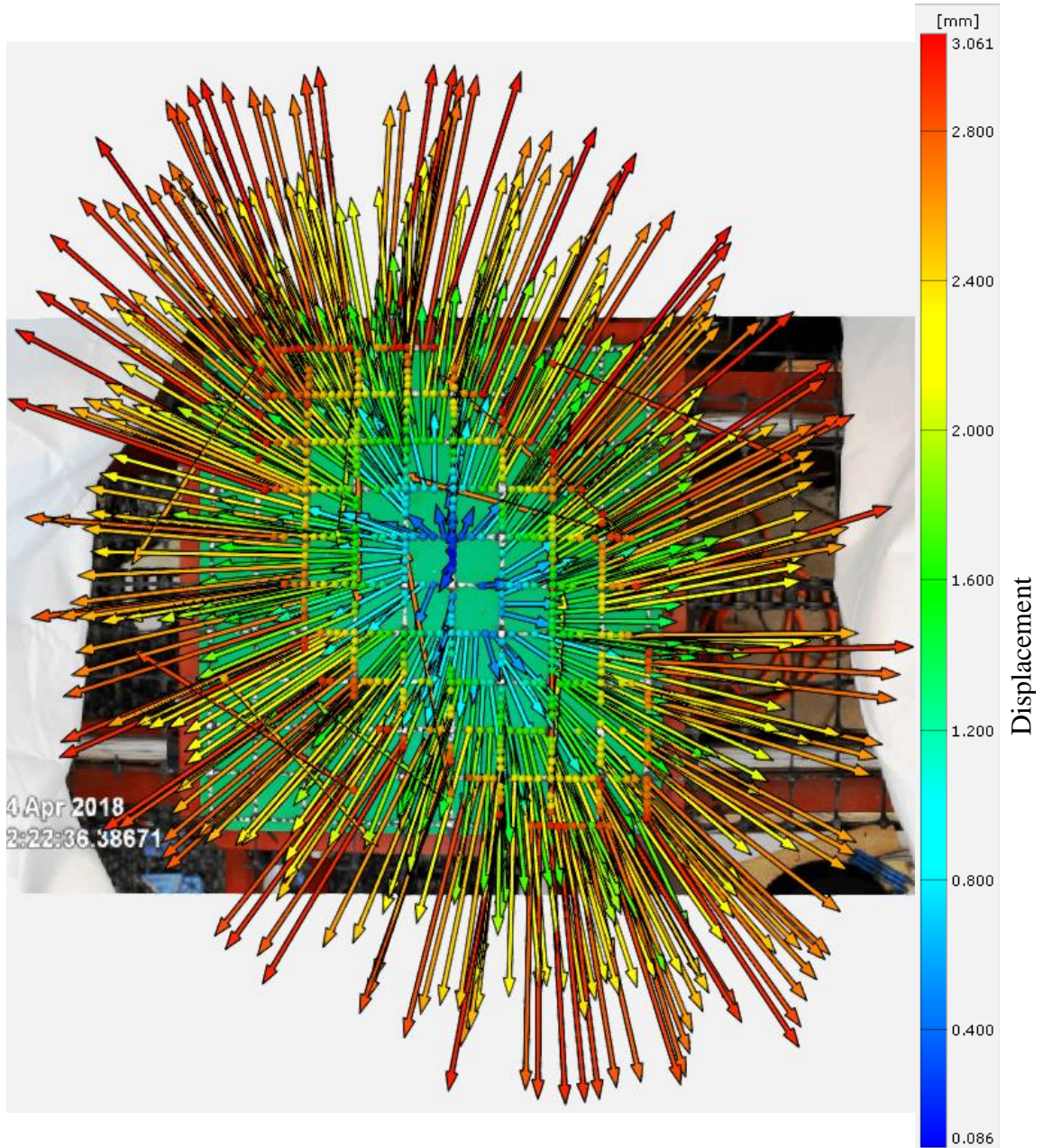


Figure 85: Non-bias GgC, stage 40, showing excellent Mode 1 biaxial behavior. Scale is approximate (units of mm).

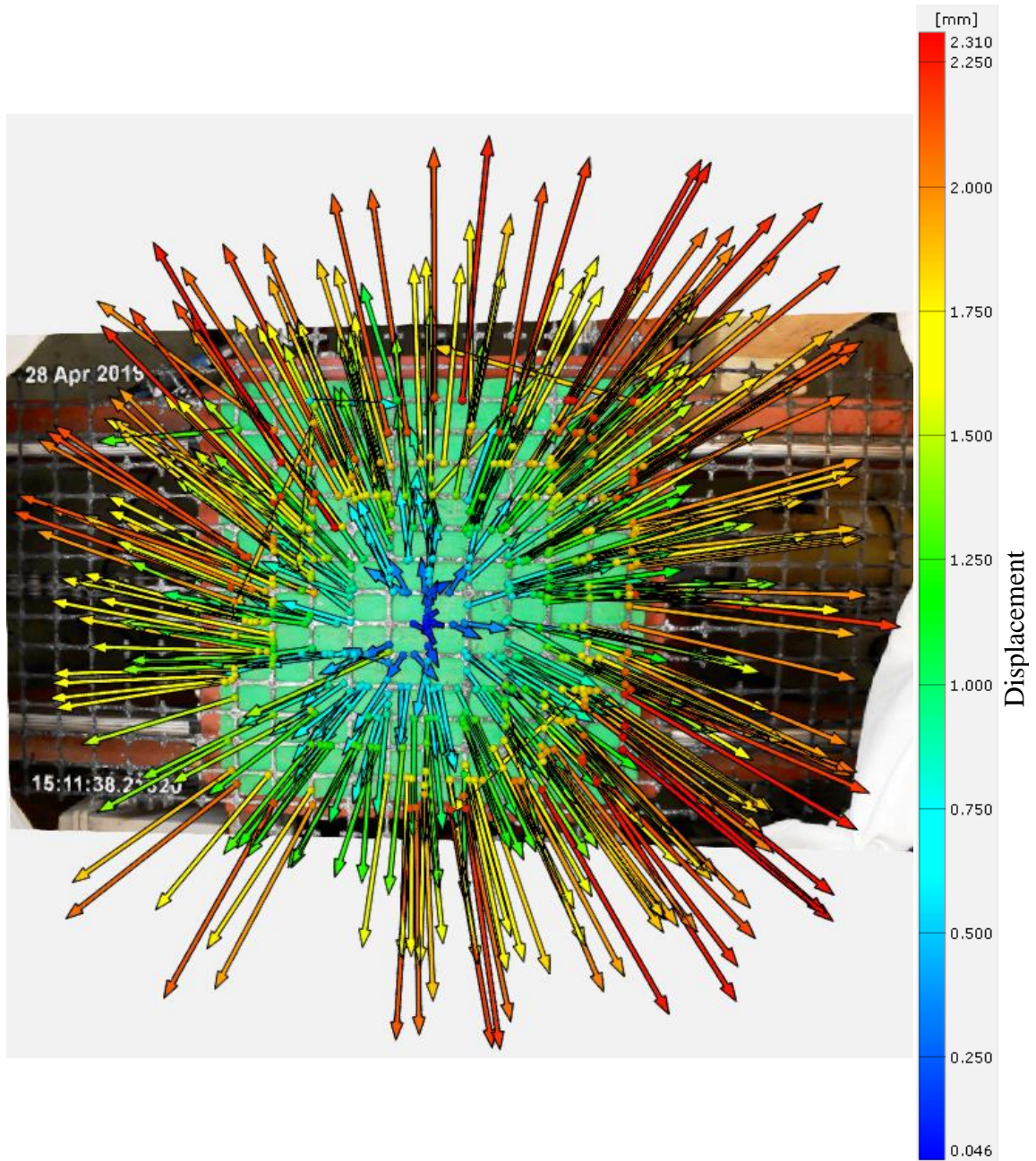


Figure 86: Non-bias GgB, stage 31, showing excellent Mode 1 biaxial behavior. Scale is approximate (units of mm).

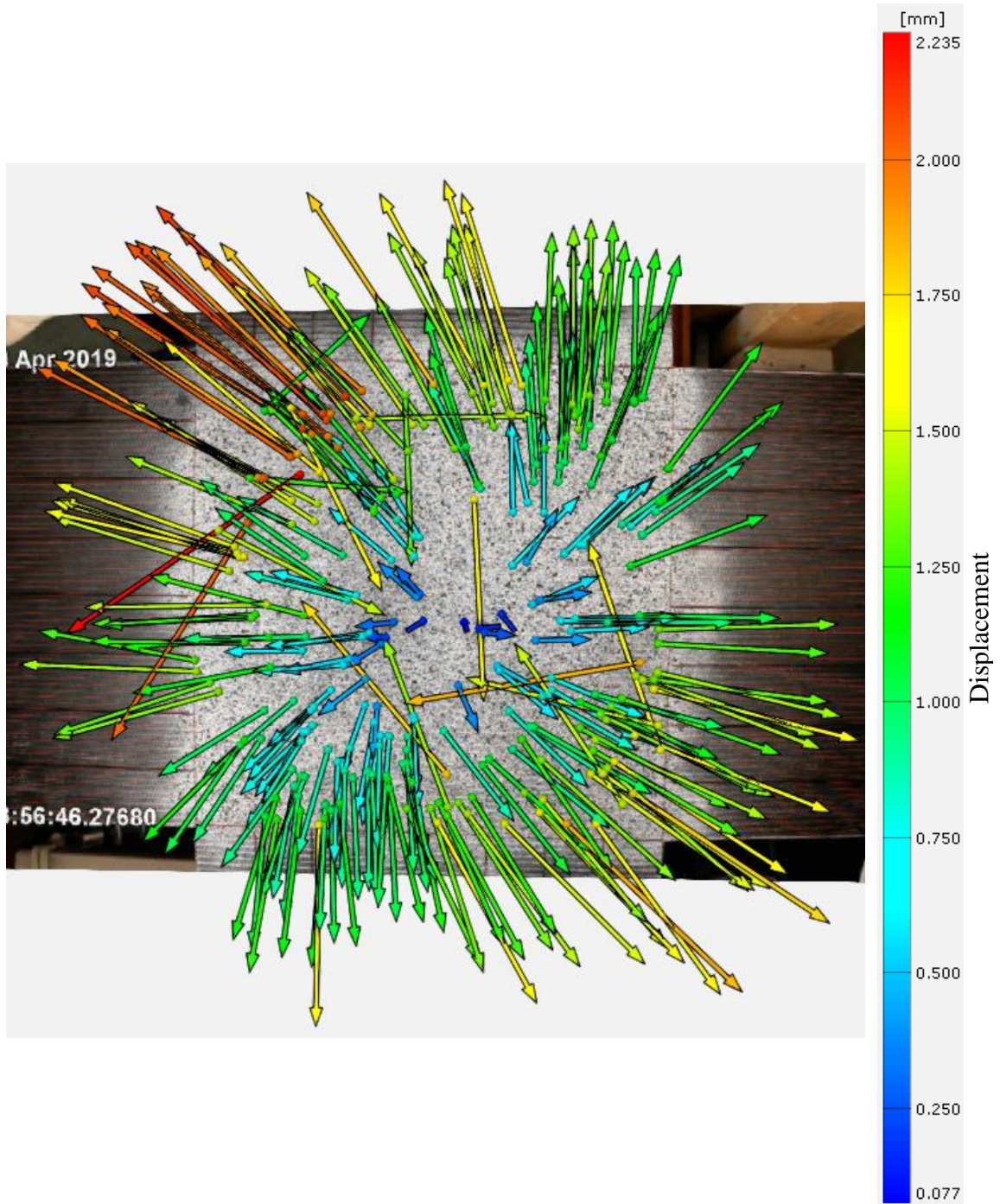


Figure 87: Vector analysis for non-bias Mode 1 geotextile test, stage 28, showing slight rotation. Scale is approximate (units of mm).

### Summary and Conclusions

Full-field DIC strain data was used to validate multiple assumptions for both this thesis and the previous work by Haselton (2018). DIC and LVDT strain equivalence was demonstrated by a dual-instrumented test, which confirms that the dataset from this thesis can be combined with that of Haselton (2018). Strain uniformity analyses showed best results for the interior of the cruciform samples corresponding to the range used by Haselton (2018), which validates his strain data as obtained from the best representative portion of the sample. Statistical strain uniformity evaluations showed overall good results. The strain uniformity COV appeared to be dependent on the strain level relative to the initial un-displaced reference image more so than on the small magnitude of strains present at the start of every load step, which it was clearly capable of measuring. High noise appeared for strains less than 1-2% relative to the reference image. Based on the apparent minimum noise asymptote, nearly all tests showed satisfactory statistical uniformity of 3-5% COV for the innermost region of the cruciform samples. The one non-bias geotextile test with poorer uniformity (10% COV) is probably an outlier since it never reached significantly high strain values. Although statistical uniformity for the non-bias geogrids appears to be satisfactory, fluctuations in the strain heatmaps suggest that even with good control of test boundary conditions, the geogrid materials may not be as uniform as was hoped. Regional influences appeared more strongly in heatmaps for the bias tests as opposed to the non-bias tests, which supports the decision to use DIC for this research. Shear strain in the loading directions was shown to be minimal for properly aligned samples of both geotextiles and geogrids. This validates the derivations used for

the shear modulus in this thesis and for the other elastic constants in Haselton's (2018) thesis, as well as proves the suitability of the biaxial device for creating reasonably pure biaxial tension in cruciform samples. However, the alignment method was optimized partway through testing, and the assumption of zero shear strain in the loading directions was observed to be less accurate for the early tests. In conclusion, the DIC data capture method, biaxial test method, and biaxial device were all shown to be adequate for tests on geosynthetics, and the innermost region of the sample AOI was shown to produce ideal strain conditions for determination of elastic constants.

## CHAPTER SIX

## SHEAR MODULUS RESULTS

Overview

The primary goal of this research was to determine the shear modulus for a set of eight common geosynthetics, thereby completing the work begun by Haselton (2018) to obtain the full set of elastic constants for these materials. As a preliminary means to help assess bias biaxial test quality, plots of load per unit width (line load) versus strain in the loading directions were evaluated for each test. Next, shear stress and shear strain were calculated from line load and DIC strain data. Shear stress-strain plots for each test were then evaluated for a consistent data range from which to calculate the shear modulus. This range was then used to calculate the shear modulus from the innermost strain data region for all load steps of all materials. Shear modulus values are compared for all load steps within each material, and the best average shear moduli are compared between materials. Last, sources of error are discussed.

Shear Modulus Determination

Since Haselton's (2018) work showed that this biaxial device and test procedure were not capable of meeting precision levels specified by ASTM D7556, a minimum of two trials for each material were tested to demonstrate repeatability and accomplish testing within a reasonable timeframe. Data quality was evaluated for all tests individually to determine whether additional trials were necessary. Quality was

determined from several measures: 1) satisfactory image tracking in the DIC software as discussed in Chapter Four, 2) plots of load per unit width vs. strain in the loading directions ( $\epsilon_x$  and  $\epsilon_y$ ), 3) individual shear stress-strain plots for all concentric regions, and 4) superimposed re-zeroed shear stress-strain plots for all load steps of each material. The shear modulus was determined using a best-fit linear trendline for the shear stress-strain plots of the innermost strain regions, since the strain uniformity analysis showed this region to be the most uniform. Shear stress was calculated from the best average shear modulus and measured shear strain, and this data was compared to the measured shear stress to evaluate the appropriateness of the shear modulus value. For this research, the warp-weft angle used in the derivations by Gao et al. (2018), Chen et al. (2018), and Shi et al. (2018) was not calculated.

#### Load per Unit Width versus Strain

Figure 88 through Figure 90 show typical plots of load per unit width (line load) versus strain in the loading directions for bias biaxial tests. In these plots, the X and Y directions correspond to the X and Y loading axes, which were at 45 degrees to the material principal axes. Black dashed lines indicate preload levels for each load step. Strain data (video) was collected only during loading portions of the test, with no data during the 20-minute stress relaxation/creep period. Creep and stress relaxation were significant in all tests based on the difference in line load and strain coordinates from the end of one load step to the beginning of the next.

As seen in Figure 88 and Figure 90, some tests showed an initial flatline or very low slope before picking up load. This behavior was attributed to the low strain rate

during motor spool-up at the very start of each load step, as this would tend to cause unexpectedly higher strain at very low loads due to the viscous nature of the geosynthetics. At maximum motor speed, the strain rate in the loading directions was approximately 5%, based on Haselton's (2018) analysis and the use of the same test procedures for this research. The sensitivity of the load cells versus the DIC instrumentation is possibly an additional factor for the presence of flatline. No consistent pattern was observed for the occurrence of the flatline, with some tests of all material architectures showing it and others not; this may be due to the approximate manual trimming method for the DIC video data (by audible click). (For the shear stress-strain plots discussed later, the data for each load step was re-zeroed based on the point after which the shear stress values consistently increased. This level of precision is not present in the line load versus strain plots, which use the full dataset produced using approximate audible/manual video trimming.)

After the initial flatline, Figure 88 shows concave load step trends, which eventually turn linear in the last load step. The concavity observed in Figure 88 was typical for the rectangular geogrids; the square geogrids had more linear responses as shown in Figure 89. The best geotextile test (Figure 90) showed a generally linear response with consistent slopes between load steps, but several of the other geotextile tests showed successively steeper slopes for each load step, most likely due to shear lock-up as discussed later in this chapter.

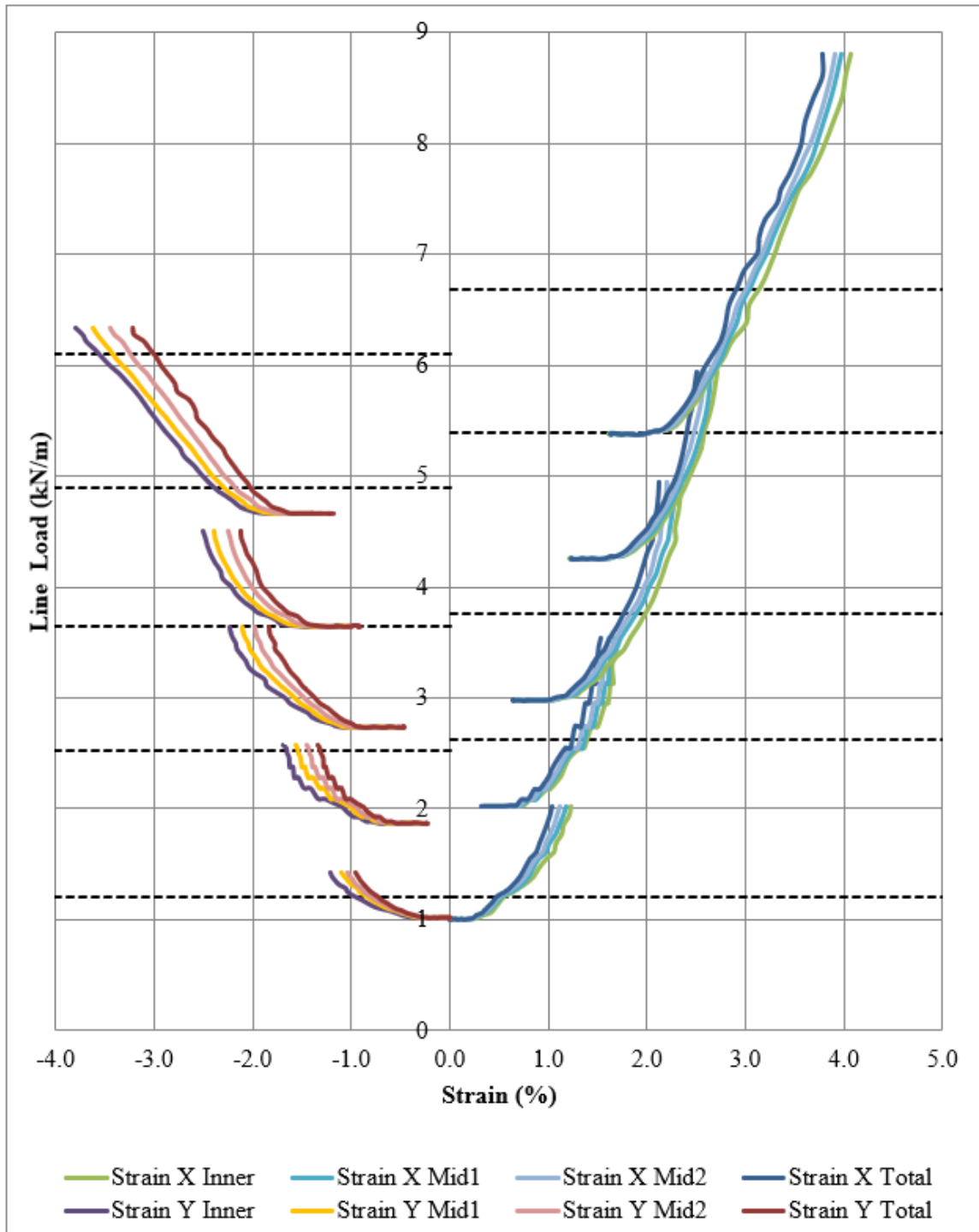


Figure 88: Line load vs. strain in the loading directions ( $\epsilon_x$  and  $\epsilon_y$ ) (GgF bias trial 1).

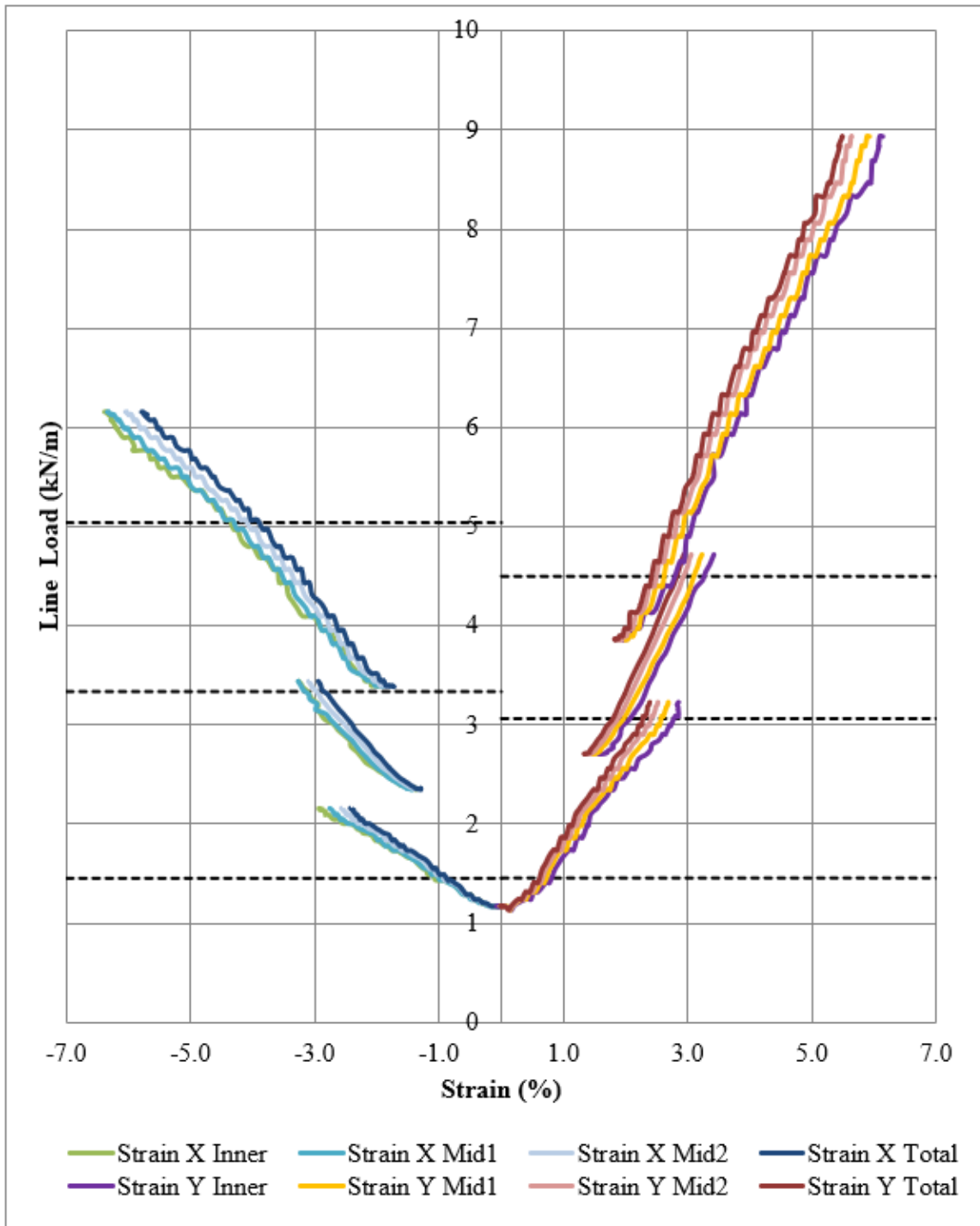


Figure 89: Line load vs. strain in the loading directions ( $\epsilon_x$  and  $\epsilon_y$ ) (GgE bias trial 6, Mode 3).

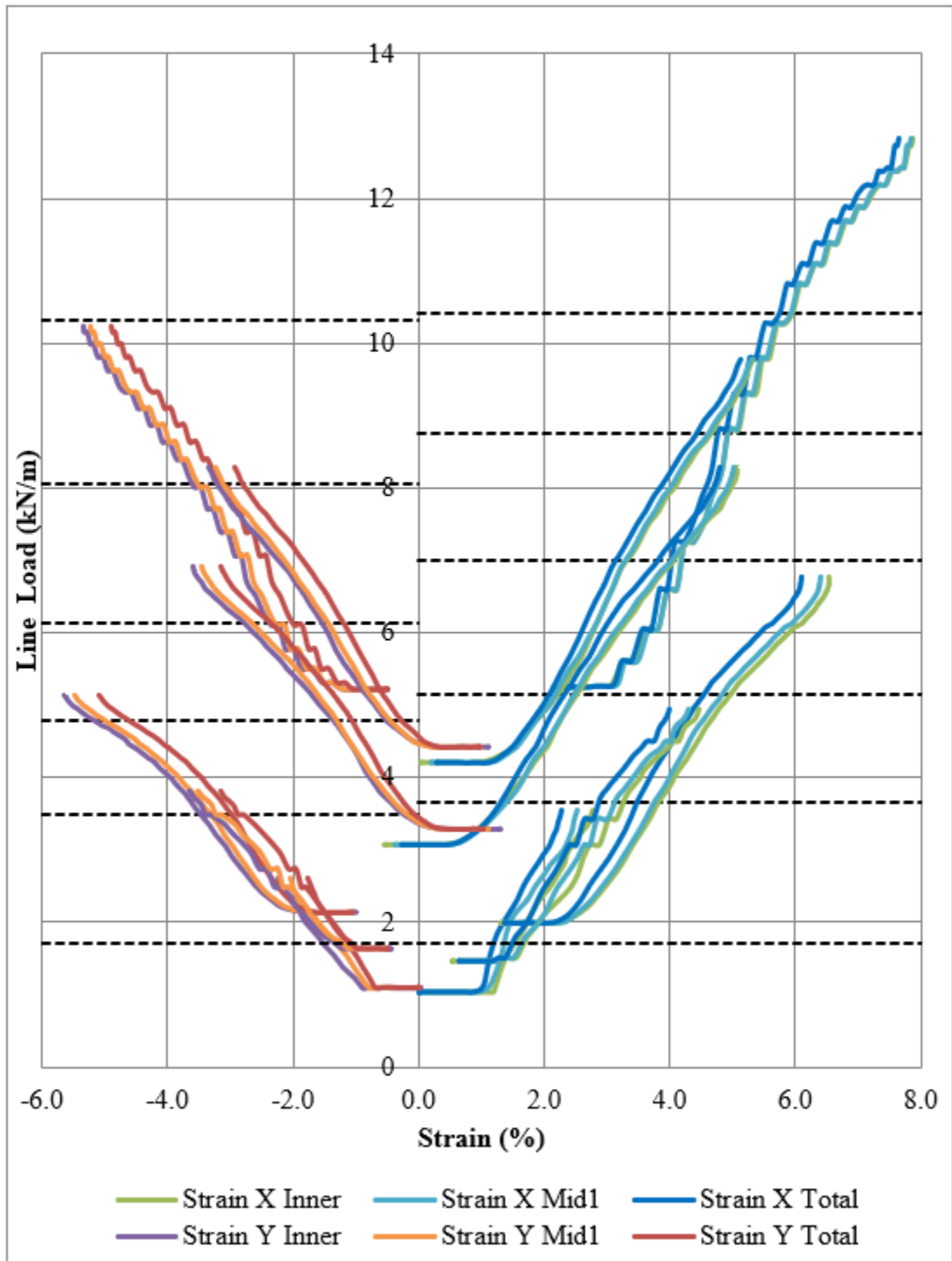


Figure 90: Line load vs. strain in the loading directions ( $\epsilon_x$  and  $\epsilon_y$ ) (GtB bias trial 4).

### Shear Stress-Strain Plots

Shear strain was calculated from the average strains in the loading directions using Equation (14), and shear stresses were calculated from the load data record in each of the loading directions using Equation (15). These equations were derived in Chapter Three and are shown again below.

$$\gamma_{12} = (\varepsilon_x - \varepsilon_y) \quad (14)$$

$$\tau_{12} = \frac{\sigma_x - \sigma_y}{2} \quad (15)$$

Shear stress-strain plots were created for all load step data referenced to the initial non-displaced state as well as for re-zeroed load step data. All re-zeroed load steps for the innermost strain region were then superimposed on the same shear stress-strain plot for 1) each test, and 2) each material to determine the most consistent linear data range from which to determine the shear modulus. This chapter includes shear stress-strain plots for the tests with the approximate best and worst scatter for each material architecture, and the full plot set for all materials is included in Appendix B.

Figure 91 presents example shear stress-strain plots for the square geogrids, with Figure 91 top showing one of the least smooth datasets and Figure 91 bottom showing one of the best datasets (smooth trend and consistent slopes). The roughness in Figure 91 top is the result of the biaxial device motor stalling, followed by manual restarts. The stalling appeared to be a maintenance issue since it would also occur under no load whatsoever, and the problem was eventually solved by a combination of adding oil to the gear reducer case, removing a vent plug that should have been removed at installation,

and running the biaxial device up and down at no load to warm it up before each test. As seen by comparing these best and worst datasets, the square geogrids produced generally consistent data between specimens. A slight difference in shear modulus (slope) was typical between the load steps for each trial, with small stiffness gains (steeper slopes) apparent in subsequent load steps. As seen in Figure 91, this divergence was most pronounced after 2-3% shear strain, and modulus (slope) values appeared overall consistent within each test for shear strains below this level. A few load steps particularly from Geogrid E bias trial 4 (Figure 92) showed a very low modulus at low shear strain, abruptly followed by the typical material modulus slope for the rest of the load step. This is suspected to be an artifact linked to the sensitivity of the load cell at very low loads, motor spool-up, and/or DIC noise, since it occurred in only a few load steps for all materials tested. The square geogrids only have three load steps per trial since they were the first materials tested; the number of load steps was subsequently increased from three up to six for the other materials.

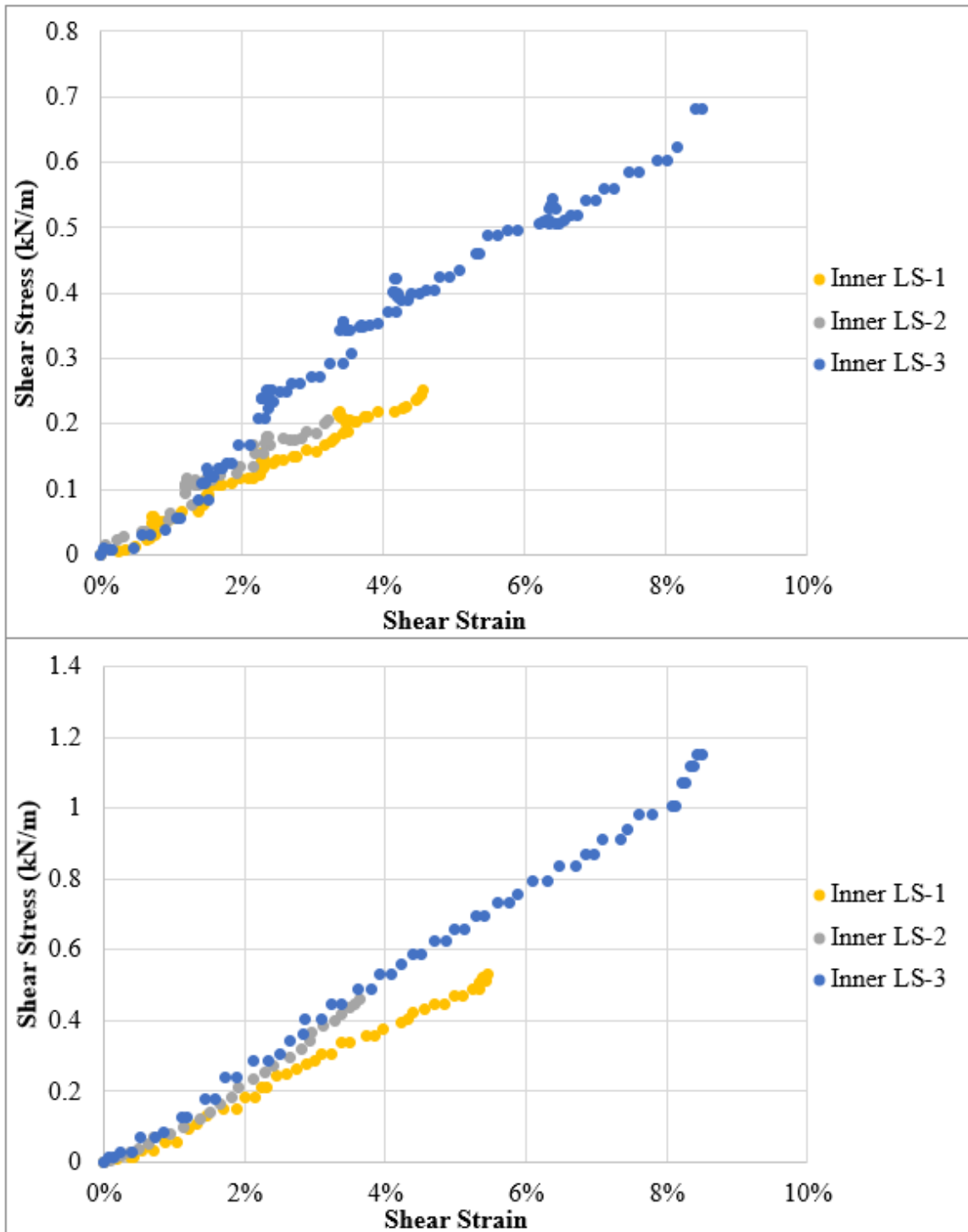


Figure 91: Example square geogrid shear stress-strain plots. Top: GgC bias trial 2.  
Bottom: GgE bias trial 6.

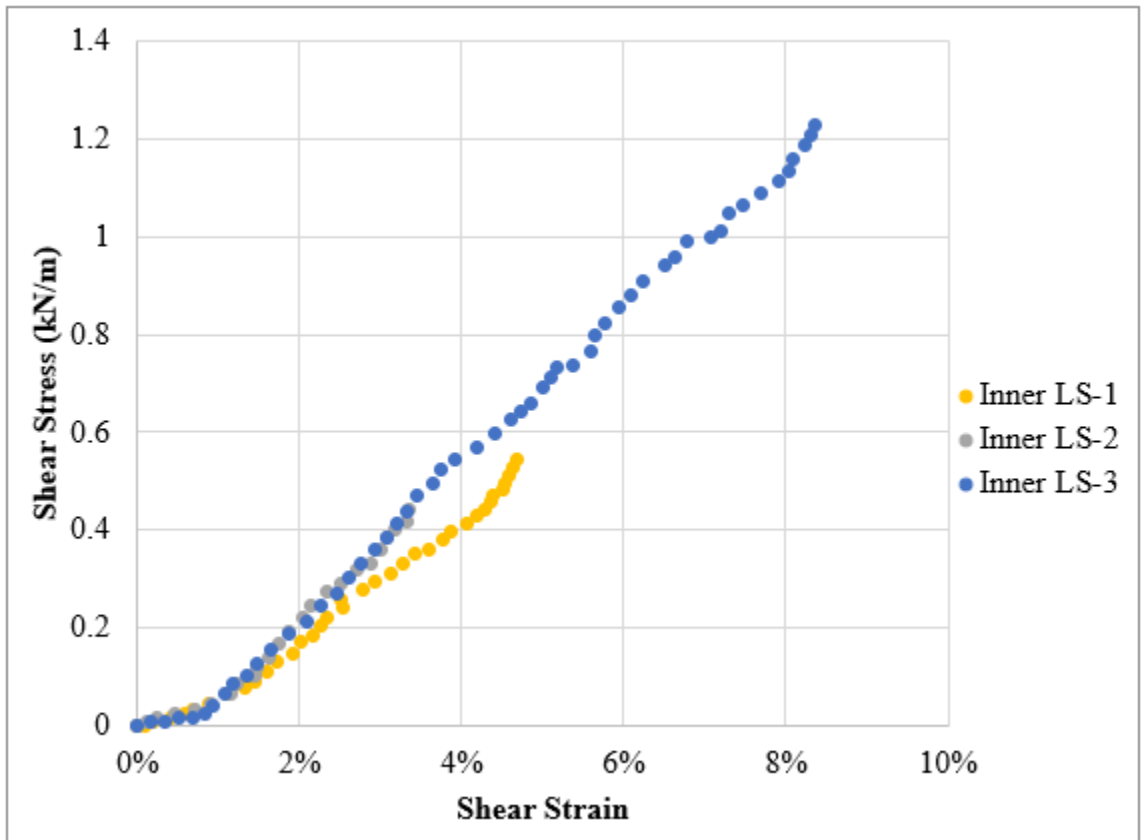


Figure 92: Shear stress-strain plot for GgE bias trial 4 showing initial low modulus slope.

Figure 93 presents example shear stress-strain plots for the rectangular geogrids, where Figure 93 top shows the least typical dataset for these materials and Figure 93 bottom shows the most typical dataset. Figure 93 bottom has a concave shear stress-strain curve which was typical of nearly all load steps for the rectangular geogrids. The primary exception was Geogrid A bias trial 1 (Figure 93 top), which had very linear trends. Geogrid A bias trial 1 (Figure 93 top) may be influenced by the many stall restarts that happened during this test, which would tend to lower the overall strain rate due to frequent periods of motor spool-up. The second trial for Geogrid A was much more similar to the trials from the other rectangular geogrids, including the concaved

form. Concaved shear stress-strain trends were most pronounced for Geogrid B (Figure 93 bottom). The curvature seen in the rectangular geogrids appears to be unrelated to the abrupt modulus change discussed in the square geogrids, since in this case the modulus change is gradual and occurs well beyond 1.0% shear strain. This gradual change suggests a strain stiffening response. A comparison of the Y-axes on Figure 93 bottom and Figure 91 or Figure 92 shows that the square geogrids consistently reached about 5.0% shear strain, whereas most load steps for the rectangular geogrids ended near 2.5% shear strain. This shortened strain range also seems to align with a strain stiffening behavior.

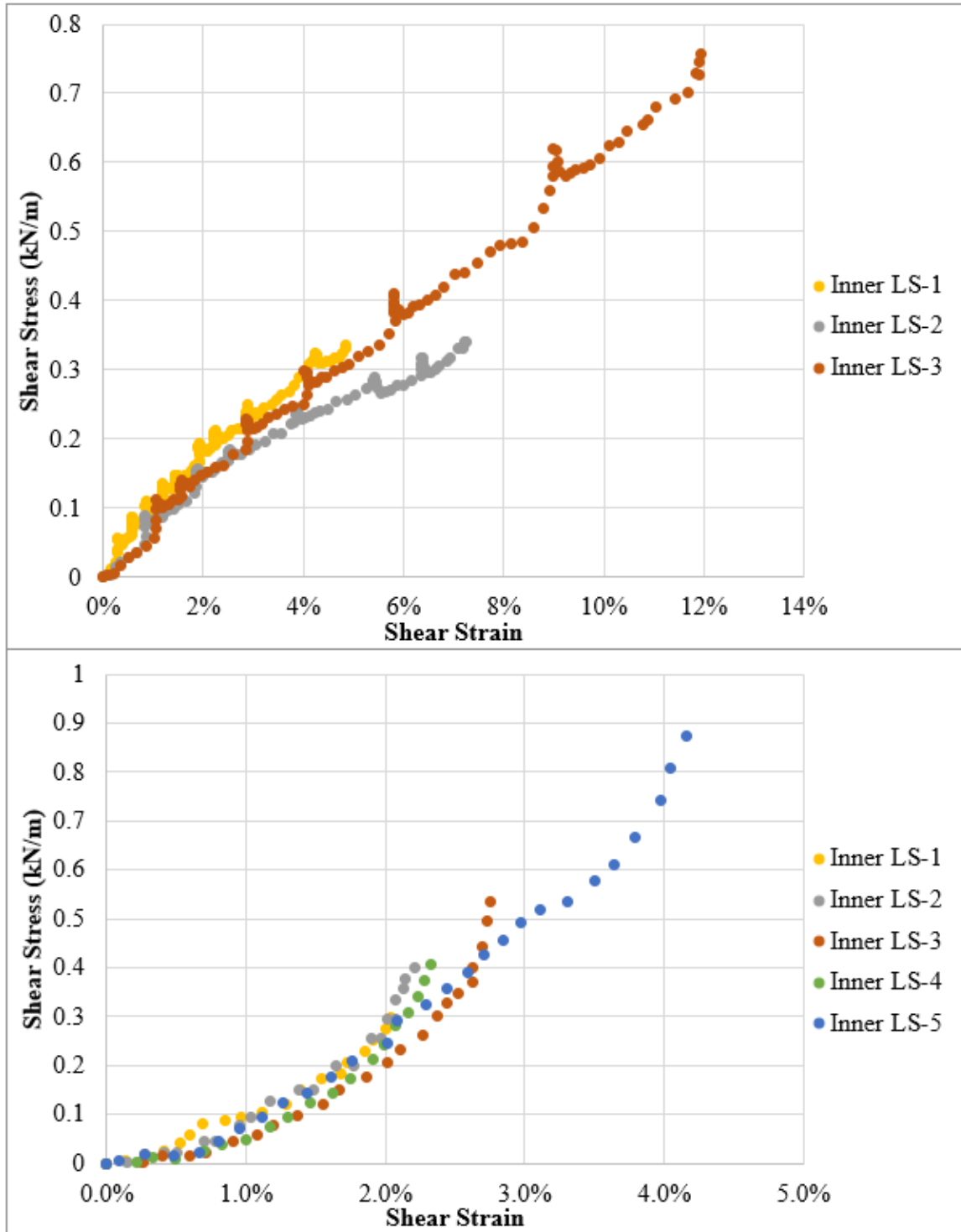


Figure 93: Example rectangular geogrid shear stress-strain plots. Top: GgA bias trial 1. Bottom: GgF bias trial 1.

Figure 94 presents example shear stress-strain plots for the geotextiles. As seen in Figure 94 top, the shear modulus slopes of some of the geotextile tests had notably more spread than those of the geogrids. The higher modulus curves were consistently from later load steps, which suggests that these materials may have reached shear lock-up and/or that the shear strength is dependent on the biaxial pretension level, such as Colman et al. (2014) observed in bias picture frame tests on architectural membranes. However, Geotextile B bias trial 4 (Figure 94 bottom) shows consistent shear-stress strain curves for five full load steps, which suggests that shear lock-up is the cause of the increased shear stiffness in load steps from other trials as opposed to biaxial tension levels. Shear lock-up may have occurred in other load steps because the manually tensioned axis was load-controlled rather than displacement-controlled: If the manually loaded axis reached the next load limit before reaching a displacement equal to the machine loaded axis, the following load step would have started from a partially sheared state, risking lock-up. Partial shear remaining in the sample would likely tend to compound, with lock-up risk increasing with the number of load steps. It should be noted that Geotextile B bias trial 4 (Figure 94 bottom) was load-controlled like all the other tests, but then additionally displacement-controlled based on approximate visual measures, which further supports the hypothesis for shear lock-up in the other tests.

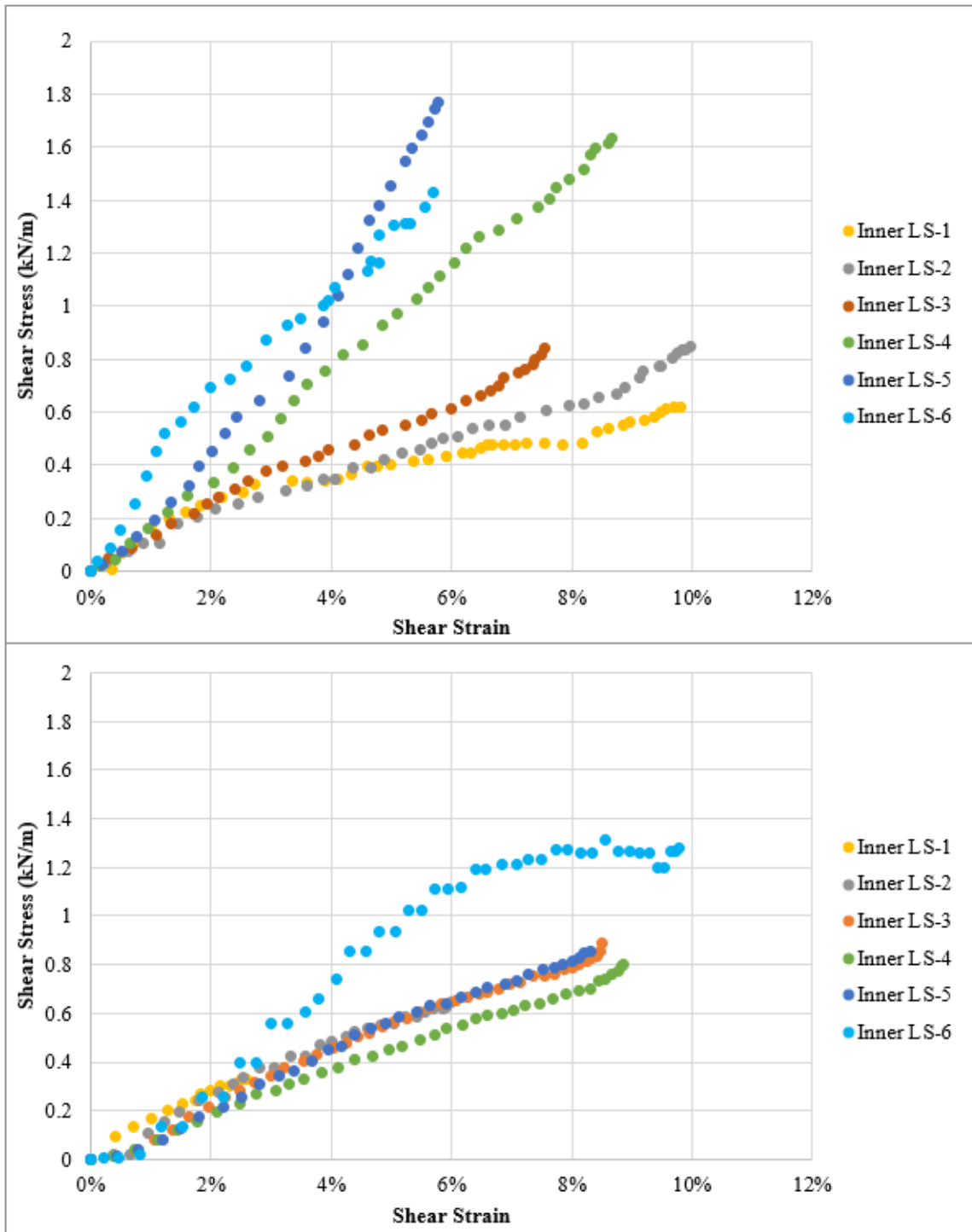


Figure 94: Example geotextile shear stress-strain plots. Top: GtB bias trial 2. Bottom: GtB bias trial 4.

As a secondary check to assess overall trends, the entire set of re-zeroed shear stress-strain data from all regions was plotted for each material. Based on a visual comparison of these plots (including Figure 91 through Figure 94, above), a shear strain range of 1.0% to about 5.0% appeared to be the most consistently linear across all tests. Non-linear shear stress-strain behavior appeared for several materials in the 0.0-1.0% shear strain range, which is why the range start was truncated at 1.0%. This nonlinearity may be a result of the high DIC noise at low strains as discussed in Chapter Five, or a result of motor spool-up, or a combination of both. For the rectangular geogrids, a simplifying assumption was made to treat their shear moduli as linear within the same strain range as used for the square geogrid shear moduli. Further analyses for all tests were performed strictly on data from the innermost strain region.

#### Shear Modulus Curve-Fit Ranges

Within the overall best linear shear strain range, the shear modulus for each load step was determined by the slope of a linear trendline. Multiple shear strain ranges of 1.0-2.0%, 1.0-2.5%, and 1.0-5.0% in each material were compared for confidence. An example curve-fit plot from Geogrid C is shown in Figure 95, and the full plot set for all materials is provided in Appendix C. Figure 96 through Figure 98 provide summary plots of modulus versus the trendline  $R^2$  value for all data. As seen here, most of the  $R^2$  values were 0.90 or higher, with many up near 1.00 regardless of which strain range was used. Lower  $R^2$  values often appeared in load steps with rough curves due to stall restarts, and visual inspection confirmed that overall, the trendlines for these were reasonable even if the  $R^2$  values were low. Particularly in the rectangular geogrids

(Figure 97), some load steps did not reach strain values higher than 2.0% or 2.5%, and these appear as the same data point for all three strain ranges.

Modulus values for each load step are provided in Table 12. Numbers shown in **red font** appear to be outliers based primarily on the shear modulus value—in particular, note the absurdly high shear modulus of 60 kN/m appearing in Geogrid B. The 20-30 kN/m values are much more reasonable for Geogrid B, and these numbers also agree well with the tighter grouping of modulus values observed in Geogrid F, which was expected to be closely similar to Geogrid B based on manufacturers' data. For the geotextiles, outliers were identified based on load steps that appeared to exhibit lock-up in the full data range. For most of the materials, the strain range selection did not appear to be particularly critical, especially in comparison to the effect of outliers. Geogrid F showed the greatest dependency on strain range, with shear modulus values ranging 21 to 25 kN/m.

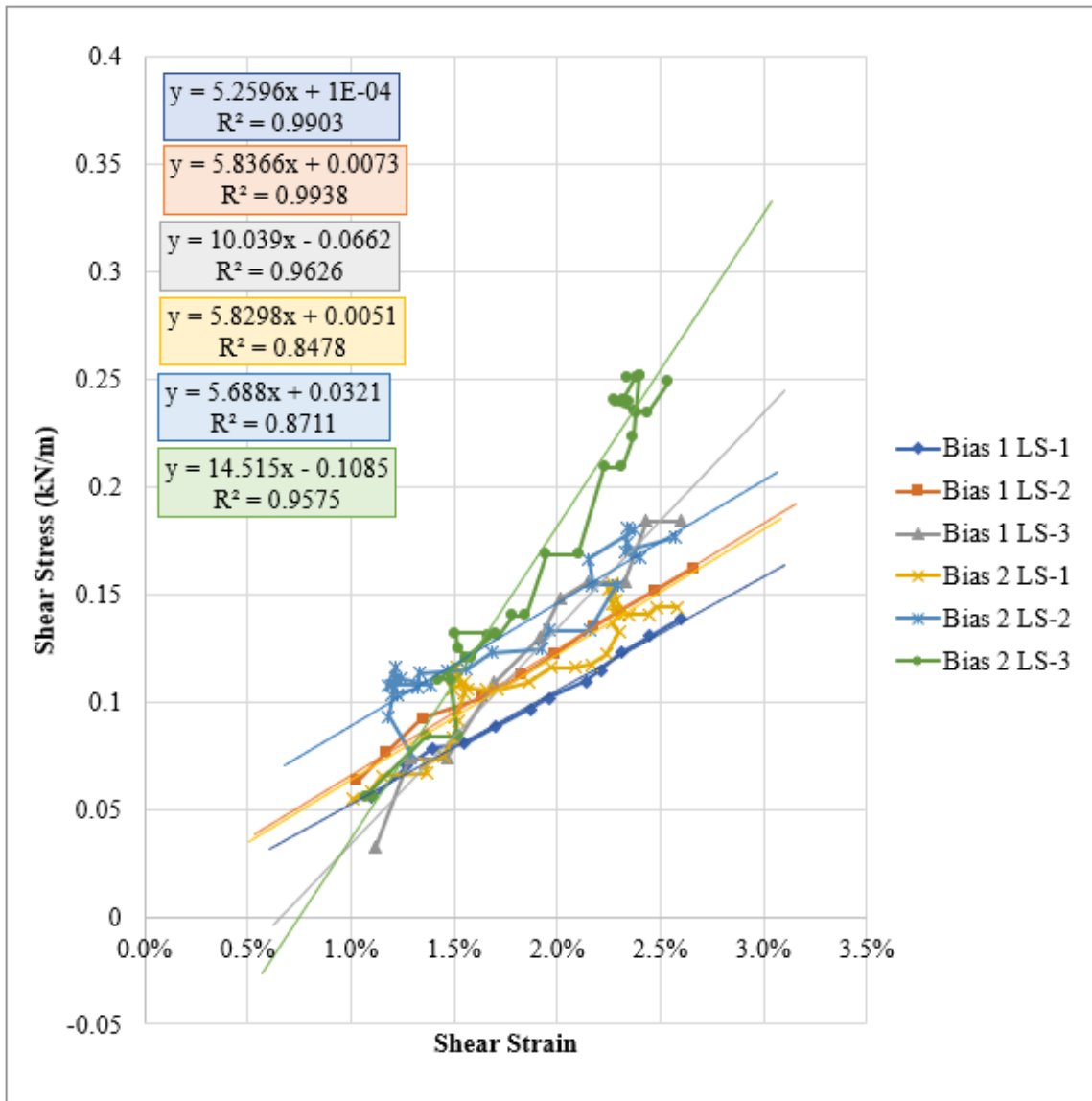


Figure 95: Shear modulus trendline fit for GgC: shear strain range 1.0-2.5%.



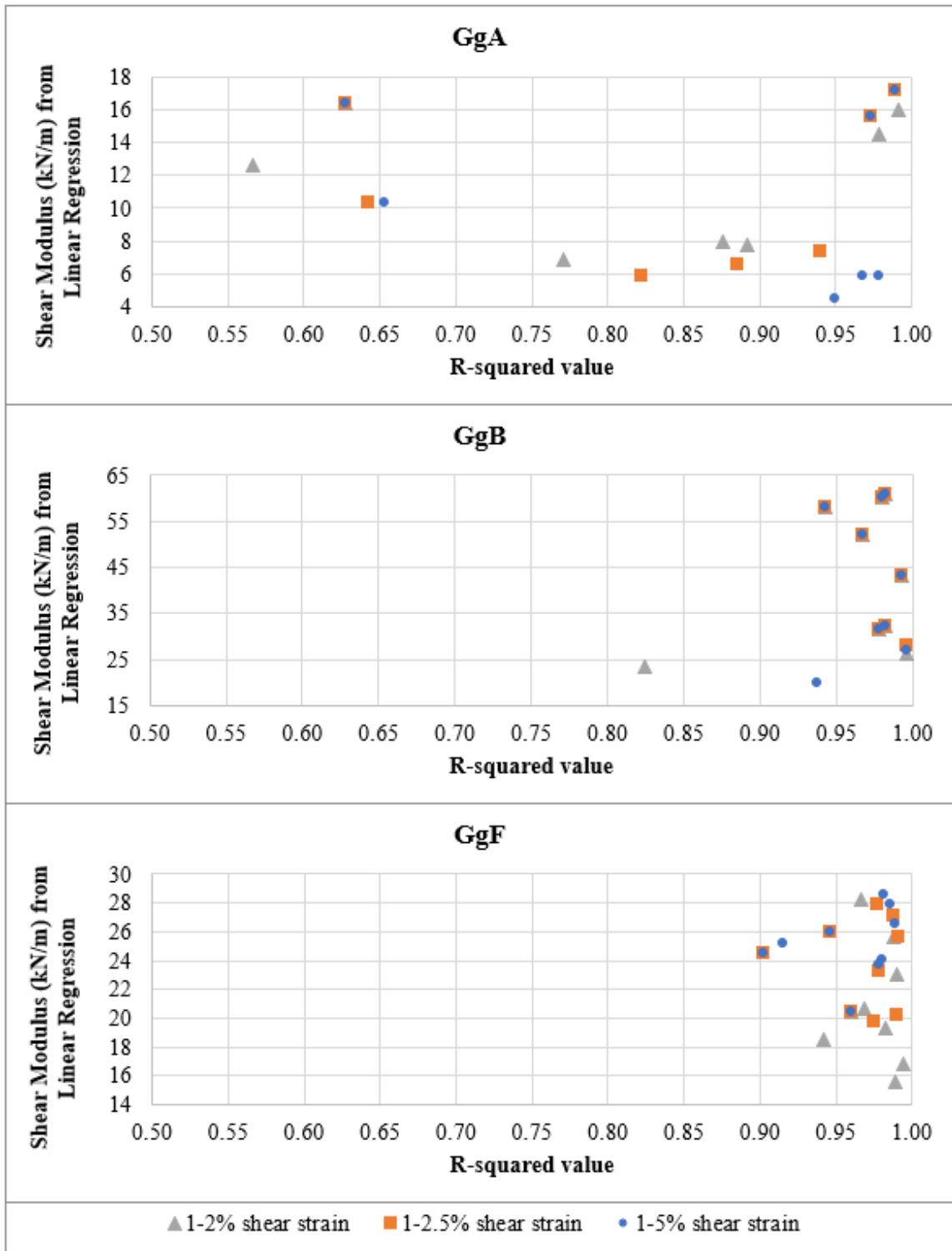


Figure 97: Shear modulus versus trendline R<sup>2</sup> value for rectangular geogrids.

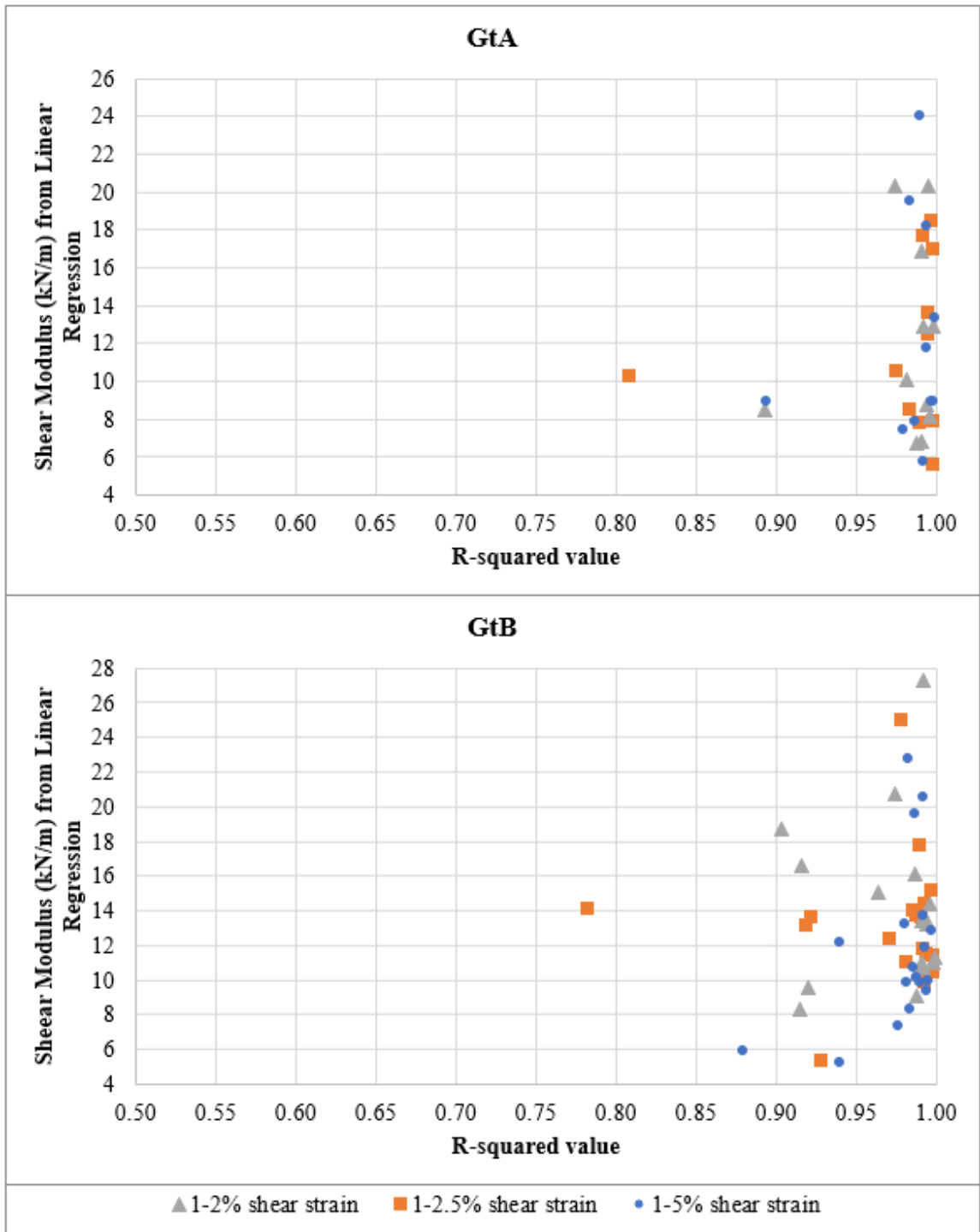


Figure 98: Shear modulus versus trendline  $R^2$  value for geotextiles.

Table 12: Shear modulus values for three strain ranges.

<b>Material:</b>	<b>GgA - rectangular</b>			<b>GgC - square</b>		
Shear strain range (%):	1-2	1-2.5	1-5	1-2	1-2.5	1-5
G average (kN/m):	11.74	11.33	10.83	7.30	7.86	6.66
<b>G avg (kN/m), no outliers:</b>	7.55	6.58	5.42	5.75	5.64	6.66
G (kN/m)	7.7907	7.3501	5.8781	4.8956	5.2596	5.264
	7.9697	6.5566	4.4951	5.851	5.8366	6.5494
	6.9016	5.8408	5.899	11.789	14.515	8.1667
	16.414	16.414	16.414	6.5057	5.8298	5.0835
	14.464	15.627	15.627	11.473	5.688	5.1263
	15.996	17.194	17.194	3.3031	10.039	9.7503
	12.657	10.326	10.326			
<b>Material:</b>	<b>GgB - rectangular</b>			<b>GgD - square</b>		
Shear strain range (%):	1-2	1-2.5	1-5	1-2	1-2.5	1-5
G average (kN/m):	43.09	42.99	42.78	6.56	7.18	7.95
<b>G avg (kN/m), no outliers:</b>	28.36	28.14	27.66	6.56	7.18	7.95
G (kN/m)	58.085	58.085	58.085	6.5788	6.916	6.675
	60.101	60.101	60.101	4.2348	7.5634	7.8919
	52.201	52.201	52.201	9.033	9.4502	9.2064
	26.128	27.93	26.992	7.396	6.6806	7.3616
	31.506	31.506	31.506	5.5744	5.3093	8.6102
	60.844	60.884	60.844			
	32.21	32.21	32.21			
	43.114	43.114	43.114			
23.604	20.899	19.939				
<b>Material:</b>	<b>GgF - rectangular</b>			<b>GgE - square</b>		
Shear strain range (%):	1-2	1-2.5	1-5	1-2	1-2.5	1-5
G average (kN/m):	20.90	23.86	25.21	15.10	13.95	13.24
<b>G avg (kN/m), no outliers:</b>	20.90	23.86	25.21	14.12	13.95	13.24
G (kN/m)	20.41	20.41	20.41	15.801	12.636	9.6667
	18.451	24.502	24.502	11.745	11.238	10.883
	15.516	19.737	25.208	13.027	15.855	14.496
	20.692	25.978	25.978	11.635	13.21	12.846
	16.776	20.163	23.656	17.531	17.274	16.435
	19.249	23.275	24.102	15.024	15.106	16.216
	23.051	27.855	26.591	14.482	12.469	14.407
	28.285	25.649	28.576	14.844	13.644	10.652
	25.685	27.15	27.898	25.937	16.822	15.3
				10.654	11.509	9.8987
				14.191	13.767	14.617
				16.358	13.818	13.479

Table 12 continued: Shear modulus values for three strain ranges.

<b>Material:</b>	<b>GtA</b>			<b>GtB</b>		
Shear strain range (%):	1-2	1-2.5	1-5	1-2	1-2.5	1-5
G average (kN/m):	11.79	12.03	12.26	13.23	13.92	11.85
<b>G avg (kN/m), no outliers:</b>	9.17	8.85	8.52	12.43	11.98	10.51
G (kN/m)	5.5685	6.7608	7.8892	10.454	11.059	9.8361
	7.8402	8.1487	24.028	9.8831	9.0788	20.588
	12.429	12.88	8.9458	13.112	9.5925	7.3204
	16.979	20.309	13.377	13.722	13.246	9.8329
	10.541	10.06	8.9393	24.975	20.783	19.6
	8.5039	8.7838	8.9059	17.744	27.296	13.211
	13.594	12.869	11.746	14.376	16.118	5.2622
	7.8773	6.8189	5.8022	5.3171	8.3218	5.8661
	10.24	8.5296	7.4217	11.771	10.762	8.3476
	18.477	20.326	19.564	11.006	11.051	9.9125
	17.668	16.855	18.202	12.368	15.092	13.663
				13.66	16.593	12.124
				11.517	10.354	10.194
				13.589	13.432	10.731
				15.185	14.365	11.89
				11.406	11.306	9.4185
			13.971	13.464	12.814	
			14.068	18.687	22.778	

Box and whisker plots for each material and strain range are shown in Figure 99 through Figure 101 to help visualize the data spread for both the full dataset and the reduced dataset with apparent outliers removed. These plots show the second through third quartiles of the data as a box, with the first and fourth quartiles marked as “whisker” lines extending from the box. Within the box, the median is shown by a line and the mean by an X. Individual data points that do not fall on quartile marks are shown as circles.

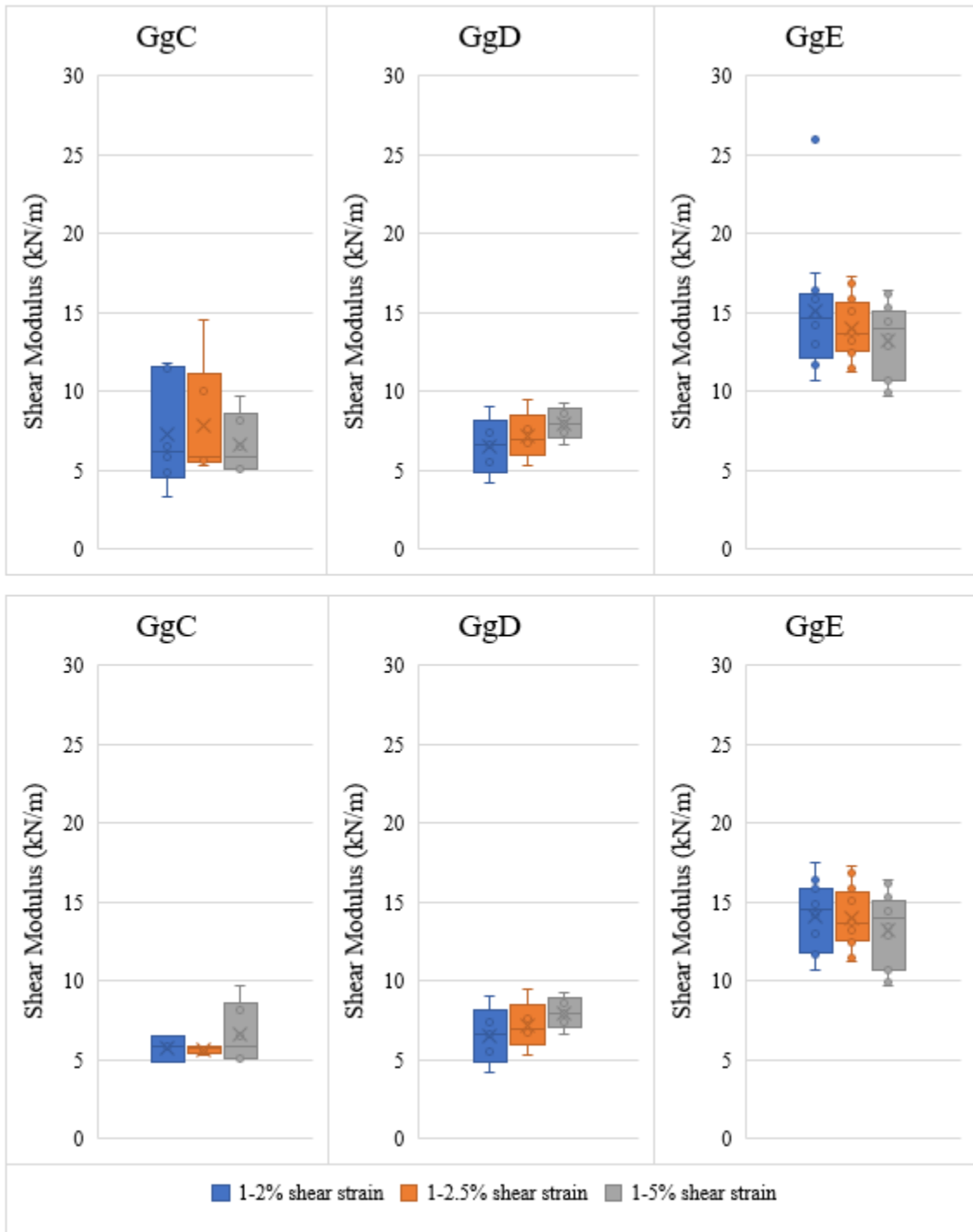


Figure 99: Box and whisker plots for square geogrids. Top: Full dataset. Bottom: Apparent outliers removed (no change to GgD).

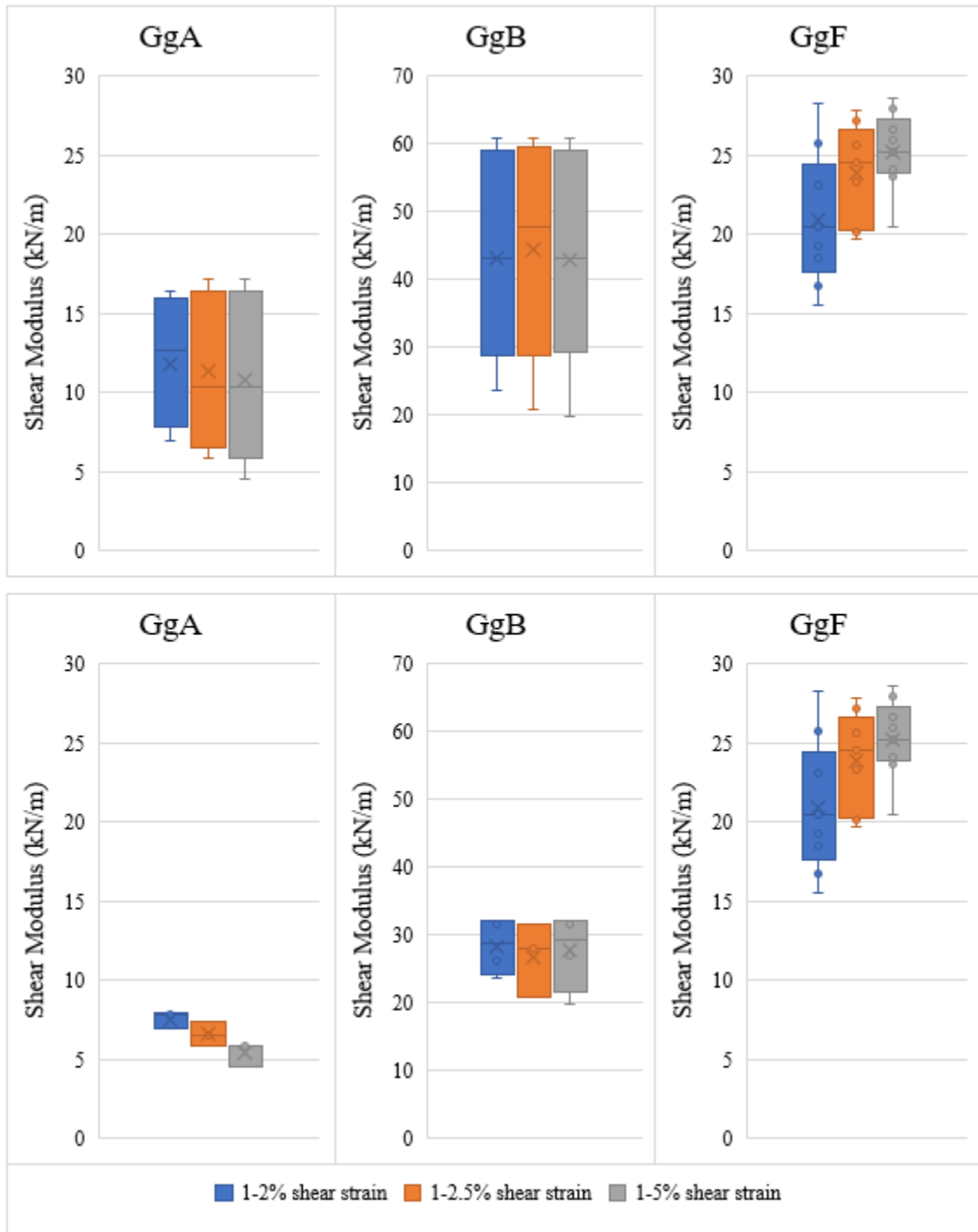


Figure 100: Box and whisker plots for rectangular geogrids. Top: Full dataset. Bottom: Apparent outliers removed (no change to GgF). Note different scale on GgB.

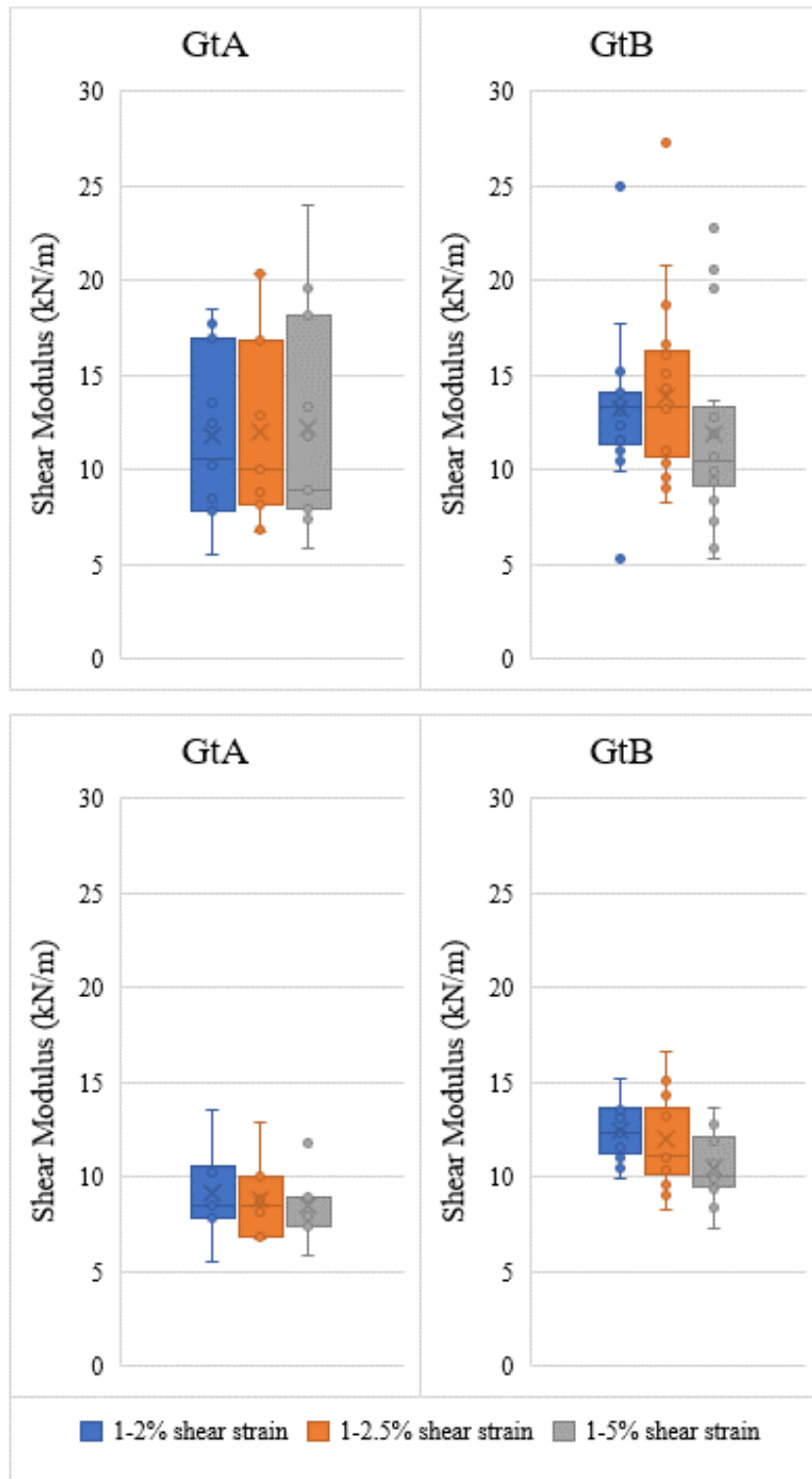


Figure 101: Box and whisker plots for geotextiles. Top: Full dataset. Bottom: Apparent outliers removed.

### Material Comparisons

Shear modulus values from all load steps were compared for the 1%-2.5% strain range for each material. Load step numbers were used instead of percent average ultimate tensile strength (% Avg UTS) values to simplify the plot presentation. Figure 102 shows the modulus summary for square geogrids, Figure 103 shows the modulus summary for rectangular geogrids, and Figure 104 shows the modulus summary for geotextiles. Average shear modulus values across all load steps for each material are shown as lines in the figures. Figure 105 shows the average values (outliers removed) for all the materials and strain ranges together.

The square geogrids (Figure 102) showed some scatter in all the materials, but the average values appear to be reasonable. Geogrid C gave a particularly close grouping except in the last load step for each trial, which produced significantly higher shear modulus values in comparison to the other load steps. With these two values removed, the average shear modulus drops from 7.9 kN/m to 5.6 kN/m. The average shear modulus for Geogrid D was 7.2 kN/m, and the average for Geogrid E was 13.9 kN/m. The square geogrids should become progressively stiffer from Geogrid C to Geogrid E based on manufacturers' data and the research done by Haselton (2018), and the sequence of shear modulus values from small (using the lower average value for Geogrid C) to large makes sense in this regard.

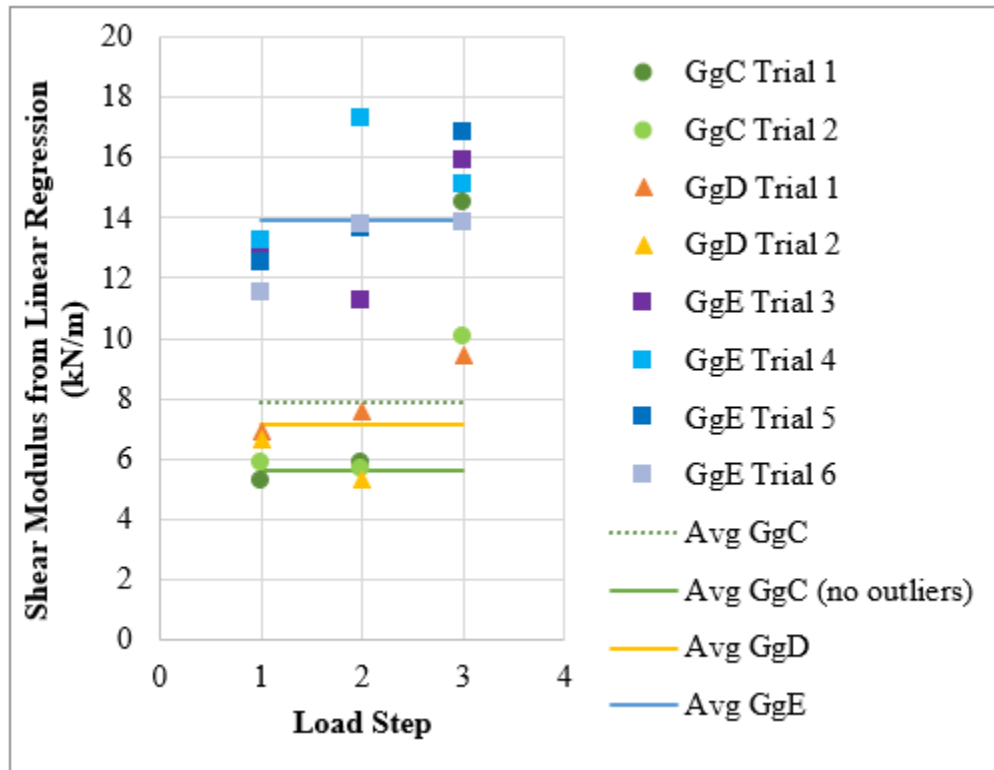


Figure 102: Square geogrid shear modulus summary by load step.

For the rectangular geogrids (Figure 103), the most consistent values came from Geogrid F, with an overall average shear modulus of 23.9 kN/m. Geogrid A was relatively consistent within each trial, but its consistency between two trials was poorer than that of Geogrid F. The last load step for Geogrid A trial 2 dropped much lower than the rest of the load steps for trial 2, suggesting that lower values of about 8-10 kN/m may be most reasonable for this material. The overall average for Geogrid A was 11.3 kN/m, which does not appear to be unreasonable. For Geogrid B, the average shear modulus was very high at 43.0 kN/m, but this dropped to 28.1 kN/m after the outliers higher than 40 kN/m were removed from the dataset. A shear modulus of 28.1 kN/m seems rather high, but then the excellent dataset from Geogrid F produced a similarly high shear

modulus of nearly 24 kN/m. As mentioned earlier, Geogrid B and Geogrid F were expected to be closely similar based on manufacturers' data. Additionally, the material samples for Geogrid B were salvaged from the very end of the geogrid roll, so Geogrid B may show more material variability due to non-ideal samples. Since this dataset would be combined with that of Haselton (2018), it was considered more important to use material from the same geogrid roll he used rather than obtain a new roll and risk variability between batch lots.

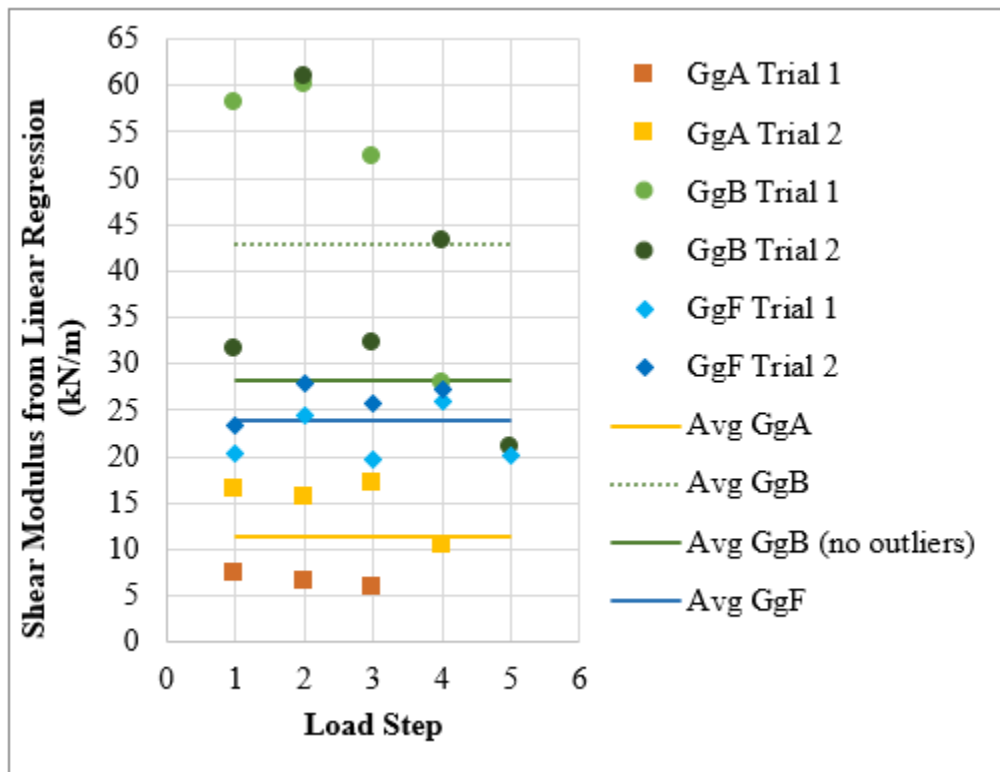


Figure 103: Rectangular geogrid shear modulus summary by load step.

The geotextiles (Figure 104) showed a trend of increasing shear modulus value with the number of load steps. As discussed earlier, this is probably due to shear lock-up occurring in later load steps. Average values from the complete dataset (including load

steps suspected of shear lock-up) are shown in Figure 104 as broken lines, and average values from the reduced dataset (no lock-up) are shown as solid lines. Note that the full dataset for Geotextile A plots on top of the reduced dataset for Geotextile B. For both the complete and the reduced datasets, Geotextile A gave a lower average shear modulus than Geotextile B. The average shear modulus for Geotextile A was 12.0 kN/m for the full dataset, or 8.9 kN/m for the reduced dataset. The average shear modulus for Geotextile B was 13.9 kN/m for the full dataset, or 12.0 kN/m for the reduced dataset.

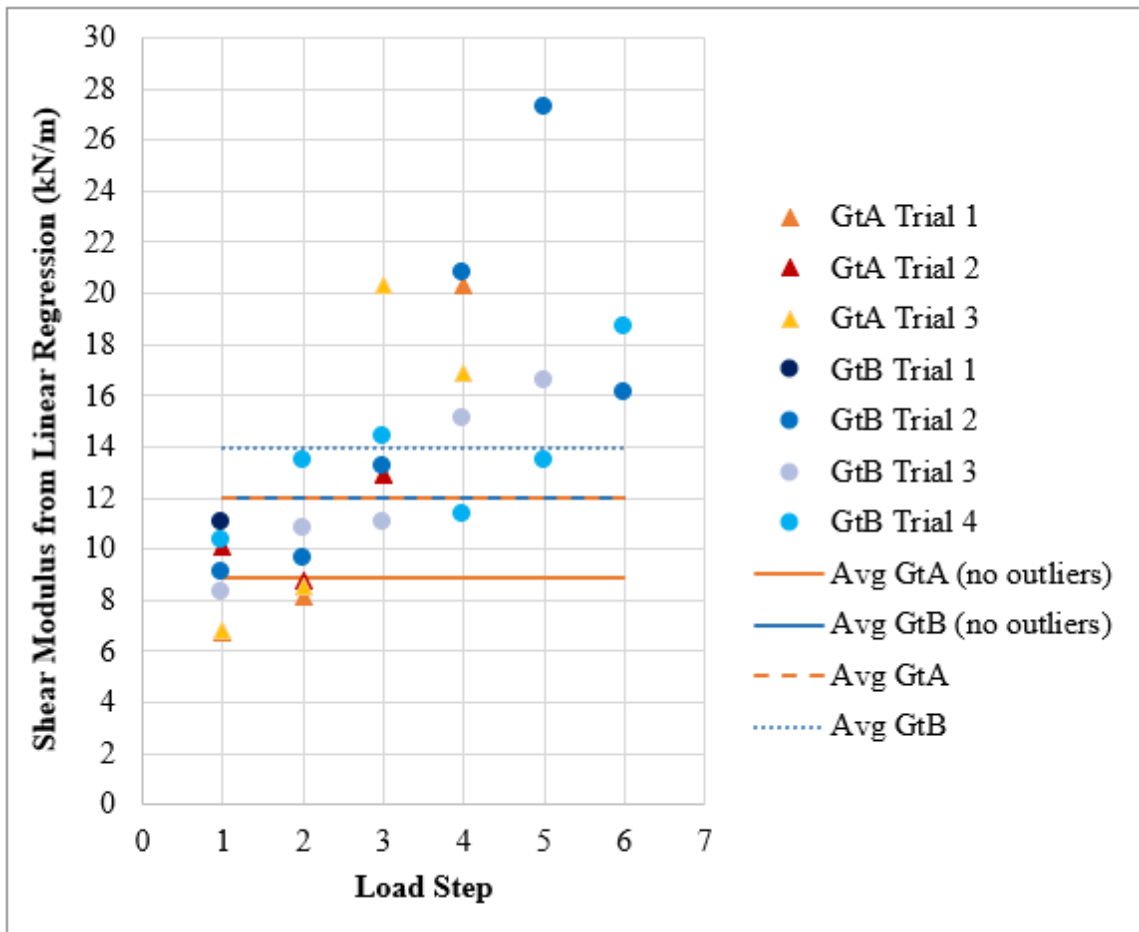


Figure 104: Geotextile shear modulus summary by load step.

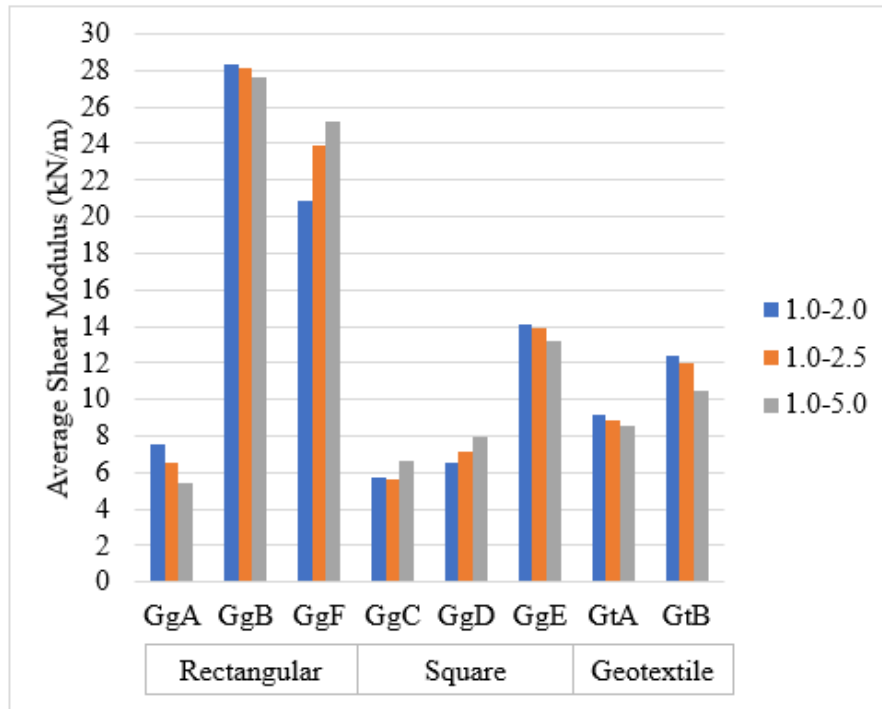


Figure 105: Average shear modulus values for each material by shear strain range (%).

### Comparison of Measured versus Calculated Shear Stresses

To evaluate how well the shear moduli for each material fit the data measured from the bias biaxial tests, the shear stress values were calculated using Equation (19) and compared to the measured shear stress values for a representative test from each material. Equation (19) is obtained from Equations (15) and (16), which were originally derived in Chapter Three and are shown again below.

$$\tau_{12} = \frac{\sigma_x - \sigma_y}{2} \quad (15)$$

$$G = \frac{\sigma_x - \sigma_y}{2(\varepsilon_x - \varepsilon_y)} \quad (16)$$

$$G(\varepsilon_x - \varepsilon_y) = \frac{\sigma_x - \sigma_y}{2} = \tau_{12} \quad (19)$$

Haselton's (2018) work showed a good fit for measured and calculated stress values regardless of using the elastic constants for each load step or a single set of elastic constants taken as the average for all load steps at low strain levels (0.5 - 4%). In light of this, only a single shear modulus value was used for each material in this comparison. Most materials showed good fit using the average shear modulus value suggested from the trendline fit analysis; however, Geogrid B, Geogrid F, and Geogrid E appeared to have a better fit with an adjusted modulus value. These materials are discussed here to justify the refined shear modulus values summarily recommended. See Appendix D for comparative plots for all materials.

For Geogrid B, Figure 106 shows the fit for an average trendline shear modulus of 28 kN/m, and Figure 107 shows the apparent best fit for a shear modulus of 23 kN/m. This reduced value is sensible given the large scatter in the few non-outlier load steps. Moreover, it is now the same as the average trendline shear modulus for Geogrid F, which was expected from the manufacturers' data as mentioned previously.

For Geogrid F, Figure 108 shows the fit for an average trendline shear modulus of 23 kN/m, and Figure 109 shows a possible best fit (for a shear modulus of 16 kN/m). A great fit was impossible regardless of the value selected for the shear modulus, possibly because of the non-linear, concaved shear stress-strain data. As seen in Figure 108, the original 23 kN/m value consistently overpredicts the measured shear stress by about 0.2

kN/m. In Figure 109, reducing the shear modulus to 16 kN/m produced an apparently better fit, but the calculated shear stress first overpredicts, then underpredicts the measured shear stress. Consequently, the 23 kN/m value appears to be the better shear modulus, but a correction factor may need to be applied.

For Geogrid E, Figure 110 shows the fit for an average trendline shear modulus of 14 kN/m, and Figure 111 shows a possible best fit (for a shear modulus of 12 kN/m). This material may be similar to Geogrid F such that the original 14 kN/m value is better but could use a correction factor, or the reduced 12 kN/m value could be better. The data spread does not clearly justify either case. Since the difference is small and the overall magnitude is small in comparison to the elastic moduli, this is not a critical difference.

Table 13 presents the trendline and adjusted fit modulus values as well as the recommended summary values based on the preceding discussion.

Table 13: Shear modulus values for shear stress comparison.

<b>Architecture:</b>	<b>Rectangular Geogrid</b>			<b>Square Geogrid</b>			<b>Geotextiles</b>	
<b>Material:</b>	<b>GgA</b>	<b>GgB</b>	<b>GgF</b>	<b>GgC</b>	<b>GgD</b>	<b>GgE</b>	<b>GtA</b>	<b>GtB</b>
Best Avg Trendline G (kN/m):	7	28	23	6	7	14	9	12
Adjusted Best Fit G (kN/m):	--	23	16	--	--	12	--	--
<b>Recommended G (kN/m):</b>	<b>7</b>	<b>23</b>	<b>23</b>	<b>6</b>	<b>7</b>	<b>12</b>	<b>9</b>	<b>12</b>

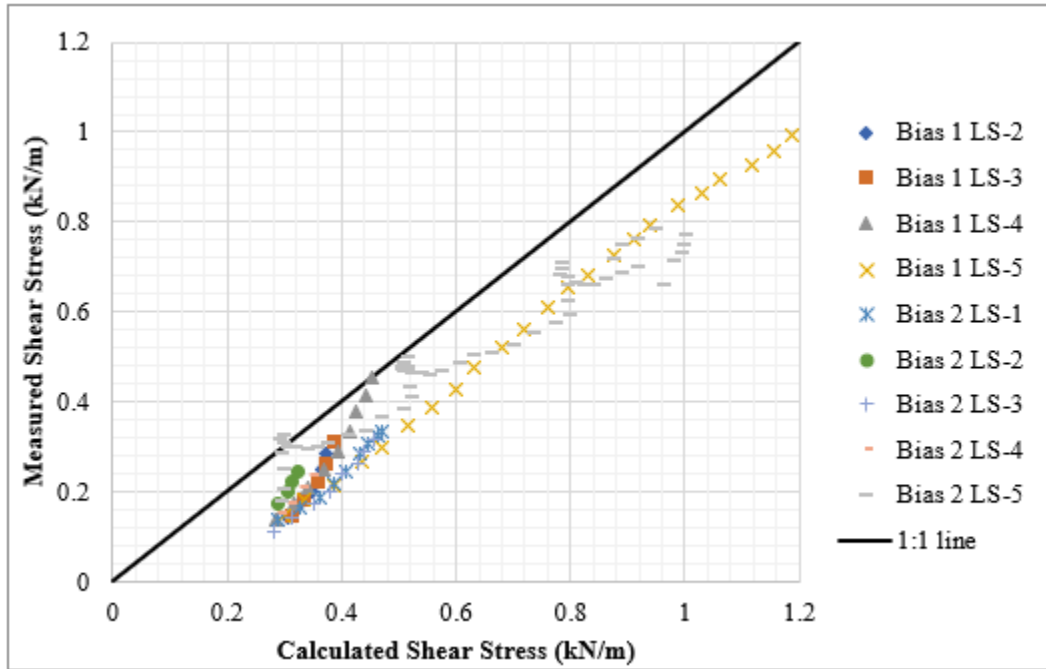


Figure 106: GgB calculated vs. measured shear stress, average trendline G.

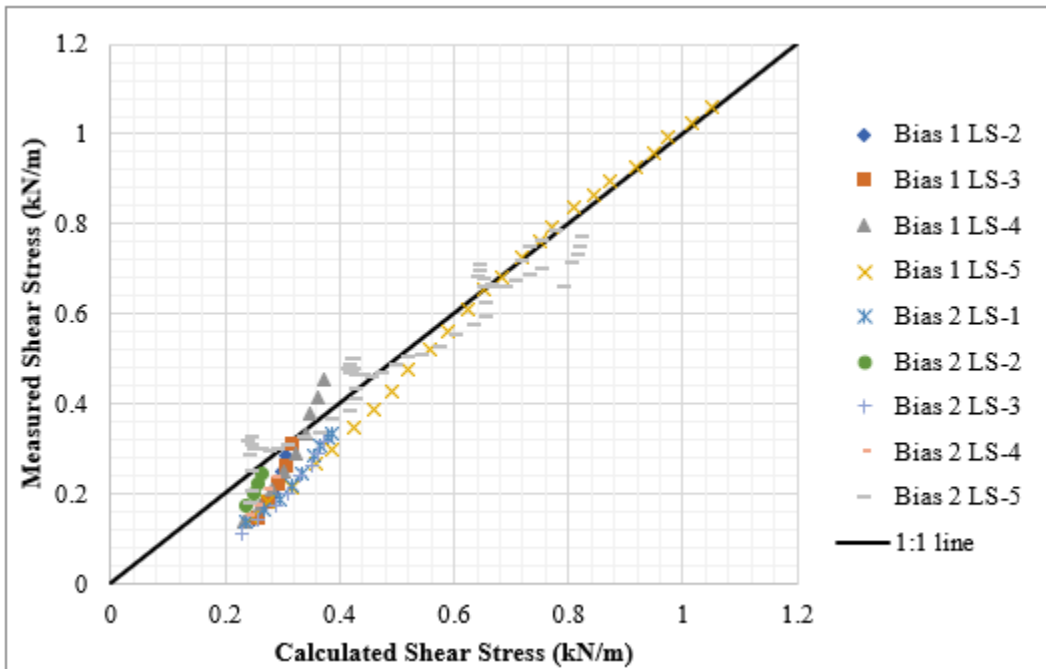


Figure 107: GgB calculated vs. measured shear stress, best fit G.

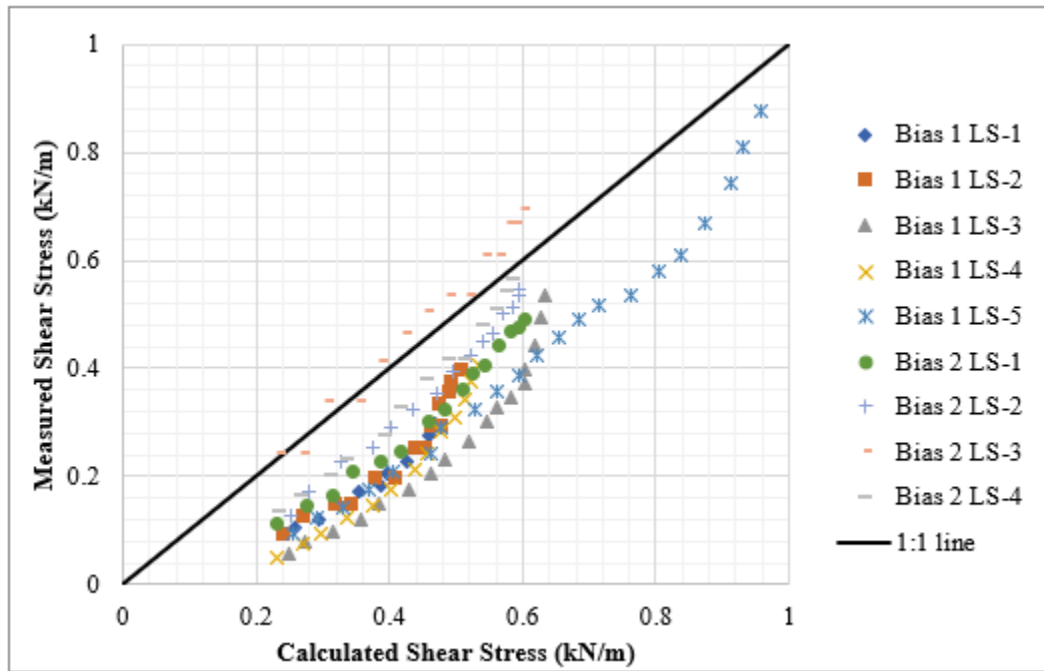


Figure 108: GgF calculated vs. measured shear stress, average trendline G.

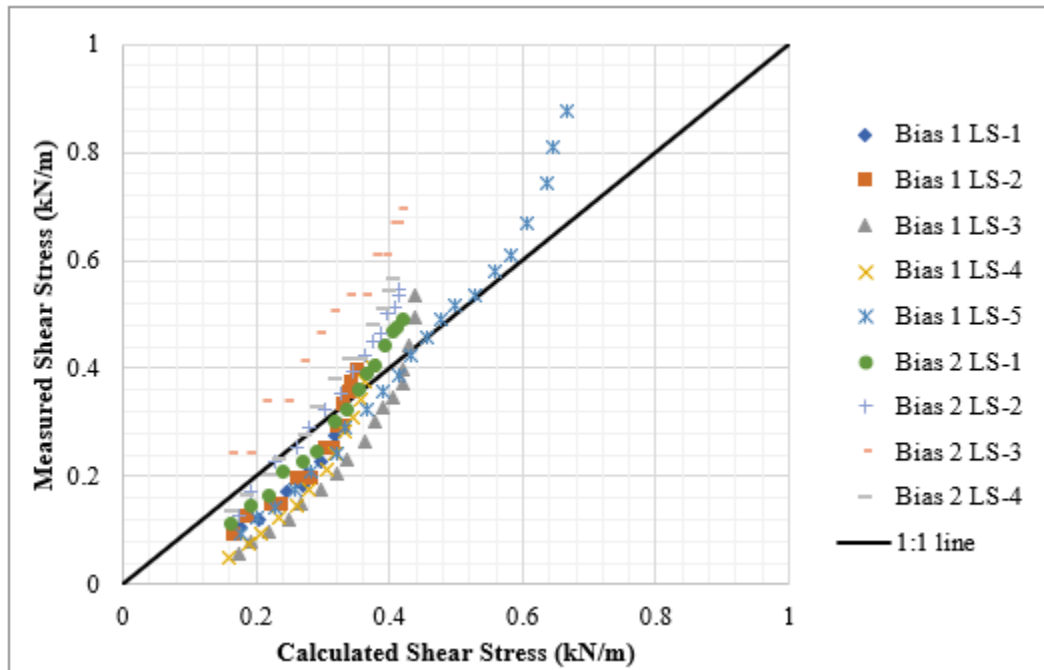


Figure 109: GgF calculated vs. measured shear stress, possible best fit G.

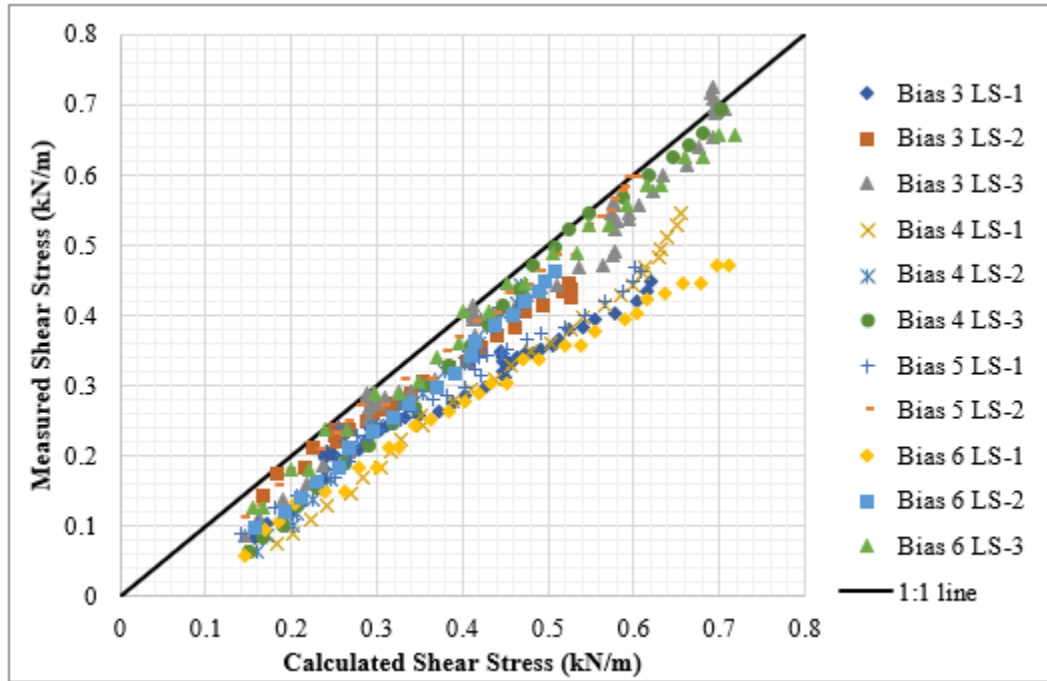


Figure 110: GgE calculated vs. measured shear stress, average trendline G.

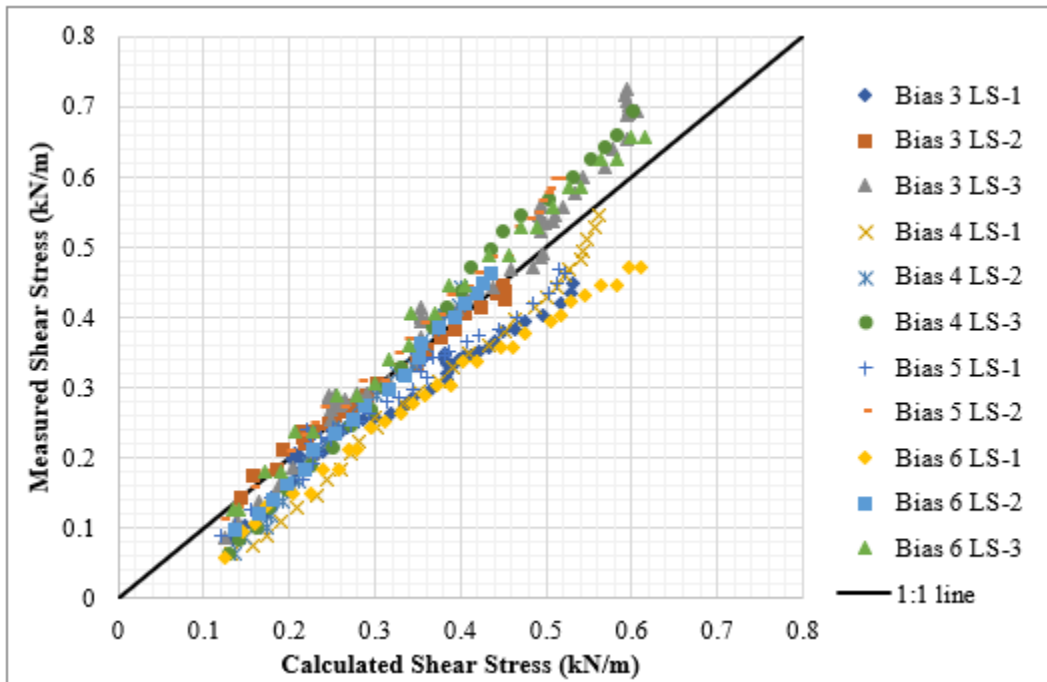


Figure 111: GgE calculated vs. measured shear stress, possible best fit G.

### Sources of Error

Multiple sources of error exist in this research as discussed below. These were minimized as much as possible, but the expected impact on data is also included for each potential error source.

#### Limited Sample Material

Some samples, particularly those for Geogrid B, were cut from the ends of a material roll, possibly introducing more variability within the sample as compared to an ideal sample cut from further inside the roll. As described earlier, it was considered more important to use material from the same roll as Haselton (2018) rather than obtain a new roll and risk variation between batch lots.

#### Material Alignment in Grips

As discussed in Chapter Five, for the bias tests, the material axes were to be oriented at 45 degrees to the load axes. Alignment was easy to ensure at the central AOI, but less so out at the grip. Initially, the central AOI was aligned and the arms smoothed out to the grips from there. Partway through testing, a 45-45-90 triangle template was discovered as an easy way to ensure grip alignment as shown previously in Figure 78, in addition to alignment of the central AOI. However, this highlighted the occasional warping present in the samples, since they did not always lay perfectly flat when aligned this way. It is not known whether the data would receive a greater impact from warping or from any slight misalignment from the initial method, and it is possible that they create similar levels of noise.

### Manual Control of Machine Loaded Axis

As noted by Haselton (2018), using the on/off switch to reach set load step limits (strain limits for Haselton 2018 or load limits in this thesis) required practice and was difficult to do precisely. A combination of factors contributed to the difficulty: motor spool down required anticipating the desired stopping limit, and the lead time changed depending on the rate each material picked up load. Most load steps could be reached close enough to be satisfactory, but high precision would require automated control.

### Manual Axis Loading

Loading of the manual axis was highly approximate. For one-person testing, the sides could not be loaded simultaneously. Equal displacement on both sides of the axis was approximately maintained by the number of turns of the wrench. Manual loading was performed as quickly as possible due to rapid stress relaxation, and it was impossible to hit loading marks precisely. The wrench loading method almost certainly created an unknown, different strain rate from the machine-loaded axis, so the validity of load control for this axis is questionable. The improvement observed in Geotextile B bias test 4 due to additional displacement control shows that while this manual load-controlled method may work well enough, it is not ideal and should include at least an approximate visual check of equal displacement between the axes.

### Grip Slippage

Slippage was not observed based on the imprint of the grip texture on the geogrid arms. Grip texture imprint also worked to evaluate slippage of woven geosynthetics

since the glued portion of the arms extended slightly into the grip. Moreover, loads were relatively low, which would help minimize grip slippage.

### Fisheye in Camera Lens

The video data is overall good quality, but it does show a slight, unavoidable fisheye (distortion caused by reduction of image scale toward the image perimeter), which is evident by placing a straightedge or straight line on the video images. Fisheye would affect the data by the creation of pseudo strains as the geometry moved toward or away from the center of the image. For geometry moving away from the center, strains would appear to become larger than they should be due to increasing fisheye stretch in the image. The reverse is true for geometry moving toward the center. Geometry that remains the same distance from the image center (even if it rotates about the center) would not be affected, since the length from which the strains are defined remains unstretched. Since the data of record was taken from the center of the image and since the overall fisheye is slight, the strain data used for this thesis should not be significantly affected.

### Camera Setup

If the camera was not sufficiently level, pseudo strains would be present in the 2D DIC data, and if the image center was off-center from the AOI, any fisheye would also not be centered. These errors were minimized by checking the camera setup prior to each test, including through the remote-control PC viewfinder to evaluate centering. Any minor issues with these factors should be negligible, given the comparatively large

camera angling present in the 2D DIC research by Karadogan and Tamer (2017) that still produced reasonable results as mentioned in Chapter Two.

#### Surface Errors in GOM Correlate

Particularly in the geotextiles, surface errors such as twinning (false high/low strain pairs) and moiré (false strain patterns or stripes) appeared depending on the facet size. Multiple factors are known to influence these errors, including stochastic pattern size relative to the DIC facet size, pattern clarity, lighting, and surface texture (Correlated Solutions 2017). As discussed in Chapter Five, surface texture is suspected to be the main cause of the geotextile error, possibly in combination with the spray paint pattern scale. Changing the geotextile facet size greatly reduced these errors, but moiré patterns were still observed in very low strain conditions.

#### Pixel Resolution

Resolution appeared to be sufficient for data collection since a small facet size and high accuracy calculation setting produced good data for all point-and-segment based analyses (all the shear modulus data). However, improved camera resolution would most likely benefit the surface analyses for geotextiles and enable the use of the same small facet for strain heatmap assessments. It would also likely improve the DIC sensitivity at low strain.

#### DIC Sensitivity at Low Displacement

As discussed in Chapter Five, the strain uniformity COV appeared to be more dependent on the strain level relative to the initial un-displaced reference image rather

than on the small magnitude of strains present at the start of every load step. The software obviously can measure the strain levels in this research, but additional refinement of DIC data capture methods may be necessary to maximize the potential of this tool. GOM Correlate (both the professional and free versions) has been tested and certified by PTB and NIST institutions, earning a ranking of Category 1, the category with the smallest measurement deviations (GOM Correlate Pro 2018). Consequently, any error present using the current methods should be reduceable with the right approach.

### Summary and Conclusions

With the determination of the resilient shear modulus, this research completed the work begun by Haselton (2018) for the determination of the set of orthotropic linear elastic constants obtained from biaxial tensile testing for eight commonly used geosynthetics. Plots of load per unit width (line load) versus strain in the loading directions were used to evaluate test quality as a preliminary step. For the rectangular geogrids in the study, these plots indicated the possibility of shear stiffening; this hypothesis is also supported by concaved shear stress-strain plots and a significantly abbreviated shear strain range in comparison to the other materials. Shear stress and shear strain were calculated from DIC strain and datalogger load records using the equations derived in Chapter Three. Re-zeroed shear stress-strain plots for all data appeared to be best consistent between 1% and 5% shear strain, so this range was used to determine the shear modulus. The modulus was calculated by fitting a linear trendline to each load step using only shear strain from the innermost region, which was shown to

have the best strain uniformity. For better confidence, especially because of the low shear strain in the rectangular geogrids, modulus values were compared for three different shear strain ranges: 1% to 5%, 1% to 2.5%, and 1% to 2%. Results were similar, and outlier load steps appeared to have a stronger effect than data range. Shear lock-up was noted in many load steps for the geotextiles, and this was shown to result from insufficient displacement in the manually loaded axis. Consequently, displacement control would provide more consistent results as opposed to the load control method currently in use. For most of the materials, the shear modulus values showed rather large scatter, even with outliers removed. To verify the sensibility of the best average shear modulus values, the measured shear stress was compared to the shear stress calculated from the shear strain and the best average modulus value for each material. Most materials showed a good fit, but a few of the geogrids showed an improved fit with adjusted modulus values. Based on this evaluation, Table 14 presents the recommended shear modulus values. These are highly reasonable both based on material-to-material relationship expectations and expectations formed from the literature review. Conclusions from the literature review suggested that shear modulus values would be generally around 10 kN/m, possibly as low as 5 kN/m or as high as 20 kN/m, and the test results for the geosynthetics are within this range.

Table 14: Recommended shear modulus values.

Architecture:	Rectangular Geogrid			Square Geogrid			Geotextiles	
Material:	GgA	GgB	GgF	GgC	GgD	GgE	GtA	GtB
Recommended G (kN/m):	7	23	23	6	7	12	9	12

Multiple sources of error were present in this research, including some aspects inherent to the materials and some aspects inherent to the test method such as manual loading control. Probably the most significant sources of variability include 1) inherent material variability due to the geosynthetic manufacturing process, 2) samples cut from non-ideal portions of a few material rolls in order to use the same roll as Haselton (2018) and avoid introducing roll-to-roll variability, 3) differences in grip alignment for some of the earliest square geogrids tested, and 4) differences in tension and displacement in the manually loaded axis between load steps and tests. For as many error sources as possible, reasonable steps were taken to minimize their impact. Based on the shear modulus results, these steps appear to have been generally successful.

## CHAPTER SEVEN

## SUMMARY AND RECOMMENDATIONS

Summary of Testing and Analysis

The resilient shear modulus for eight commonly used geosynthetics, including two woven geotextiles and six biaxial geogrids, was successfully determined using a 45-degree bias biaxial test configuration with DIC strain data collection. Resilient behavior was induced using a 20-minute hold time at each preload level before loading to the next preload level, allowing the materials to creep and stress relax before each load step.

DIC strain data was validated against LVDT data through a test instrumented with both data measurement systems, which showed equivalent results for DIC and LVDT strains. For bias tests on all materials, visual and statistical strain uniformity analyses showed better uniformity in the smallest central (innermost) analysis regions of the samples. The uniform area may be affected by the size of the biaxial sample: Very small samples would not produce uniform strain due to the discrete nature of the materials, whereas very large samples may show that the uniform area scales up with the sample size, or they may show non-uniform effects only within a certain band around the perimeter of the AOI. Uniformity for non-bias tests appeared to be much less dependent on the sampling region, which confirmed the wisdom of the decision to use DIC for the bias tests. Data from the innermost region for all tests satisfied the 5% COV suggested by the literature for a measure of good strain uniformity, and the zero shear strain ( $\gamma_{xy}$ )

assumption in the elastic constant derivations was demonstrated to be reasonable for both bias and non-bias tests on both geotextiles and geogrids.

Shear stress and shear strain values were calculated from the innermost DIC strain data and load data using the equations derived in Chapter Three. Preliminary plots of load per unit width (line load) versus strain in the loading directions suggested shear stiffening in the rectangular geogrids, and this was supported by concaved shear stress-strain plots and a shortened shear strain range. For all materials, re-zeroed shear stress-strain plots showed best linear consistency between 1% and 5% shear strain, and the shear modulus for each load step was calculated within this region by a best fit linear trendline. Three shear strain ranges (1% to 5%, 1% to 2.5%, and 1% to 2) produced similar results; shear lock-up (in geotextiles) influenced the data significantly more than the strain range. Even with outlier load steps removed, considerable scatter remained for many materials. As an additional check on the reasonability of the best average modulus values for each material, shear stress calculated from the measured shear strain was compared to the measured shear stress. Most materials showed a good fit, but Geogrid B and Geogrid E showed an improved fit with modulus values that were slightly lower than the best average moduli obtained from regression analysis. The best-fit values all fell within the original spread of the data for these geogrids. Recommended modulus values were shown to be reasonable based both on material-to-material relationship expectations and general expectations obtained from similar materials in the literature review. This research generated shear modulus values ranging from 6 kN/m to 23 kN/m, with shear moduli for most materials falling in the 7 to 12 kN/m range. These values agree well

with the literature for architectural membranes, which reported shear modulus values typically on the order of 10 kN/m, ranging as low as 5 kN/m and as high as 20 kN/m.

Although it is a minor property in comparison to the behavior-dominating elastic moduli, the shear modulus was necessary for full definition of an orthotropic linear elastic model which would enable improved engineering design capability. The significance of the shear modulus and other elastic constants in the design equation is application dependent; consequently, they are best evaluated on a case-by-case basis using numerical modeling to establish acceptable or ideal parameter ranges.

#### Recommendations for Future Work

Multiple recommendations are suggested for future work. Process improvements include investigation of larger DIC patterns for the geotextiles, additional accuracy verification of the filming and DIC data collection method, updates to hardware to enable higher frequency data collection, automation of data processing using LABVIEW and/or MATLAB, and biaxial device improvements such as fully computer-controlled test capability, hydraulic grips, and a permanent camera jig. Other recommendations include continued testing to expand the data set (possibly using cyclic loading) and finite element modeling to double-check observed macro-behaviors and macro-properties.

#### Specimen Preparation Improvements

A suggested change to the bias sample preparation method for the geotextiles is to mark out the sample from the roll as usual, but then glue the arms before cutting out the sample. The bias samples (especially Geotextile A) easily deform after cutting, and

working glue into the fibers can promote distortion in a pre-cut sample even when it is taped to the floor. Applying at least one glue coat while all the fibers are held in place in the roll would help ensure no warping of the original geometry.

While the spray speckle DIC pattern worked well for the geogrids in this study, it created high noise for the geotextile analyses unless a much larger DIC facet size was used. To try to improve noise levels at small facet sizes, future work on geotextiles should include preliminary tests using a larger, more distinct stochastic dot pattern. A stencil may be ideal for continued use of spray paint, or otherwise it may be necessary to stipple with a permanent marker pen (similar to Colman et al. (2014) mentioned in Chapter Two).

Small differences in grip alignment appeared to be more significant than anticipated for avoiding shear strain  $\gamma_{xy}$ . Future tests should continue using a 45-45-90 triangle template (as discussed in Chapter Five) or other tool to ensure the 45-degree bias orientation is highly accurate at the grips as well as in the center of the sample.

#### Filming and Data Collection Improvements

The accuracy of the filming process used in this research was verified by comparison to LVDT measurements by running a test instrumented with both sets of equipment. Additionally, for this project, only strains (relative distances) were used, so no absolute distance calibration was pursued. Suggestions for future work include 1) verifying the exact accuracy of the camera system using known gage distances that can be checked and calibrated in the DIC software and 2) evaluating inherent error in the video data due to image quality and resolution.

Data record frequency was limited by the processing power of the laptop PC used to run load data collection and remote control of the camera. A faster PC processor would enable the full potential of the camera and datalogger systems to be realized. The maximum capture rate for datalogger load records is 100 Hz, and video could be captured at up to 50 Hz in “Full HD” resolution (1920 x 1080 pixels), or up to 4 Hz for still image series at a much higher resolution of 18 megapixels (5184 x 3456 pixels). Currently, the linear portion of current shear stress-strain curves may be defined by only three to five data points in some load steps, so increasing the record frequency would increase confidence in the modulus values obtained from the short data ranges of these tests.

#### Data Processing Automation

The data processing system developed for this project worked well, but it requires multiple video-processing software and significant manual involvement. For ease of use and better repeatability, test operator involvement could be simplified by developing an all-in-one data processing program. Image processing packages such as GeoPIV are already available within MATLAB, but the programming investment required to achieve the same functionality as manual processing with GOM Correlate has not yet been explored. At a minimum, even if GOM Correlate were still used as the DIC software rather than MATLAB code, MATLAB could be used to automate image preprocessing, DIC strain statistics evaluations, and load-strain curve and shear stress-strain curve production. Data processing automation would be especially desirable if data collection frequency was increased as discussed above.

### Biaxial Device Improvements

Bias biaxial testing using the WTI biaxial device is currently as much of an art as it is science. In addition to automation of data processing, ideal testing would incorporate improvements to the biaxial device to enable computer-controlled cyclic loading and data collection. Also, displacement control rather than load control would provide better consistency for bringing samples back to a neutral, non-sheared state between successive load steps and minimize the potential for shear lock-up. Test protocol precision and data processing speed would both be greatly improved by the development of a MATLAB or LABVIEW program for total control of load application, and data acquisition. This would necessitate some reworking of the biaxial device setup, specifically hardwiring multiple microcontrollers for 1) the load on-off switch, and 2) load actuation of independent arms by tightening the nut/bolt that connects the grip sprocket to the frame (this currently requires manual tightening after each load step to preload the non-machine-controlled axis). An Arduino or Raspberry PI could be used for load and camera actuation, which would enable simultaneous data capture and greatly simplify postprocessing data matchup. In addition to machine control and data collection, the same program could potentially also handle preprocessing, postprocessing, and DIC image analysis, which would enable a one-button approach for testing and data processing. Beyond simplifying the test procedure, automation would also greatly reduce human error. One other suggested improvement to the biaxial device is to change the grips from a time-consuming manual bolted system to some type of automated hydraulic grips (as also suggested by Haselton 2018), but this would not be required for loading

automation. Smaller changes that should be made for any continued work with DIC include a permanent rigid camera jig and lighting control fixture. Ideally, this would bolt to the biaxial device mainframe and would be similarly fabricated from welded steel. In addition to supporting and aiming the camera, this fixture would also need to spread out the sheeting drape (e.g., a king-size bedsheet) in a canopy over the filming area.

### Further Testing

This research sought to prove the feasibility and repeatability of obtaining the resilient shear modulus from bias biaxial tests. This goal was achieved; however, further testing is recommended because the number of samples was small (generally only two specimens per each of eight materials).

For future work, cyclic biaxial tests are recommended to further explore low-strain behaviors in the rectangular geogrids, which showed non-linear shear stress-strain behavior. The rectangular geogrids appeared to mildly strain stiffen at low strains, and the full hysteresis loop from cyclic testing would help to verify this behavior. Moreover, with cyclic tests, the strain range could be increased while still obtaining a resilient response, and a large hysteresis loop would help distinguish behaviors resulting from motor spool-up and spool-down versus strain stiffening under a constant displacement rate. Crude cyclic testing using the current biaxial device has been demonstrated to be possible following a single-axis loading schedule similar to that shown in Figure 112, but this discovery was made too late to be used in the data collection for this thesis. In Figure 112, both axes are cycled between zero load and a biaxial preload before beginning shear cycles with only one axis loaded at a time while the other is held fixed

(similar to the non-cyclic shear schedule used in this thesis). The current biaxial device is capable of this kind of cyclic shear testing, but only for one axis at a time (unable to alternate the loaded and fixed axes mid-test), and without the equal biaxial preload cycles.

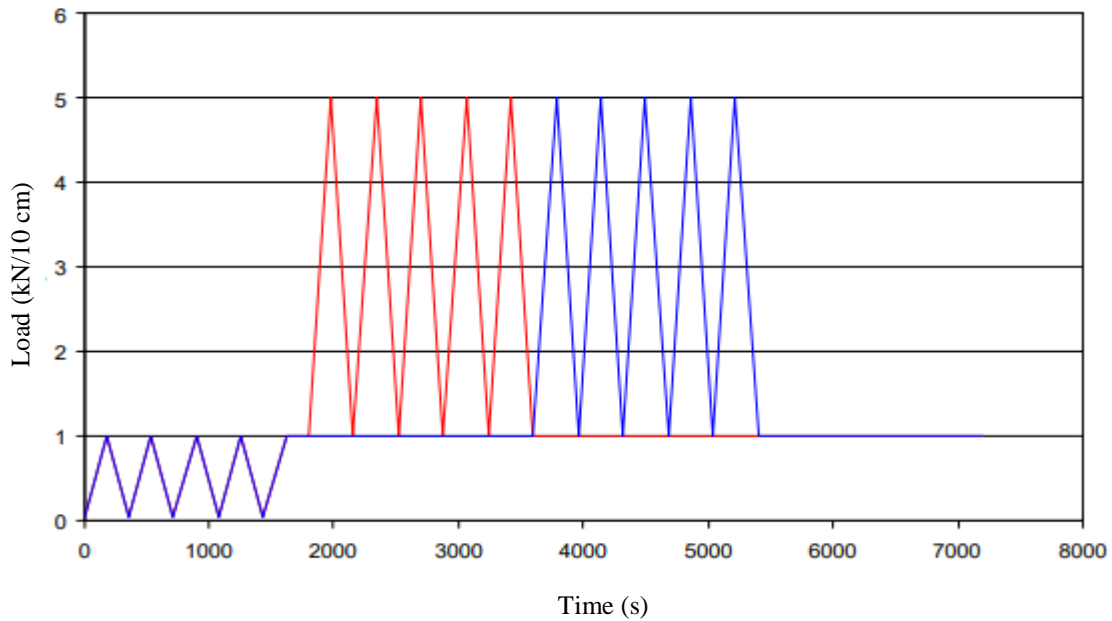


Figure 112: Biaxial cyclic shear loading schedule from Bögner (2004). Warp is shown in red; weft is shown in blue.

The recommended cyclic shear loading schedule in the literature involved loading one axis while simultaneously releasing the other axis, but the current biaxial device is not capable of this form of loading. Automated load control using microcontrollers as recommended earlier would certainly enable this form of loading as well as enable precision cycling. An alternate possibility to achieve simultaneous unloading is to modify the biaxial device to include additional sprockets for the release axis chains, such that the chains are tensioned from the bottom of the load plate rather than the top. Figure

113 shows a sketch of the current load path and the suggested modifications. (Further schematics and description of the biaxial device are provided by Haselton 2018.) With this setup, load would automatically release from one axis while load increases in the other.

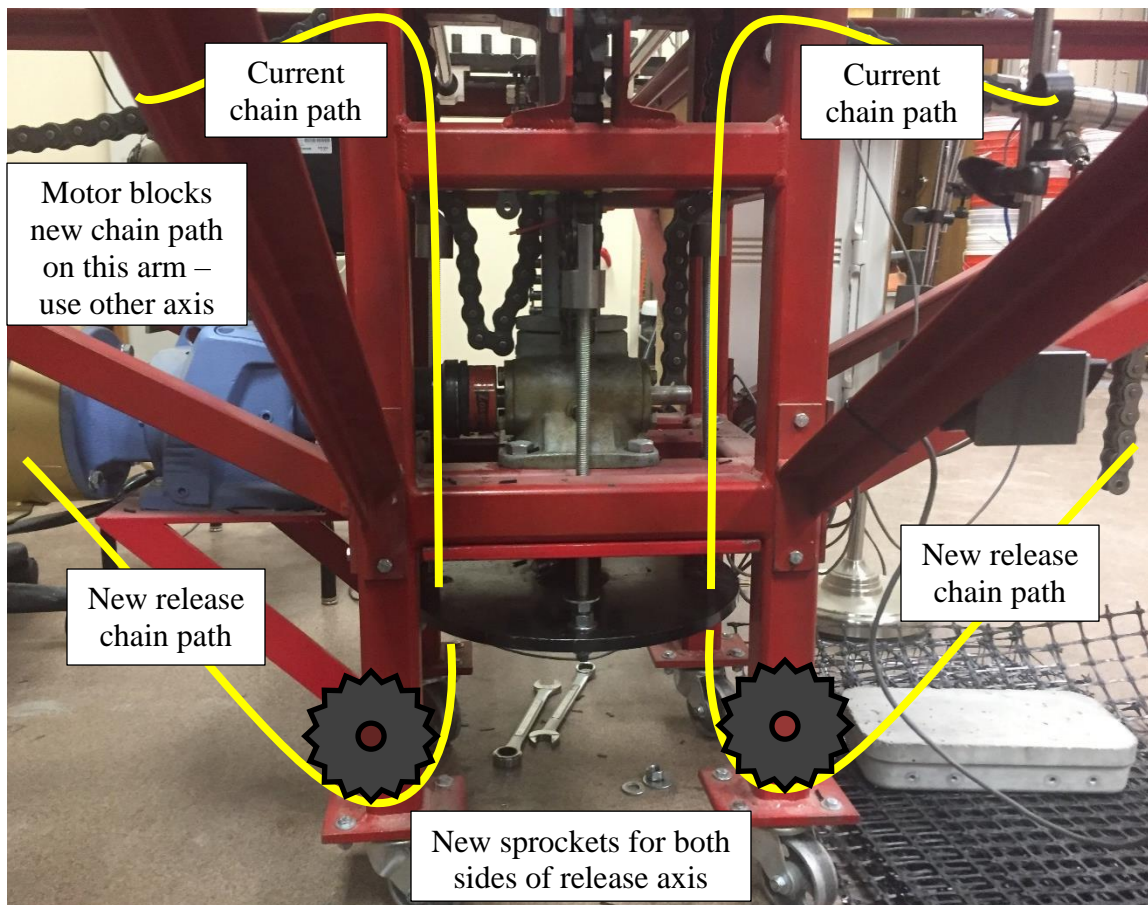


Figure 113: Additional sprocket location for release axis.

Only one axis would require this modification since this thesis demonstrated Mode 2 and Mode 3 45-degree bias biaxial shearing to produce equivalent results, which is good since the motor mount would most likely block the new chain path on one arm. Also, with the addition of new sprockets, the legs of the biaxial device may need to be lengthened to

accommodate loading plate range in the release direction as seen in Figure 113.

Additional benefits include intrinsic equal displacement (positive and negative) of all axes and an overall low-cost, low-tech mechanical solution in keeping with the original intent for this biaxial device.

### Finite Element Modeling

Finite element modeling (FEM) is suggested to help with understanding bias biaxial behavior, especially the possible shear stiffening behaviors observed at low strain in the rectangular geogrids. It is suspected that these behaviors may be linked to the asymmetric tensile structure created by the bias sample orientation; these grids would probably develop significantly unbalanced off-axis forces, especially in comparison to the square geogrids. FEM analysis would also require the completion of a uniaxial testing program to obtain tensile properties of the individual webs and nodes in each principal direction of each geogrid.

REFERENCES CITED

- Aboelwafa Ahmed, M. M. (2018). *Effect of Orientation on In-isolation and In-soil Geosynthetic Properties*. (Master of Science in Engineering), The University of Texas at Austin,
- Aboelwafa, M. M., Roodi, G. H., & Zornberg, J. G. (2019). *In-Isolation Properties of Biaxial and Triangular Geogrids along Various Directions*. Paper presented at the Geosynthetics Conference, Houston, TX USA.
- ARAMIS (Version 6.2.0-6). (2008). Braunschweig, Germany: GOM mbH.
- ARAMIS User Manual - Software. (2007). In. Braunschweig, Germany: GOM mbH.
- ASTM D1774-93. Standard Test Methods for Elastic Properties of Tensile Fibers (Withdrawn 2000). West Conshohocken, PA, ASTM International.
- ASTM D6637-15. Standard Test Method for Determining Tensile Properties of Geogrids by the Single or Multi-Rib Tensile Method. West Conshohocken, PA, ASTM International.
- ASTM D7556-10(2019). Standard Test Methods for Determining Small-Strain Tensile Properties of Geogrids and Geotextiles by In-Air Cyclic Tension Tests. West Conshohocken, PA, ASTM International.
- Aydilek, A. H., Guler, M., & Edil, T. B. (2004). Use of Image Analysis in Determination of Strain Distribution During Geosynthetic Tensile Testing. *Journal of Computing in Civil Engineering*, 18(January 1, 2004), 65-74. doi:10.1061/(ASCE)0887-3801(2004)18:1(65)
- Bathurst, R. J., & Ezzein, F. M. (2015). Geogrid and Soil Displacement Observations During Pullout Using a Transparent Granular Soil. *Geotechnical Testing Journal*, 38(5). doi:10.1520/gtj20140145
- Beccarelli, P. (2015). Biaxial Testing Apparatuses and Procedures. In *Biaxial Testing for Fabrics and Foils* (pp. 35-72).
- Birdair.com. (2004). Hampton Roads Convention Center. Retrieved from <http://www.birdair.com/projects/hampton-roads-convention-center>
- Bögner, H. (2004). *Vorgespannte Konstruktionen aus beschichteten Geweben und die Rolle des Schubverhaltens bei der Bildung von zweifach gekrümmten Flächen aus ebenen Streifen*. Bau- und Umweltingenieurwissenschaften. Stuttgart, Germany, Universität Stuttgart. Doktor-Ingenieurs (Dr.-Ing.) genehmigte Abhandlung.

- Bridgens, B., Gosling, P., Jou, G. T., & Hsu, X. Y. (2012). Inter-laboratory comparison of biaxial tests for architectural textiles. *Journal of the Textile Institute*, 103(7), 706-718. doi:10.1080/00405000.2011.602824
- Canon EOS Utility (Version 2.8). (2010): CANON INC.
- Cen, W. J., Wang, H., Li, D. J., & Wen, L. S. (2018). Large-strain tensile behaviour of geomembranes with defects using 3D digital image correlation. *Geosynthetics International*, 25(6), 644-655. doi:10.1680/jgein.18.00031
- Chen, S., Ding, X., & Yi, H. (2016). On the Anisotropic Tensile Behaviors of Flexible Polyvinyl Chloride-coated Fabrics. *Textile Research Journal*, 77(6), 369-374. doi:10.1177/0040517507078791
- Chen, W., Gao, C., Zhang, D., Wang, L., & Qiu, Z. (2018). A new biaxial tensile shear test method to measure shear behaviour of coated fabrics for architectural use. *Composite Structures*, 203, 943-951. doi:10.1016/j.compstruct.2018.06.063
- Colman, A. G., Bridgens, B. N., Gosling, P. D., Jou, G. T., & Hsu, X. Y. (2014). Shear behaviour of architectural fabrics subjected to biaxial tensile loads. *Composites Part A: Applied Science and Manufacturing*, 66, 163-174. doi:10.1016/j.compositesa.2014.07.015
- Correlated Solutions (2017). Application Note AN-1701 Speckle Pattern Fundamentals, Correlated Solutions.
- Teledyne DALSA. (2019). CCD vs. CMOS. Retrieved from <https://www.teledynedalsa.com/en/learn/knowledge-center/ccd-vs-cmos/>
- Ezzein, F. M., & Bathurst, R. J. (2014). A new approach to evaluate soil-geosynthetic interaction using a novel pullout test apparatus and transparent granular soil. *Geotextiles and Geomembranes*, 42(3), 246-255. doi:10.1016/j.geotexmem.2014.04.003
- Ferreira, J. A. Z., & Zornberg, J. G. (2015). A Transparent Pullout Testing Device for 3D Evaluation of Soil–Geogrid Interaction. *Geotechnical Testing Journal*, 38(5). doi:10.1520/gtj20140198
- Galliot, C., & Luchsinger, R. H. (2010a). *Biaxial testing of architectural membranes and foils*.
- Galliot, C., & Luchsinger, R. H. (2010b). The shear ramp: A new test method for the investigation of coated fabric shear behaviour – Part II: Experimental validation. *Composites Part A: Applied Science and Manufacturing*, 41(12), 1750-1759. doi:10.1016/j.compositesa.2010.08.014

- Gao, C., Chen, W., Shi, T., Hu, J., Zhao, B., & Qiu, Z. (2018). Shear Properties of PVDF-Coated Fabrics under Multicyclic Biaxial Bias Extension. *Journal of Materials in Civil Engineering*, 30(10). doi:10.1061/(asce)mt.1943-5533.0002404
- George, D. (2018). CCD versus CMOS: Which is Better? Retrieved from <http://diffractionlimited.com/ccd-versus-cmos-better/>
- GOM Correlate Pro (Version Inspection Kernel GOM v2.0.1). (2018). Braunschweig, Germany: GOM Software 2018. Retrieved from [www.gom.com](http://www.gom.com)
- Haselton, H. N. (2018). *Determination of Elastic Constants for Geosynthetics using In-Air Biaxial Tension Tests*. (Master of Science in Civil Engineering), Montana State University, Bozeman, Montana.
- Iadicola, M. A., Creuziger, A. A., & Foecke, T. (2013). *Advanced Biaxial Cruciform Testing at the NIST Center for Automotive Lightweighting*. Gaithersburg, MD, USA: National Institute of Standards and Technology.
- Jackson, A. L., Bridgens, B. N., & Gosling, P. D. (2009). *A new biaxial and shear protocol for architectural fabrics*. Paper presented at the Evolution and Trends in Design, Analysis and Construction of Shell and Spatial Structures, Universidad Politecnica de Valencia, Spain.
- Jones, D. (2000). Wide-Width Geotextile Testing with Video Extensometry. In *Grips, Clamps, Clamping Techniques, and Strain Measurement for Testing of Geosynthetics*, pp. 83-88. West Conshohocken, PA: American Society for Testing and Materials.
- Karadogan, C., & Tamer, M. E. (2017). *A novel and simple cruciform specimen without slits on legs yet higher plastic strains in gauge*. Paper presented at the International Conference on the Technology of Plasticity, Cambridge, United Kingdom.
- Kutay, M. E., Guler, M., & Aydilek, A. H. (2006). Analysis of Factors Affecting Strain Distribution in Geosynthetics. *Geotechnical and Geoenvironmental Engineering*, 132(1), 1-11. doi:10.1061/(ASCE)1090-0241(2006)132:1(1)
- Lomov, S. V., Boisse, P., Deluycker, E., Morestin, F., Vanclooster, K., Vandepitte, D., . . . Willems, A. (2008). Full-field strain measurements in textile deformability studies. *Composites Part A: Applied Science and Manufacturing*, 39(8), 1232-1244. doi:10.1016/j.compositesa.2007.09.014
- McGown, A., et al. (2004). "Current Approaches to the Determination of the Design Stiffness and Strength of Polymeric Biaxial Geogrids." *Vorträge der Baugrundtagung*: 123-130.

- Mishra, S. R., Mohapatra, S. R., Sudarsanan, N., Rajagopal, K., & Robinson, R. G. (2017). A simple image-based deformation measurement technique in tensile testing of geotextiles. *Geosynthetics International*, 1-15. doi:10.1680/jgein.17.00003
- Nilsson, P. (2017). *Measuring material properties of thin films with DIC and tearing test of laminate*. (Master of Science in Engineering Mechanical Engineering with Emphasis on Applied Mechanics), Blekinge Institute of Technology, Karlskrona, Sweden.
- Perkins, S. W. (2000). Constitutive Modeling of Geosynthetics. *Geotextiles and Geomembranes*, 18, 273-292.
- Sharma, S. B., Sutcliffe, M. P. F., & Chang, S. H. (2003). Characterisation of material properties for draping of dry woven composite material. *Composites Part A: Applied Science and Manufacturing*, 34(12), 1167-1175. doi:10.1016/j.compositesa.2003.09.001
- Shi, T., Chen, W., Gao, C., Hu, J., Zhao, B., Zhang, D., & Qiu, Z. (2018). Shear behavior of architectural coated fabrics under biaxial bias-extension. *Construction and Building Materials*, 187, 964-973. doi:10.1016/j.conbuildmat.2018.08.030
- Shinoda, M., & Bathurst, R. J. (2004a). Lateral and axial deformation of PP, HDPE and PET geogrids under tensile load. *Geotextiles and Geomembranes*, 22(4), 205-222. doi:10.1016/j.geotexmem.2004.03.003
- Shinoda, M., & Bathurst, R. J. (2004b). Strain Measurement of Geogrids Using a Video-Extensometer Technique. *Geotechnical Testing Journal*, 27(5), 456-463.
- Sigmaplot 14.0. (2017): Systat Software, Inc.
- Skelton, J. (1976). Fundamentals of Fabric Shear. *Textile Research Journal* (December 1976), 8.
- Skochdopole, T. R., Cassady, L., Pihs, D., & Stevenson, P. E. (2000). Comparative Study of Roller and Wedge Grips for Tensile Testing of High Strength Fabrics with Laser Extensometry: Comparisons to LVDT and Crosshead Extension. In *Grips, Clamps, Clamping Techniques, and Strain Measurement for Testing of Geosynthetics*. West Conshohocken, PA: American Society for Testing and Materials.
- Stanier, S. A., Blaber, J., Take, W. A., & White, D. J. (2016). Improved image-based deformation measurement for geotechnical applications. *Canadian Geotechnical Journal*, 53(5), 727-739. doi:10.1139/cgj-2015-0253

Stranghöner, N., Uhlemann, J., Bilginoglu, F., Bletzinger, K., Bögner-Balz, H., Corne, E., . . . Thomas, J. (2016). *Prospect for European Guidance for the Structural Design of Tensile Membrane Structures*. Luxembourg: Publications Office of the European Union.

Valero, S. N., Sprague, C. J., & Wrigley, N. E. (2014). *Full Scale Trafficking of Geogrid Reinforced Sections under Realistic Service Conditions*. Paper presented at the 10th International Conference on Geosynthetics, Berlin, Germany.

Visual MP4/MOV Time Stamp 1.4.0 (Version 1.4.0). (2017).

VSDC Free Video Editor (Version 5.8.5.803). (2017): Flash-Integro LLC.

APPENDICES

APPENDIX A

PLOTS OF COV VERSUS STRAIN IN THE LOADING DIRECTIONS

Overview

This appendix is organized by material architecture (rectangular geogrid, square geogrid, and geotextile), and then alphabetically by material ID (e.g. GgA). Each test specimen has its own figure containing all the load steps from that test. For this thesis, COV is the average strain divided by the standard deviation of strain at each point in time. Outlier data higher than 50% COV has been cropped for clarity. All data is from the inner region (best strain uniformity).

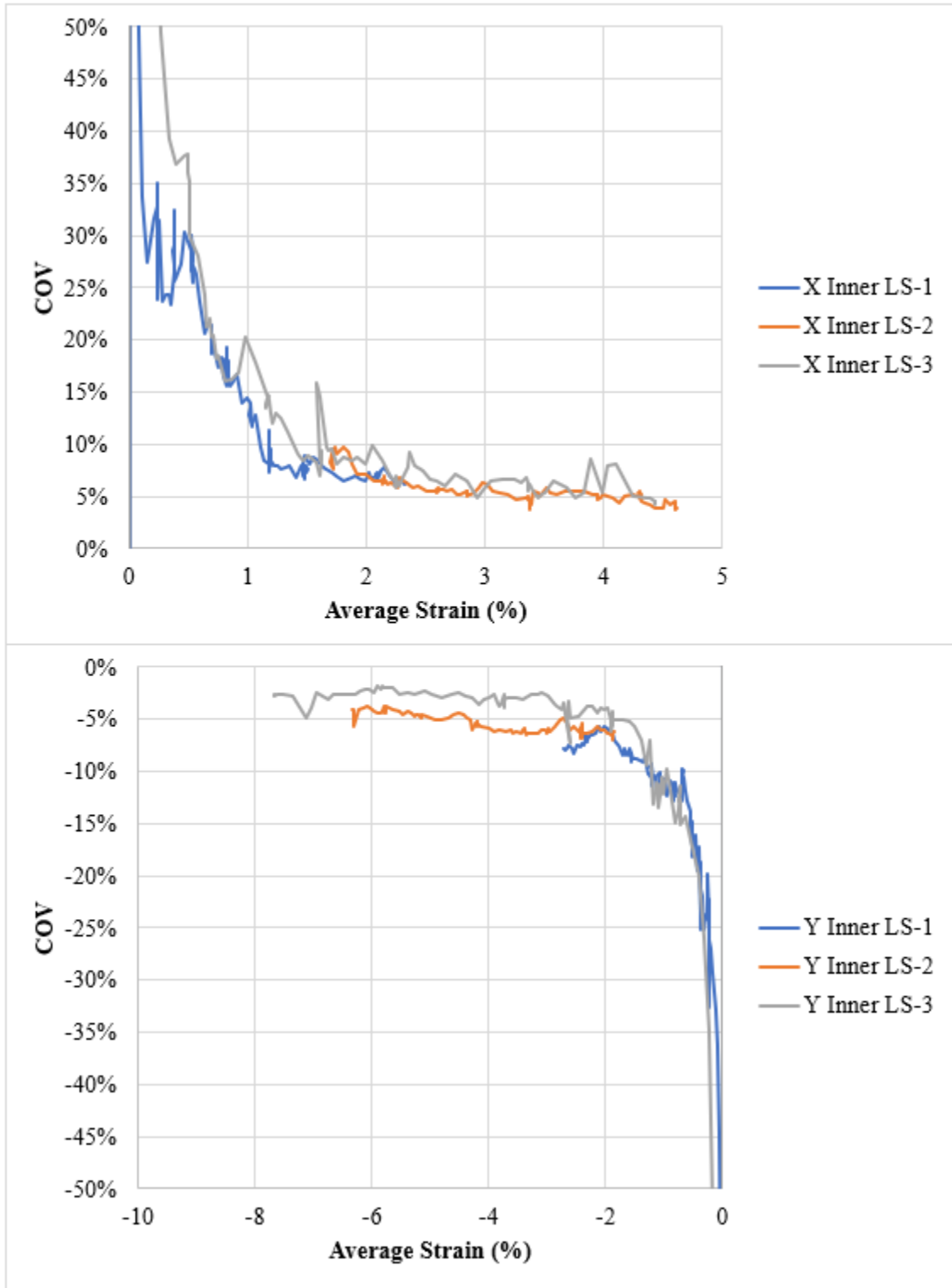


Figure 114: GgA bias trial 1.

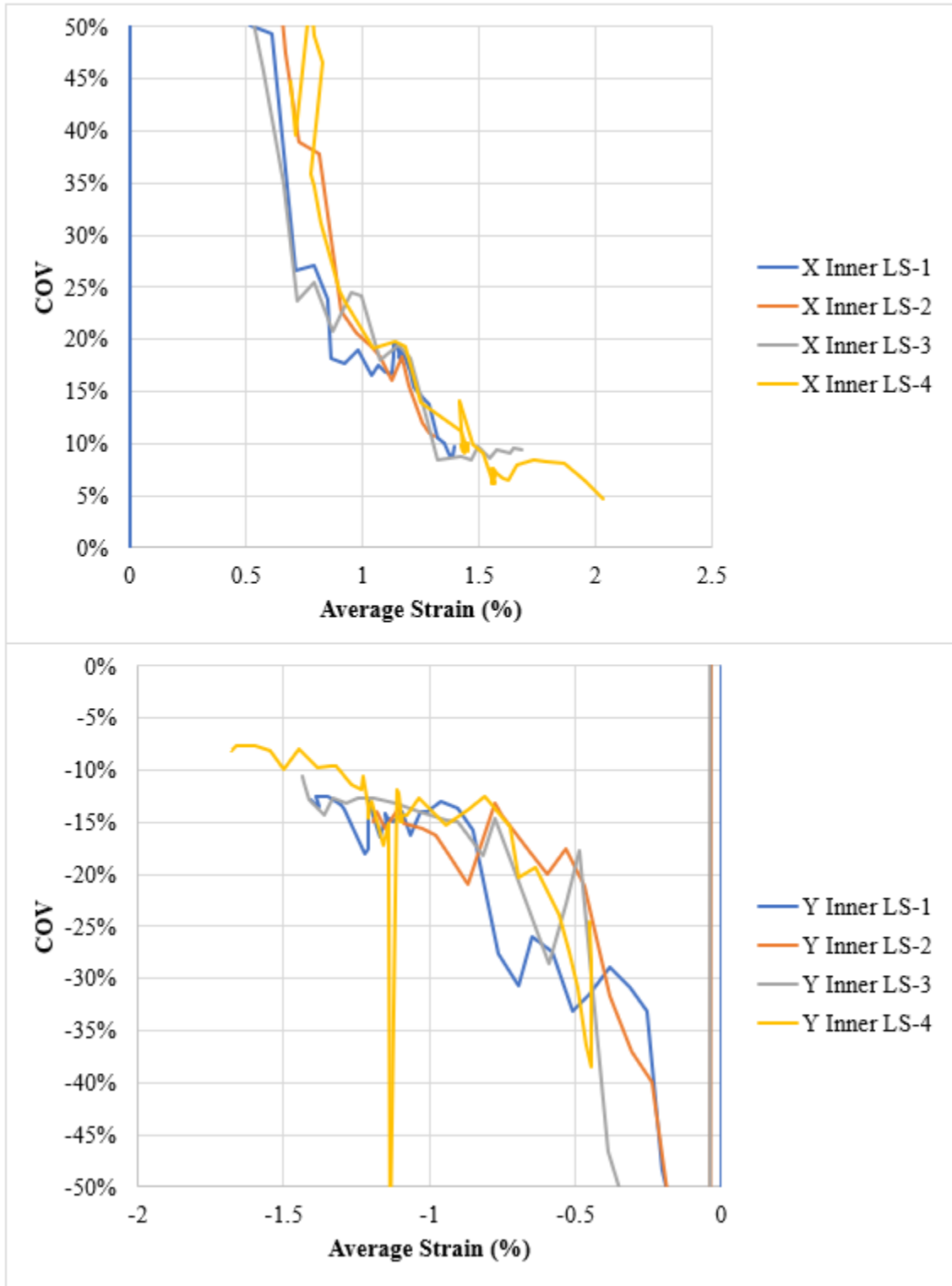


Figure 115: GgA bias trial 2.

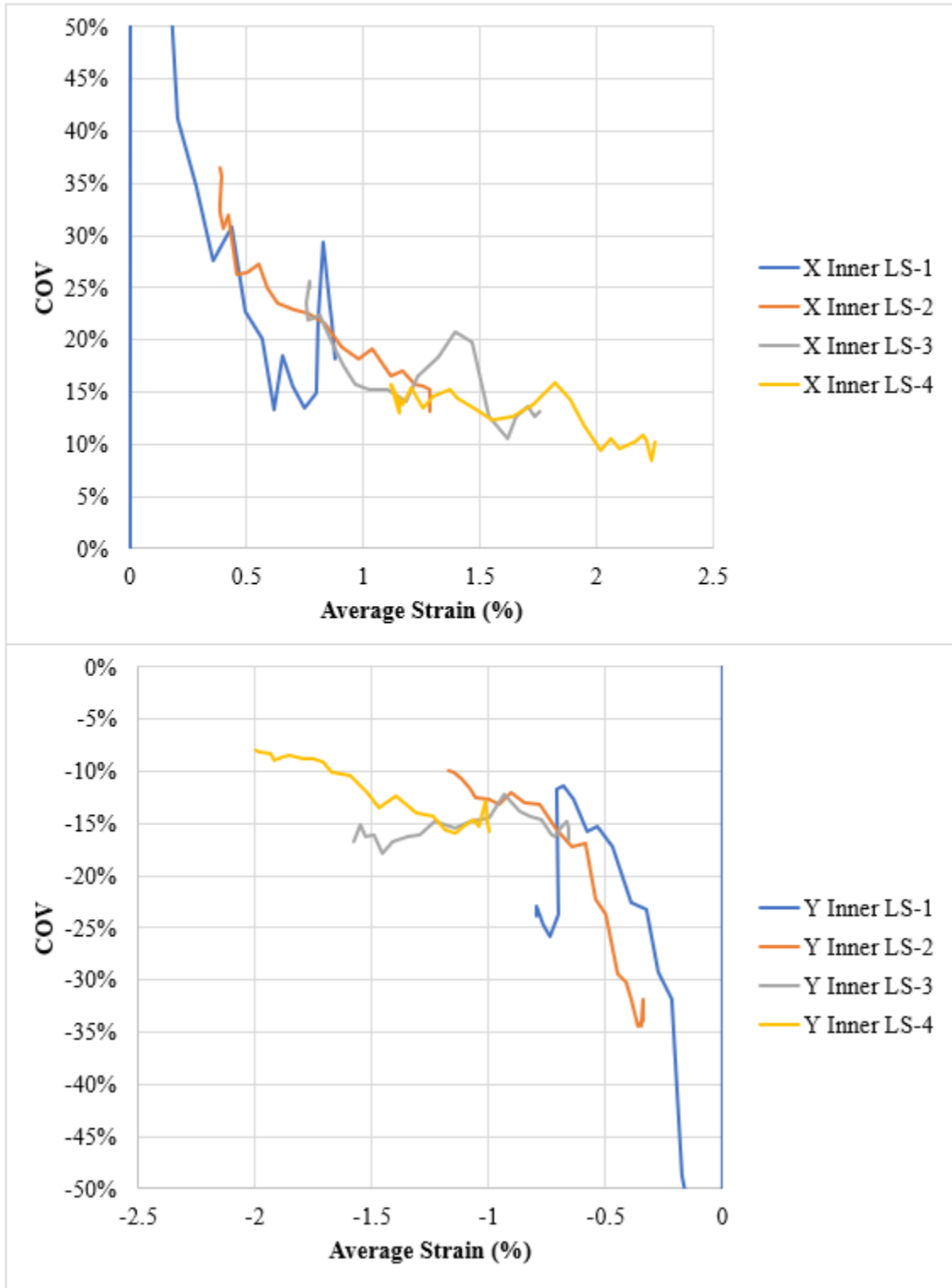


Figure 116: GgB bias trial 1.

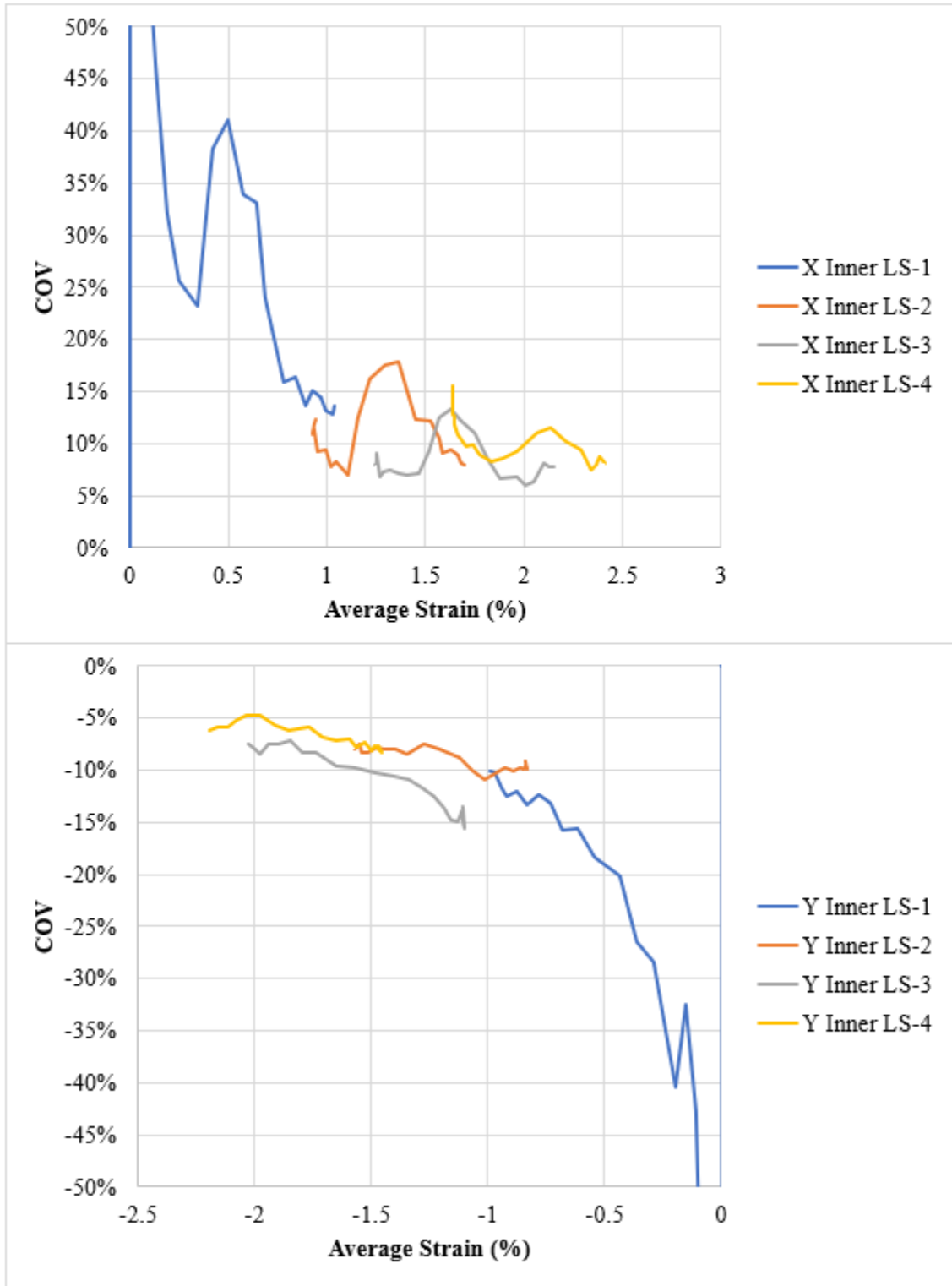


Figure 117: GgB bias trial 2.

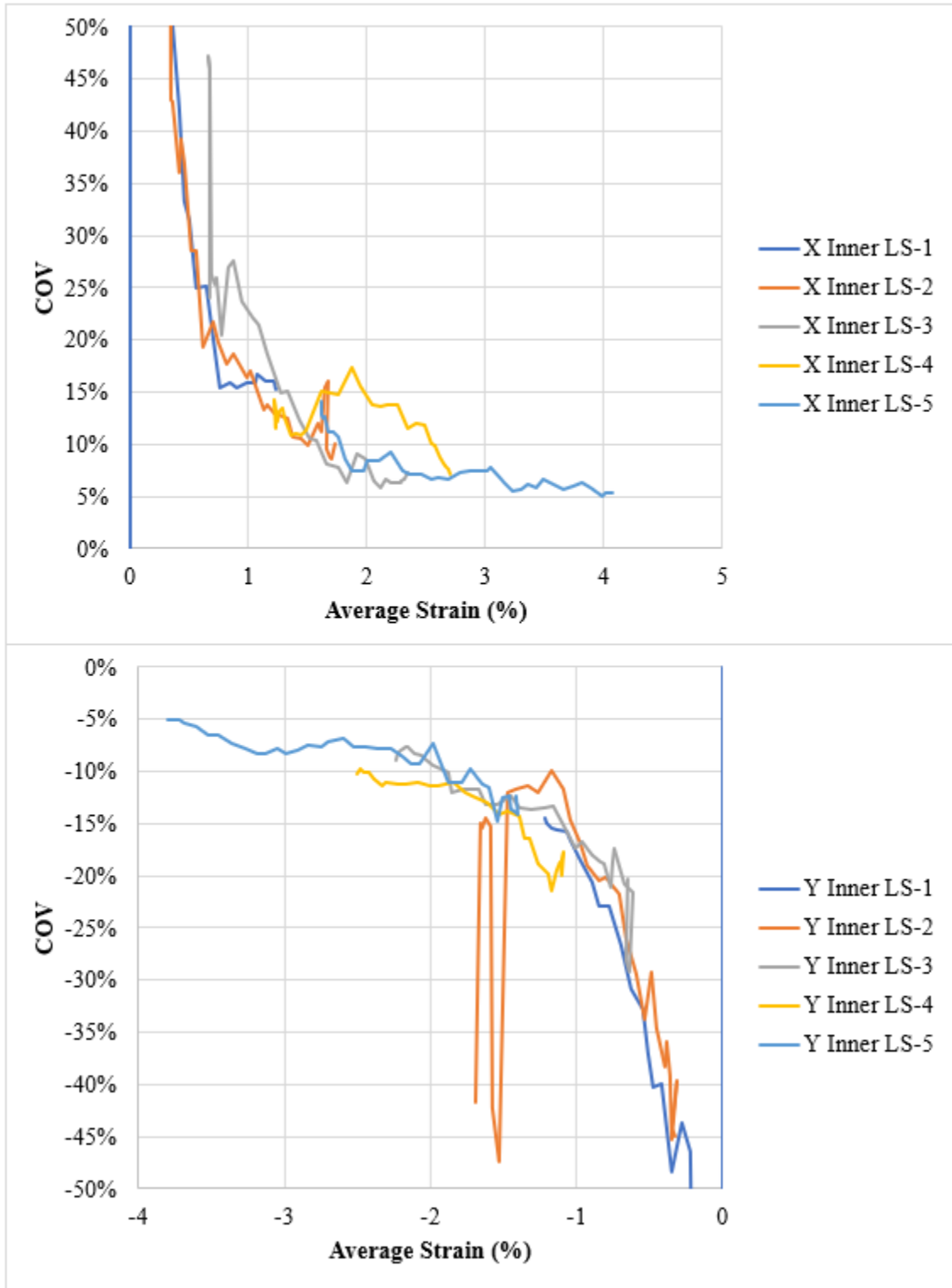


Figure 118: GgF bias trial 1.

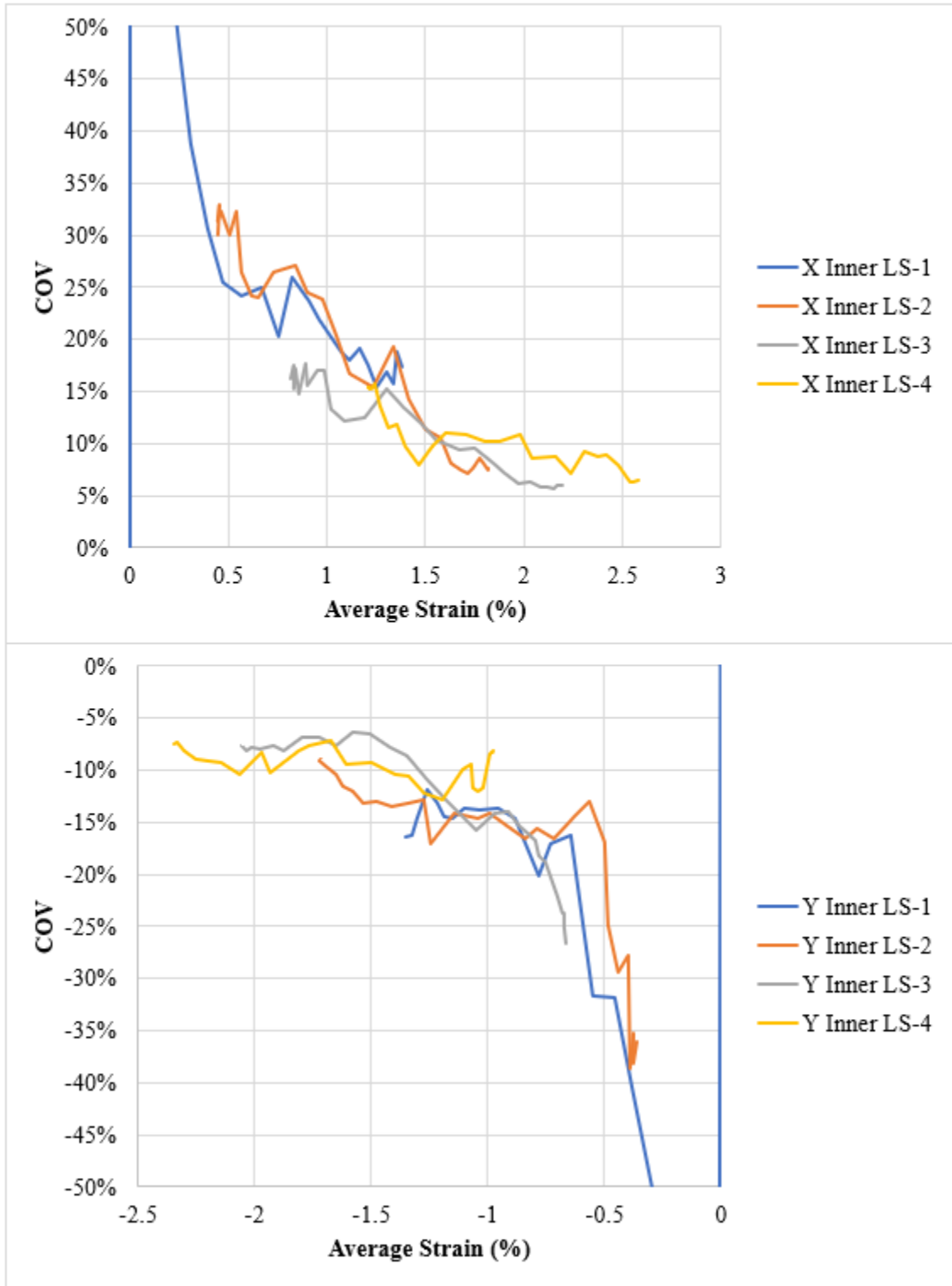


Figure 119: GgF bias trial 2.

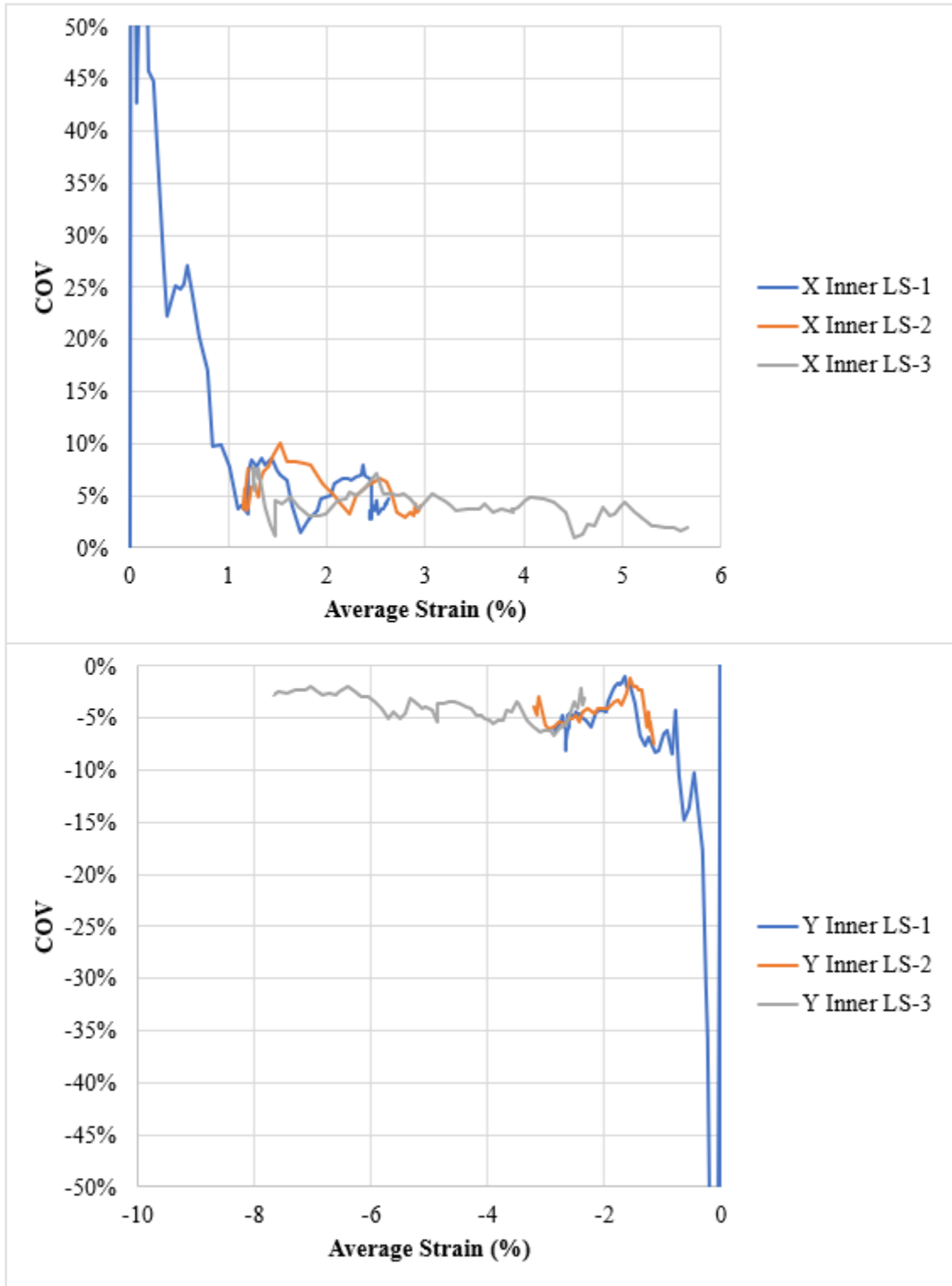


Figure 120: GgC bias trial 1.

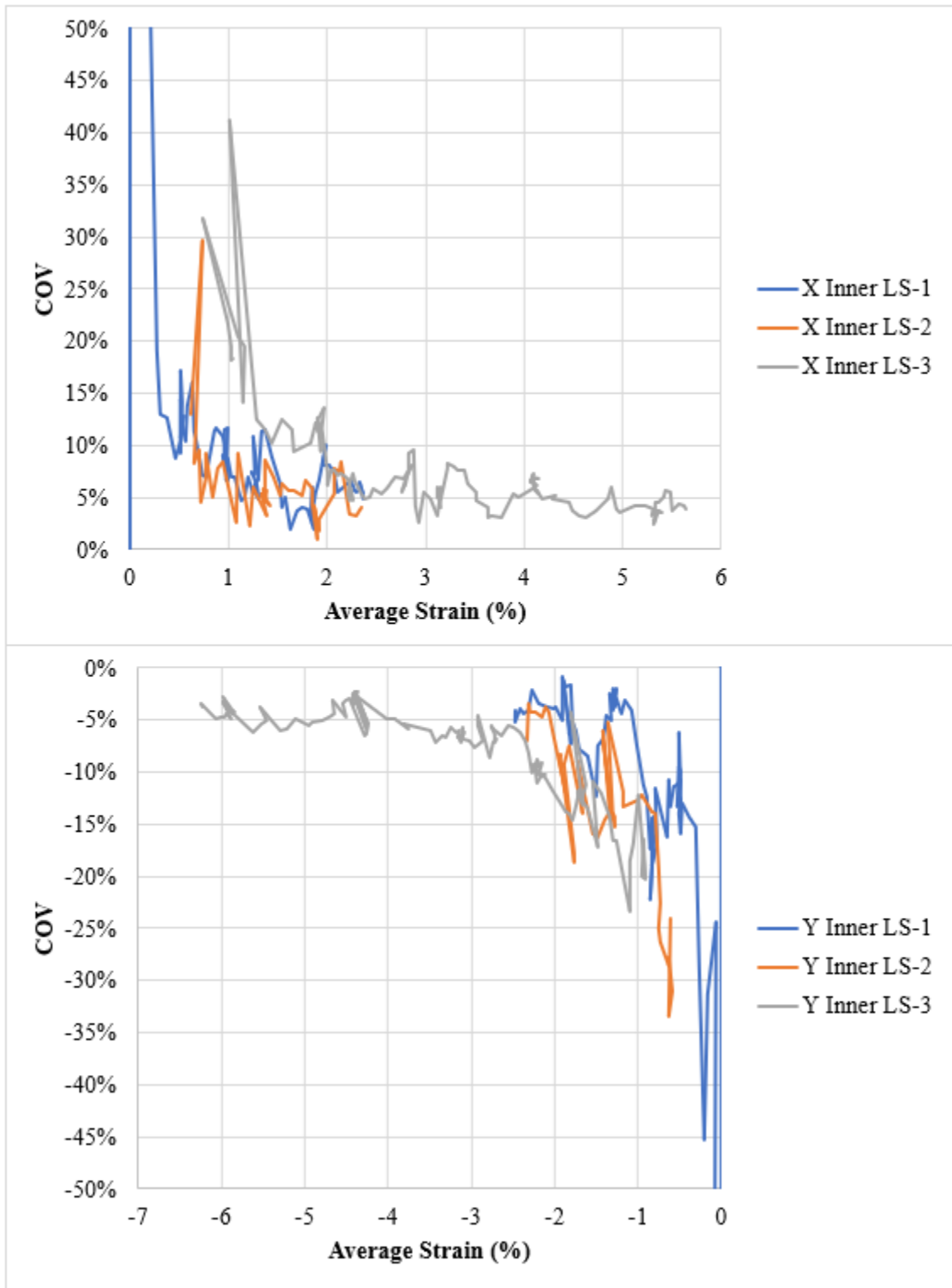


Figure 121: GgC bias trial 2.

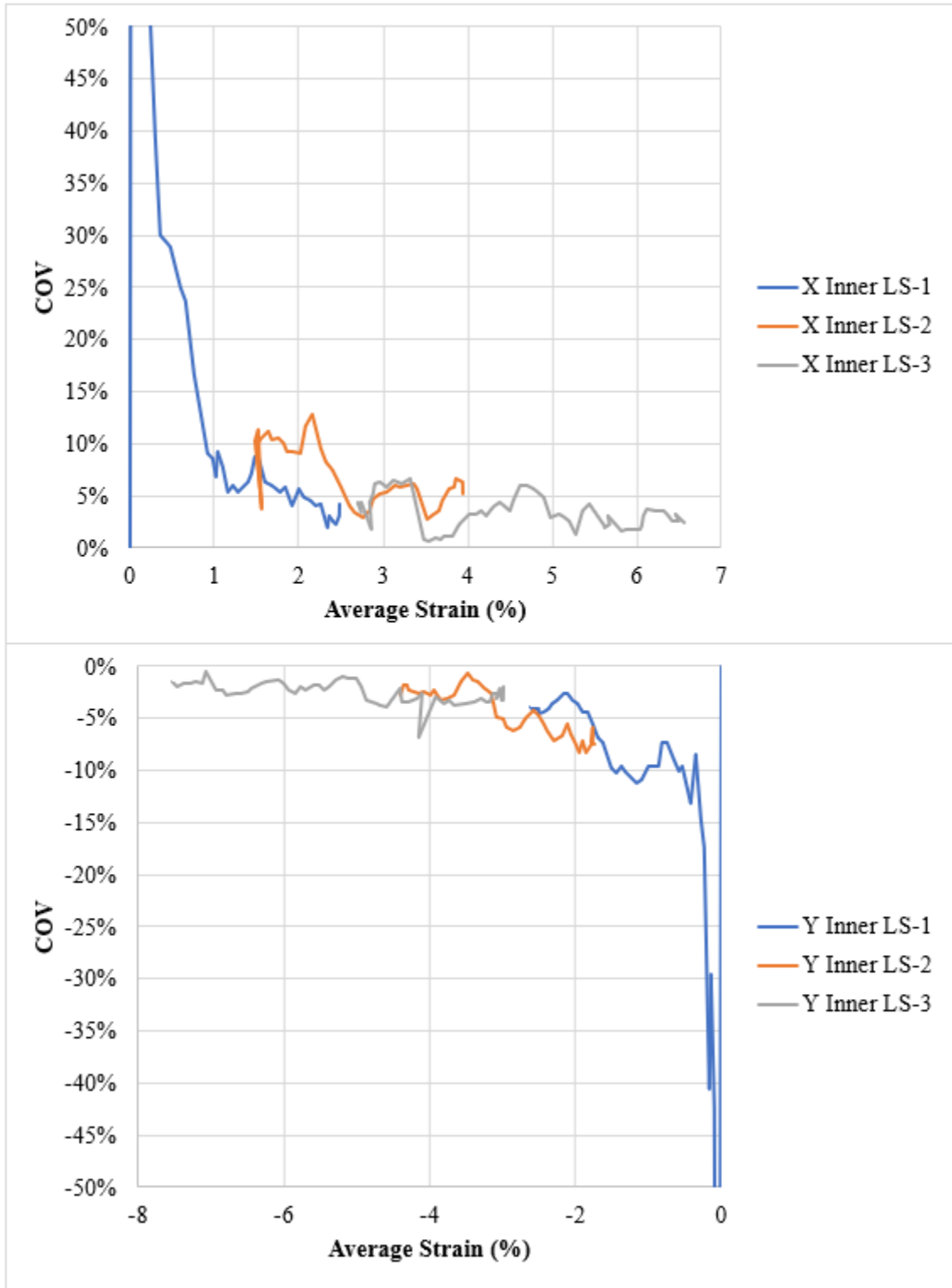


Figure 122: GgD bias trial 1.

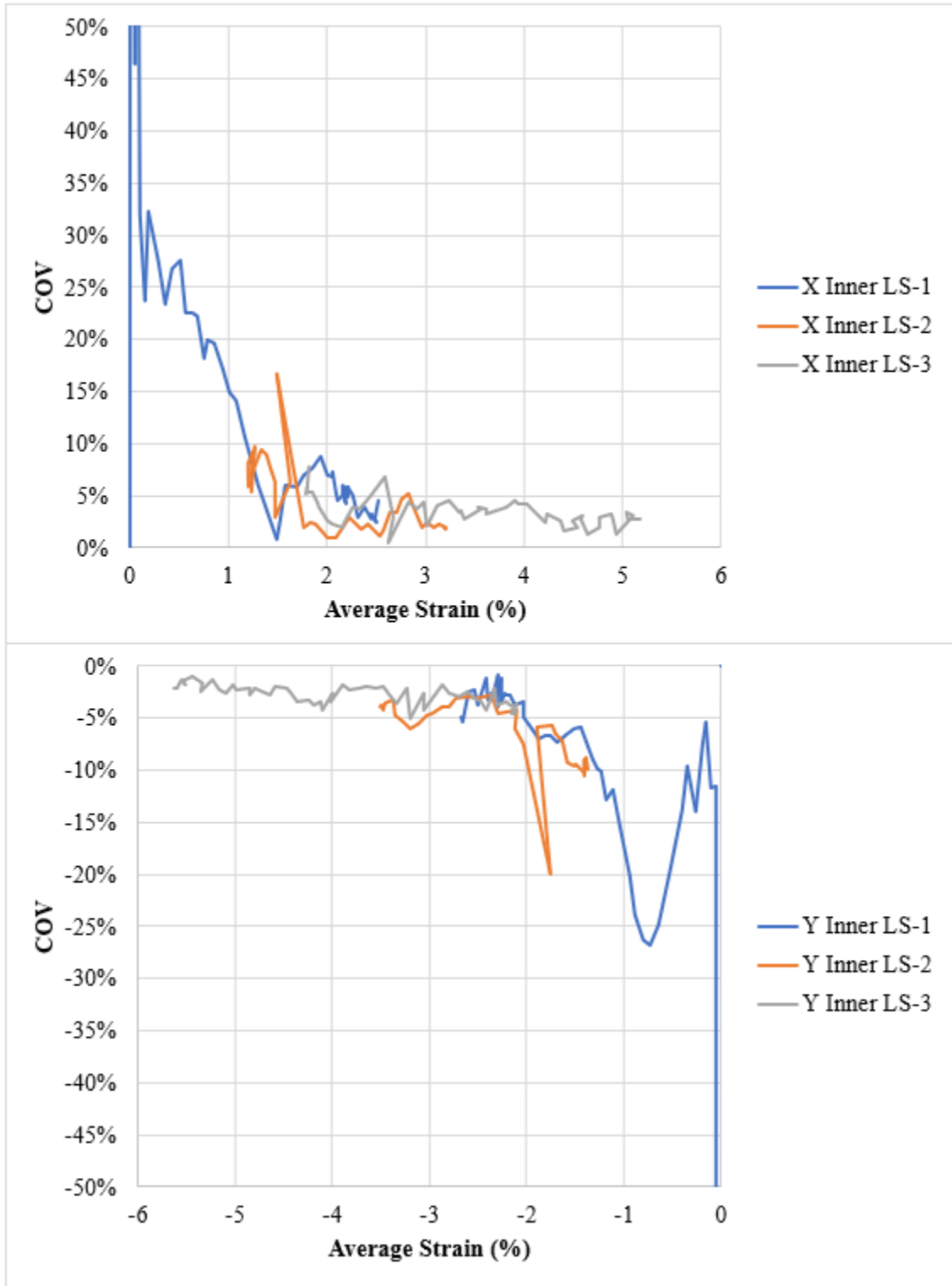


Figure 123: GgD bias trial 2.

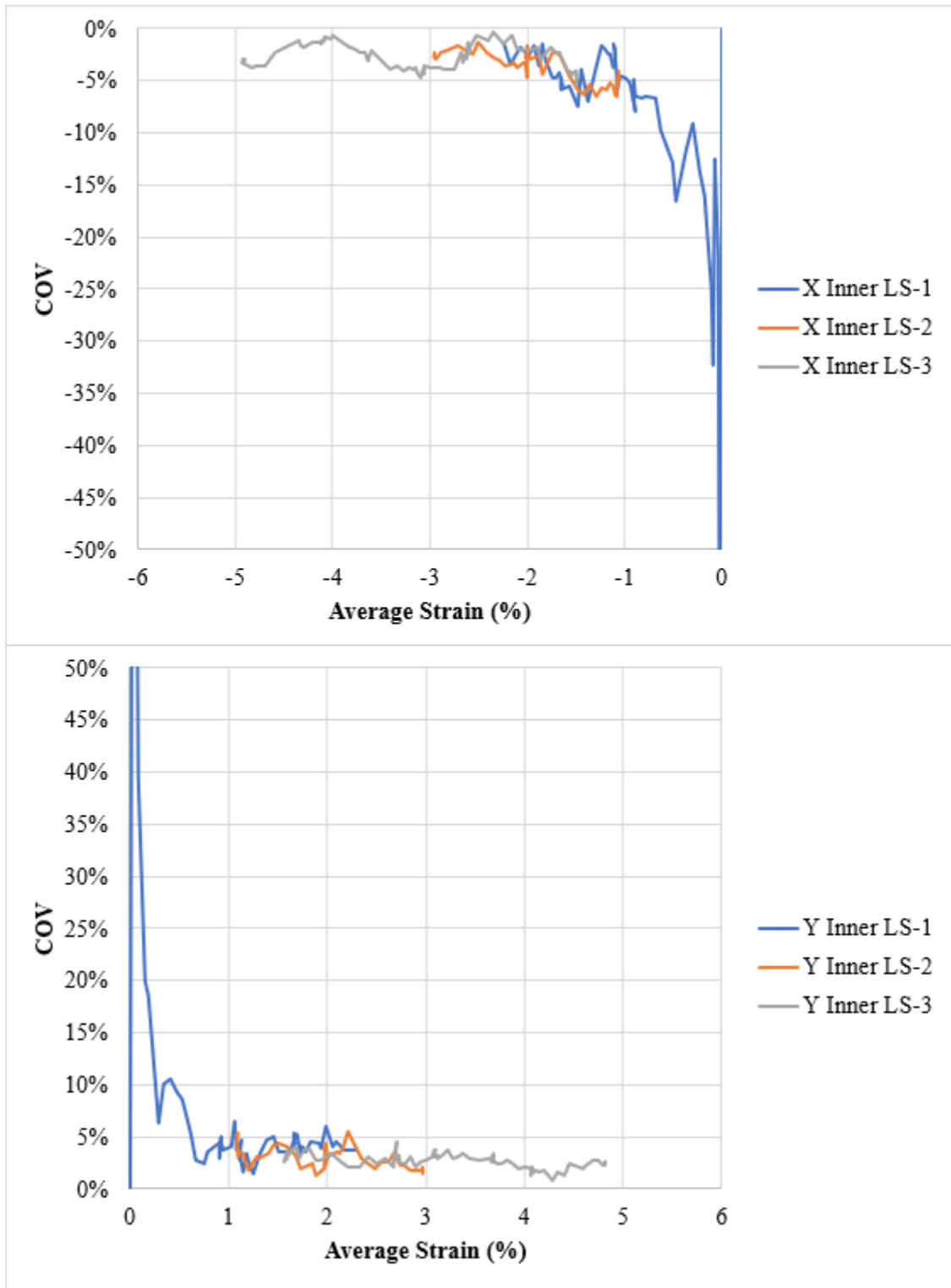


Figure 124: GgE bias trial 3 (Mode 3).

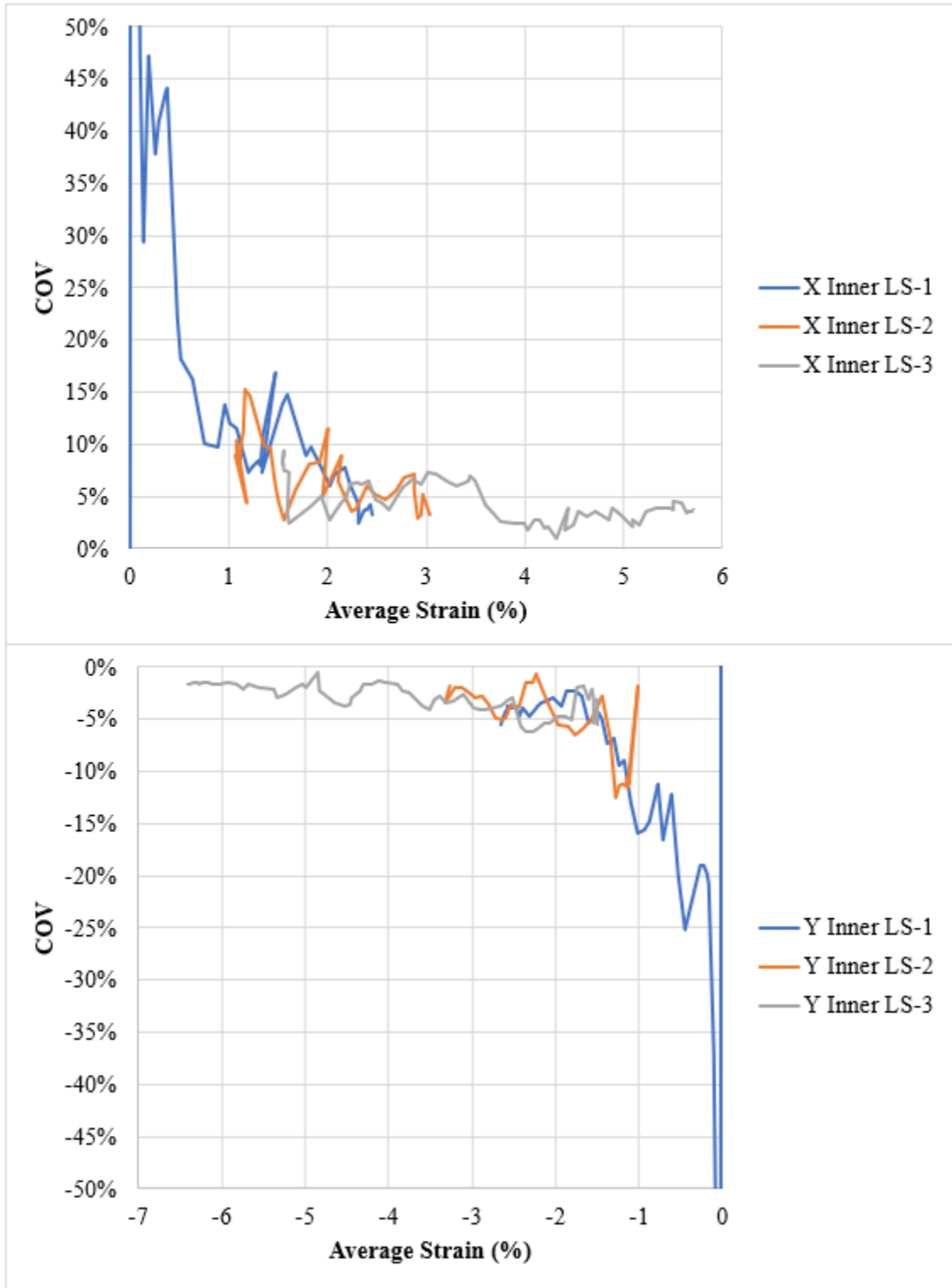


Figure 125: GgE bias trial 4.

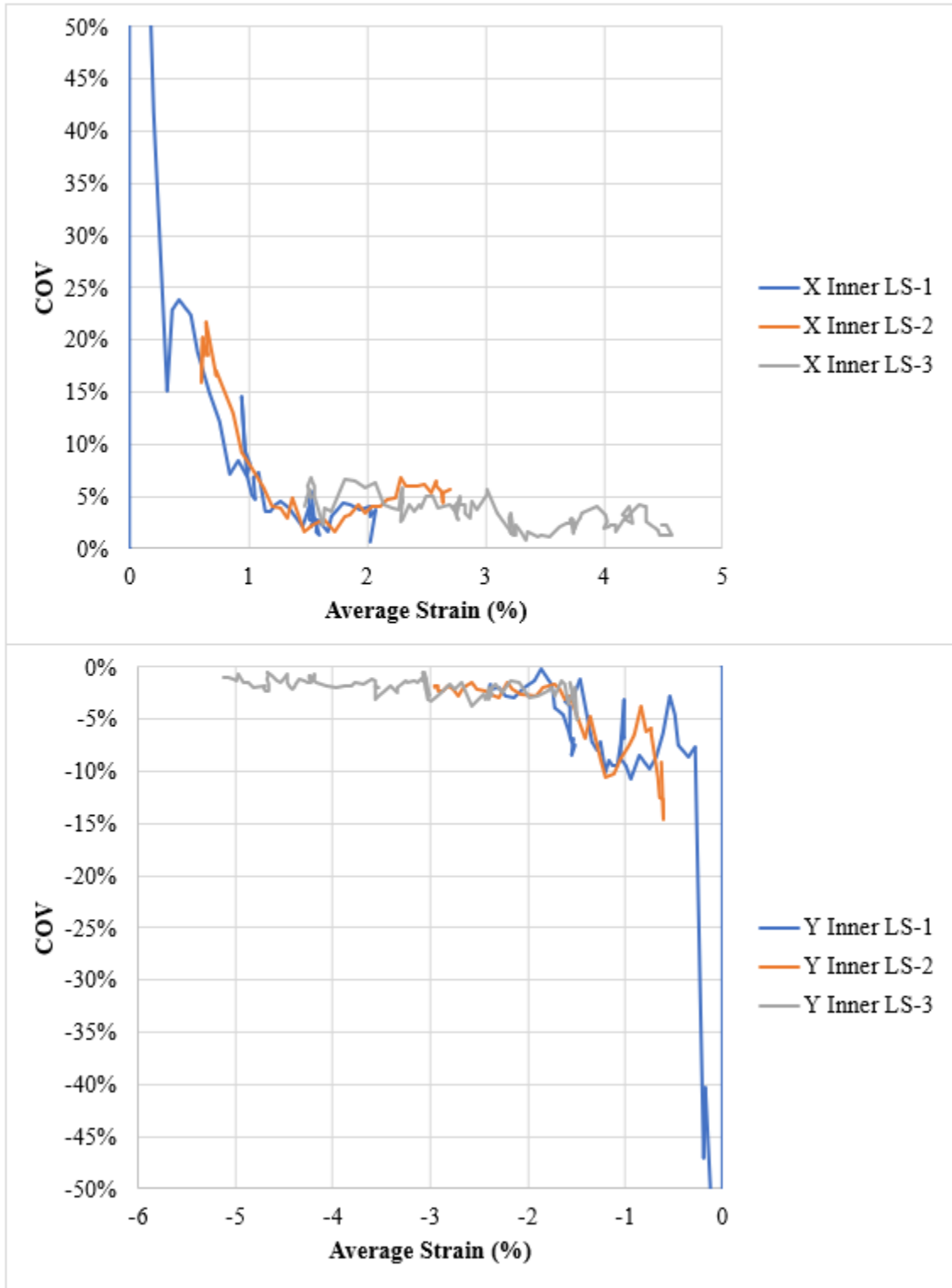


Figure 126: GgE bias trial 5.

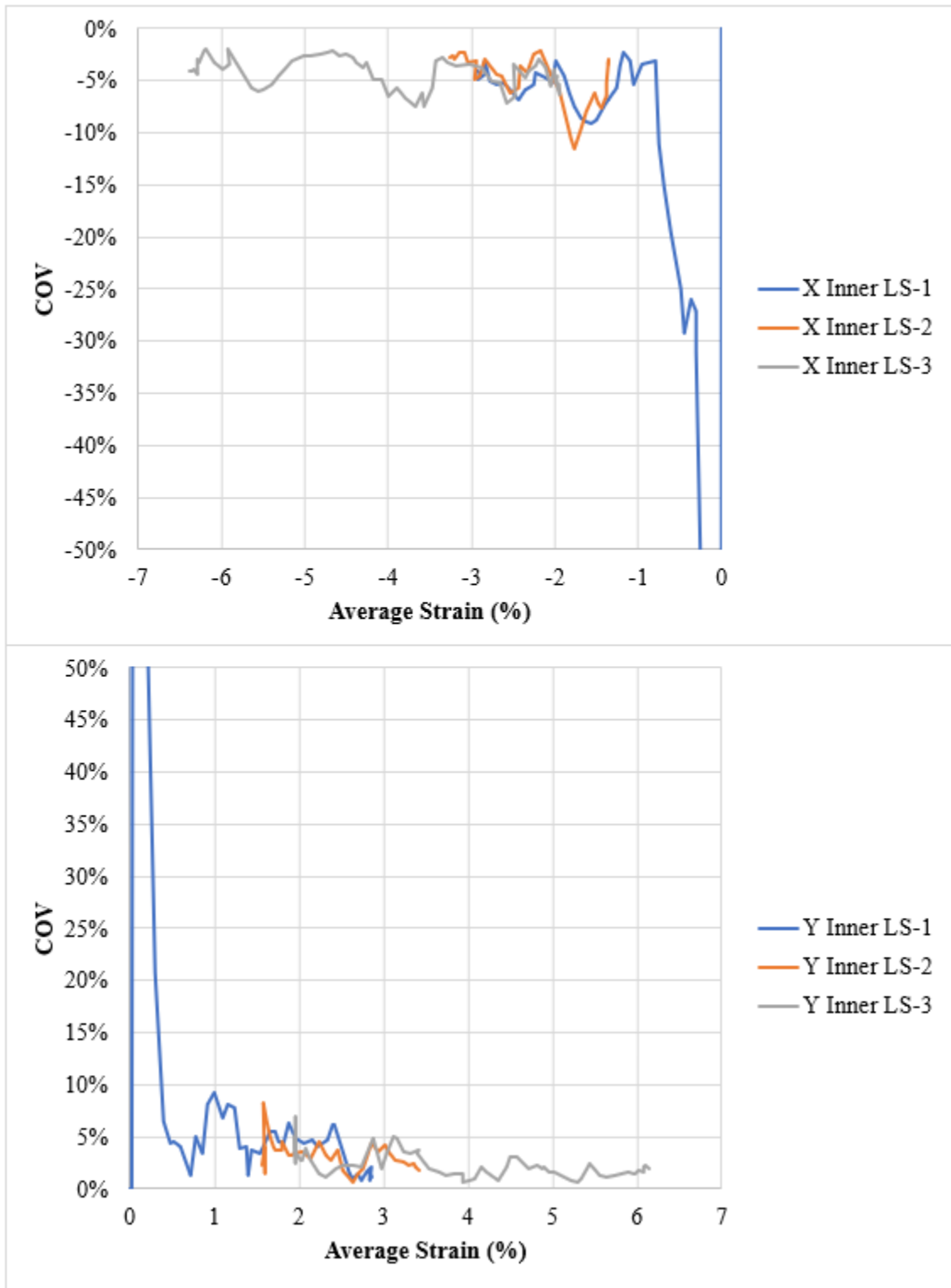


Figure 127: GgE bias trial 6 (Mode 3).

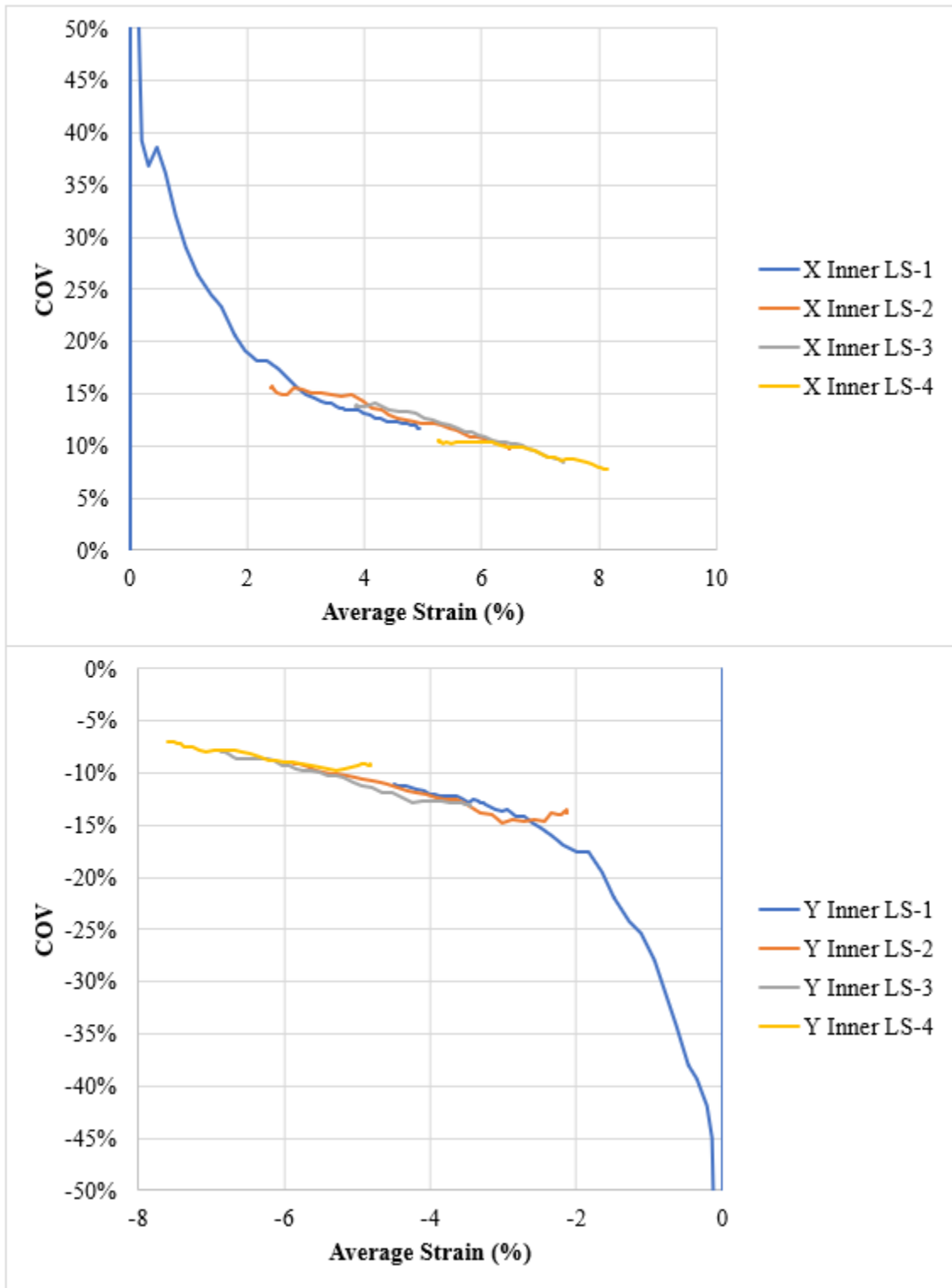


Figure 128: GtA bias trial 1 (no arm slits).

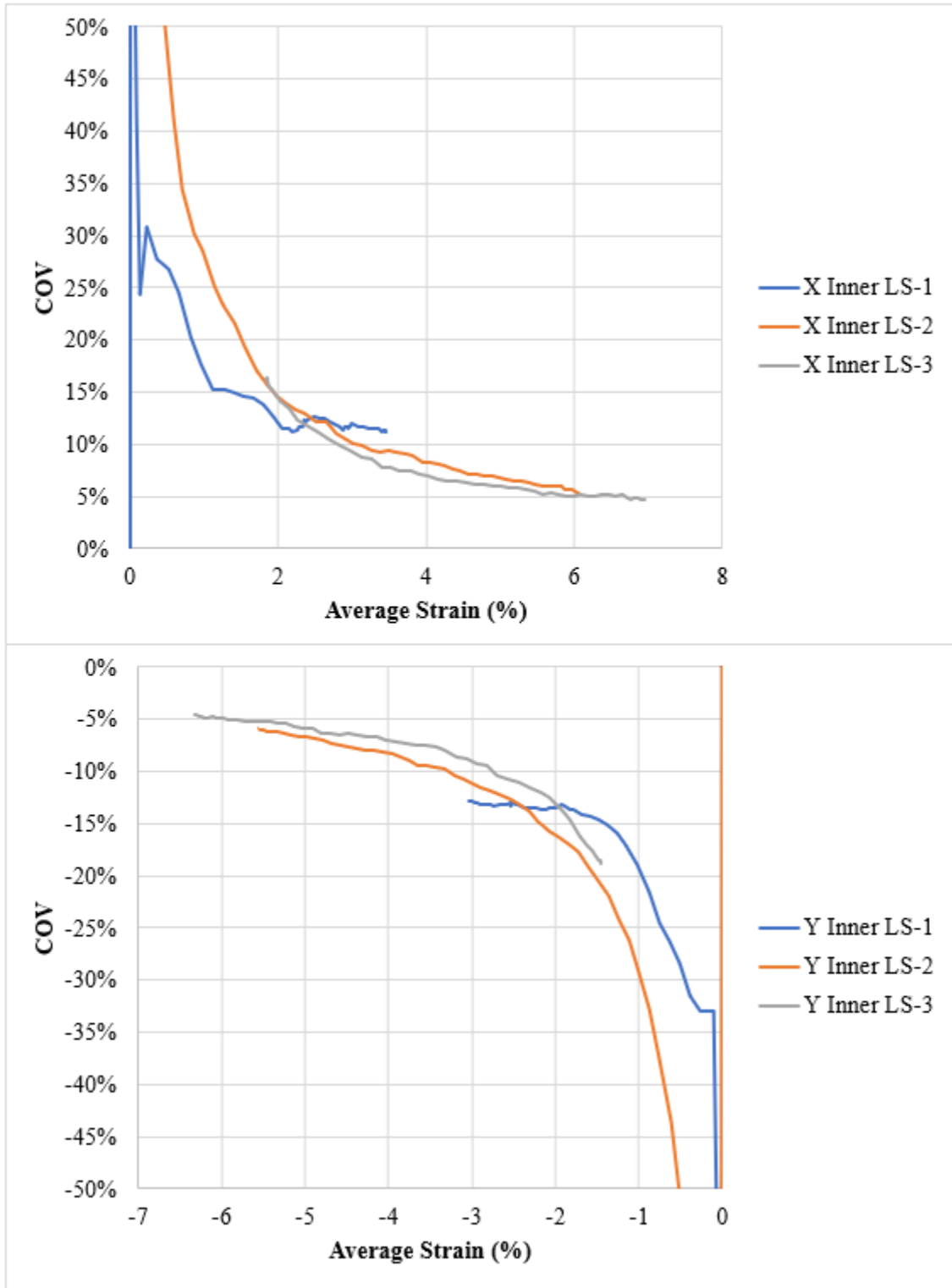


Figure 129: GtA bias trial 2.

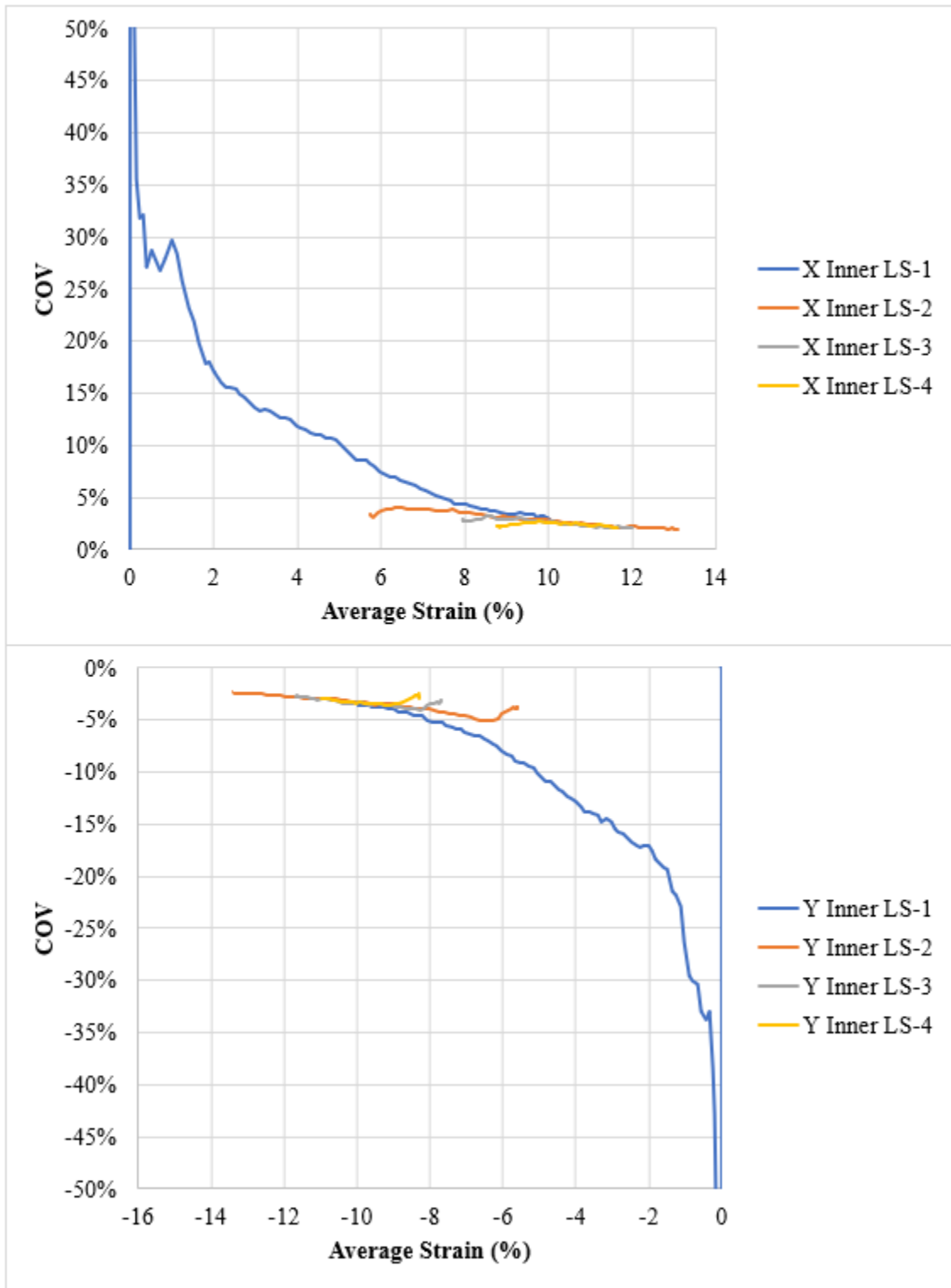


Figure 130: GtA bias trial 3.

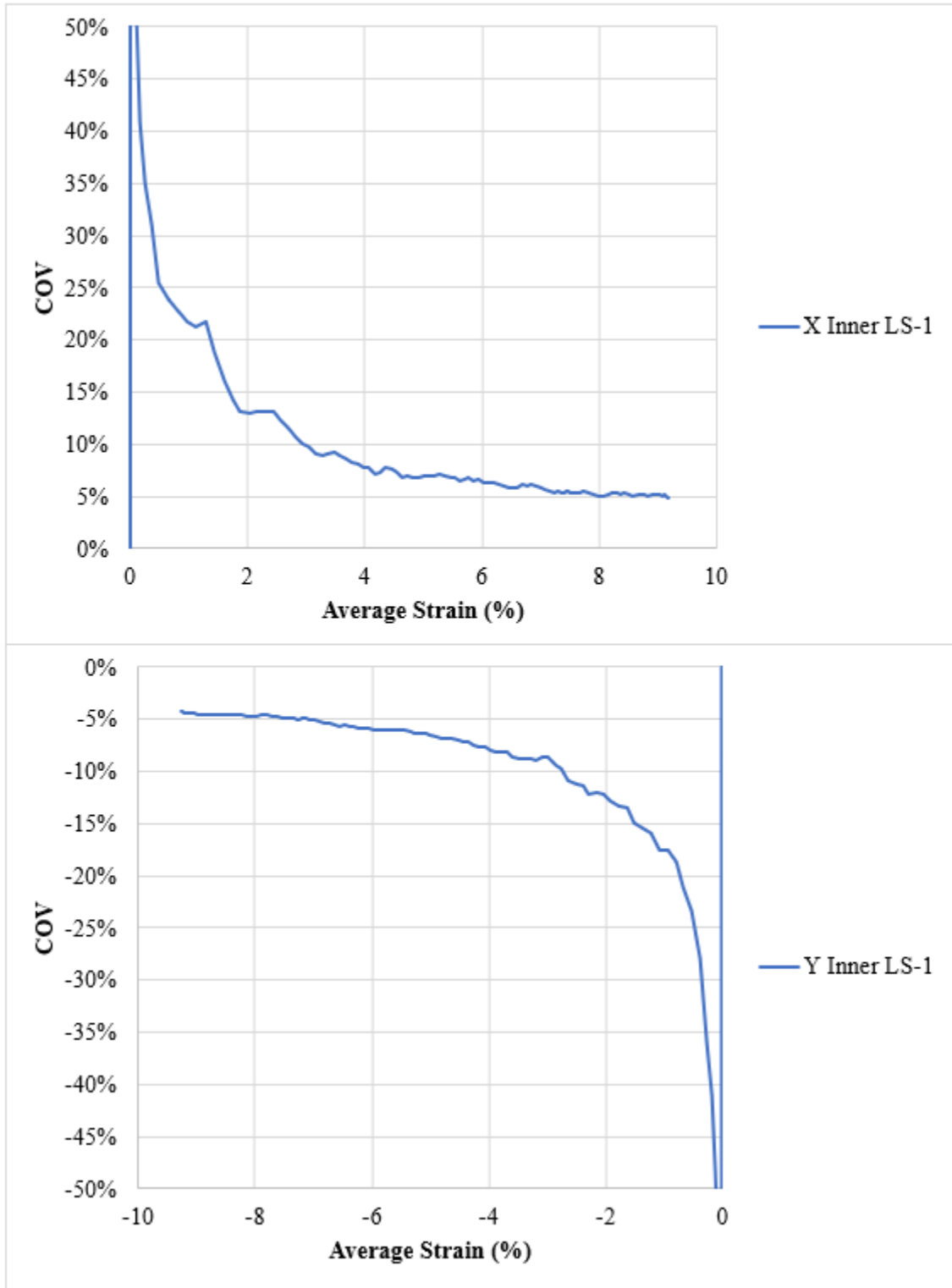


Figure 131: GtB bias trial 1 (only one load step).

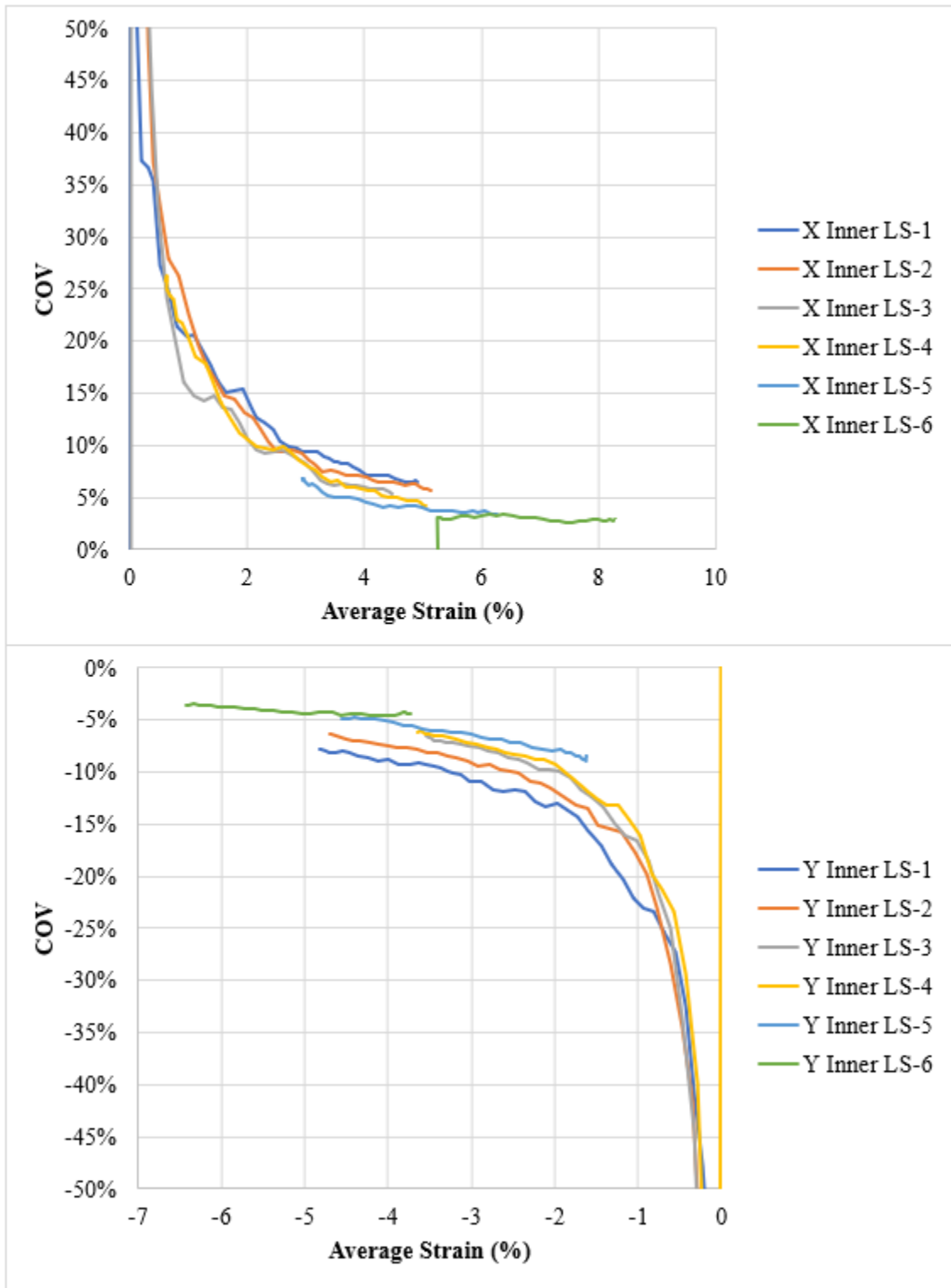


Figure 132: GtB bias trial 2.

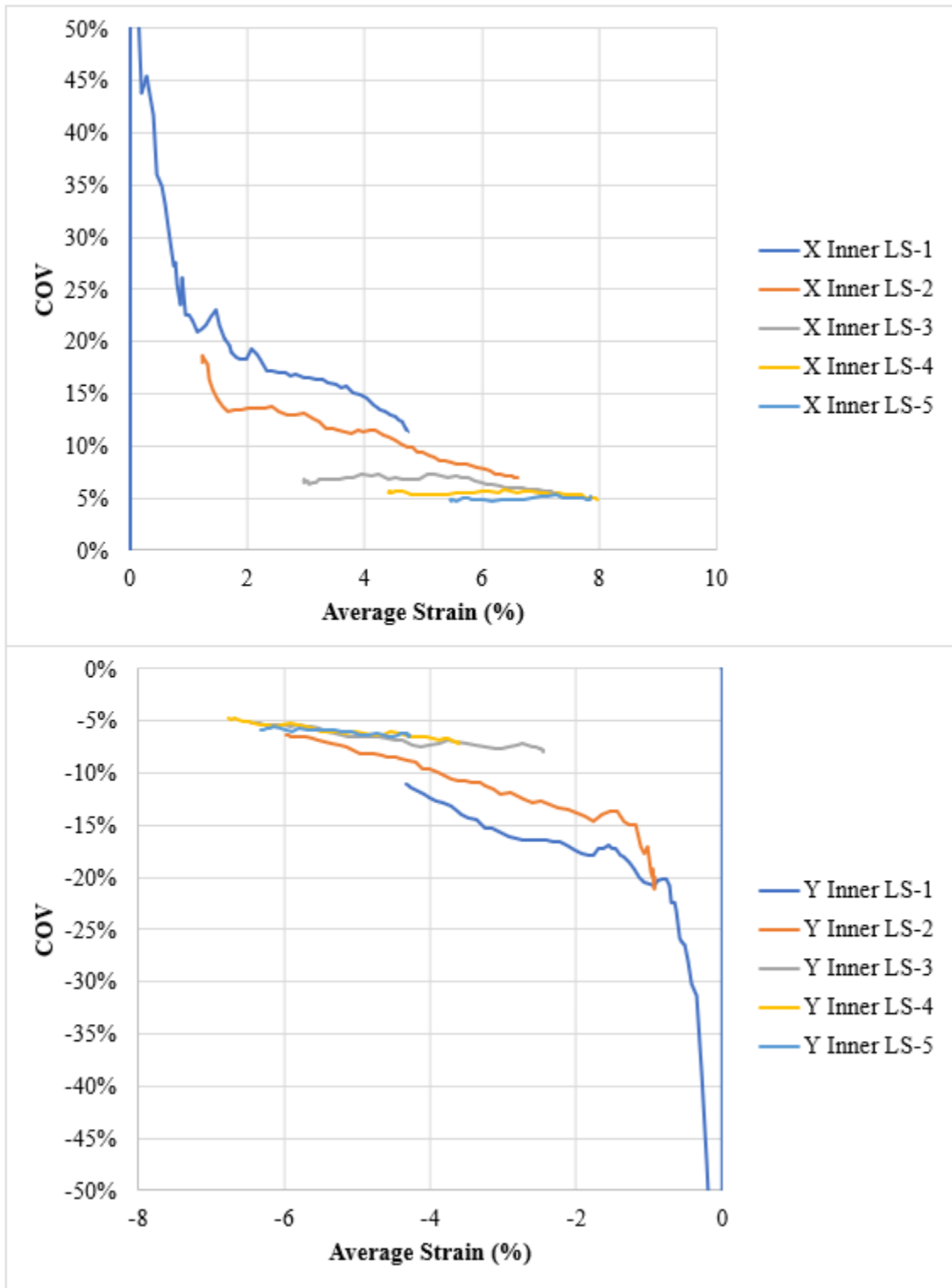


Figure 133: GtB bias trial 3.

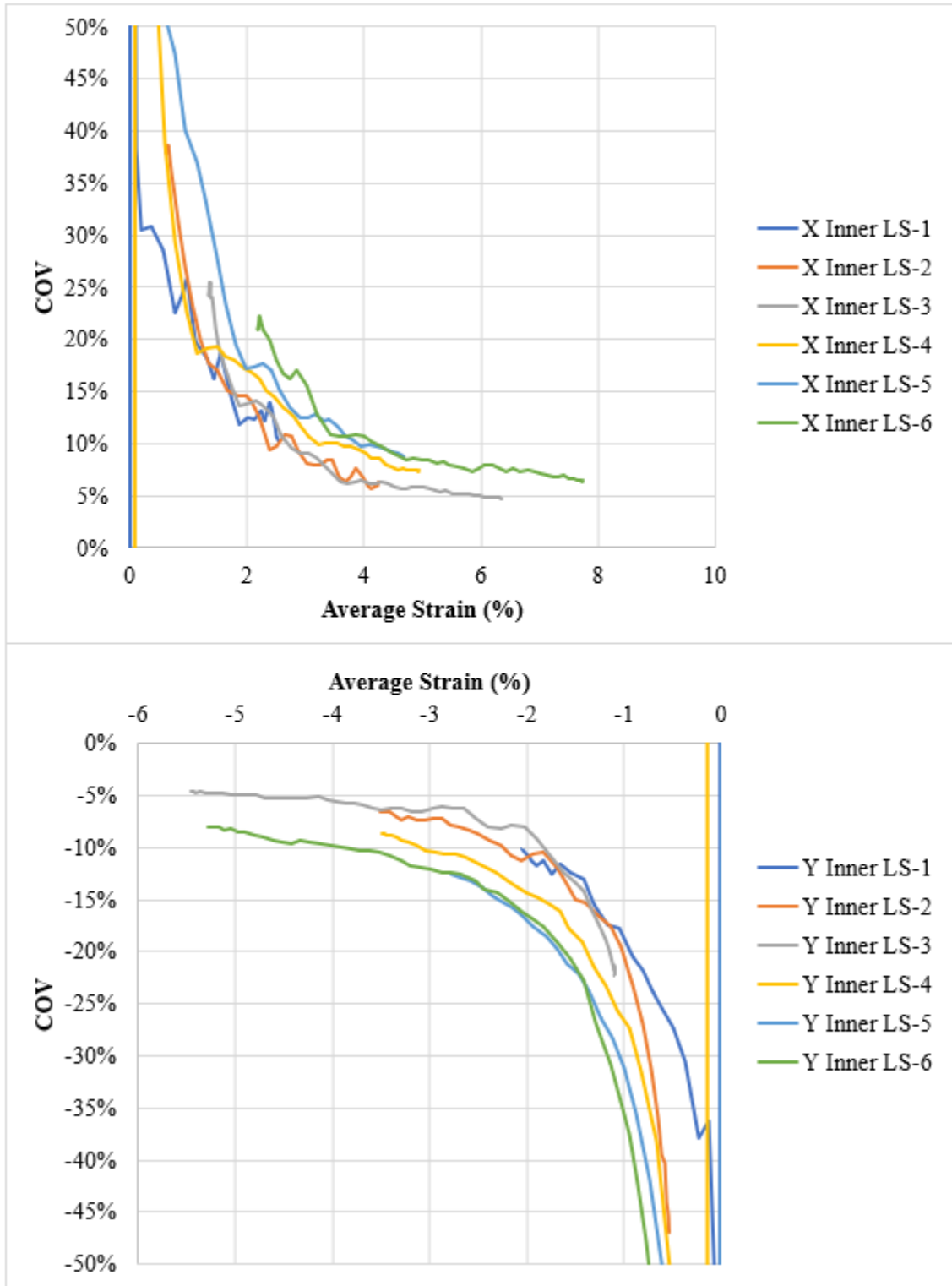


Figure 134: GtB bias trial 4.

APPENDIX B

SHEAR STRESS-STRAIN PLOTS

Overview

This appendix is organized by material architecture (rectangular geogrid, square geogrid, and geotextile), and then alphabetically by material ID (e.g. GgA). Each test specimen has its own plot containing all the load steps from that test as re-zeroed shear stress-strain data. All data is from the inner region (best strain uniformity).

Rough curves are present particularly in Geogrid A (Figure 135), Geogrid B (Figure 136), and Geogrid C bias trial 2 (Figure 138 bottom) due to biaxial device stalling and restarting during the load step. Geogrid D bias trial 2 (Figure 139 bottom) has a very short third load step due to running out of displacement range with the biaxial device. Geogrid E bias trials 1 and 2 were preliminary trials that were tested using Mode 1 loading, which was not conducive to shearing; consequently, these are not included in the dataset.

The wide spread of modulus slopes in most of the geotextile trials suggests that shear lock-up was occurring in the later load steps as discussed in Chapter Six. Geotextile A bias trial 1 (Figure 142) had no arm slits; this was subsequently changed for the rest of the geotextile tests. Geotextile B bias trial 1 (Figure 144 top) strained much more than expected, and only one load step was reached. For the rest of the Geotextile B trials, an additional coat of glue helped to stiffen the arms and reduce necking such that up to six load steps could be achieved.

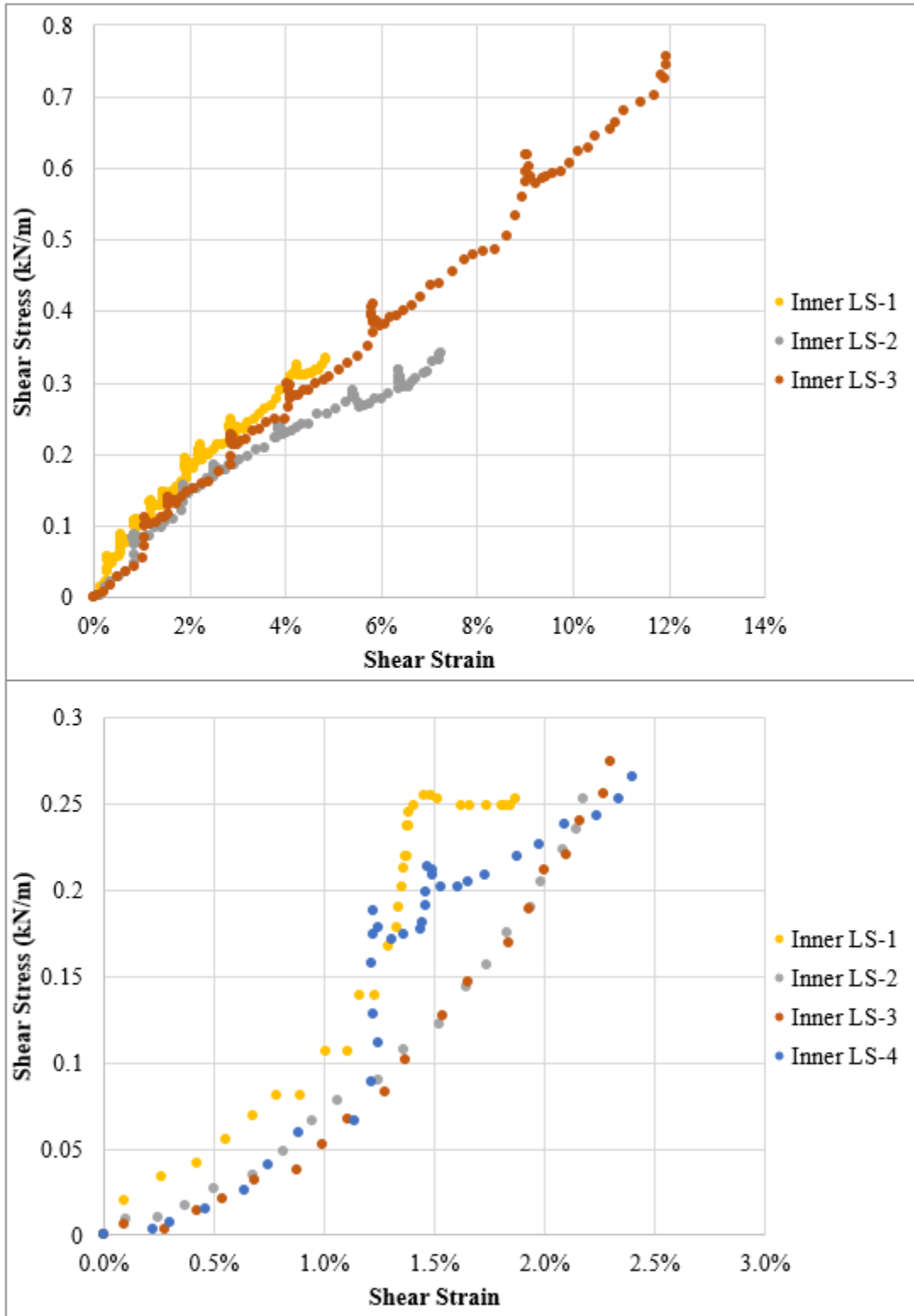


Figure 135 Top: GgA bias trial 1. Bottom: GgA bias trial 2.

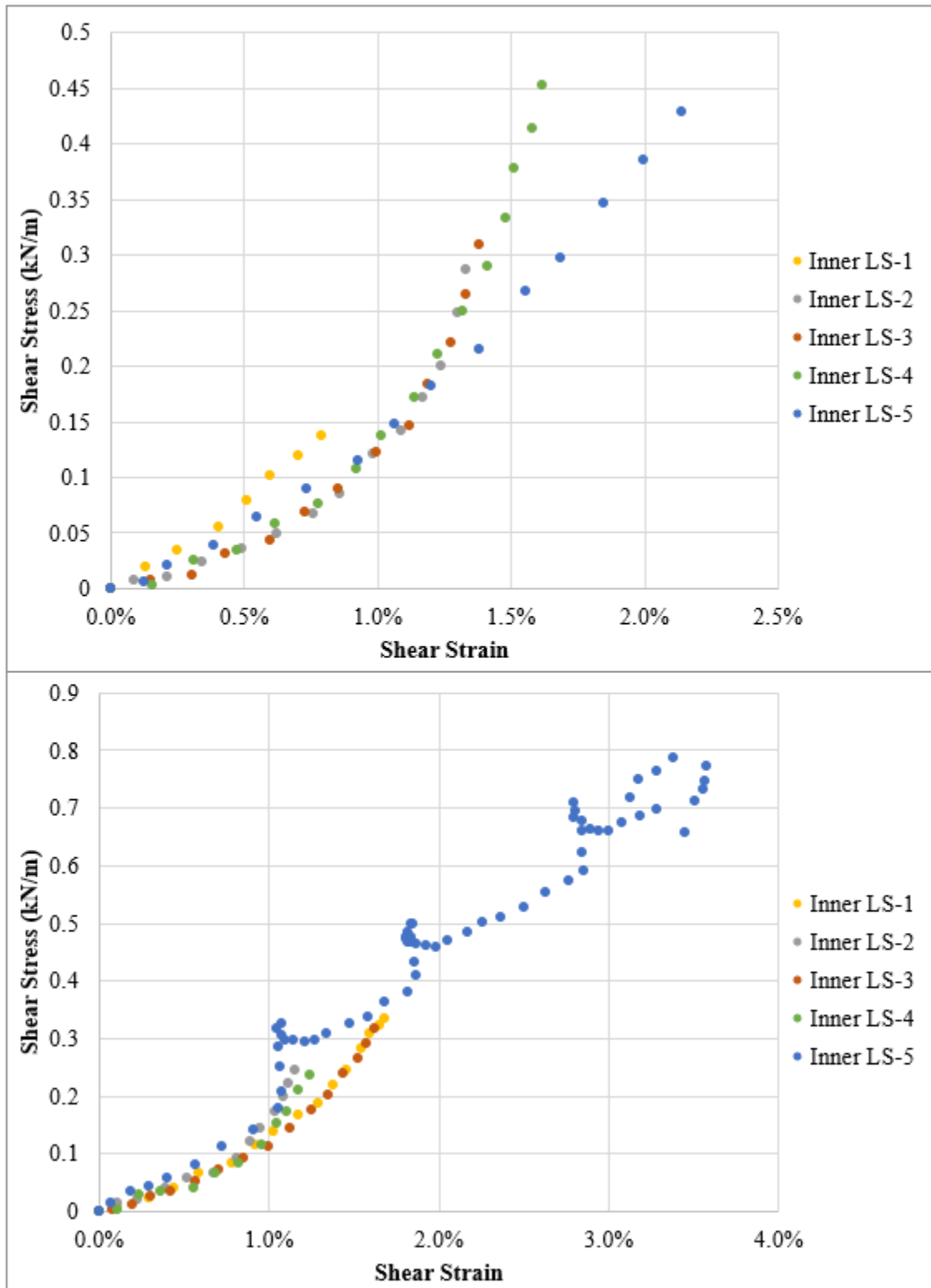


Figure 136 Top: GgB bias trial 1. Bottom: GgB bias trial 2.

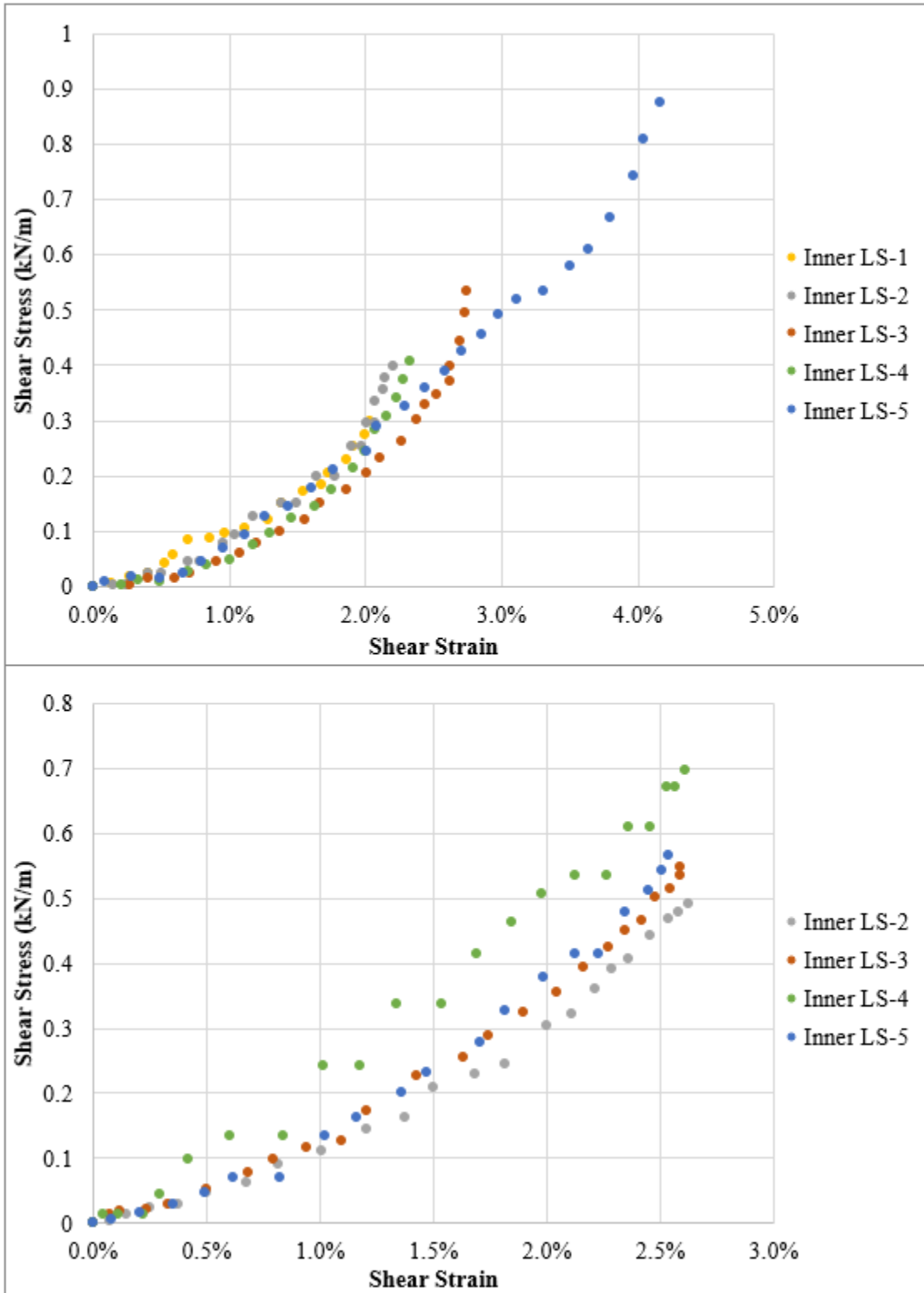


Figure 137 Top: GgF bias trial 1. Bottom: GgF bias trial 2.

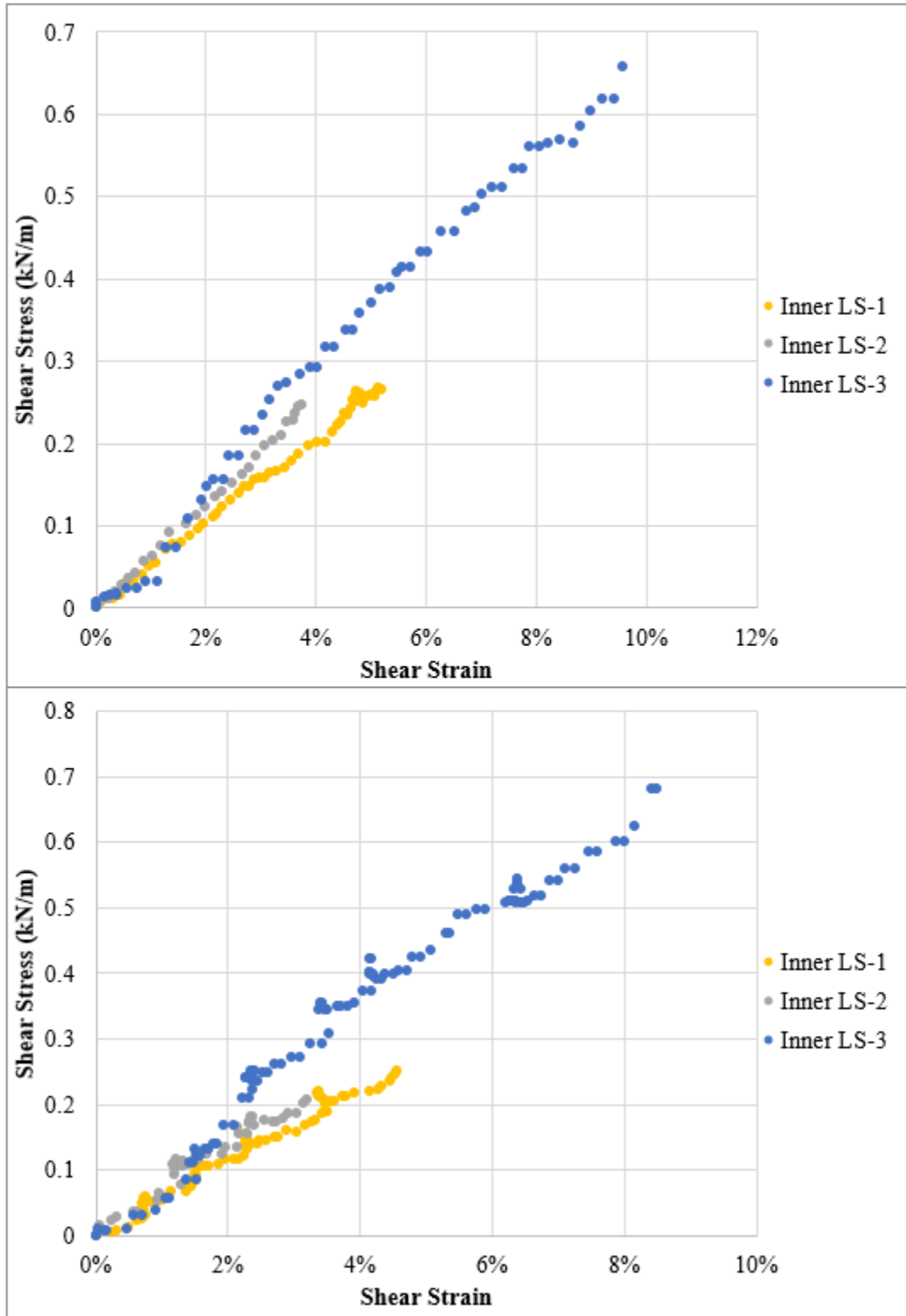


Figure 138 Top: GgC bias trial 1. Bottom: GgC bias trial 2.

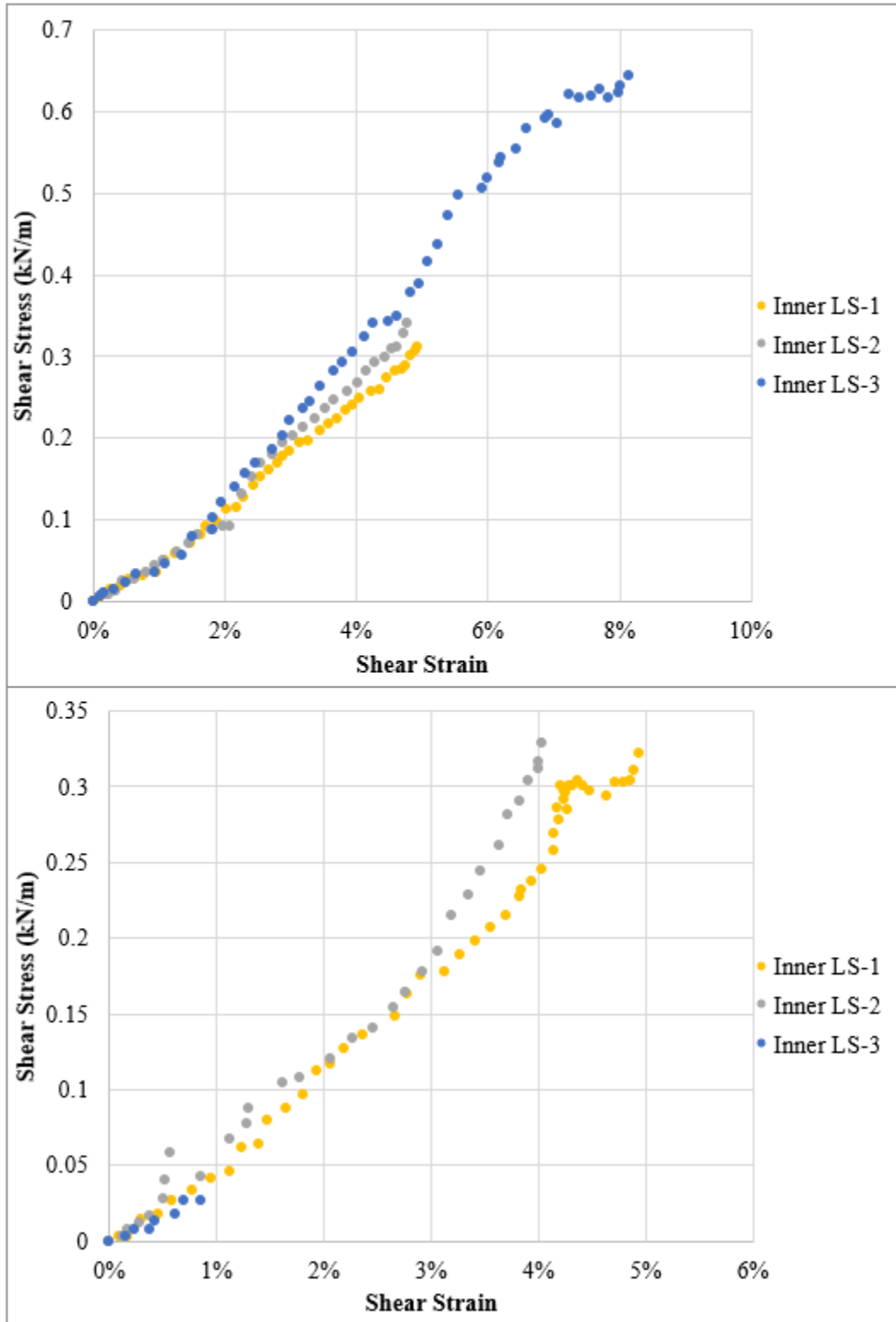


Figure 139 Top: GgD bias trial 1. Bottom: GgD bias trial 2.

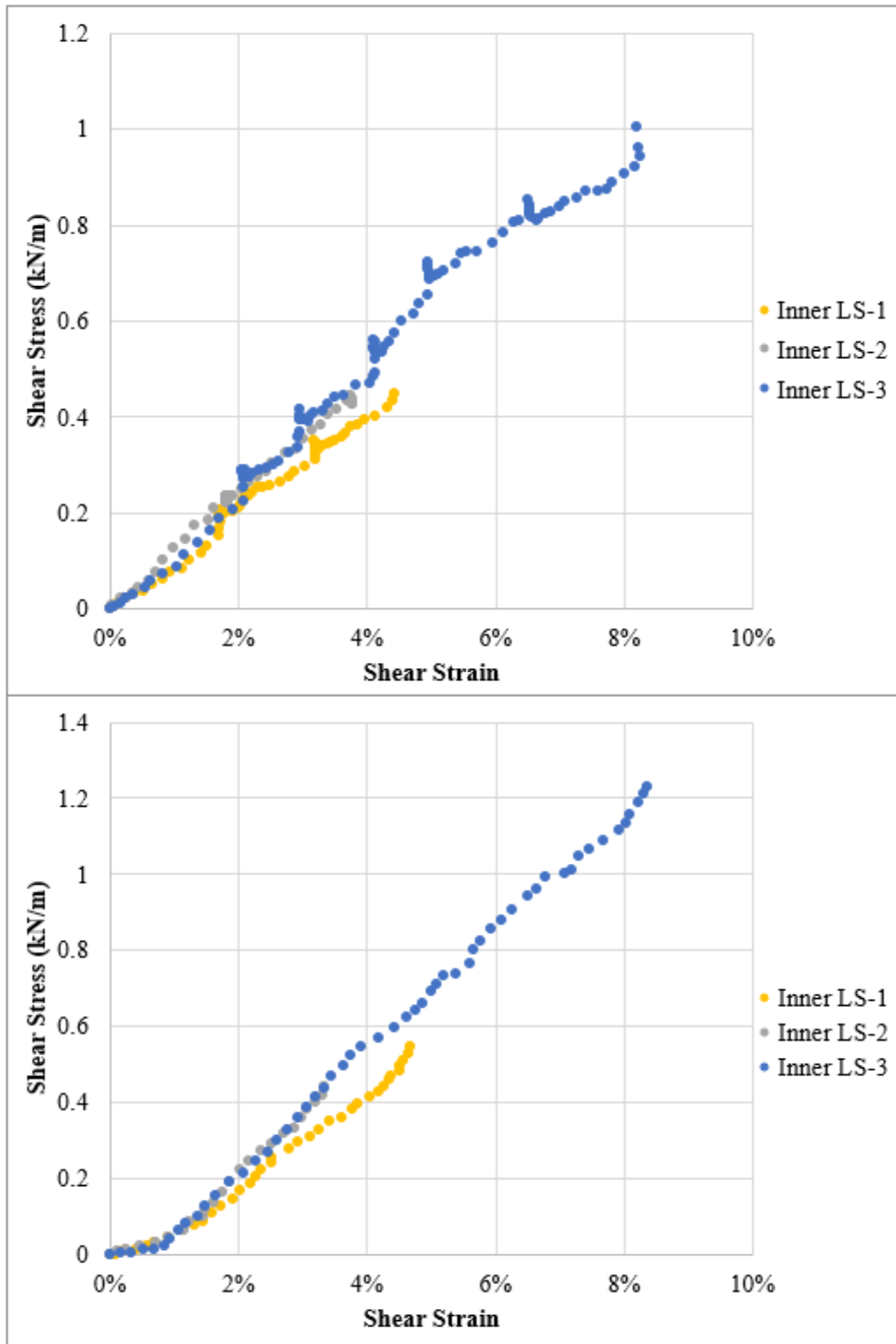


Figure 140 Top: GgE bias trial 3. Bottom: GgE bias trial 4.

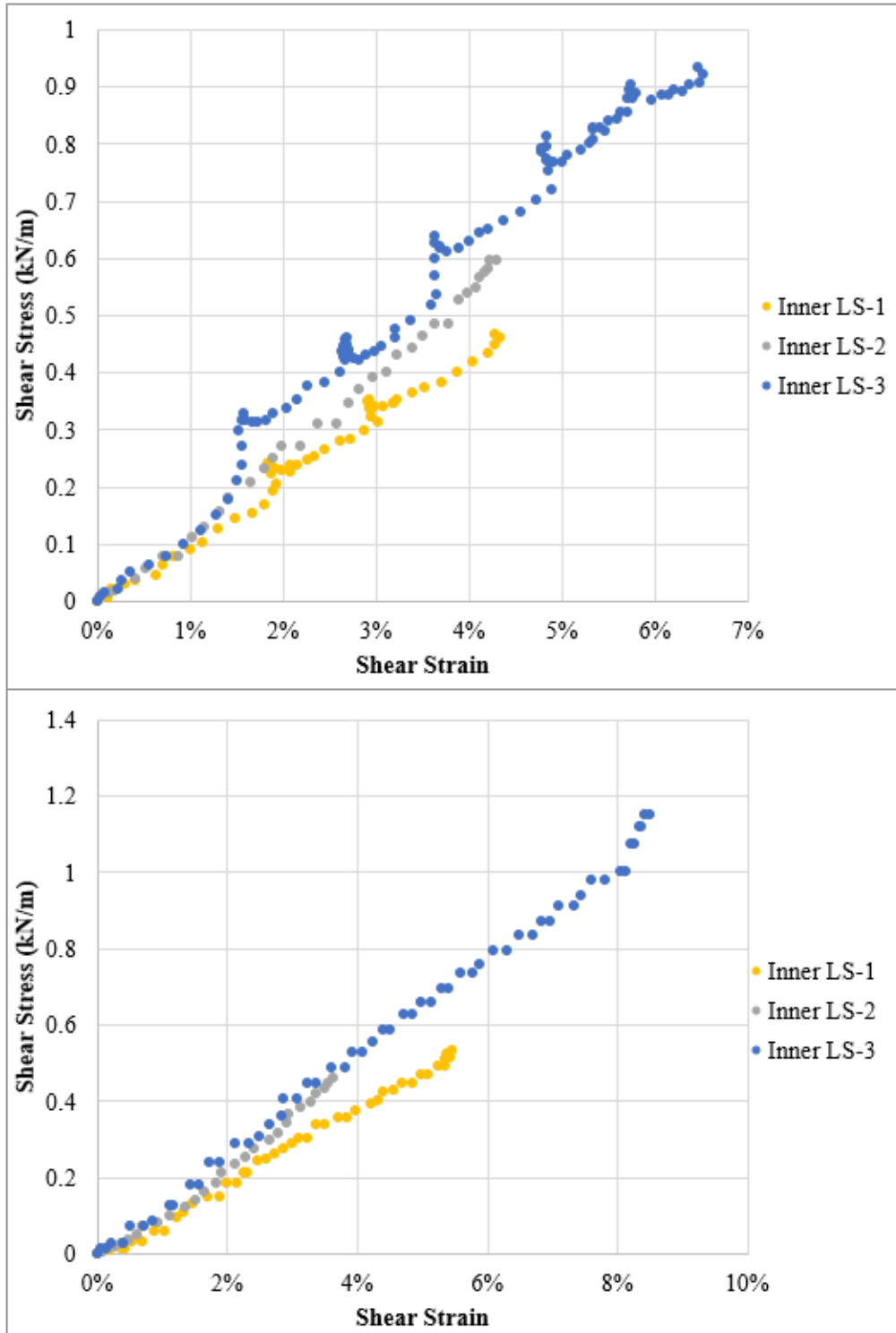


Figure 141 Top: GgE bias trial 5. Bottom: GgE bias trial 6.

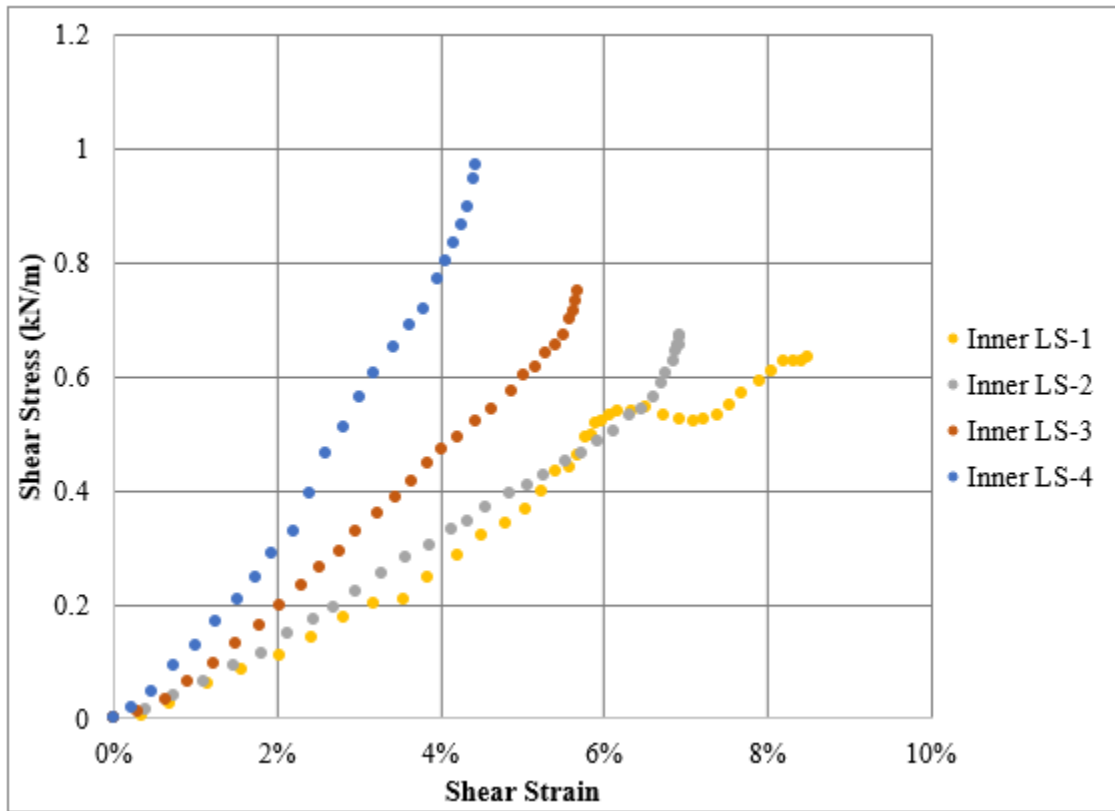


Figure 142: GtA bias trial 1.

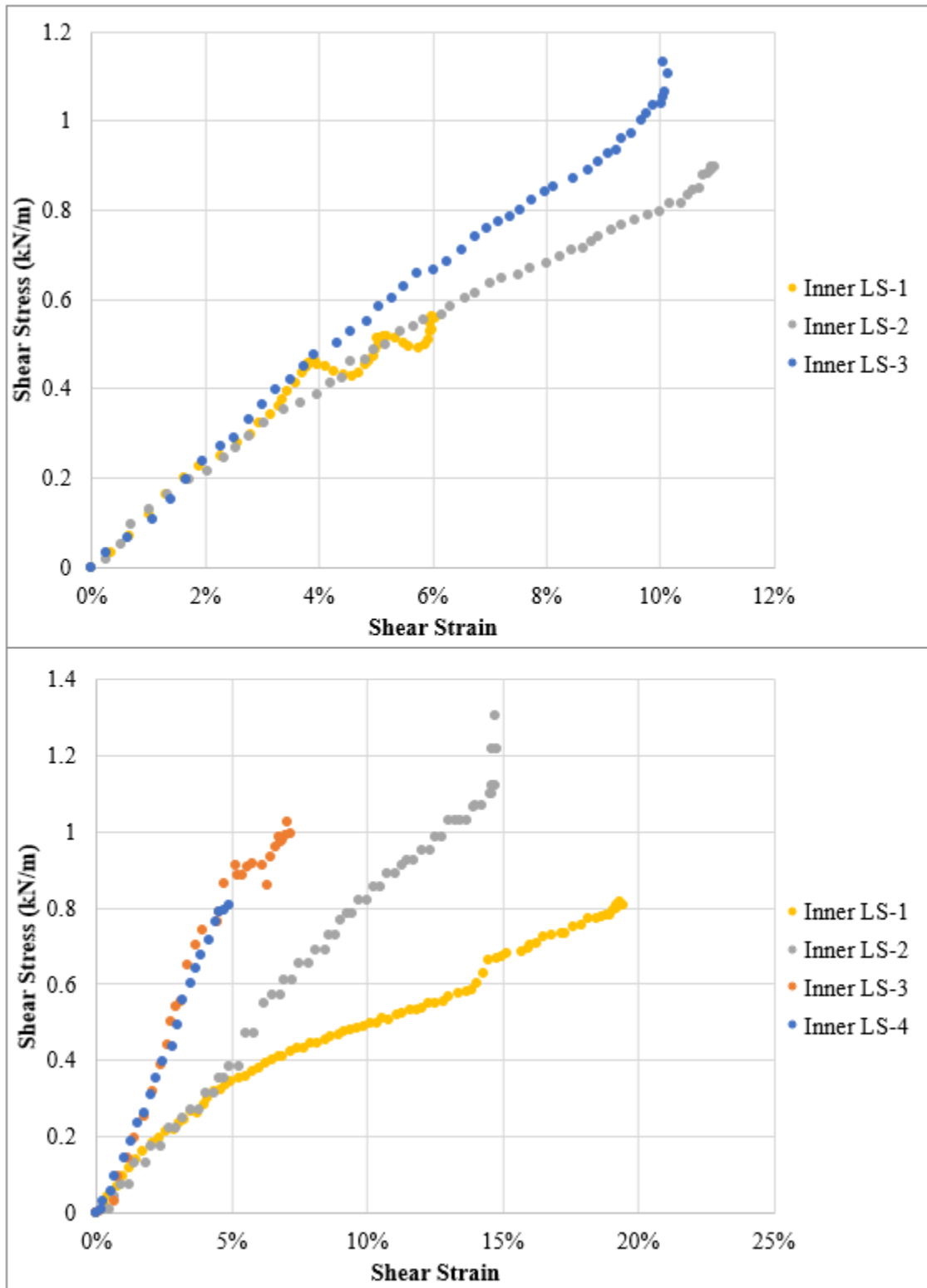


Figure 143 Top: GtA bias trial 2. Bottom: GtA bias trial 3.

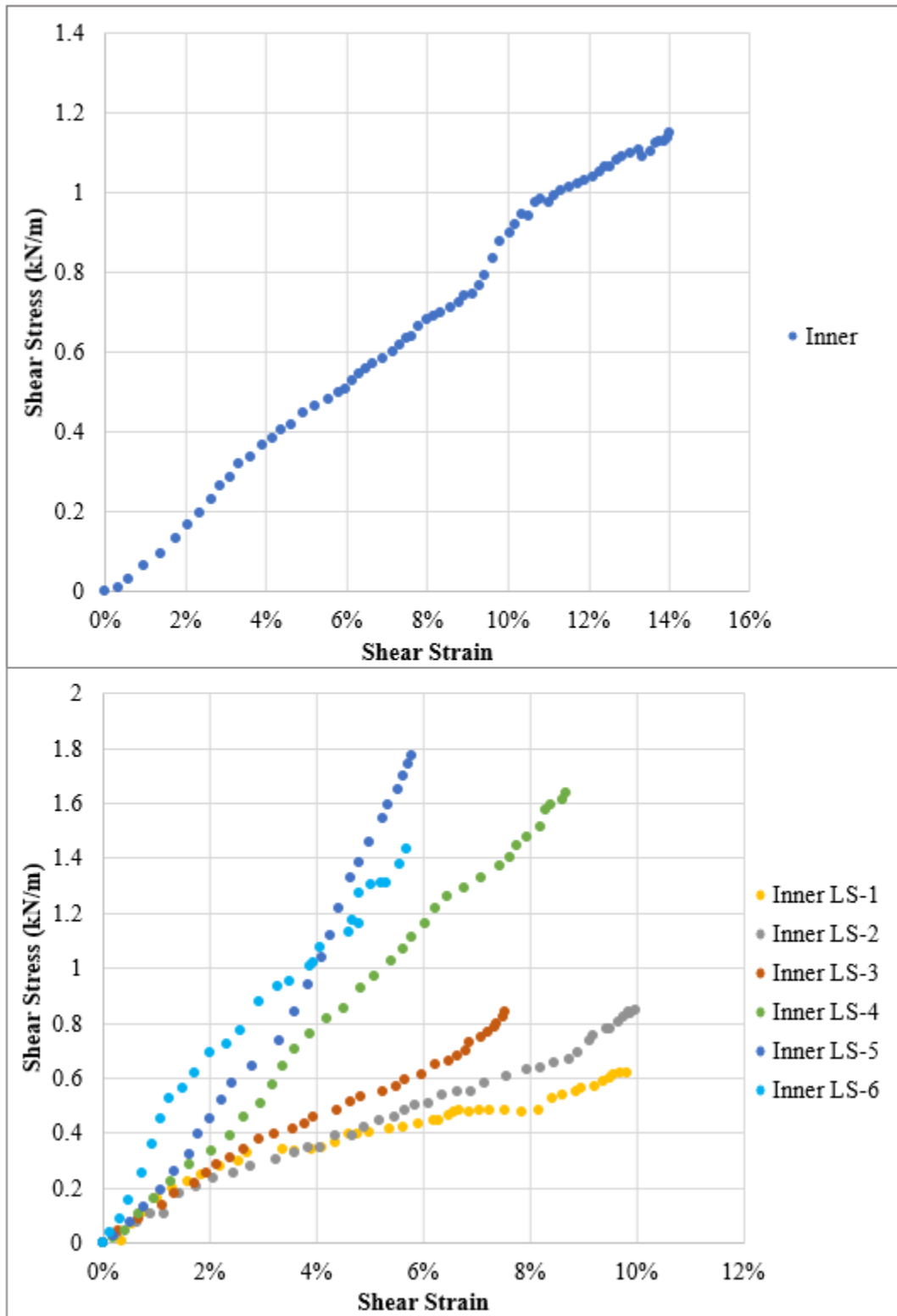


Figure 144 Top: GtB bias trial 1. Bottom: GtB bias trial 2.

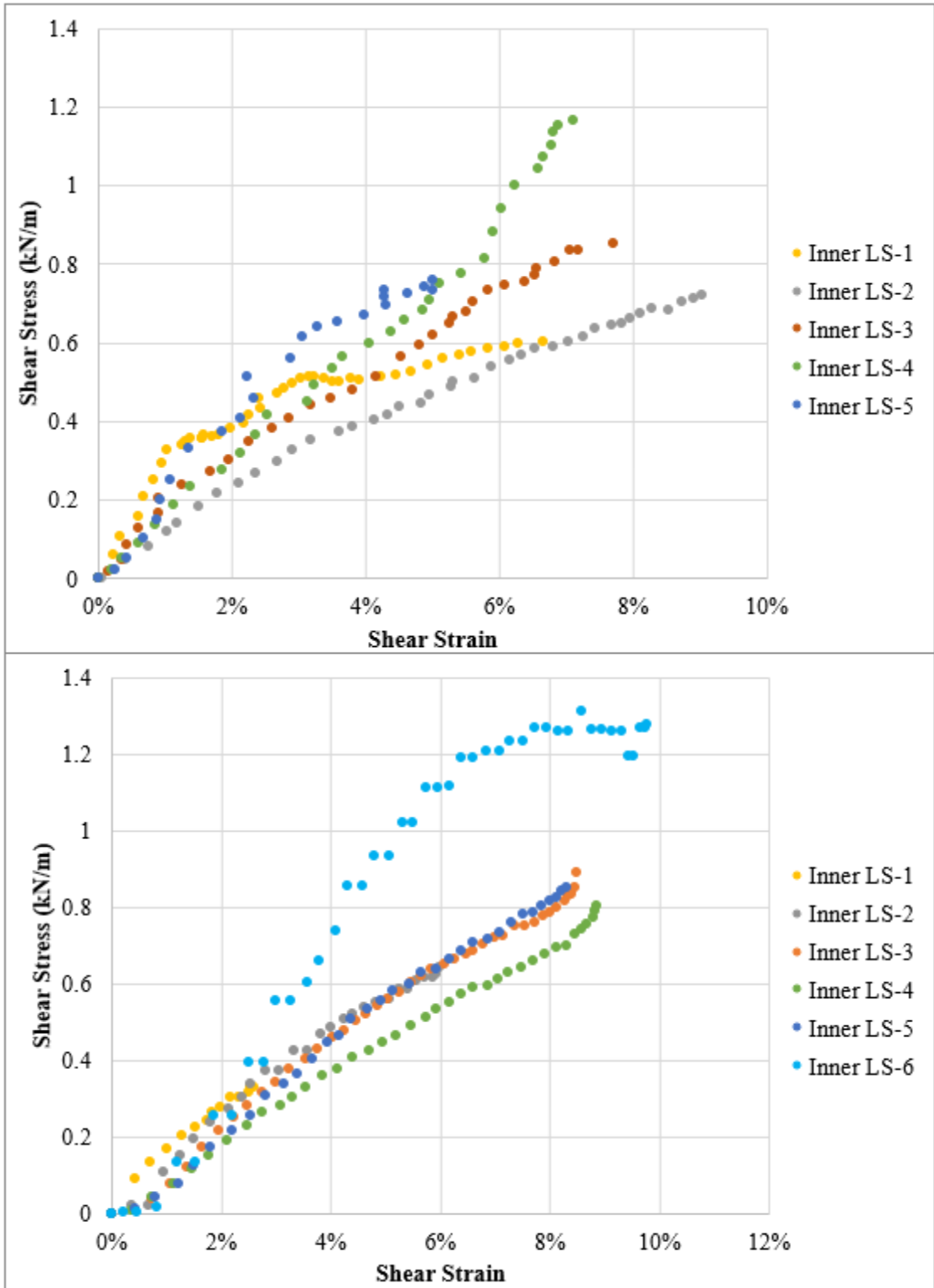


Figure 145 Top: GtB bias trial 3. Bottom: GtB bias trial 4.

APPENDIX C

SHEAR MODULUS TRENDLINE FIT PLOTS

Overview

This appendix is organized by material architecture (rectangular geogrid, square geogrid, and geotextile), and then alphabetically by material ID (e.g. GgA). Each material has three plots corresponding to the three different shear strain ranges evaluated. These plots are listed in the following order: 1-5% shear strain, 1-2.5% shear strain, and 1-2% shear strain. All plots contain shear stress-strain data from the inner region with a linear best-fit trendline for each load step. Trendline equations and  $R^2$  values are listed in columns following the same order as the load steps (LS) in each plot legend. Trendline slopes (shear modulus values) and  $R^2$  values are summarized in Chapter Six, pages 167-171 (Table 12 and Figure 99 through Figure 101).

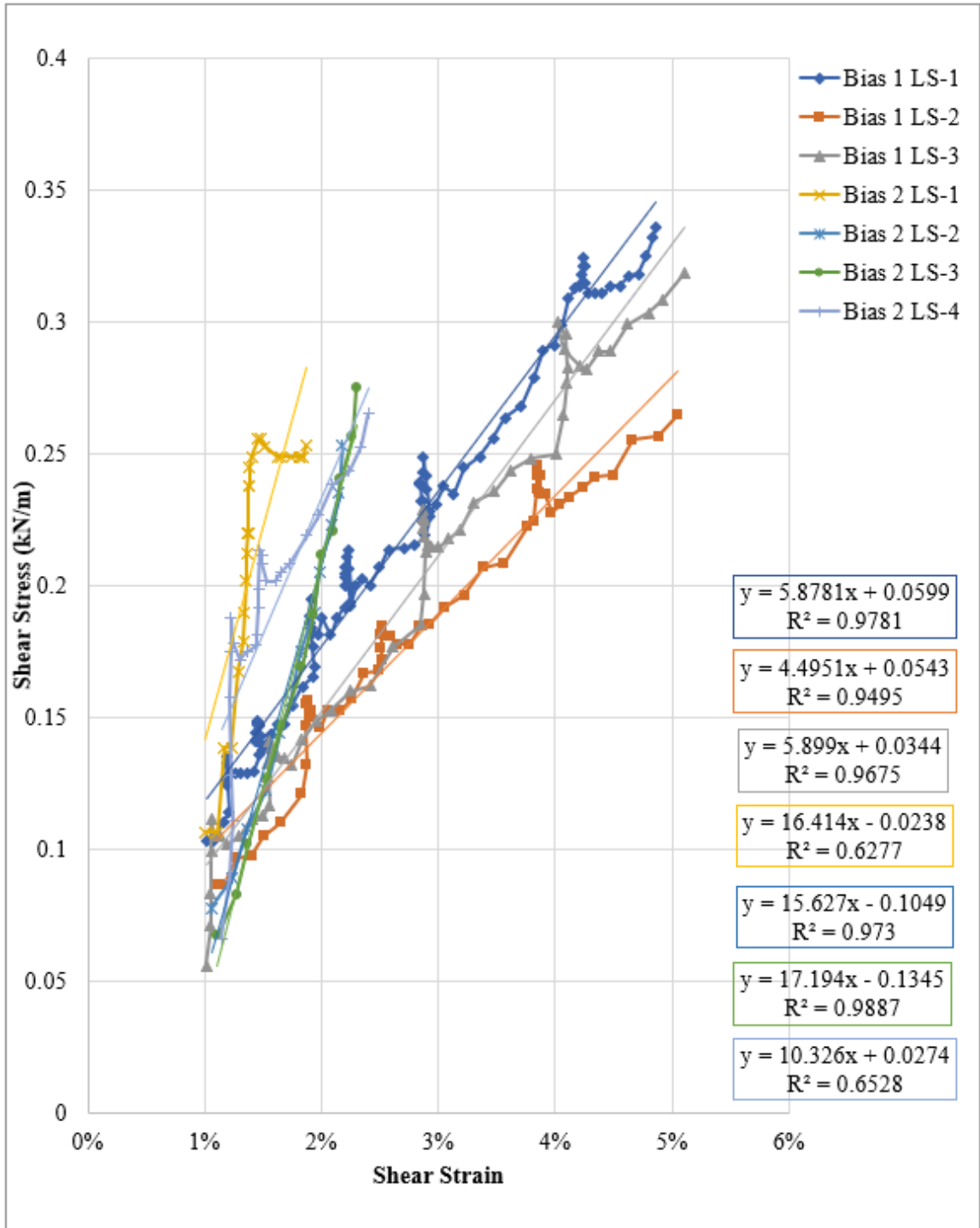


Figure 146: GgA bias trials 1-2, 1-5% shear strain range.

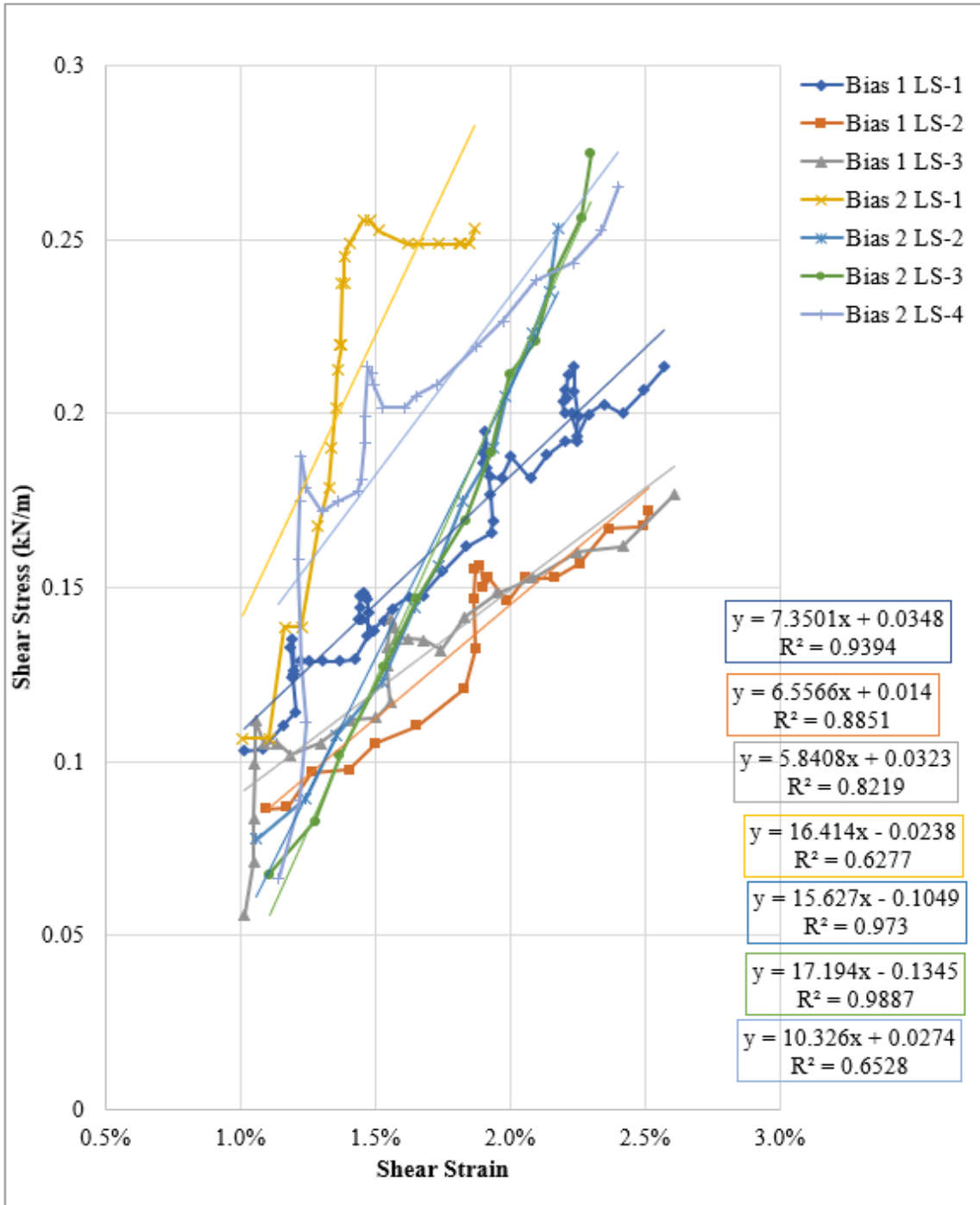


Figure 147: GgA bias trials 1-2, 1-2.5% shear strain range.

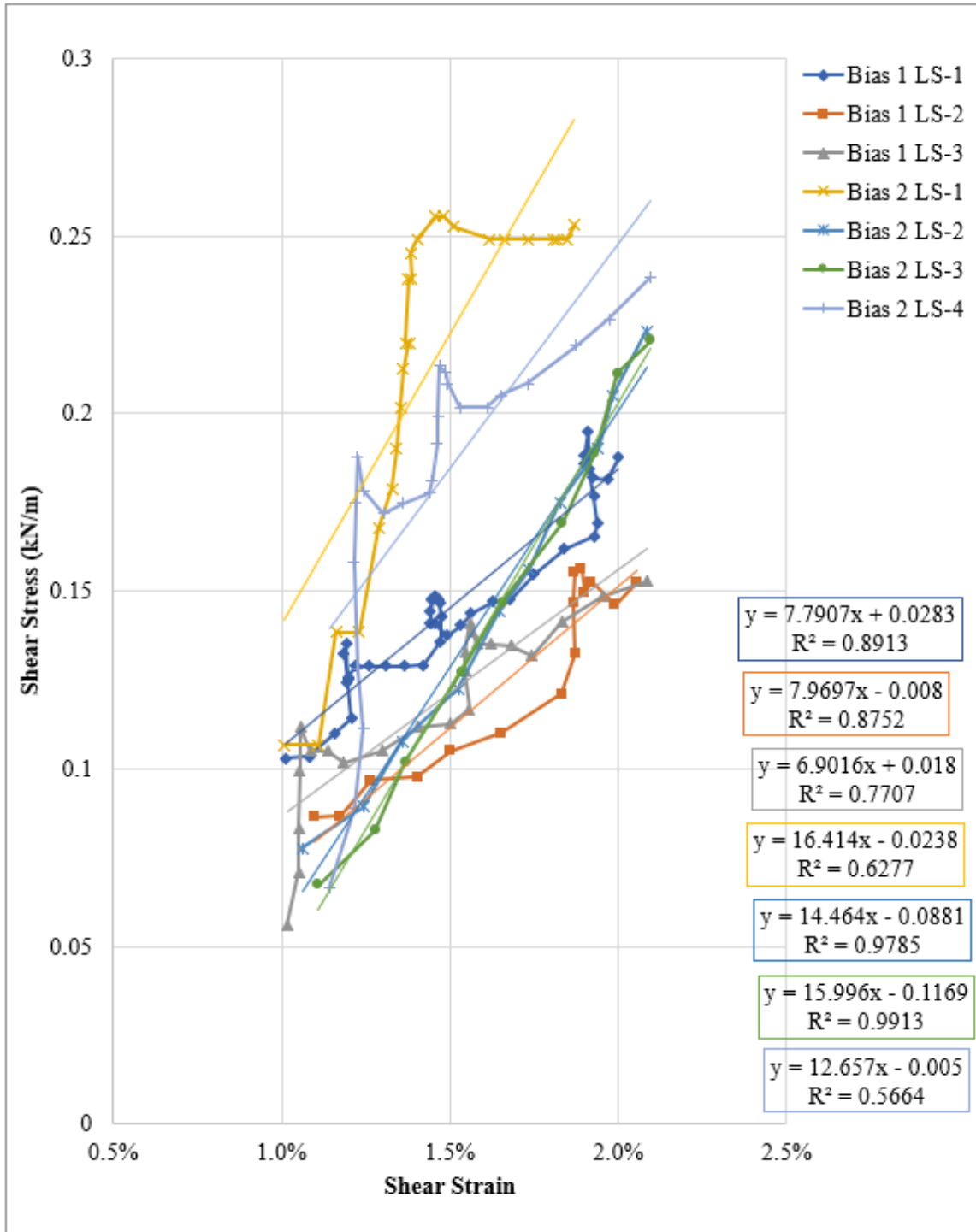


Figure 148: GgA bias trials 1-2, 1-2% shear strain range.

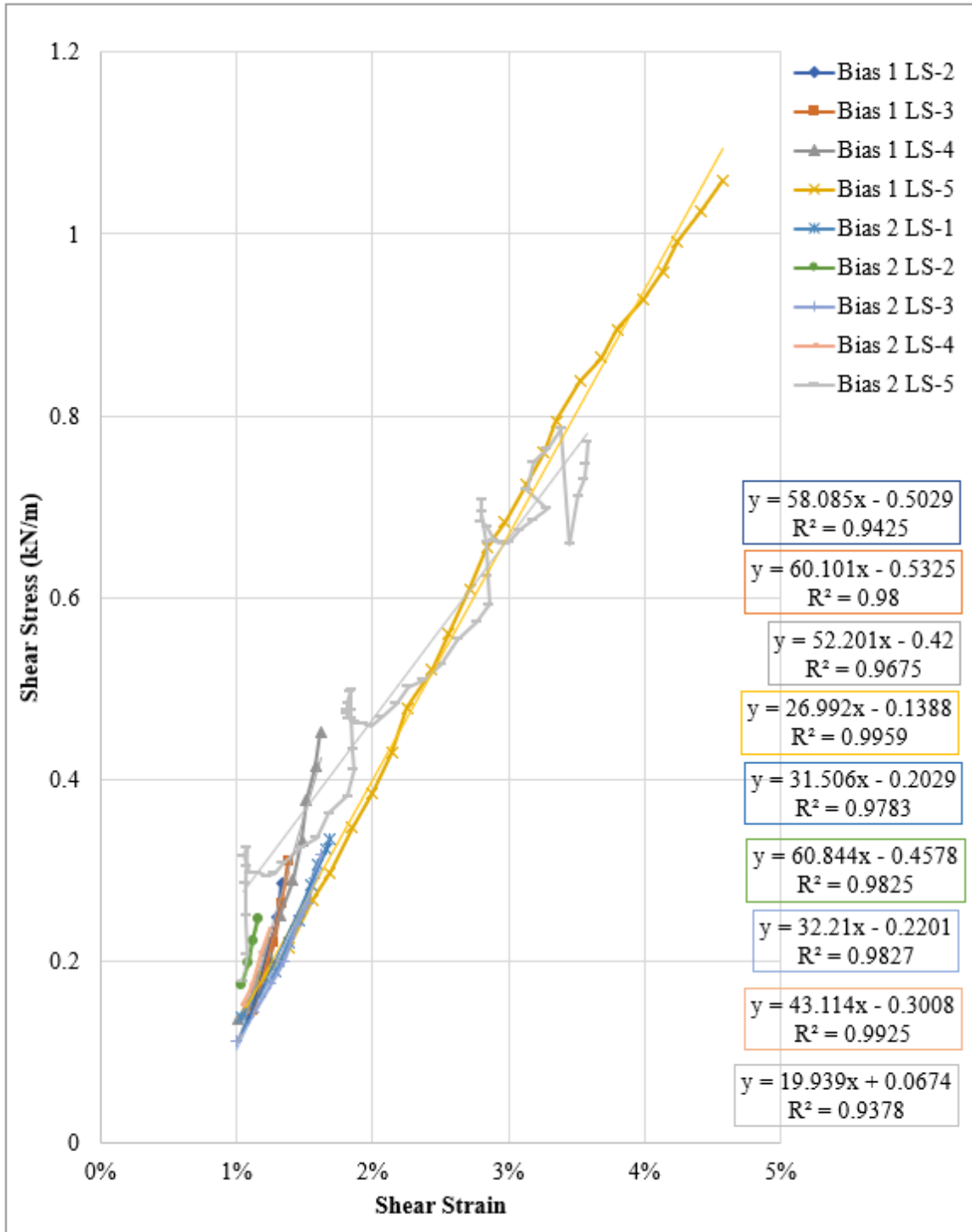


Figure 149: GgB bias trials 1-2, 1-5% shear strain range.

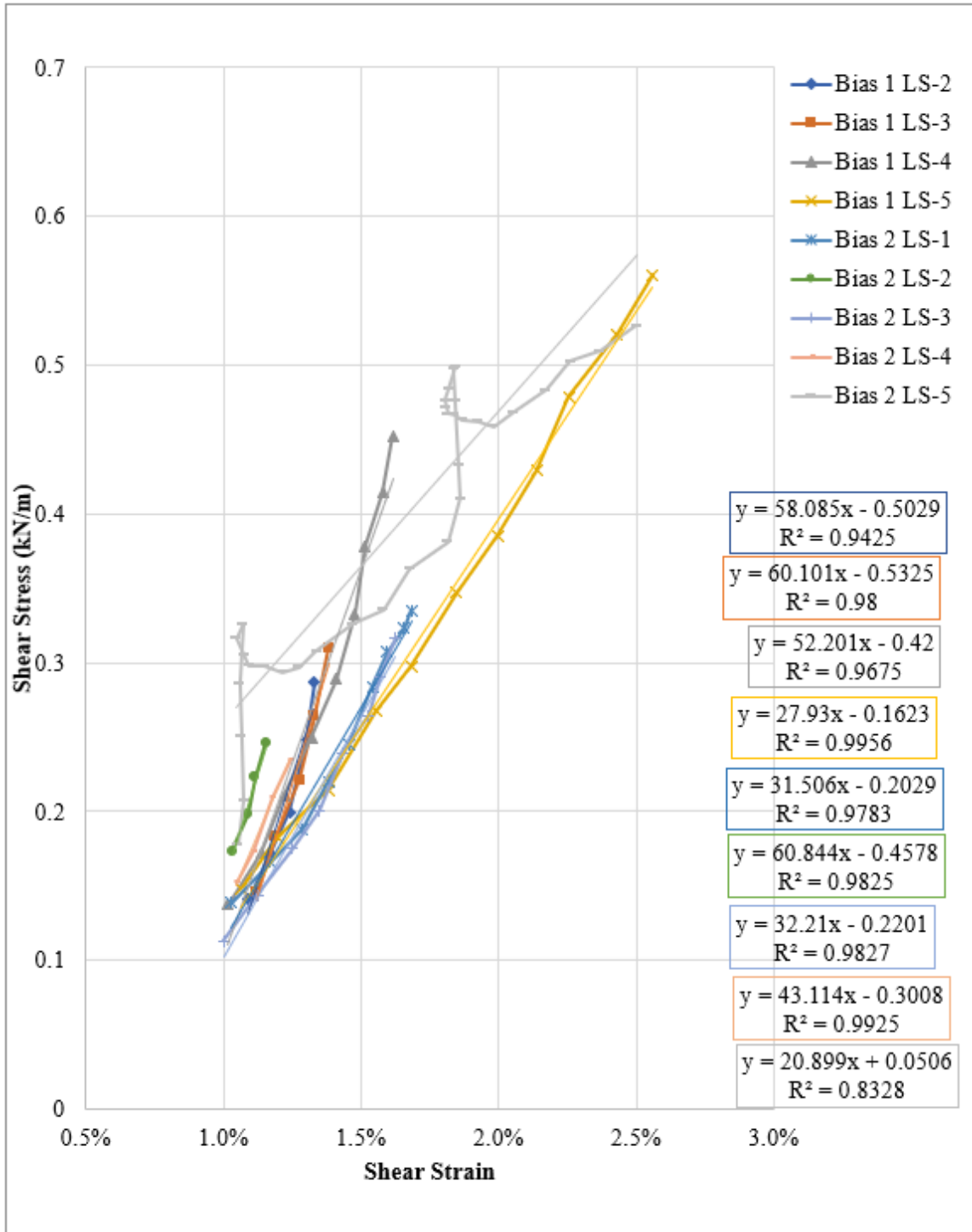


Figure 150: GgB bias trials 1-2, 1-2.5% shear strain range.

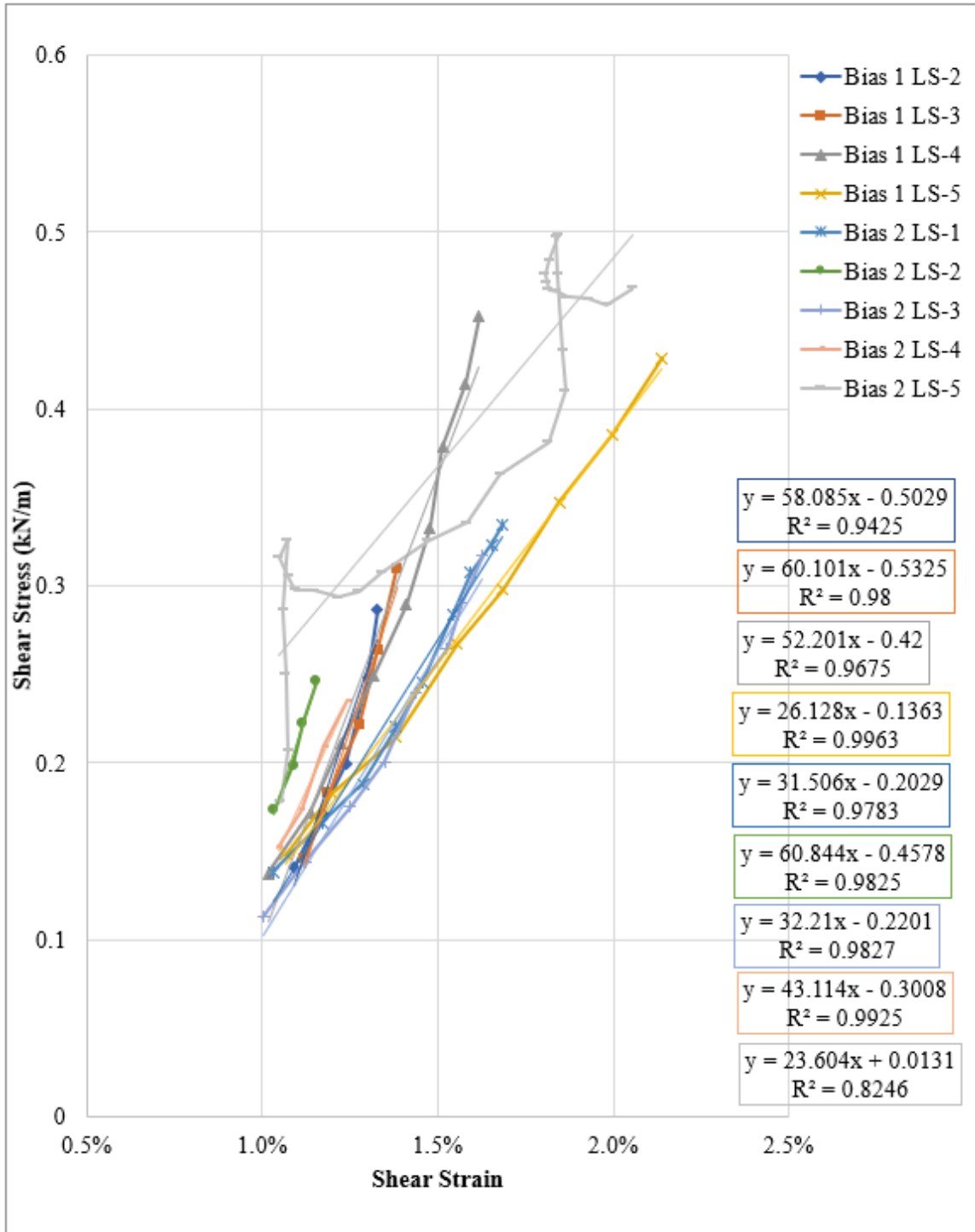


Figure 151: GgB bias trials 1-2, 1-2% shear strain range.

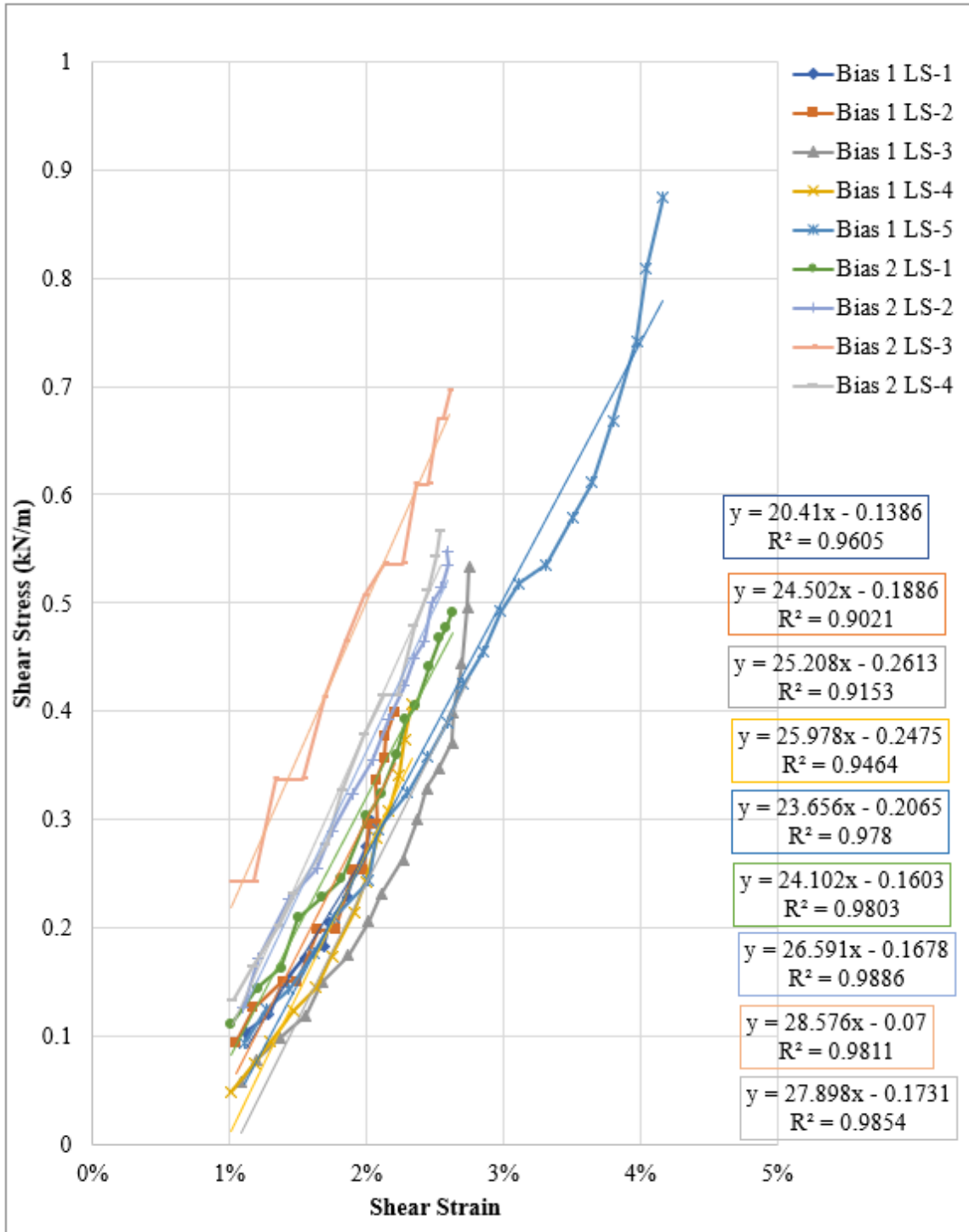


Figure 152: GgF bias trials 1-2, 1-5% shear strain range.

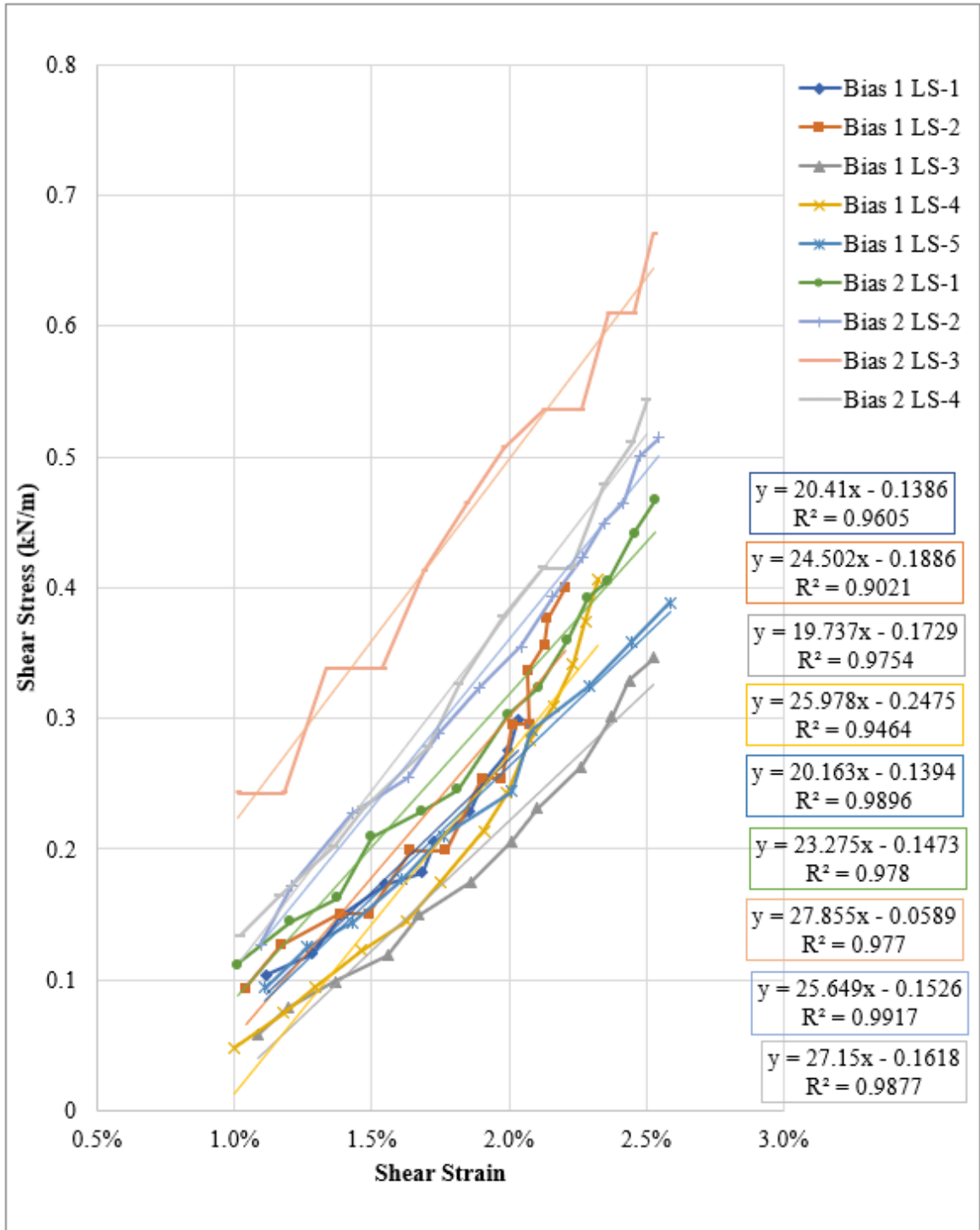


Figure 153: GgF bias trials 1-2, 1-2.5% shear strain range.

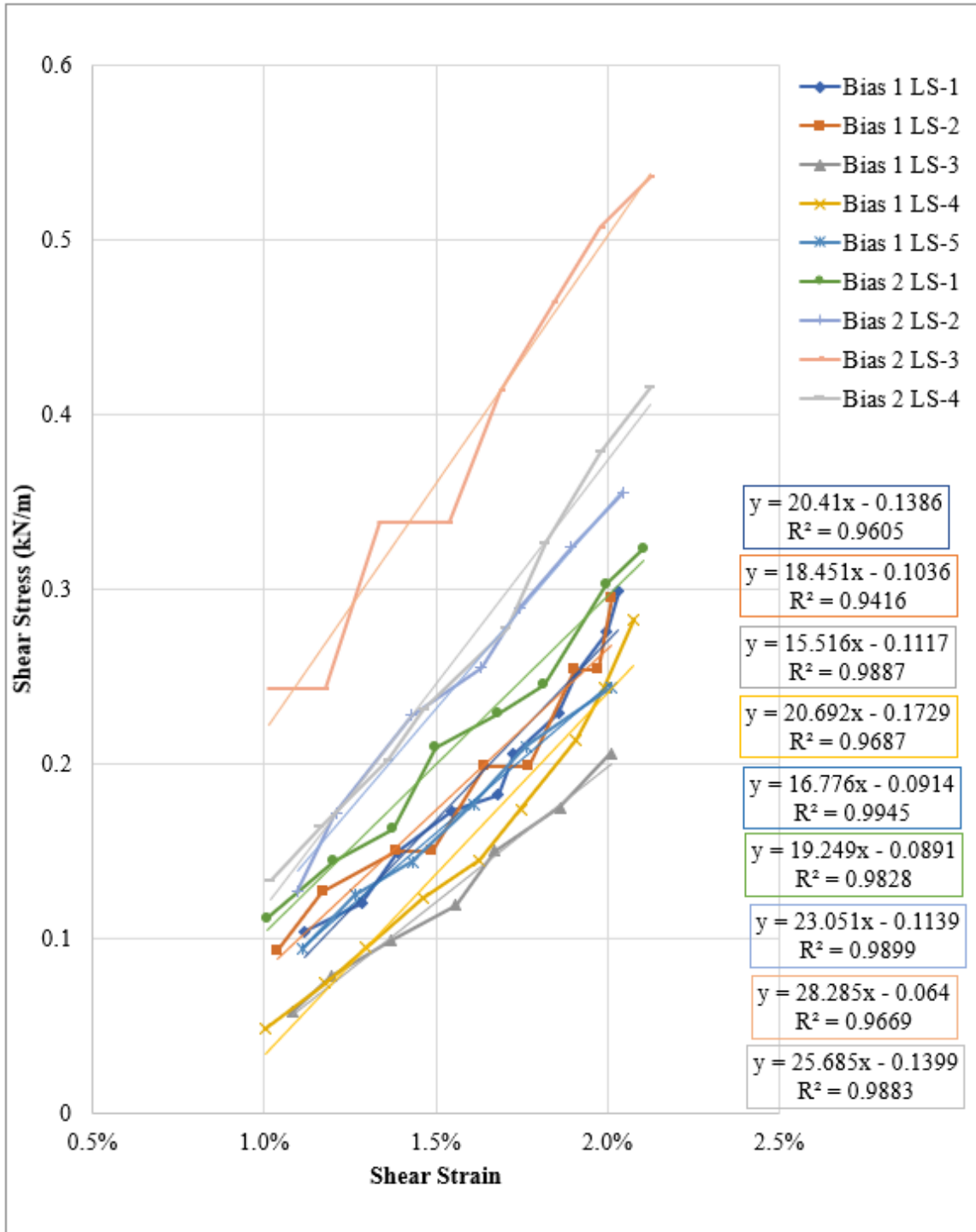


Figure 154: GgF bias trials 1-2, 1-2% shear strain range.

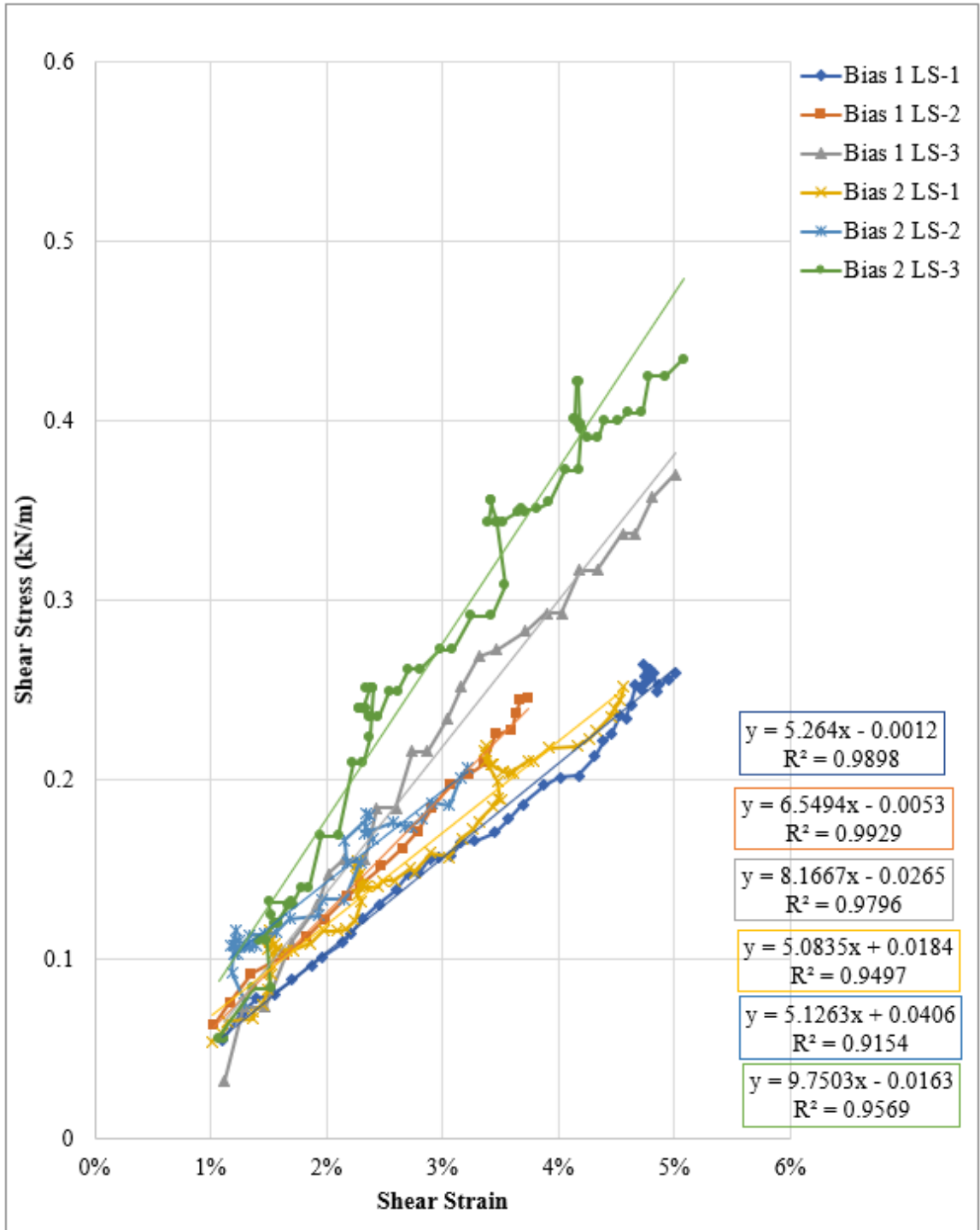


Figure 155: GgC bias trials 1-2, 1-5% shear strain range.

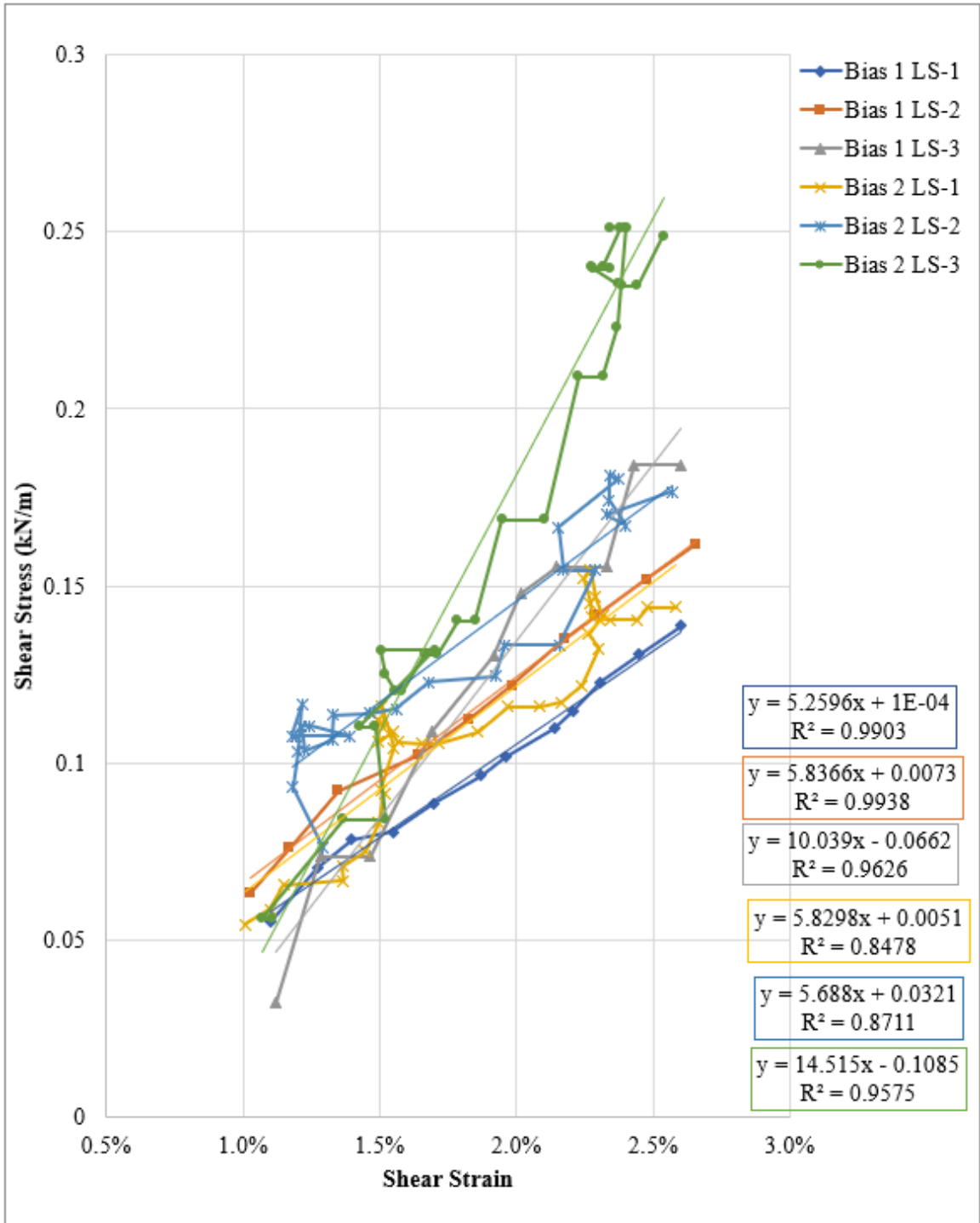


Figure 156: GgC bias trials 1-2, 1-2.5% shear strain range.

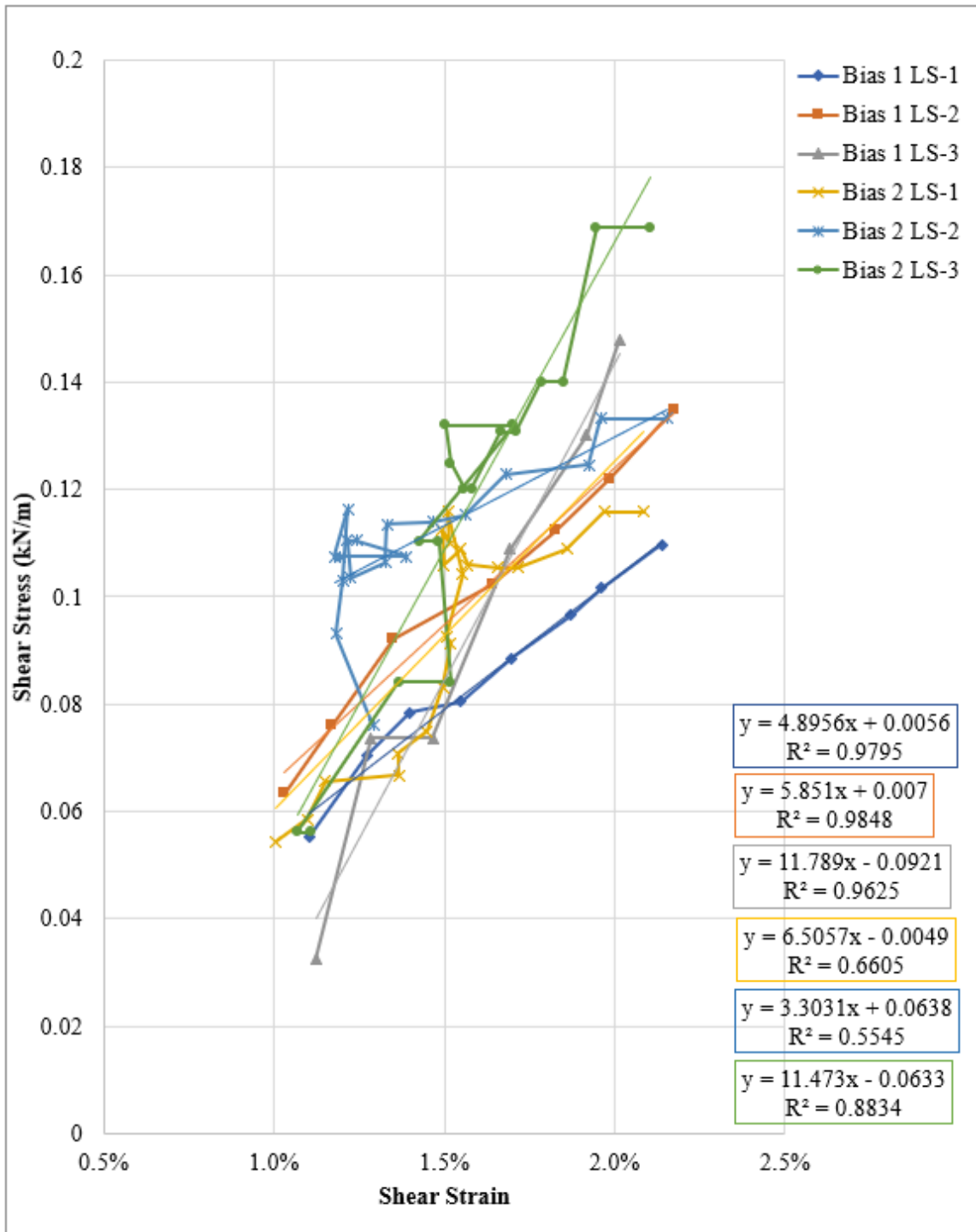


Figure 157: GgC bias trials 1-2, 1-2% shear strain range.

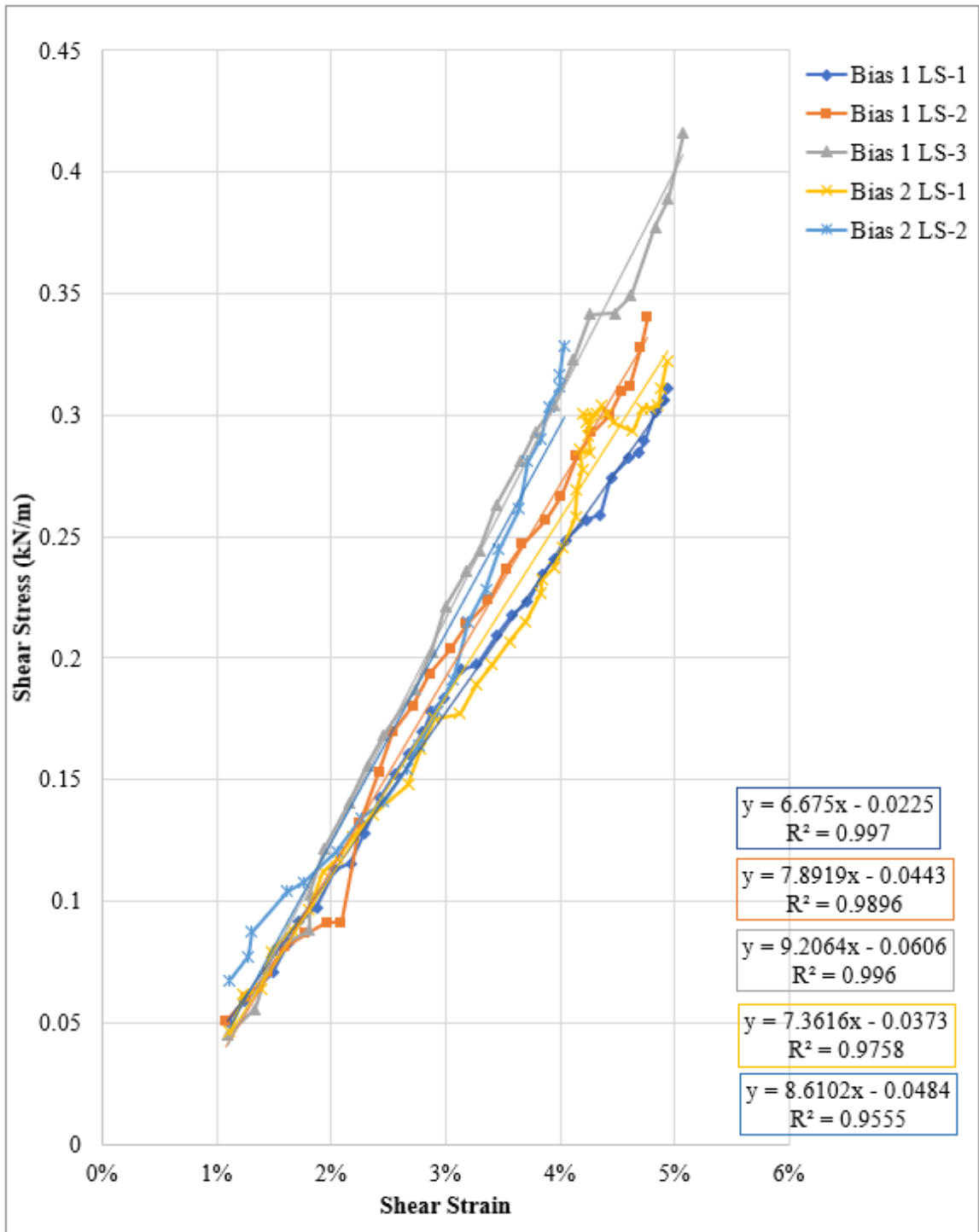


Figure 158: GgD bias trials 1-2, 1-5% shear strain range.

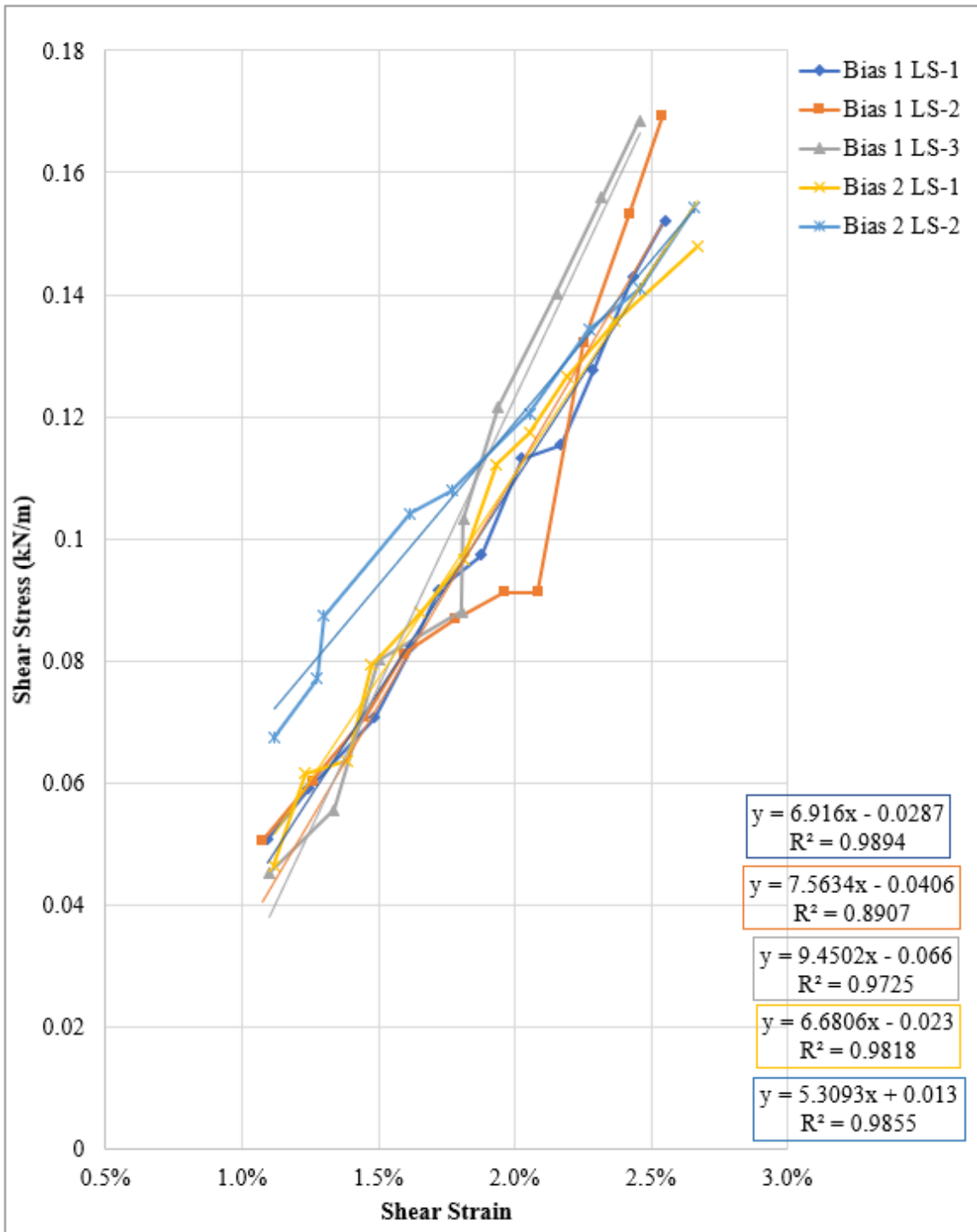


Figure 159: GgD bias trials 1-2, 1-2.5% shear strain range.

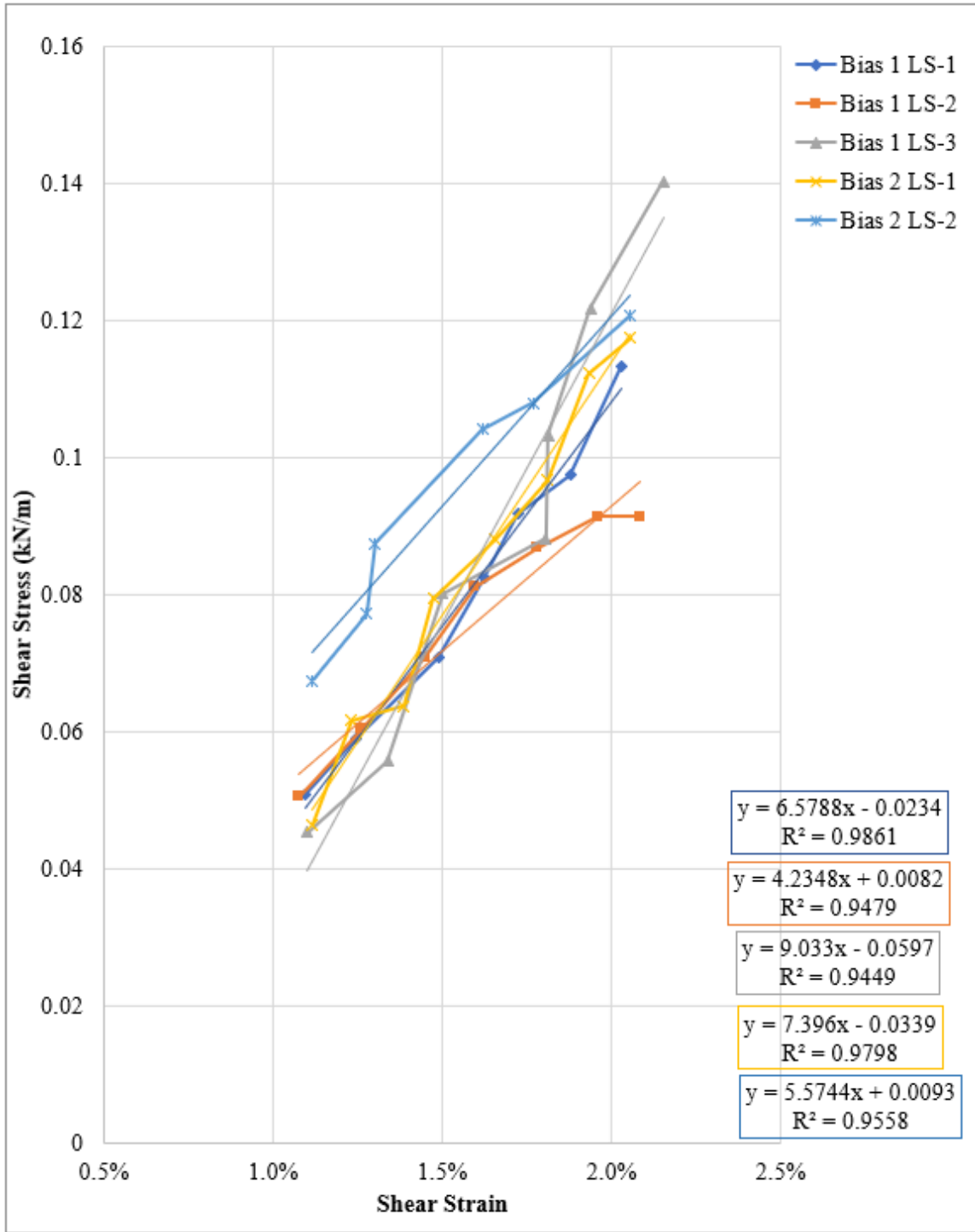


Figure 160: GgD bias trials 1-2, 1-2% shear strain range.

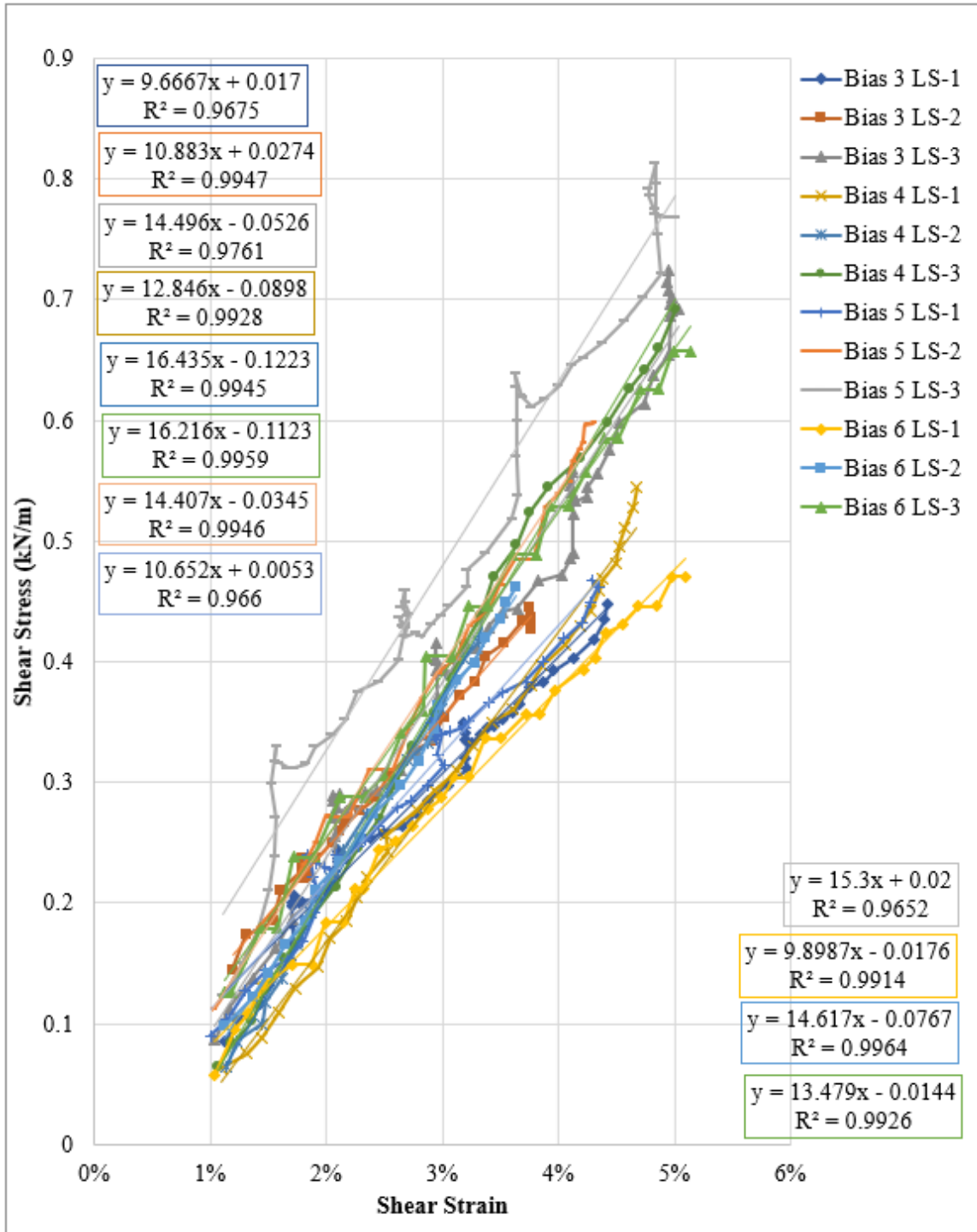


Figure 161: GgE bias trials 3-6, 1-5% shear strain range.

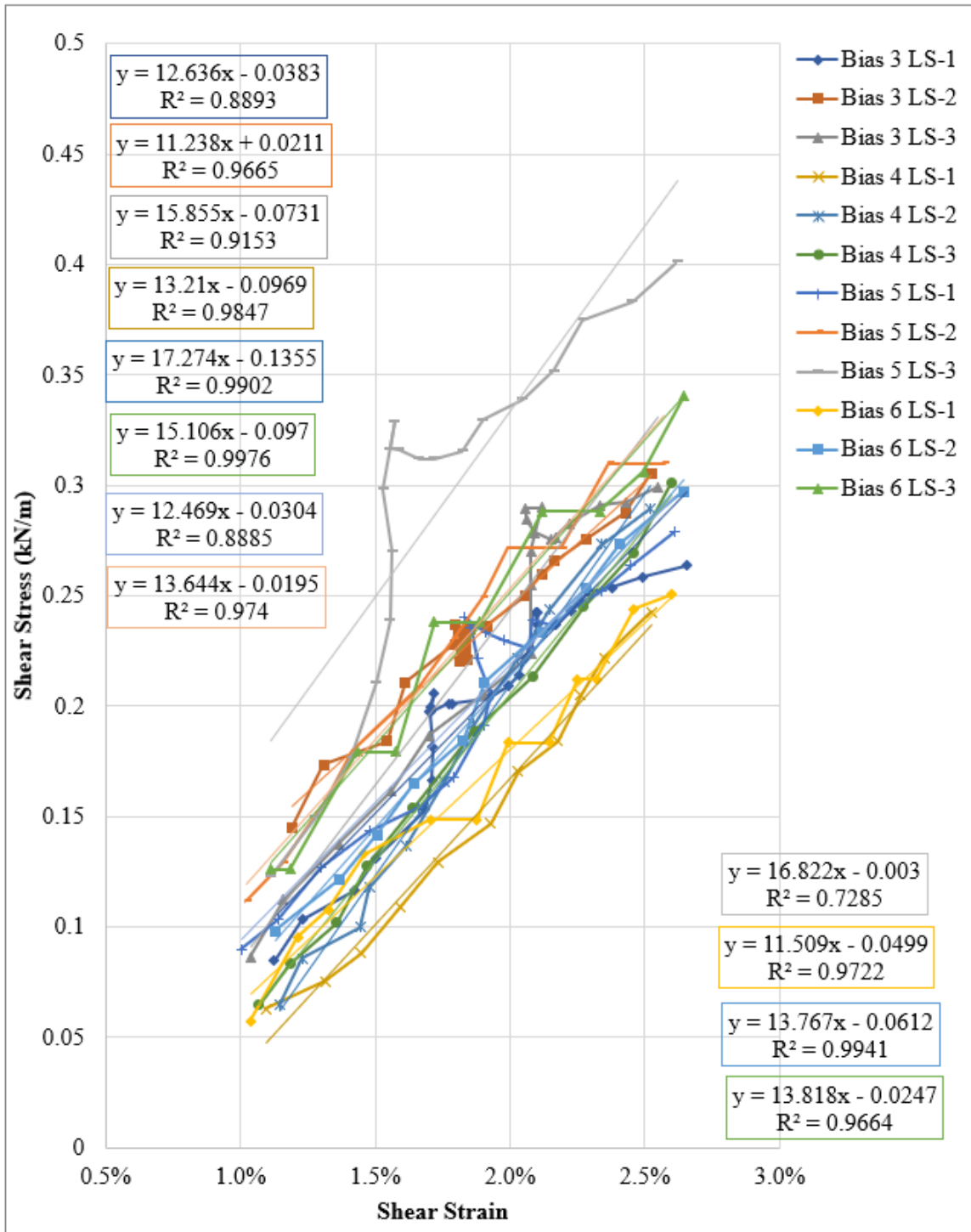


Figure 162: GgE bias trials 3-6, 1-2.5% shear strain range.

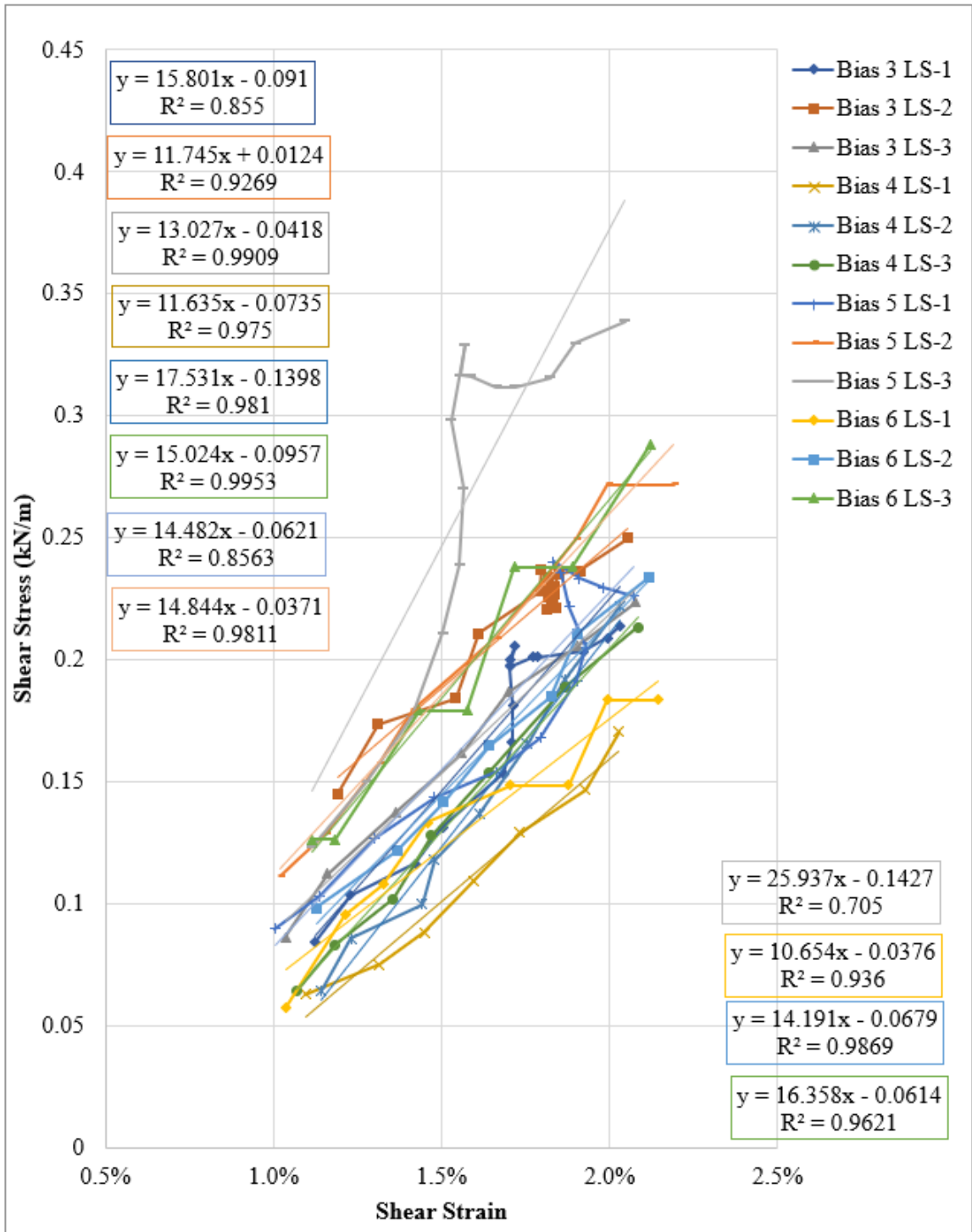


Figure 163: GgE bias trials 3-6, 1-2% shear strain range.

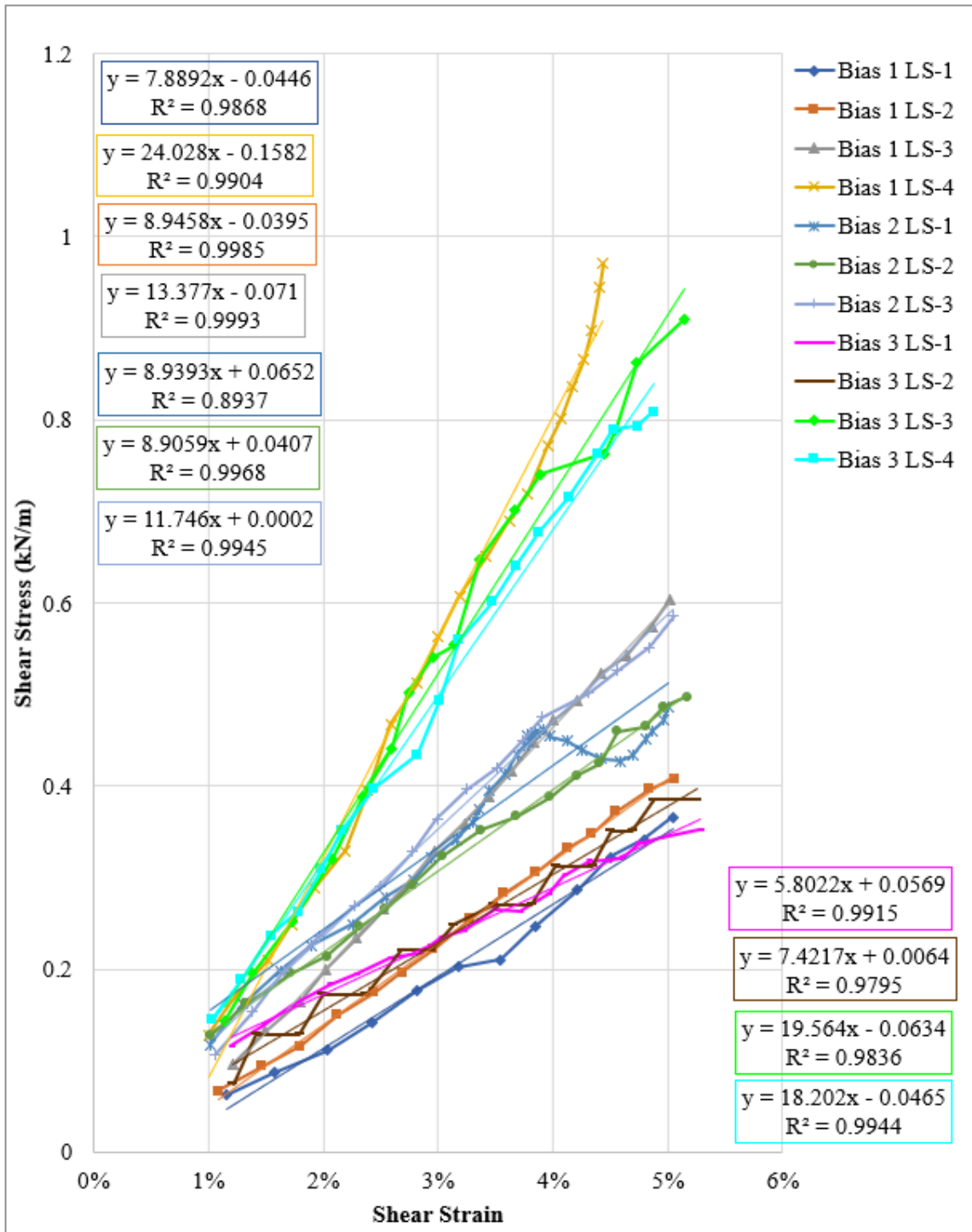


Figure 164: GtA bias trials 1-3, 1-5% shear strain range.

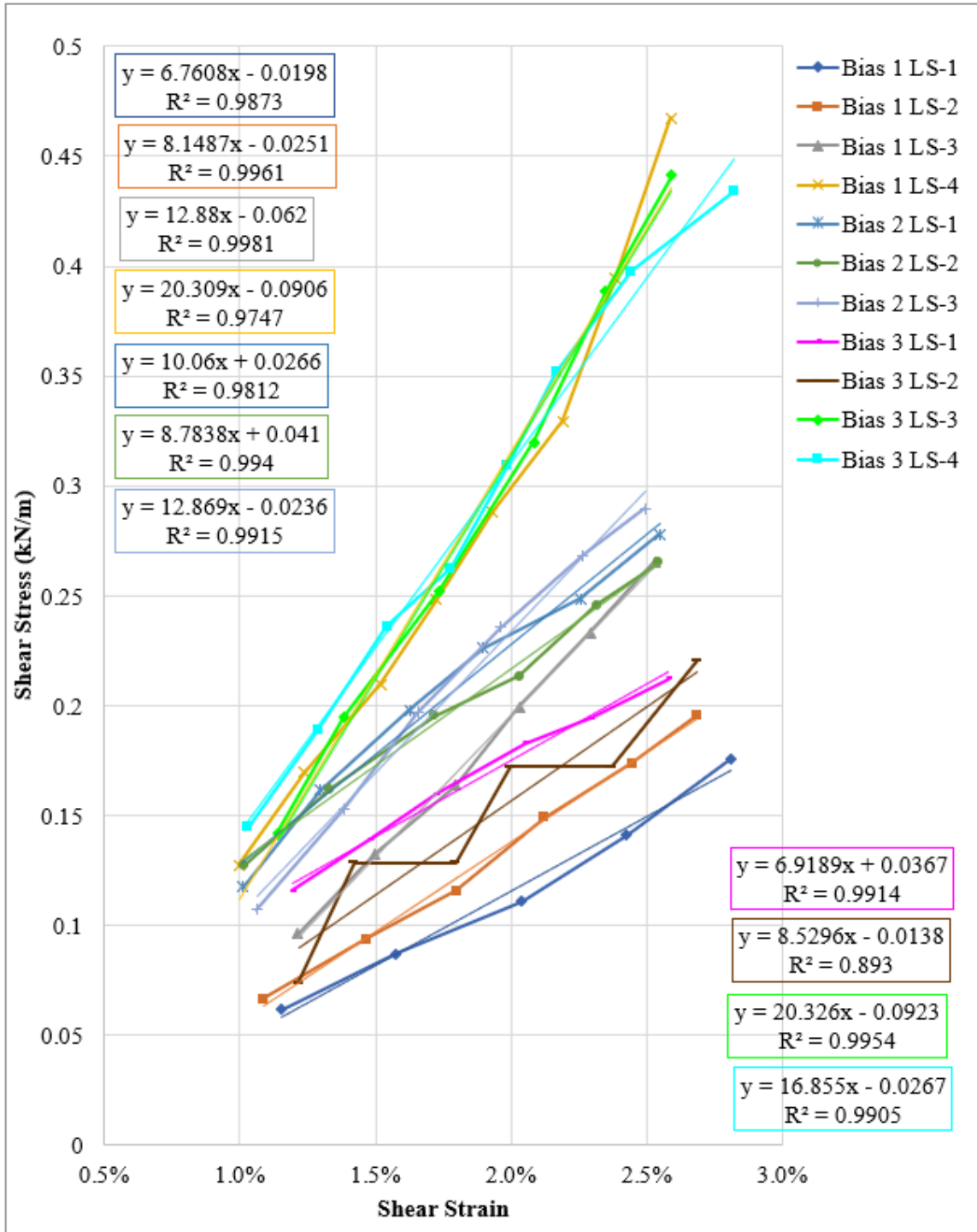


Figure 165: GtA bias trials 1-3, 1-2.5% shear strain range.

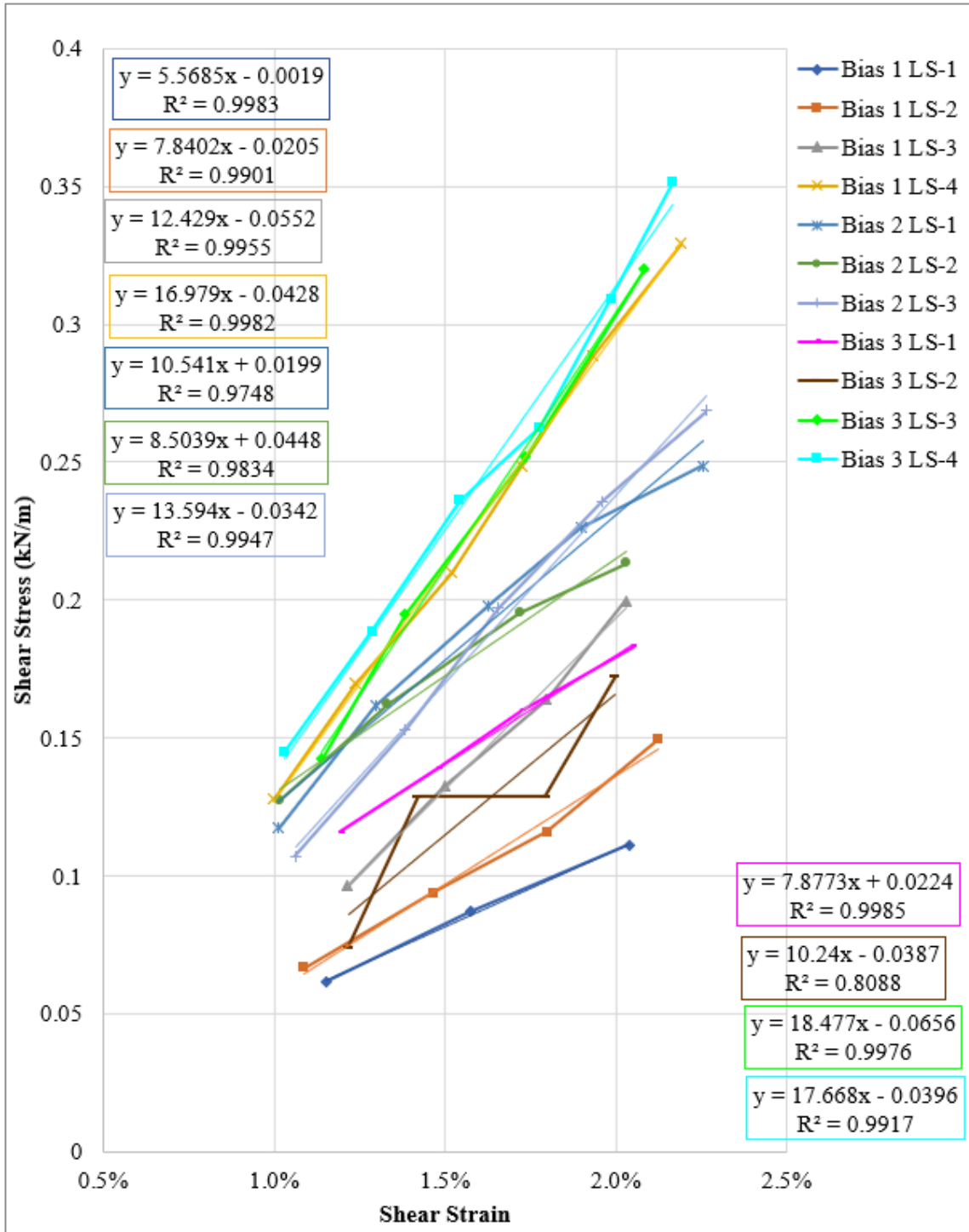


Figure 166: GtA bias trials 1-3, 1-2% shear strain range.

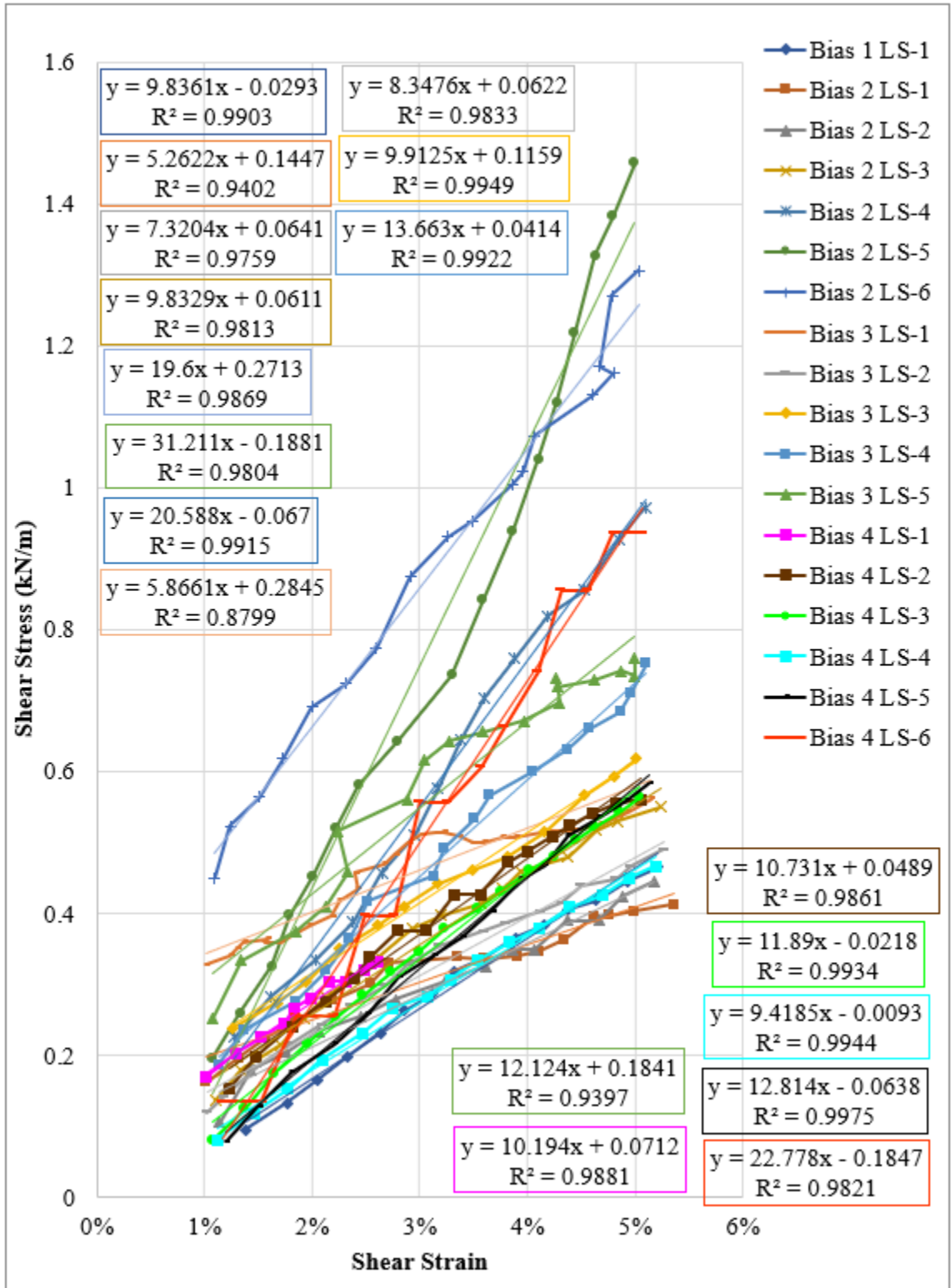


Figure 167: GtB bias trials 1-4, 1-5% shear strain range.

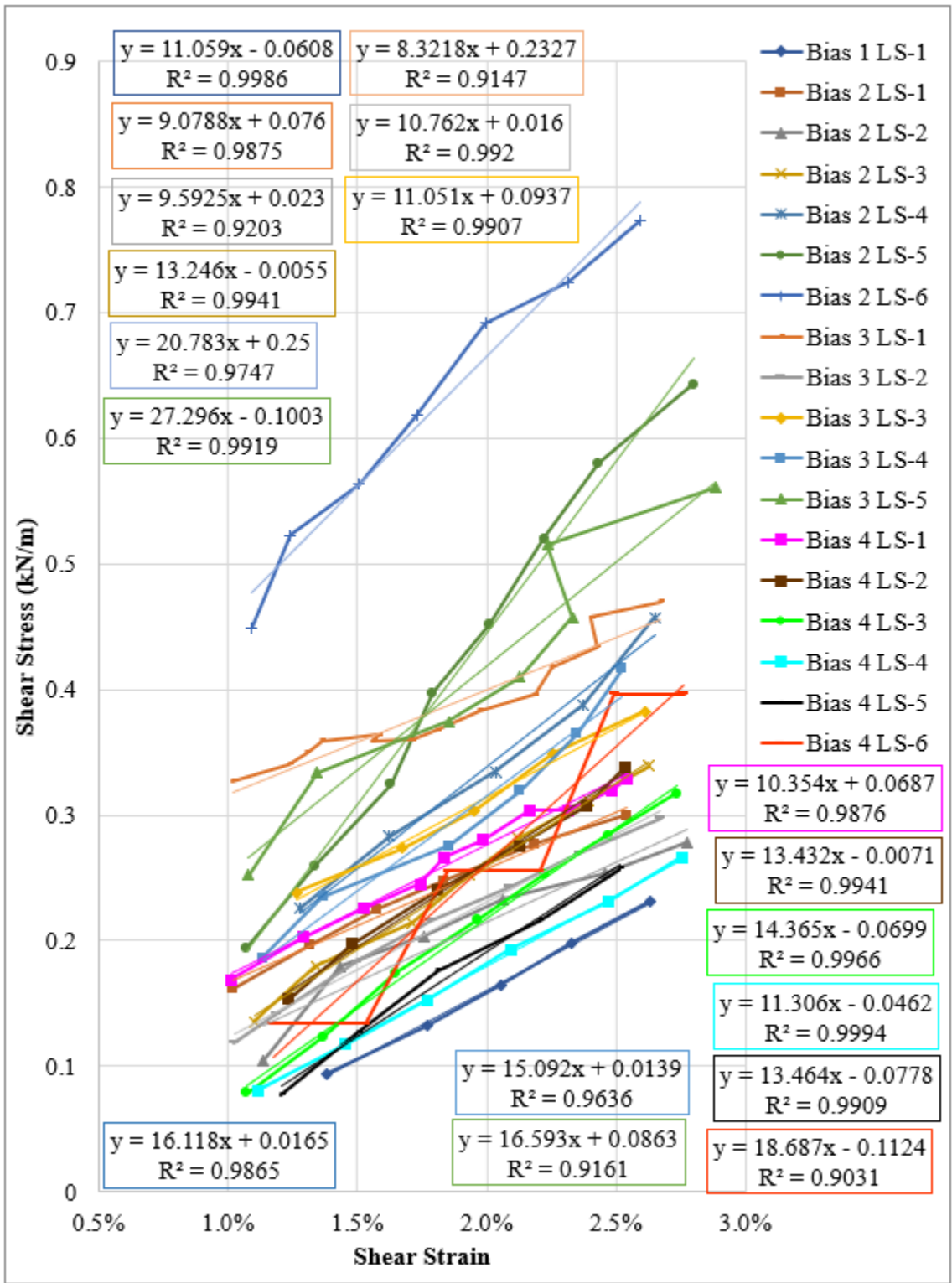


Figure 168: GtB bias trials 1-4, 1-2.5% shear strain range.

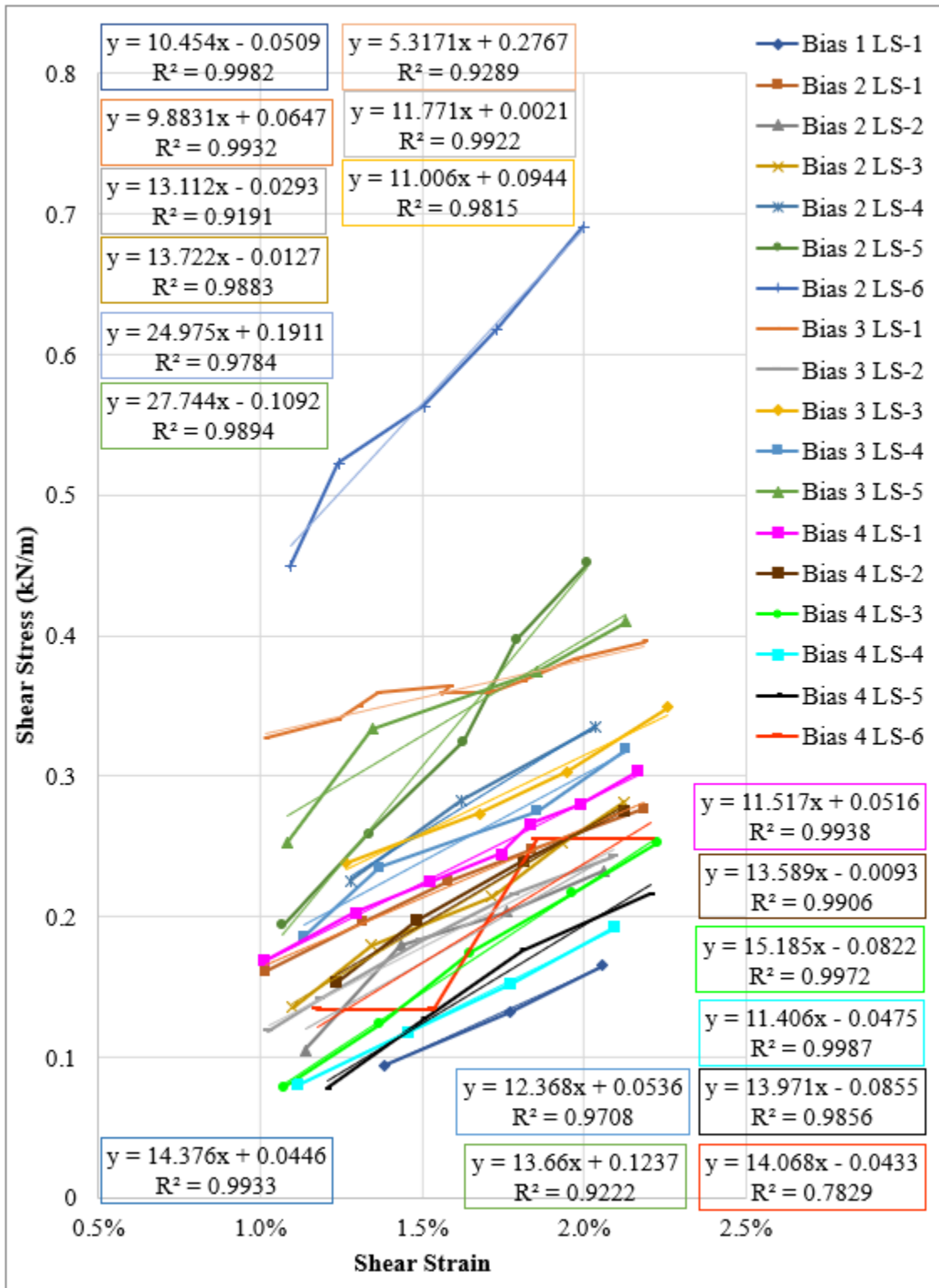


Figure 169: GtB bias trials 1-4, 1-2% shear strain range.

APPENDIX D

CALCULATED VERSUS MEASURED SHEAR STRESS PLOTS

Overview

This appendix is organized by material architecture (rectangular geogrid, square geogrid, and geotextile), and then alphabetically by material ID (e.g. GgA). Plots show measured shear stress on the Y axis and calculated shear stress on the X axis. The calculated shear stress was obtained using shear modulus values from Table 15 and measured shear strain data from the inner region. Most materials showed good fit using the average shear modulus value suggested from data analysis; however, Geogrid B, Geogrid F, and Geogrid E appeared to have a better fit with an adjusted modulus value, and these have plots for both values. The adjusted modulus values are also presented in Table 15. The range of shear stress for all plots corresponds to a shear strain range of 1-5%, and outlier load steps noted in Table 12 (Chapter Six, page 167) have been removed.

Table 15: Shear modulus values for shear stress comparison.

Architecture:	Rectangular Geogrid			Square Geogrid			Geotextiles	
Material:	GgA	GgB	GgF	GgC	GgD	GgE	GtA	GtB
Best Avg Trendline G (kN/m):	7	28	23	6	7	14	9	12
Adjusted Best Fit G (kN/m):	--	23	16	--	--	12	--	--

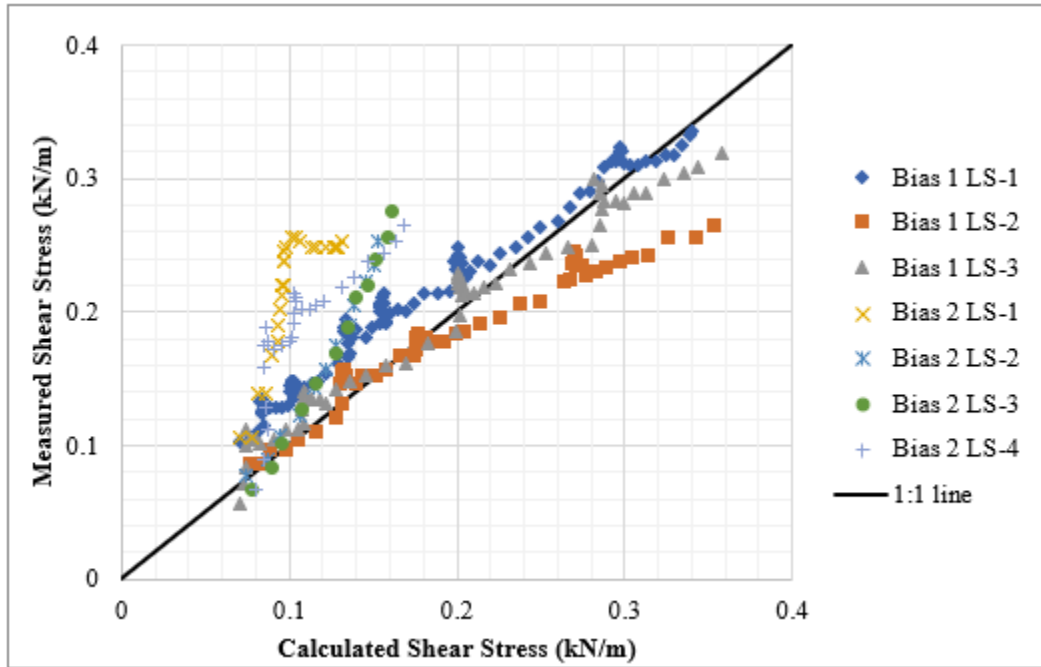


Figure 170: GgA calculated vs. measured shear stress, average trendline G.

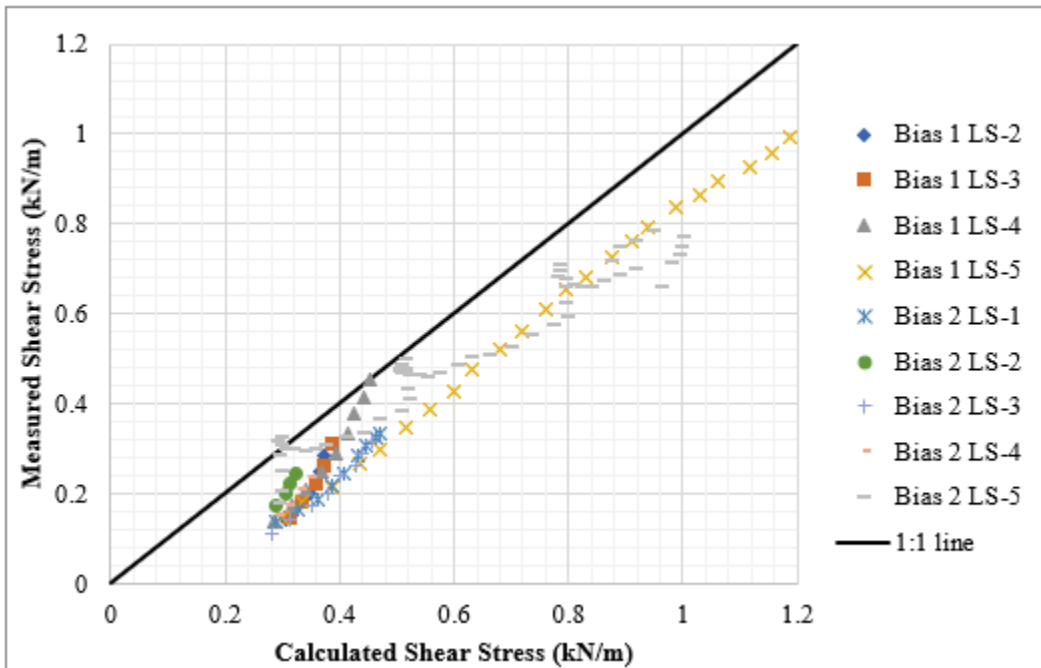


Figure 171: GgB calculated vs. measured shear stress, average trendline G.

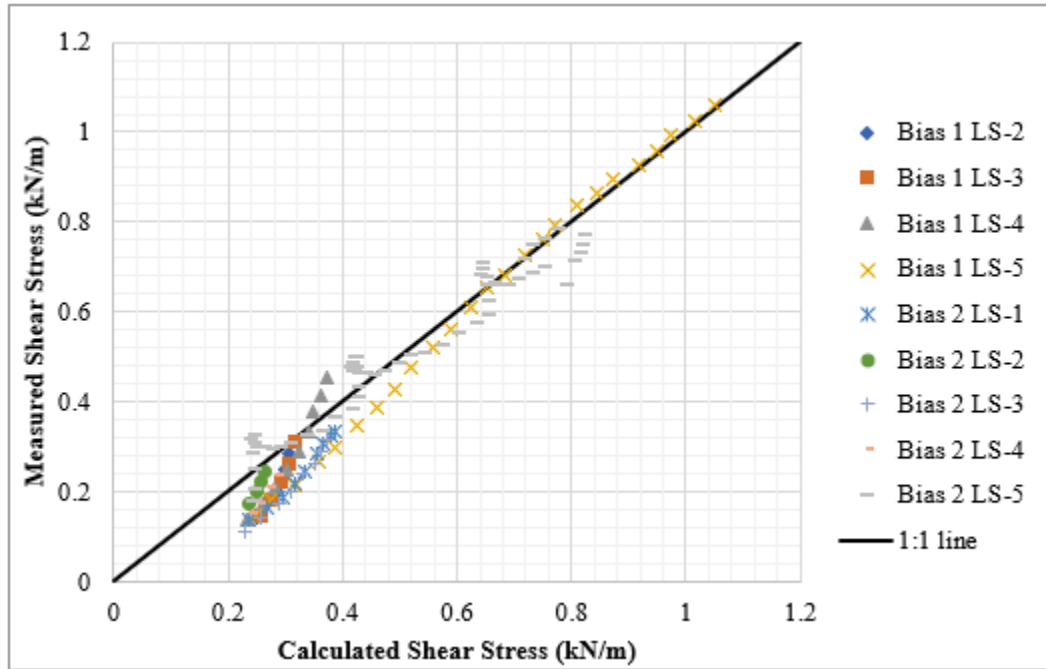


Figure 172: GgB calculated vs. measured shear stress, best fit G.

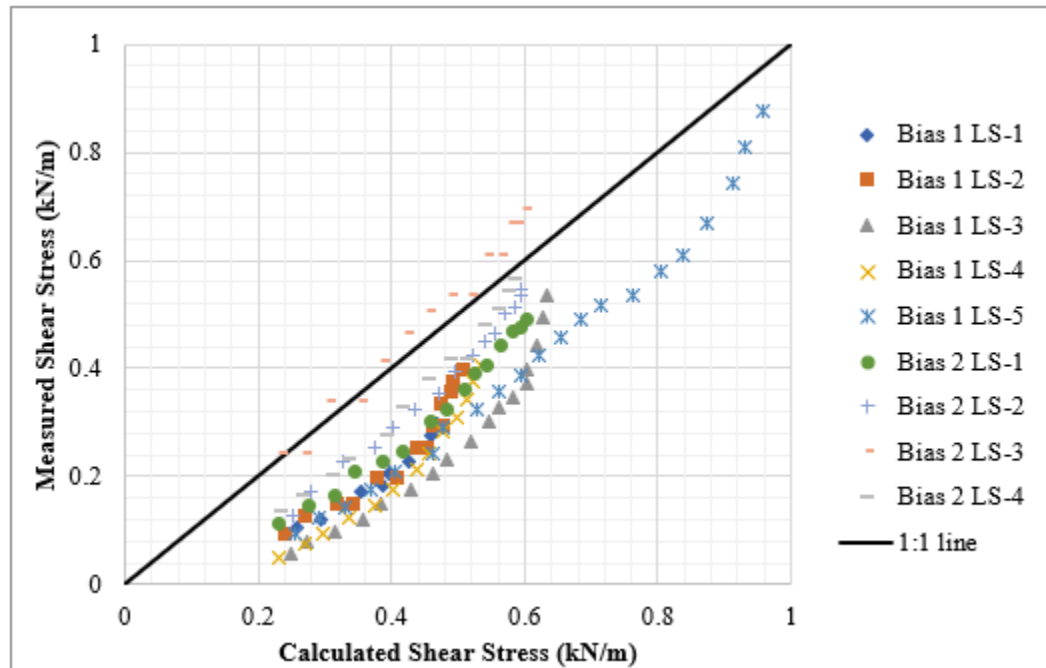


Figure 173: GgF calculated vs. measured shear stress, average trendline G.

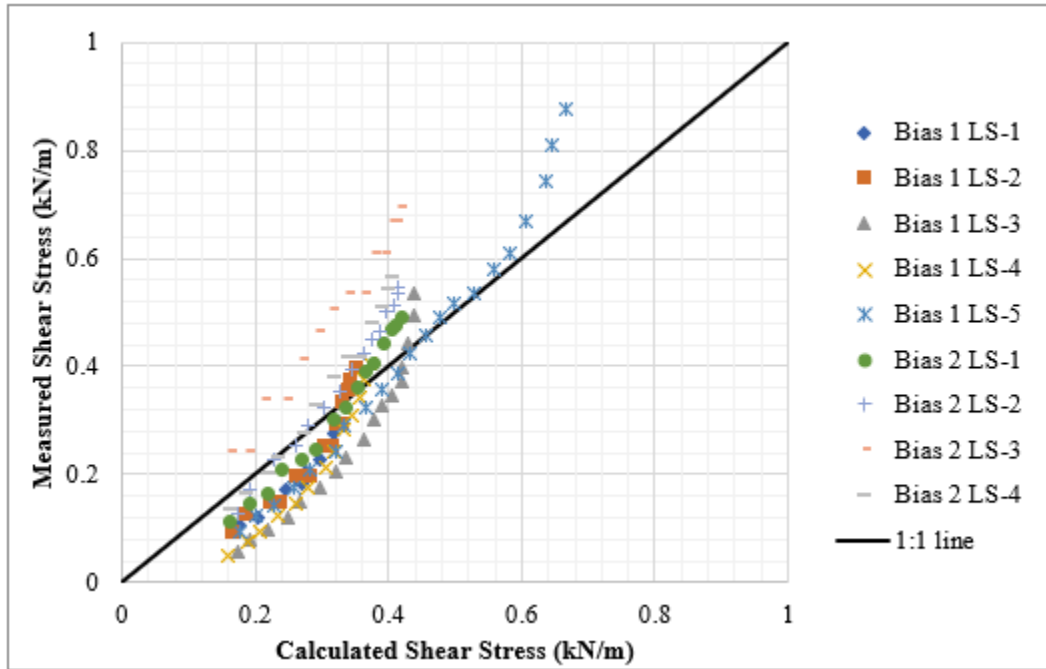


Figure 174: GgF calculated vs. measured shear stress, possible best fit G.

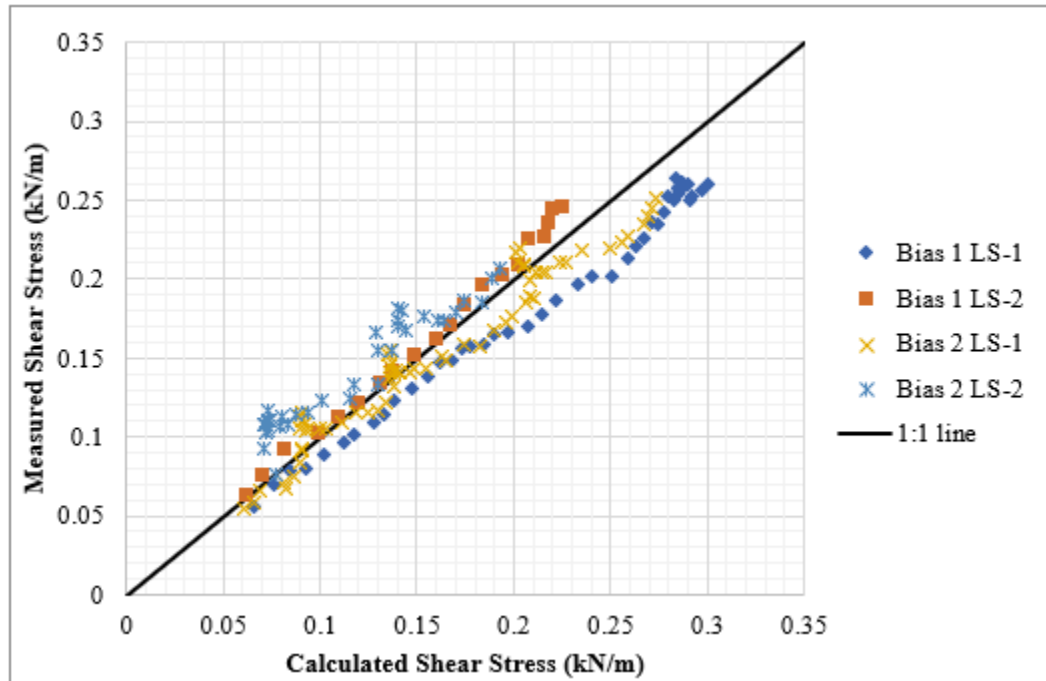


Figure 175: GgC calculated vs. measured shear stress, average trendline G.

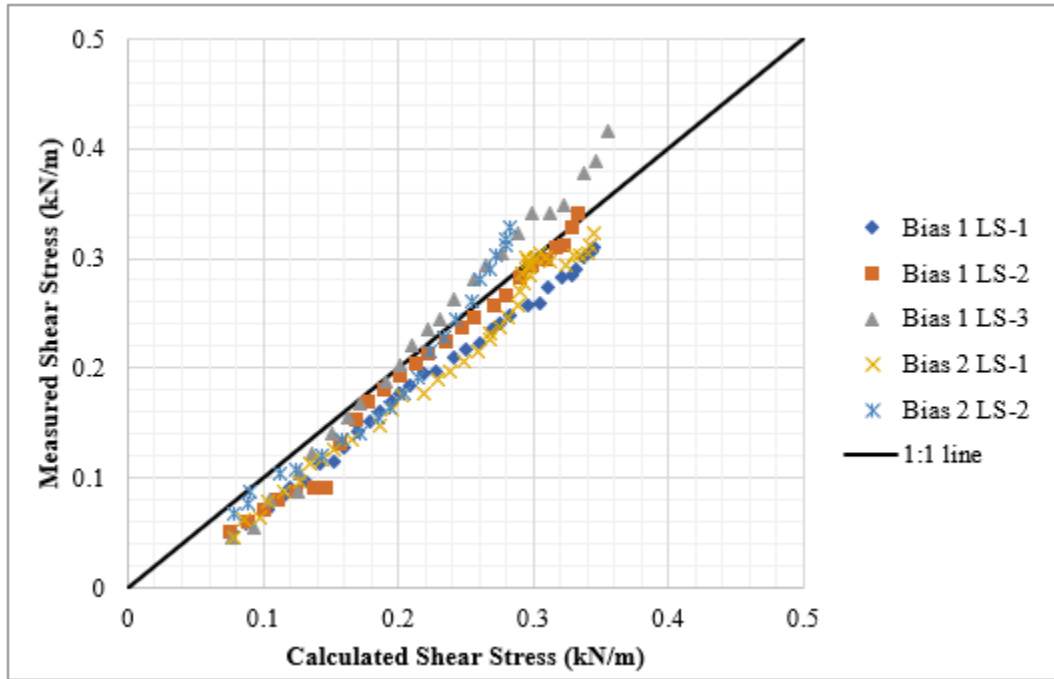


Figure 176: GgD calculated vs. measured shear stress, average trendline G.

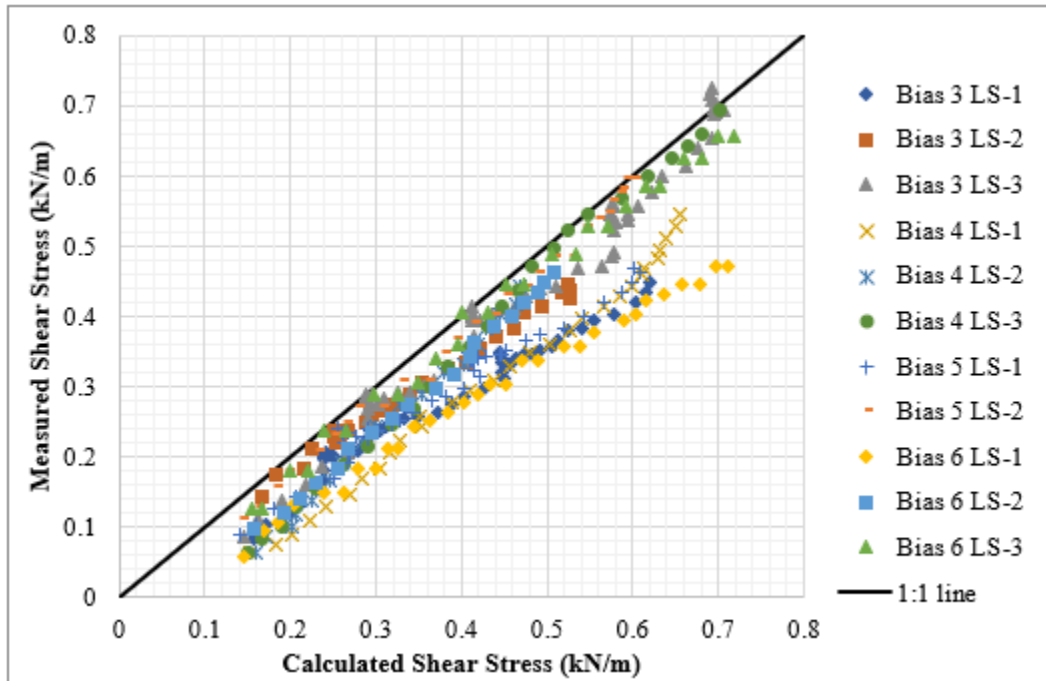


Figure 177: GgE calculated vs. measured shear stress, average trendline G.

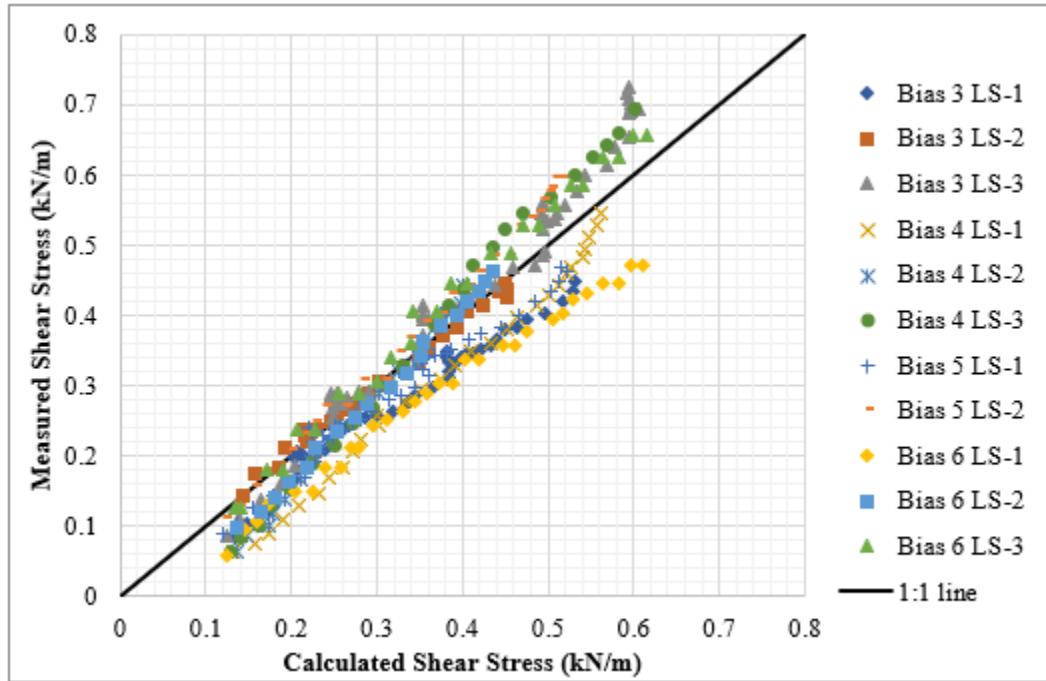


Figure 178: GgE calculated vs. measured shear stress, possible best fit G.

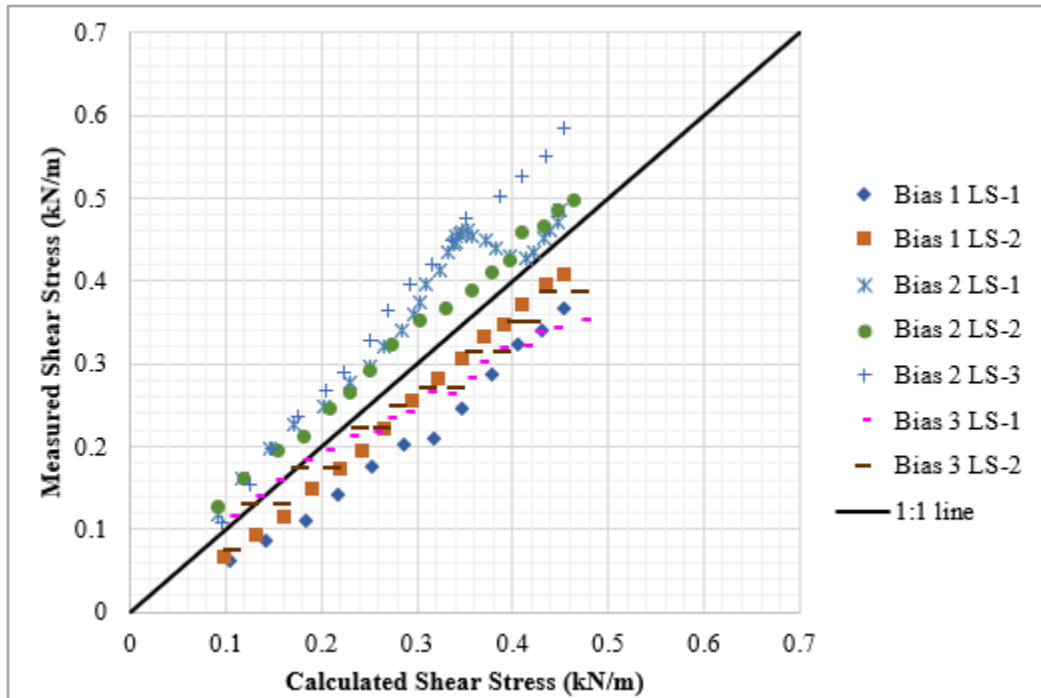


Figure 179: GtA calculated vs. measured shear stress, average trendline G.

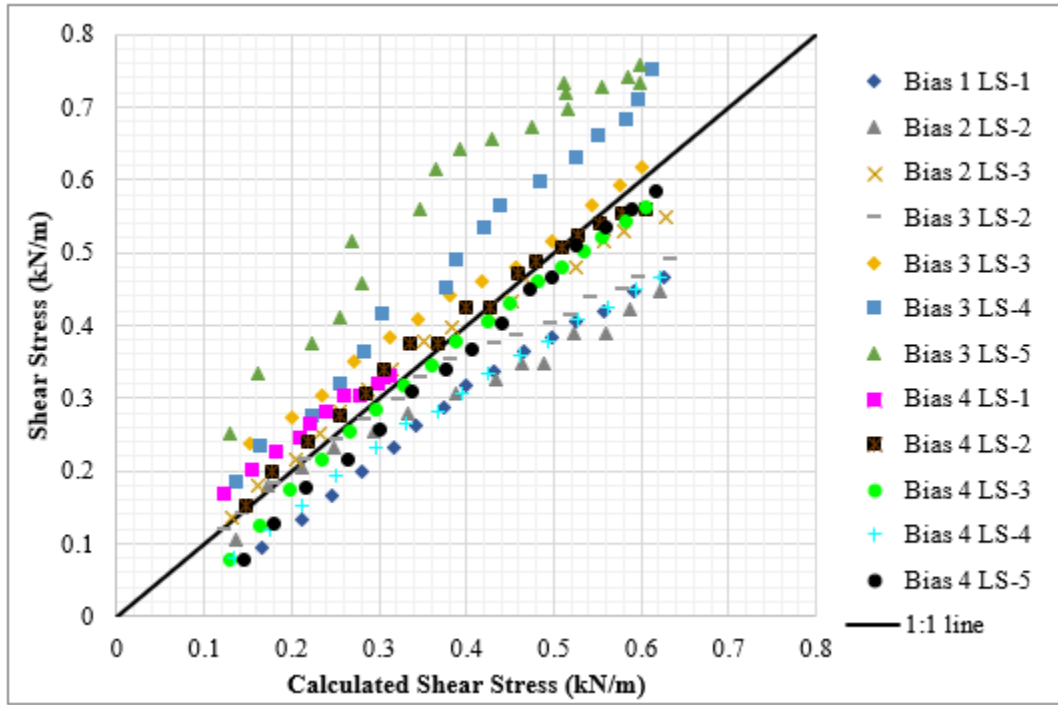


Figure 180: GtB calculated vs. measured shear stress, average trendline G.